Domain wall spintronics in novel magnetic nanostructures

Héctor Corte-León

Department of Physics

Royal Holloway, University of London

A thesis for the degree of Doctor of Philosophy

July 2017

Declaration of authorship

I Héctor Corte-León hereby declare that this thesis and the work presented in it is entirely my own. Where I have consulted the work of others, this is always clearly stated.

Signed: …………………………………………………..

Date:………………………………………………….

Declaration of authorship

Abstract

Magnetic domain walls (DWs) could form the basis of potential novel magnetic based memory, logic, and Lab-On-a-Chip devices, with a great potential to increase performance and enable new processes. Being DW detection and manipulation the main obstacle to overcome to achieve integration into new devices. The aim of this thesis is to investigate the manipulation and tracking of DWs through electrical measurements, and study the effect of localized magnetic moments on DW dynamics.

Study of DW dynamics inside of in-plane magnetization devices is performed using L-shaped magnetic nanostructures. The L-shaped devices are used as a DW trap to study DW tracking using magnetoresistance (MR) measurements. It is shown, through magnetic force microscopy (MFM) imaging, that the L-shaped nanostructures of certain dimensions geometrically constrain the magnetization to four specific remanent states (i.e. referring to the magnetization at the corner of the L-shape: head-to-head DW, tail-to-tail DW, tail-to-head and head-to-tail magnetization), thus allowing the use of L-shaped devices as DW traps. Due to these simple magnetization states and using anisotropic magnetoresistance effect (AMR), which links magnetization with electrical resistance, we demonstrate that it is possible to track the magnetization and identify the magnetic state of the devices by performing MR measurements.

To ease detecting the effect of external influences on the DW dynamics, variations of the design of the L-shaped DW traps are tested. MR measurements, in combination with *in situ* MFM and micromagnetic simulations, demonstrate that square corner L-shaped nanostructures with circular disks at the end of the nanowires show a larger difference between DW pinning/depinning fields, and have a more symmetric behaviour when magnetic field is applied at different angles.

Magnetic bead (MB) detection experiments are performed by placing a single superparamagnetic bead near the DW pinning position on top of the L-shaped nanostructure. The placement is done using micromanipulation. The results demonstrate detectable influence of the MB for L-shaped devices with widths below 200 nm. Additionally, simulations demonstrate existence of two DW depinning mechanisms, which appear at different field orientations. In the first depinning mechanism, the DW at the corner remains pinned and is annihilated by another moving DW, hence, no influence of the MB is detected. In the second

depinning mechanism, the original DW depins by moving from the corner and, hence, it is affected by the MB.

To complement the detection experiments, atomic force microscopy (AFM) probes modified with a MB attached are used. Magnetic scanning gate microscopy (mSGM) is used to move the MB around the L-shaped nanostructure at different heights, and measure the sensing volume of the L-shaped devices.

Planar Hall effect (PHE) measurements, perform on hybrid Py/Au junctions demonstrate larger changes in resistance than the analogous AMR-based magnetization tracking techniques. Moreover, by performing mSGM in the PHE geometry, we demonstrate that PHE type of measurements can also be used to detect single MB, with a sensing volume similar that of the L-shaped nanostructures.

Study of DW dynamics in out-of-plane magnetization nanostructures is carried out on CoFeB nanostructures. We study the anomalous Hall effect (AHE) and the anomalous Nernst effect (ANE) and how these two effects can be used to track magnetization in nanostructures and potentially be implemented to detect MBs. Additionally, the experiments with CoFeB devices measuring the AHE and ANE, in combination with differential phase contrast imaging, allow to measure the stray field of the MB used for measuring the sensing volume in in-plane devices.

MFM imaging complements MR measurements when studying magnetization evolution. However, when studying DW dynamics, probe-sample interaction has to be carefully analysed. In the last part of this thesis we study custom-made MFM probes with nanostructures lithographically defined onto the probe's tip and compare them with standard MFM probes. Electron holography experiments in combination with *in situ* MFM imaging demonstrate that the magnetization states of the custom-made probes can be controllably switched into two high magnetic moment states, and two low moment states, both exhibiting high switching fields. This enables the use of custom-made probes to study samples that exhibit appreciable probe/sample interaction, and therefore require a probe with high coercivity and low moment.

Table of contents

Acknowledgements

List of publications

First author

[1]   Corte-León H., Krzysteczko P., Schumacher H. W., Manzin A., Antonov V. and Kazakova O., Tailoring of domain wall devices for sensing applications *IEEE Trans. Magn.* 2–5, (2014)

[2]   Corte-León H., Nabaei V., Manzin A., Fletcher J., Krzysteczko P., Schumacher H. W. and Kazakova O., Anisotropic Magnetoresistance State Space of Permalloy Nanowires with Domain Wall Pinning Geometry *Sci. Rep.* **4** 6045, (2014)

[3]   Corte-León H., Krzysteczko P., Schumacher H. W., Manzin A., Cox D., Antonov V. and Kazakova O., Magnetic bead detection using domain wall-based nanosensor *J. Appl. Phys.* **117** 17E313, (2015)

[4]   Corte-Leon H., Beguivin A., Krzysteczko P., Schumacher H. W., Manzin A., Cowburn R. P., Antonov V. and Kazakova O., Influence of Geometry on Domain Wall Dynamics in Permalloy Nanodevices *IEEE Trans. Magn.* **51** 1–4, (2015)

[5]   Corte-León H., Gribkov B., Krzysteczko P., Marchi F., Motte J-F., Schumacher H. W., Antonov V. and Kazakova O., Magnetic scanning gate microscopy of a domain wall nanosensor using microparticle probe *J. Magn. Magn. Mater.* **400** 225–9, (2016)

[6]   Corte-León H., Krzysteczko P., Marchi F., Motte J-F., Manzin A., Schumacher H. W., Antonov V. and Kazakova O., Detection of a magnetic bead by hybrid nanodevices using scanning gate microscopy *AIP Adv.* **6** 056502, (2016)

[7]   Corte-León, H. et al. Magnetic scanning gate microscopy of CoFeB lateral spin valve. AIP Adv. 7, 56808, (2017).

[8]   Corte-León H., Manzin A., Krzysteczko P., Schumacher H. W., Antonov V. and Kazakova O. Hybrid normal metal/ferromagnetic nanojunctions for domain wall tracking. *Sci. Rep.* **17** 09186, (2017)

[9] Corte-León H., Rodríguez L. A., Pancaldi M., Cox D., Snoeck E., Antonov V., Vavassori P. and Kazakova O., Magnetic Force Microscopy Imaging Using Domain Walls. *ACS Nano.* (Submited)

Co-author

[1] Beguivin A., Corte-León H., Manzin A., Nabaei V., Krzysteczko P., Schumacher H. W., Petit D., Cowburn R. P. and Kazakova O., Simultaneous magnetoresistance and magneto-optical measurements of domain wall properties in nanodevices *J. Appl. Phys.* **115** 17C718, (2014)

[2] Manzin A., Nabaei V., Corte-León H., Kazakova O., Krzysteczko P. and Schumacher H. W., Modeling of Anisotropic Magnetoresistance Properties of Permalloy Nanostructures *IEEE Trans. Magn.* **50** 1–4, (2014)

[3] Puttock R., Corte-Leon H., Neu V., Cox D., Manzin A., Antonov V., Vavassori, P.; Kazakova, O. V-Shaped Domain Wall Probes for Calibrated Magnetic Force Microscopy. IEEE Trans. Magn. 2017, 1–1. (2017)

[4] Mohammed H., *et al.* Angular Magnetoresistance of Nanowires with Alternating Cobalt and Nickel Segments. *IEEE Trans. Magn.* **9464,** 1–1 (2017).

[5] Panchal V., *et al.* Calibration of multi-layered probes with low/high magnetic moments. *Sci. Rep.* **(In Press).**

List of figures

List of tables

List of abbreviations

AFM: Atomic force microscopy.

AHE: Anomalous Hall effect.

AMR: Anisotropic magnetoresistance.

ANE: Anomalous Nernst effect.

DW: Domain wall.

EH: Electron holography.

FIB: Focused ion beam.

GMR: Giant magnetoresistance.

HH: Head to head domain wall.

LSV: Lateral spin valve.

MB: Magnetic bead.

MFM: Magnetic force microscopy.

MOKE: Magneto-optical Kerr effect.

MR: Magnetoresistance.

mSGM: Magnetic scanning gate microscopy.

MTJ: Magnetic tunnel junction.

PHE: Planar Hall effect.

PLC: Power line cycle.

PSD: position sensitive detector.

SPM: Scanning probe microscopy.

SV: Spin valve.

TMR: Tunnel magnetoresistance.

TT: Tail to tail domain wall.

a.u.: Arbitrary units.

1 Introduction

Improving human health is one of the main challenges faced by science. New imaging techniques, such as magnetic resonance imaging, combined with the discovery of new drugs, have cured many illness and prevented many others. However, we are at a point now where **personalized treatments which change from patient to patient are required**, and hence laboratory tests need to have a qualitative improvement in order to deal with the high demand. In particular, **analytical laboratories need to be automated and miniaturized to reduce costs** and improve speed. To achieve this goal, the concept of Lab-On-a-Chip and high-throughput screening was developed[1]–[4], which consists in automatized tests realized on the surface of a chip. In this way, it is possible to design specific chips to perform individual tasks, and by combining them together, replicate the capabilities of a fully equipped laboratory.

For instance, one successful approach uses microfluidic channels where small droplets (or a continuous flow of fluid) are injected and carry cells[1], [3], proteins[5], or drugs[6], tagged with micron-sized beads. The attachment of substances to micron beads is done by **functionalizing the surface of the beads** with proteins that only form strong covalent bonds with specific targets[7]. In this way, the presence of the targets can be detected by the properties added by the beads, for instance fluorescence or magnetic moment. In the case of using **magnetic beads** (MBs), it is possible not only to detect but also to manipulate targets by applying external magnetic fields, thus overcoming the spatial resolution imposed by the size of the droplets in microfluidic channels, and allowing for new experiments[7]. For instance, by manipulating MBs with an external magnetic field it is possible to test the mechanical properties of the cell membrane[8].

With development of new nanofabrication capabilities, enabling the fabrication of nanostructures with features < 10 nm, targeted **manipulation of MBs using magnetic nanostructures has become a trend of research**[9]. For instance, the magnetic stray fields at the edges of the nanostructures, in combination with externally applied magnetic fields, allow moving a single MB along predefined paths. Using this approach it has been possible to perform mechanical excitation of cells[8], or even nanosurgery, using magnetic *swimmers* of few micrometres in length, which were navigated by magnetic fields[10], [11]. In addition, it has been demonstrated that it is possible to manipulate cells with MBs[6].

Another approach consists in **manipulation/detection of MBs using the stray field generated when a domain wall (DW) is formed between two different magnetic domains**

inside a magnetic nanostructure[12], [13]. Since the DWs can be manipulated with external fields, or better with electrical currents, this approach enables high throughput screening applications by the manipulation of MBs using the DWs[14], [15]. Moreover, since electrical current in metallic ferromagnets is carried by electrons with spin, there is an interaction between magnetization and the electrical current. This interaction allows **detecting changes in magnetization through magnetoresistance (MR) measurements**, or manipulating the magnetization using high density currents[16]. Thus, studies of DW dynamics, interactions between DWs and localized magnetic fields (e.g. from a MB) are directly linked with the development of Lab-On-a-Chip devices and contribute towards single cell/protein manipulation for biomedical applications.

In this thesis, the research is focused on DW-based detection of localized magnetic moments. To do so, we track DW movement inside of magnetic nanostructures using electrical measurements and *in situ* magnetic force microscopy (MFM) imaging. The thesis structure starts with theory and background, **chapter 2**, where the basic concepts of micromagnetism are reviewed, including the magnetoresistive effects used later on in the thesis. **Chapter 3** is dedicated to literature review, focusing the attention in tracking DWs in magnetic nanostructures at room temperature by means of electrical measurements. **Chapter 4** is a detailed summary of the experimental techniques used in this thesis. Chapters 5 to 8 describe experimental results. **Chapter 5** focuses on L-shaped nanostructures made of Py, where anisotropic magnetoresistance (AMR) is used to track DW movement. Chapter 5 underlines conditions, at which L-shaped devices can be used to detect the presence of MBs. The detection experiments are carried on using a MB either fixed on top of the nanostructure or attached to an atomic force microscopy (AFM) probe. These experiments outline the experimental conditions (i.e. applied field and geometry of the devices) under which detection of the bead can be achieved using DW dynamics. The experiments with a MB attached to the AFM probe represent a novel approach that allows comparing performance of several different devices against the same MB, and estimating the sensing volume of the specific device. **Chapter 6**, studies the planar Hall effect (PHE) using hybrid Au/Py junctions in Py nanodevices with in-plane magnetization. The purpose of this chapter is to compare PHE with AMR effect (studied in chapter 5), evaluate the possibility of using PHE to track magnetization, and to demonstrate the possibility of single MB detection using PHE. The main result of this chapter is that for the same type of devices PHE produces a larger output signal than AMR, and thus can be used to replace AMR in DW tracking. In addition, we demonstrate single MB detection using PHE,

and measure the sensing volume of the hybrid Au/Py junctions. Motivated by DW manipulation using spin currents, **chapter 7** presents results of the anomalous Hall and Nernst effects (AHE and ANE respectively) in devices with out-of-plane magnetization made of CoFeB. The out-of-plane devices form a lateral spin valve (LSV) where the spin diffusion has been suppressed by using Ta in the channel. The purpose of this chapter is to show the contribution of the AHE and the ANE to the voltage measured in LSV geometries (i.e. in the non-local spin-detection configuration). Understanding those effects (i.e. AHE and ANE) is a requirement to integrate DW-based devices with spin sources (e.g. LSV). The last results chapter, **chapter 8**, explores the application of the L-shaped devices as a part of an AFM probe. This chapter demonstrates a possibility of trapping a DW inside of the nanostructure built on the side of an AFM probe, and thus create a bi-stable probe with low/high moment. This approach allows imaging inhomogeneous samples that have areas with both hard/soft magnetization. Thus easing imaging DW-based devices as the ones studied in the previous chapters. The last chapter of the thesis, **chapter 9**, summarizes the main results and provides a future outlook in this field of research.

2 Theory and background

This chapter provides an overview of some of the basic concepts related to the magnetic properties of metal thin films. The discussed topics include the fundamental concept of ferromagnetism, the formation of domains and DWs, and the magnetoresistive effects covered in this thesis (i.e. AMR and PHE)

2.1. Ferromagnetic materials

For an electron inside an atom, the magnetic moment has two contributions, the electron spin (intrinsic magnetic moment), and the orbital moment (associated with the motion of the electron in its orbit). In the case of a free atom, the ground state is determined by taking into account the Pauli exclusion principle and the Coulomb interaction between electrons[17]. The magnetic moment of the atom appears as a combination of the individual magnetic moments of the electrons and how they are distributed among the orbitals. Inside of a solid, the interaction between the individual magnetic moment from each atom gives rise to macroscopic ordered magnetic states.
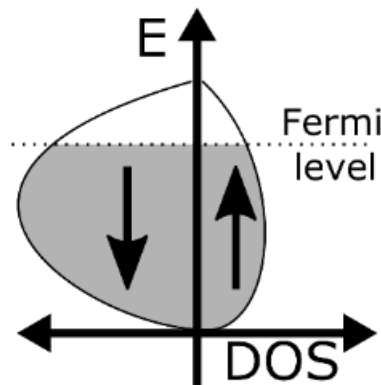
Figure 1. Energy versus density of states for electrons in a hypothetical ferromagnetic material.

In some of the transition metals (e.g. Fe, Co, and Ni) and their alloys, the unpaired electrons partially filling the 3d shells giving rise to a non-zero magnetic moment. These materials are known as ferromagnetic materials because they have a spontaneous parallel alignment of the atomic magnetic moments through a strong exchange interaction. According to the band model[18], the exchange interaction creates a difference in energy between electrons with spin up or spin down. One example is Figure 1 where the density of states (DOS) for a hypothetical ferromagnet is schematically drawn. Given a certain Fermi level, the band for spins down in Figure 1 is occupied by more electrons than the band for spins up, and thus there are more electrons with spin down. This imbalance is what creates a non-zero moment per atom.

2.1.1. Domain theory

Inside of a magnetic material, the magnetic induction $\vec{B}$ can be described as proportional to the magnetic field strength $\vec{H}$ plus the magnetization per unit of volume, $\vec{M}$, being the proportionality constant the vacuum permeability, $\mu_0 = 4\pi 10^{-2}\ N/A^2$.

$$\vec{B} = \mu_0(\vec{H} + \vec{M}) \tag{1}$$

In vacuum, $\vec{M}$ is zero, and thus $\vec{B}$ and $\vec{H}$ are proportional, but inside of the magnetic material $\vec{M}$ can be different from zero, and it is related to the magnetic field strength through the magnetic susceptibility χ_v

$$\overline{M} = \chi_v \overline{H} \tag{2}$$

This relation between $\vec{M}$ and $\vec{H}$ allows distinguishing between different types of behaviours: diamagnetic materials when $\chi_v < 0$, paramagnetic materials for $\chi_v > 0$, and ferromagnetic materials for $\chi_v \gg 0$. In order to understand the origin of relation (2) in ferromagnetic materials, it is necessary to consider the energies that appear when ferromagnetic atoms are placed in a crystal to form a bulk material.

Inside of a ferromagnetic material, the individual magnetic moments of each atom interact with each other, and the total free energy, due to magnetization-dependent terms, can be written as the next integral applied to all the volume [19]:

$$\underbrace{E_{tot}}_{Total} = \int [\underbrace{A(\nabla \vec{m})^2}_{exchange} + \underbrace{F_{an}(\vec{m})}_{anisotropy} - \underbrace{\vec{H}_{ex} \cdot \vec{M}}_{ext.field} + \underbrace{\frac{1}{2}\vec{H}_d \cdot \vec{M}}_{stray\ field} \tag{3}$$

$$- \underbrace{\vec{\sigma}_{ex} \cdot \boldsymbol{\epsilon}^0}_{ext.stress} + \underbrace{\frac{1}{2}(\vec{p}_e - \vec{\epsilon}^0) \cdot \boldsymbol{c} \cdot (\vec{p}_e - \vec{\epsilon}^0)}_{magnetostrictive}]\, dV$$

where the magnetization vector is $\vec{M} = M_s\vec{m}$ being M_s the saturation magnetization and the magnetization unit vector $m^2 = 1$.

In eq.(3) the **exchange** term has its origin in quantum mechanics and it's the result of the indistinguishable nature of electrons and the Pauli Exclusion Principle[20]. The exchange term takes into account interaction between magnetic moments and it is minimum when the magnetization is uniform. A is the exchange constant.

The **anisotropy** term is related to the crystalline anisotropy and it occurs because of the crystal lattice symmetries. Here we use the generic term F_{an} because the anisotropy term depends on the crystal structure of the solid. The two more common anisotropies are the uniaxial (one main symmetry axis) and the cubic. In spherical coordinates and expanding along z direction, the energy density for the uniaxial anisotropy can be written as:

$$\frac{E_{uniaxial}}{V} = K_0 + K_1 sin^2(\theta) + K_2 \sin^4 \theta + \cdots \tag{4}$$

where K_i are the anisotropy constants and they depend on the material. Generally eq.(4) is truncated to the second term and the sign of K_1 determines the direction of the anisotropy (i.e. $K_1 > 0$ along z axis and $K_1 < 0$ in the x-y plane).

Similarly, for the cubic anisotropy, in Cartesian coordinates we have:

$$\frac{E_{cubic}}{V} = K_0 + K_1(m_x^2 m_y^2 + m_y^2 m_z^2 + m_z^2 m_x^2) + K_2 m_x^2 m_y^2 m_z^2 \dots \tag{5}$$

The **external field** term, also called **Zeeman energy,** is the energy associated with a dipole inside of the external field $\vec{H}_{ex}$.
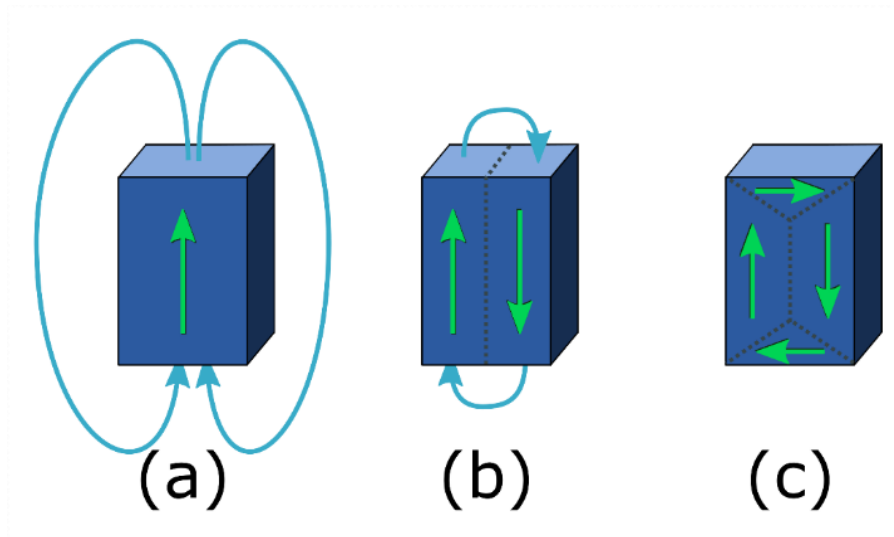
Figure 2. Green arrows represent magnetization direction inside of the material and blue arrows represent stray magnetic field. The stray field interaction determines if the material forms a single domain (a), multiple domains with stray field (b), or multiple domains without stray field (c).

The **stray field** term, also called the **magnetostatic** term or the **demagnetization energy**, is the result of the dipolar interaction. The exchange term is reduced by aligning magnetic moments parallel, thus reducing the energy of the system at the cost of producing stray

magnetic fields (see Figure 2(a) and (b)). However, the dipolar interaction tries to align magnetic moments antiparallel, thus decreasing the total energy of the system by reducing the stray magnetic fields (Figure 2(c)). The valance between the two terms, is what generates magnetic domains inside of the material (Figure 2(b)). The term $\vec{H}_d$ is called demagnetizing field. A way to interpret the demagnetizing field is as if the magnetic moments induce magnetic charges at the surface of the material and these charges produce the demagnetizing field inside of the material.

The frontiers between different magnetic domains are called DWs. Generally divided into three types (see Figure 3): Bloch (a), Néel (b), transversal (c). However, sometimes the frontier between different domains is more complex, and cannot be classified as one of the 3 main types of DWs (e.g. a vortex formation can be seen in Figure 3 (d)).
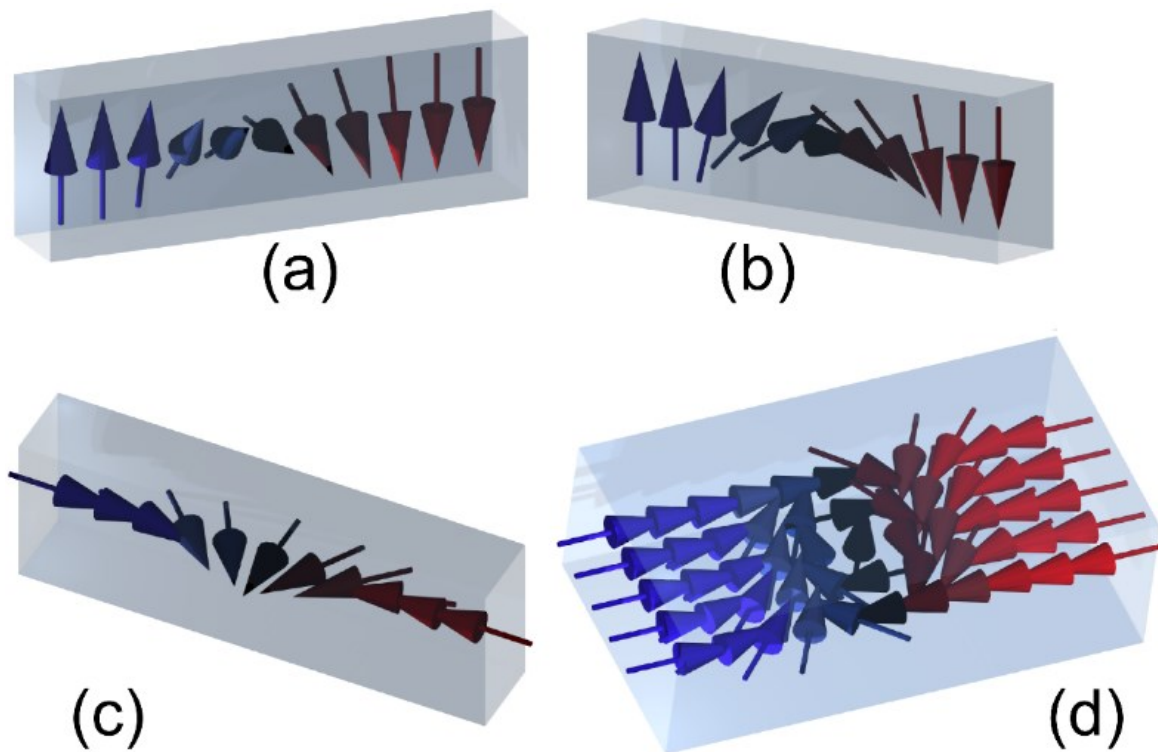
Figure 3. Schematic representation of most common types of DWs: (a) Bloch wall; (b) Néel wall; (c) transverse wall; (d) vortex formation.

The **external stress** term takes into account the elasticity of the magnetic material and the deformations that could happen due to influence of the magnetic interaction or due to external forces. The tensor $\vec{\sigma}_{ex}$ takes into account non-magnetic stresses, $\vec{\epsilon}^0$ is the free magneto-elastic deformation and c is the tensor of elastic constants. $\vec{p}_e$ is the distortion.

2.1.2. Magnetization evolution

Magnetization evolution $\vec{M}(t)$ is calculated by minimizing the energy functional (3) with respect to the magnetization, where the stray field $\vec{H}_d$ and the distortion $\boldsymbol{p}_e$ must fulfil the following conditions:

$$\nabla\left(\mu_0\vec{H}_d + \vec{M}\right) = 0 \qquad \nabla \times \vec{H}_d = 0 \tag{6}$$

$$\nabla(c \cdot (\vec{p}_e - \vec{\epsilon}^0)) = 0 \qquad \nabla \times \vec{p}_e = 0 \tag{7}$$

Using variational calculus, to find the state $\vec{m}$ that minimizes the free energy, it is possible to derive from the total energy expression and the conditions (6) and (7) the next set of differential equations [19]:

$$-2A\Delta\vec{m} + \frac{\partial F_{an}}{\partial\vec{m}} - \left(\vec{H}_{ex} + \vec{H}_d\right)M_s - (\vec{\sigma}_{ex} + \vec{\sigma}^{ms})\frac{\partial\vec{\epsilon}^0}{\partial\vec{m}} = 0 \tag{8}$$

$$\nabla\left(\mu_0\vec{H}_d + \vec{M}\right) = 0 \qquad \nabla \times \vec{H}_d = 0 \tag{9}$$

$$\nabla(c \cdot (\vec{p}_e - \boldsymbol{\epsilon}^0)) = 0 \qquad \nabla \times \vec{p}_e = 0 \tag{10}$$

where $\vec{\sigma}^{ms} = \boldsymbol{c} \cdot (\vec{p}_e - \vec{\epsilon}^0)$ is the magnetostrictive stress.

Expression (8) can be rewritten as the next condition for the magnetization:

$$\vec{M} \times \vec{H}_{eff} = 0 \tag{11}$$

where $\vec{H}_{eff}$ is the effective field[21]:

$$\vec{H}_{eff} = \vec{H}_{ex} + \vec{H}_d + \left[2A\Delta\vec{m} - \frac{\partial F_{an}}{\partial\vec{m}} + (\vec{\sigma}_{ex} + \vec{\sigma}^{ms})\frac{\partial\vec{\epsilon}^0}{\partial\vec{m}}\right]/M_s \tag{12}$$

This condition, eq(11), means that in static equilibrium, the torque exerted by the effective field must vanish. In a non-equilibrium situation, the momentum connected with the magnetic moment will lead to a gyrotropic reaction that can be described by

$$\dot{\vec{M}} = -\gamma\vec{M} \times \vec{H}_{eff} \qquad \gamma = \frac{\mu_0 g e}{2m_e} = g \cdot 1.105 \cdot 10^5 m/As \tag{13}$$

where γ is the gyromagnetic ratio, and the Landé factor g has values close to 2 for many ferromagnetic materials. When a torque is applied, this equation describes a precession where the angle between magnetization and effective field is always the same. This is because the equation does not take into account energy dissipation. The dissipation can have different origins, e.g. Eddy currents, macroscopic discontinuities, diffusion, reorientation of lattice defects, spin-scattering and losses. These losses can be taken into account by an extra empirical term that includes local dissipative phenomena, e.g. relaxation on impurities or scattering of spin waves on the lattice defects. This extra term is called damping and the full expression is known as Gilbert equation [19]:

$$\dot{\vec{m}} = -\gamma_G \vec{m} \times \vec{H}_{eff} - \alpha_G \vec{m} \times \dot{\vec{m}} \tag{14}$$

The damping term α_G is what allows magnetization to evolve and turn towards de effective field. Equation (14) is equivalent to the original Landau-Lifshitz equation:

$$\dot{\vec{m}} = -\gamma_{LL} \vec{m} \times \vec{H}_{eff} - \alpha_{LL} \vec{m} \times (\vec{m} \times \vec{H}_{eff}) \tag{15}$$

where α_{LL} and γ_{LL} are the damping term and giromagnetic ratio, respectively in the Landau-Lifhitz formulation. Solving this equation one can calculate the evolution of the magnetization inside a ferromagnetic material.

2.1.3. Numerical solutions

In order to solve (15) numerically[22], it can be rewritten as[1]:

$$\dot{\vec{M}} = -\gamma_{LL} \vec{M} \times \tilde{H} \tag{16}$$

where $\tilde{H}$ is

$$\tilde{H} = \vec{H}_{eff} + \frac{\alpha_{LL}}{M_s} (\vec{M} \times \vec{H}_{eff}) \tag{17}$$

In order to compute the temporal evolution, time is discretised in intervals $\Delta t = t_{i+1} - t_i$ and by applying the midpoint rule[22]:

---

[1] This is the numerical approximation used by Alessandra Manzin et al. to produce the numerical results shown later on in the results chapters.

$$\begin{cases} \left.\dfrac{\partial \vec{M}}{\partial t}\right|_{i+1/2} = \dfrac{\vec{M}_{i+1} - \vec{M}_i}{\Delta t} + \mathcal{O}(\Delta t^2) \\[4mm] \vec{M}_{i+1/2} = \dfrac{\vec{M}_{i+1} - \vec{M}_i}{2} + \mathcal{O}(\Delta t^2) \end{cases} \tag{18}$$

it is possible to linearize (16) and rewrite it as

$$\vec{M}_{i+1} + \frac{\gamma_{LL}\Delta t}{2} \vec{M}_{i+1} \times \tilde{H}_{i+1/2} = \vec{M}_i - \frac{\gamma_{LL}\Delta t}{2} \vec{M}_i \times \tilde{H}_{i+1/2} \tag{19}$$

Now the problem consists in computing the evolution of $\tilde{H}$ over time. To do so it is possible to use Adam's extrapolation in expression (19) to generate[22]:

$$\tilde{H}_{i+1/2} = \frac{3}{2}\tilde{H}_i - \frac{1}{2}\tilde{H}_{i-1} + \mathcal{O}(\Delta t^2) \tag{20}$$

To solve (20) an iterative process estimating $\tilde{H}_{i+1/2}$ and $\vec{M}_{i+1/2}$ is followed until convergence. The instantaneous value of $\vec{H}_{eff}$ is obtained by applying the weak formulation directly to (12).

The geometric integration scheme used in combination with the expressions (18) to (20) is based on Cayley transformation. Further details of the micromagnetic solver can be find in Refs.[23]–[29].

2.2. Magnetoresistance

Numerical simulations of MR produced by AMR and PHE effects were performed by Alessandra Manzin et al. The assumption used is that the electrical current density is small enough not to affect the magnetization, hence magnetization can be computed independently on the electrical current distribution. The electrical current distribution was calculated solving[30]–[32]:

$$\nabla \cdot [\overleftrightarrow{\sigma}(\vec{r})\nabla\varphi(\vec{r})] = 0 \tag{21}$$

where φ is the scalar potential and $\overleftrightarrow{\sigma}$ is the conductivity tensor which can be expressed as:

$$\overleftrightarrow{\sigma}(\vec{r}) = \frac{1}{\rho_{\parallel}\rho_{\perp}} \begin{bmatrix} \rho_{\parallel} - \Delta\rho\,\cos^2\eta(\vec{r}) & -\dfrac{1}{2}\Delta\rho\,\sin 2\eta(\vec{r}) \\[3mm] -\dfrac{1}{2}\Delta\rho\,\sin 2\eta(\vec{r}) & \rho_{\parallel} - \Delta\rho\,\sin^2\eta(\vec{r}) \end{bmatrix} \tag{22}$$

where $\Delta\rho = \rho_{\parallel} - \rho_{\perp}$ and $\rho_{\parallel}$ and $\rho_{\perp}$ are the resistivities parallel and orthogonal to the magnetization direction respectively. $\eta(\vec{r})$ is the angle between the electrical current and the

magnetization. Here, for simplicity, we have adopted a phenomenological explanation of the AMR and PHE effects, an explanation based on the micromagnetic behaviour and electron conduction can be found in Refs [33]–[35].

2.3. Summary

This chapter reviews the basic concepts related with micromagnetism and numerical simulations. The concept of DW is introduced as a way to minimize the total energy of the system, and the equations leading to magnetization evolution are derived from energy considerations.

The numerical approximation of the LLG equation used later on in the next chapters to simulate magnetization evolution was shown in this chapter, in particular the electrical transport model used to simulate AMR and PHE.

Due to the experimental nature of the work presented later on, this chapter was kept as brief as possible to serve as an introduction to concepts discussed later on.

3 Literature review

This chapter provides an overview of the state-of-the-art in the area of DWs in magnetic nanostructures, widely studied due to their applicability in non-volatile memory systems with high performance and reliability [36], magneto-logic devices with low power consumption [37] and biomedical applications for detection and tracking of magnetic labels [12], [13], [38], [39].

3.1. Memory applications

Although magnetization has been used to store information since the middle of the last century, the concept of using DWs received a vast attention after the proposal of the racetrack memory[40] by S.Parkin in 2008.

The basic design of the racetrack memory, now named Racetrack Memory 1.0[41], is shown in Figure 4. In this type of memory, data bits are stored as segments along a magnetic wire with different magnetization and separated by DWs, see Figure 4(a). To operate the memory, a pulse of current is injected into the wire in order to move all the DWs and pass the data bits over the reading and writing areas. The reading area (Figure 4(b)) consists of a magnetic tunnel junction (MTJ), which resistance changes depending of the magnetization of the wire. The writing area (Figure 4(c)) consists of a metal wire where a high current pulse is used to change the magnetization of the portion of the racetrack above it.
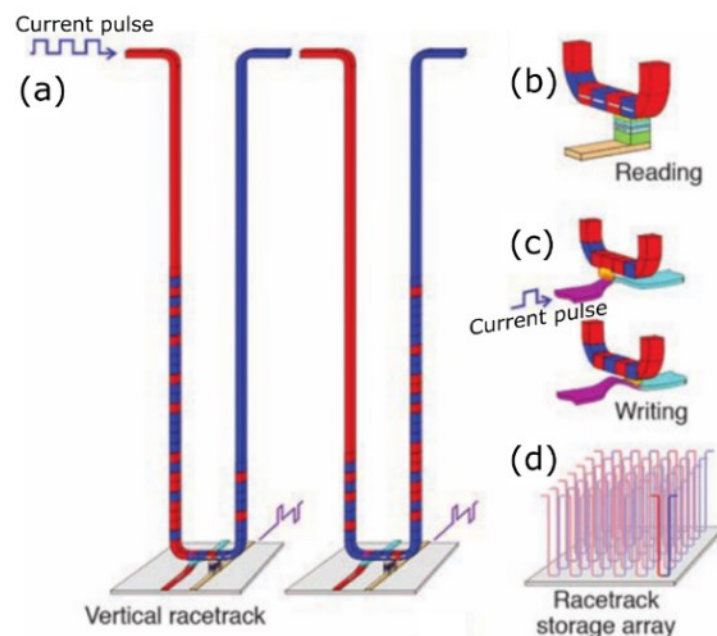
Figure 4. DW racetrack memory. (a) Schematics of the racetrack setup with DWs moved by pulses of current. (b) Reading process. (c) Writing a bit of data. (d) 3D architecture of the memory devices. Adapted from Ref[40], with permission from AAAS

The main advantages of the racetrack memory are an ability to create 3D arrays, increasing data density, its non-volatile character, and low power consumption[40]. However, the problems to overcome are very closely related to the predicted advantages. Fabrication of 3D structures remains a challenge, and has to be optimized before being able to produce a large batch of racetrack devices. Although DWs are quite stable, thermal activation and pinning remain the main problems[42], [43]. Due to thermal activation, a DW might depin from a stable position, and hence data bits will be erased. In the case of pinning, local defects, or edge roughness, produce undesired pinning sites, which leads to decreased mobility of some DWs. In terms of power consumption, the current density necessary to move DWs (in the order of $\sim$ 10^8 A/cm^2)[44]–[46] is too high at the moment, to the point that sometimes the produced heat is close to damage the nanowire[47].

In order to overcome the stated problems, there have been several different approaches. For instance, Parkin et al. [41] have evolved their initial concept from one single ferromagnetic wire in version 1.0 to two antiferromagnetically coupled wires sandwiching a heavy metal wire in version 4.0. While the antiferromagnetic coupling provides stability and high DW speed, the heavy metal allows converting the electrical current into spin current and hence moving DWs more efficiently with smaller currents. However, the stability is still not high enough to compete with other types of memories, and the power consumption remains too high (the best results are in the order of $\sim 10^7$ A/cm^2)^2[48], [49], so this design is awaiting for new materials or new ways of applying torque to DWs.
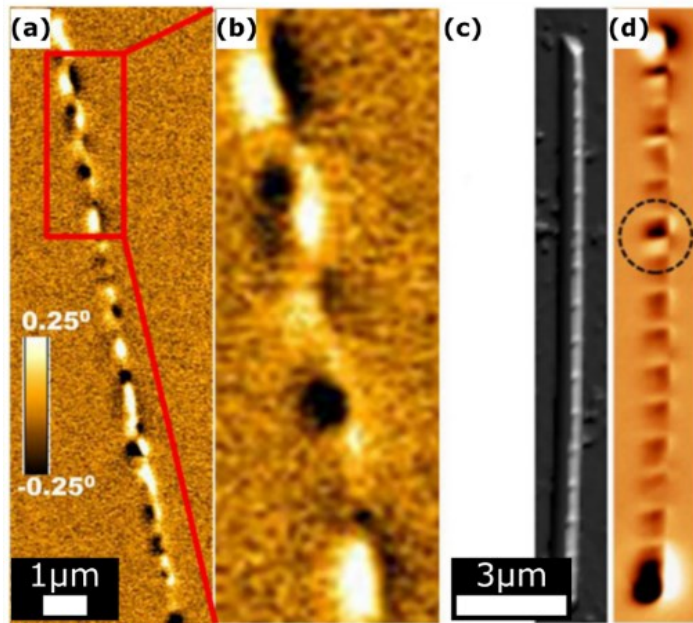
Figure 5. (a) and (b) MFM images of multisegmented Ni/Co nanowire. Adapted from Ref.[50] under CC-BY license. (c) and (d) SEM and MFM images respectively of a bamboo-like nanowire. Adapted from Ref.[51], under CC-BY license.

---

[2] In a conductor, the absolute value of the spin Hall angle is given by $|\theta_{SH}|=|J_s/J_e|$ where J_e is the charge current density and $\hbar/2e\,J_s$ is the spin current density. However, although the spin current includes $\hbar/2e$ term and the corresponding units, in the specialized literature the spin current is given simply as J_s using unis of A/m^2 or A/cm^2. In this thesis, to keep similar notation as in the references I used the same agreement.

Other approach to the racetrack memory, relays on the usage of cylindrical nanowires produced by a bottom-up method[52]. Cylindrical nanowires made of segments with different magnetic properties (Figure 5(a) and (b))[50], [52], [53], or with modulated diameter (Figure 5(a) and (b))[51], [54], [55] are one of the most promising solutions for racetrack memory. The key features of cylindrical nanowires consist in a large DW speed[56], [57], a lower critical current (as low as $\sim 10^5$ A/cm^2 in the creep regime[58]), and the possibility of fabricating large batches by chemical methods, and thus very easily scalable. However, these wires, as the patterned wires, also suffer from stochastic depinning of DWs, and fabrication of the electrical connections still remains as a challenge[59], [60].

3.2. DW-logic

Although storing information has been one of the main research topic of magnetism in electronic devices, recently there has been a considerable interest into processing information under the so-called DW-logic[37], [61]–[66]. Figure 6 shows a table with the logic elements, the CMOS equivalent and the proposed magnetic alternative[37]. The idea behind DW-logic is that information can be stored in the orientation of the magnetization, and DW movement can propagate the information through different circuits. Depending on connections of the magnetic channels, DWs nucleate or annihilate, processing the information.
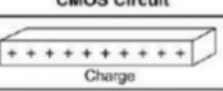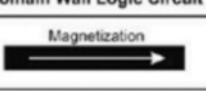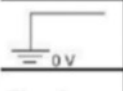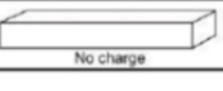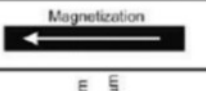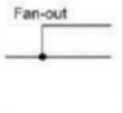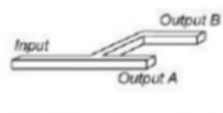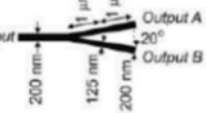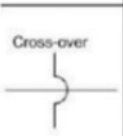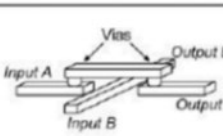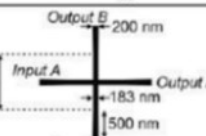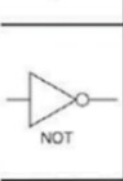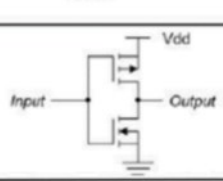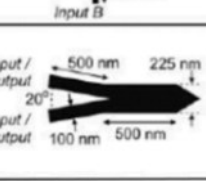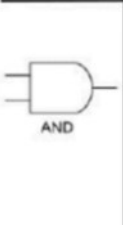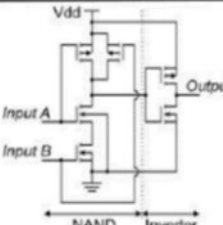
Figure 6. Table of equivalent CMOS/DW-based logic circuit elements. Adapted from Ref[37], with permission from AAAS

Figure 7 shows an example of a DW-logic circuit[37]. The magnetic track, which logic elements are highlighted in Figure 7(a), consists of a NOT-gate, a fan-out junction, and a cross-over. The circuit operates by applying an external rotating magnetic field that drags DWs through the circuit, and its output is read using a magneto optical Kerr effect (MOKE) system on the spot marked with an asterisk.
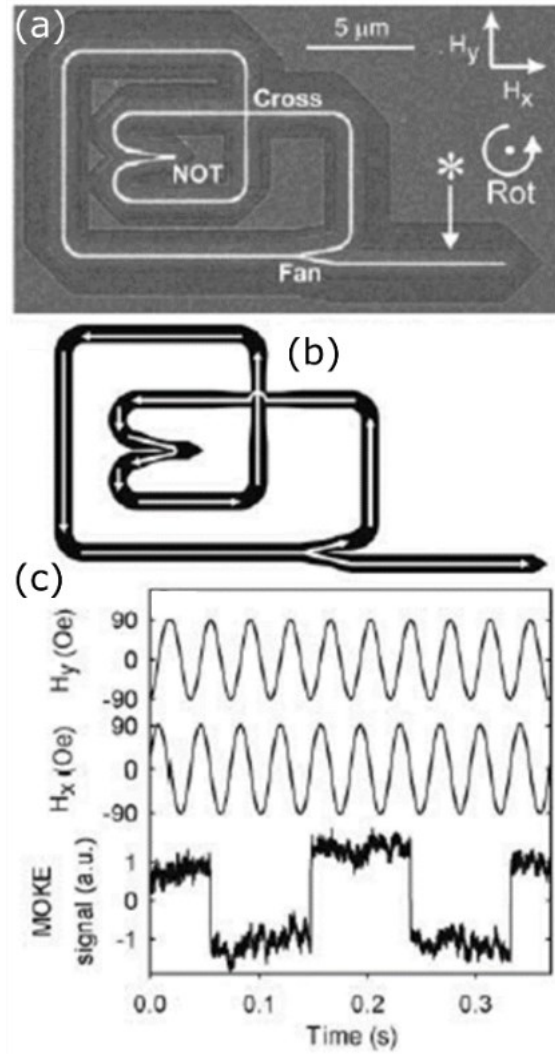
Figure 7. Example of a DW-based logic circuit. (a) SEM image of the magnetic nanostructure. Asterisk indicates the point where the MOKE microscopy laser probes the magnetization. (b) Schematics of the magnetization. (c)Evolution of the applied fields and the MOKE signal. Adapted from Ref[37], with permission from AAAS

The main advantages of such devices are simplicity of the design when compared with CMOS technology, possibility of storing the information in the circuit without the necessity of a power source or a dedicated memory[67], and operation with lower power consumption than the equivalent CMOS devices. However, most of the problems stated before for the Racetrack

Memory and the cylindrical nanowires apply also in this case, with the only difference that without a dedicated memory, part of the resources can be used in error-correcting algorithms which should account for stochastic DW pinning/depinning[68].

3.3. DW movement through spin transfer torque

As depicted in the two previous sections, moving DWs using an electrical current instead of using an external magnetic field is one of the key requirements for most of the applications related with DWs.

When an electrical current passes through a ferromagnetic material, the electrons carrying the charge align their magnetic spin with that of the magnetization[69], [70], producing a torque onto the magnetization. If the electrical current is large enough, then the transferred torque is able to turn the magnetization, and the DW at the interface changes its position[46], [71]–[74]. Due to the small magnetic moment of the electron, and because not all the electrons are polarized in the same direction, the process is very inefficient and requires high current densities to operate (in the range of $\sim 10^7$ A/cm^2)[75].
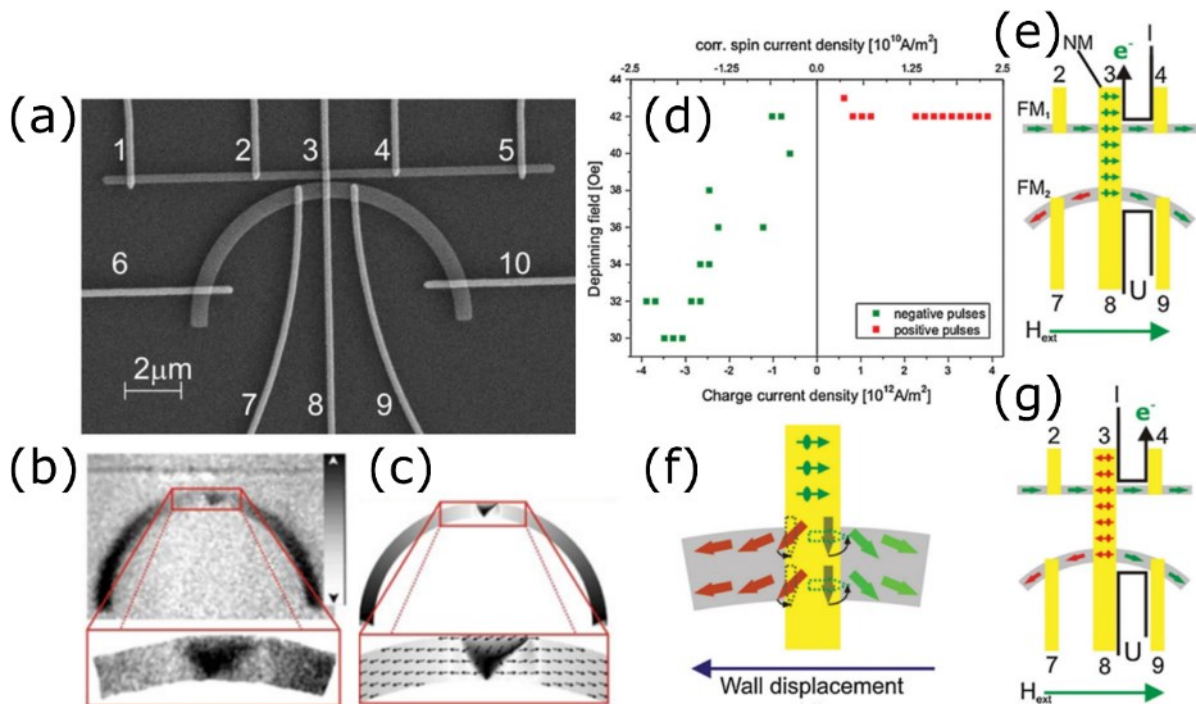
Figure 8. (a) SEM image of a nonlocal spin valve geometry with Cu contacts and Py ferromagnetic nanostructures. (b) SMCD PEEM image of the spin configuration when a DW is pinned in the half ring. (c) Micromagnetic simulation of the state shown in (b). Adapted from Figure 1 and 3 of Ref[66], with permission from the American Physical Society.

A promising alternative consists in using pure spin currents where there is no net charge transport and only spin is transferred. The limitation to overcome in this case is the amount of the electrical current that can be converted into spin current, and the spin diffusion length. For instance, Figure 8(a) shows a LSV composed of two ferromagnets (a straight wire and ring segment), connected by a metallic, non-magnetic channel[66]. The DW pinning site is beneath the channel on the ring segment (Figure 8(b) and (c)). When a charge current passes through the straight ferromagnet (either in the configuration shown in Figure 8(e) or (g)), it produces a spin accumulation at the interface with the metallic channel. The spin accumulation diffuses through the channel into the second ferromagnet (i.e. the ring segment), applying a spin torque to the DW[76], [77] (Figure 8(f)). It is shown in Figure 8(d) that for the same orientation of the DW, depending on the direction of the current, the spin torque reduces either the depinning (green dots) or has no effect at all (red dots). The necessary spin current density is $\sim 10^6$ A/cm^2, which is one order of magnitude smaller than the actual value for charge-induced DW motion in patterned nanowires ($\sim 10^7$ A/cm^2)[48], [49]. However, the charge current necessary to produce $\sim 10^6$ A/cm^2 of spin current is $\sim 10^8$ A/cm^2 (Figure 8(d)). This is due to the low efficiency of the spin accumulation, and the exponential decay of the spin current density through the channel (spin diffusion length ~1 μm for Au channel[78]). Recent studies[79] have reported similar values of spin current density (i.e. $\sim 10^6$ A/cm^2) using lower charge current densities ($\sim 10^6$ A/cm^2). Moreover, with graphene as spin diffusion channel[80] it has been achieved up to ~11 μm spin diffusion lengths[81]. Thus, this is a promising approach towards DW manipulation with electrical currents.

3.4. Biomedical applications

Biomedical applications of MBs can be roughly classified as *in vivo*: such as magnetic contrast for magnetic resonance imaging (MRI)[82], drug delivery[6], [83], hyperthermia[82]; and *in vitro* applications: such as sample purification[84], [85], agent manipulation[8], [86]–[88], and cell labelling[89][6].

In vivo applications often require not only tuning the magnetic properties of the MBs but also the physiological response of the body to certain types of materials. This requirement creates a trade-off between the desired magnetic properties and the biocompatibility.

In vitro applications are less sensitive to biocompatibility, and they are a very active field of research due to their possible integration in Lab-On-a-Chip applications. For instance, in a typical MB manipulation and detection experiment a biological agent (e.g. a DNA strand) is attached to a MB by surface functionalization. A droplet containing MBs is wet casted on top

of a chip. Magnetic nanostructures within the chip and external magnetic field can be used to concentrate the MBs in specific areas[15], [88]–[92]. A magnetoresistive sensor can then be functionalize to trap the DNA strand as it passes and, by monitoring the sensor, it is possible to measure the amount of MBs on top of it. This enables, for instance, testing the binding between different DNA strands, detecting the presence of a second biological agent (which is required to produce the link and hence fix the MBs on top of the sensor), or, by heating once the DNA strands are connected, measuring the denaturalizing temperature[93].

3.4.1. Magnetophoresis

Manipulation of MBs is a fundamental part of Lab-On-a-Chip concept, and the use of microfluidic channels in combination with "magnetic tracks" is one of the most versatile approaches because it allows single MB manipulation without the restriction imposed by the size of individual droplets[1], [86].

For instance, Figure 9 shows an example of magnetophoresis based on magnetic nanostructures[9], [92]. The stray field at the edges of the semi-disks attracts the MBs and creates a track for them to travel. An externally applied magnetic field controls the direction of travel, i.e. clockwise/anticlockwise for forward/backward movement (Figure 9(a) and (b)). By combining these structures it is possible to create junctions, buffer areas, tracks, and MBs can be manipulated towards sensing areas (Figure 9(c)).
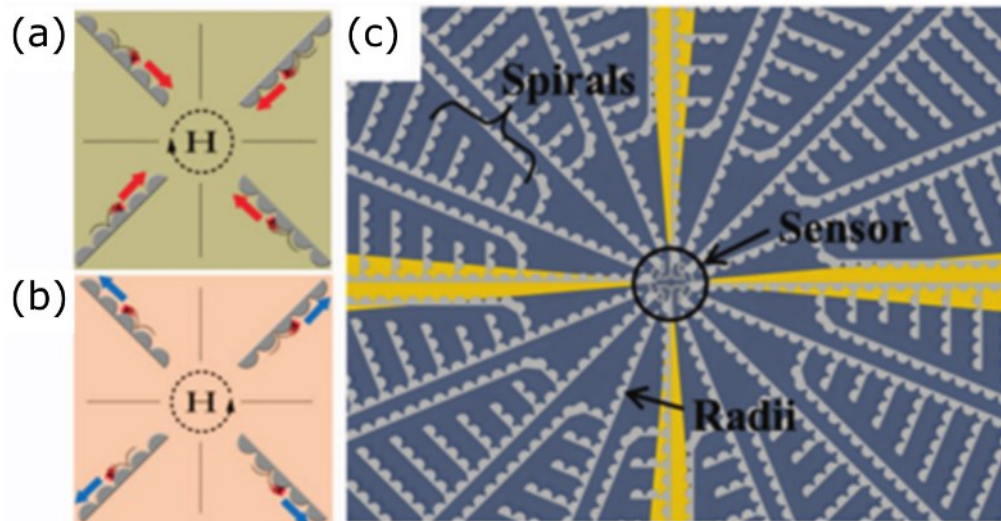
Figure 9. Magnetic nanostructures for the transport of MBs. (a) and (b) a rotating magnetic field transports the MBs along the edges of the nanostructures. (c) by arranging the nanostructures in a circular pattern, it is possible to concentrate MBs over a sensing area. Adapted from Ref.[92], under CC-BY license.

Other geometries involve dots or disks/ellipses [88], [94], [95], stripes[96]–[98], squares[99], and more complicated patterns[100], [101]. However, all these approaches have in common the use of external magnetic fields, the control of numeral MBs at once, and MB detection using a sensor which is usually fabricated from different materials than the tracks.

In order to move individual MBs, and with the aim of eliminating the necessity of an external magnetic field, it has been proposed to use the stray field generated by DWs confined in magnetic nanostructures[94], [100], [102]–[104]. For instance, Figure 10 shows an array of magnetic rings[105] used for single MB manipulation. By applying a high magnetic field it is possible to create an onion state with two DWs (Figure 10(a)), each DW can trap an individual MB. By a combination of external fields, it is possible to return the ring to a vortex state without DWs and release the MBs (Figure 10(b)), or rotate the DWs and hence move the particles (Figure 10(c)). By combining trapping-movement-releasing, it is possible to navigate the MBs from one ring to another (Figure 10(d)).

By having an array of rings it is possible to move MBs along custom paths and for instance use the MBs to test the mechanical properties of cell membrane[8].
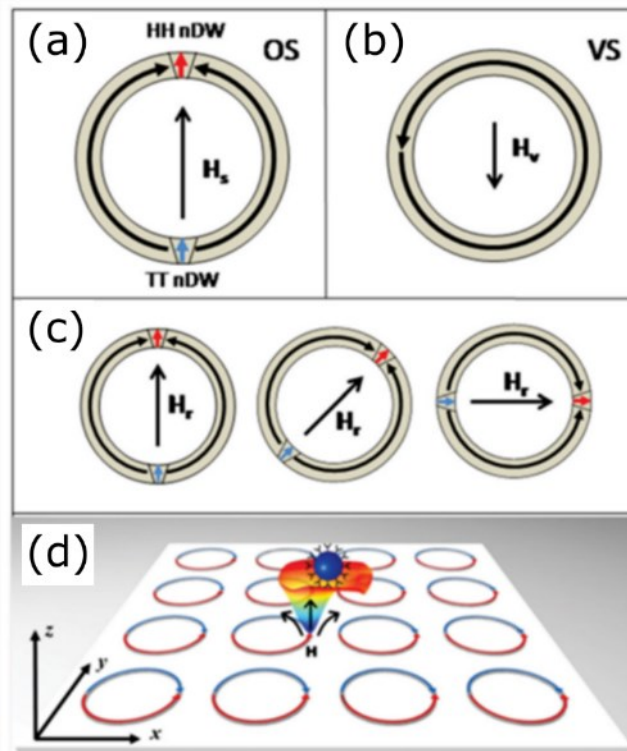
Figure 10. Arrays of ferromagnetic rings for MB manipulation using DWs. (a) Onion state with two DWs. (b) Vortex state without DWs. (c) DW movement under the action of a rotating magnetic field. (d) An array of disks allows moving MBs along complex paths. Adapted from Ref.[105], under CC-BY license with permission from John Wiley and Sons.

Other designs aim at more specific tasks (e.g. automatization) by predefining the path for MB manipulation. For instance, paths can be defined by having nanowires with DW pinning sites (e.g. by adding notches[13] or corners[104], [106]–[108]) and MBs movement takes place under an external magnetic field that moves the DWs from one pinning site to another[13], [14], [109]–[111]. Figure 11 shows different frames of a movie (taken with an optical microscope) where a single MB is moved along pinning sites in a zig-zag magnetic nanowire. In this case the pinning sites are corners and the sequence (1-5) in Figure 11 describes the order of applied magnetic fields necessary to depin the DW from one corner and move it to the next one. Using this approach it has been shown also that it is possible to move MBs from one wire to an adjacent one, or chose path at an intersection[38].
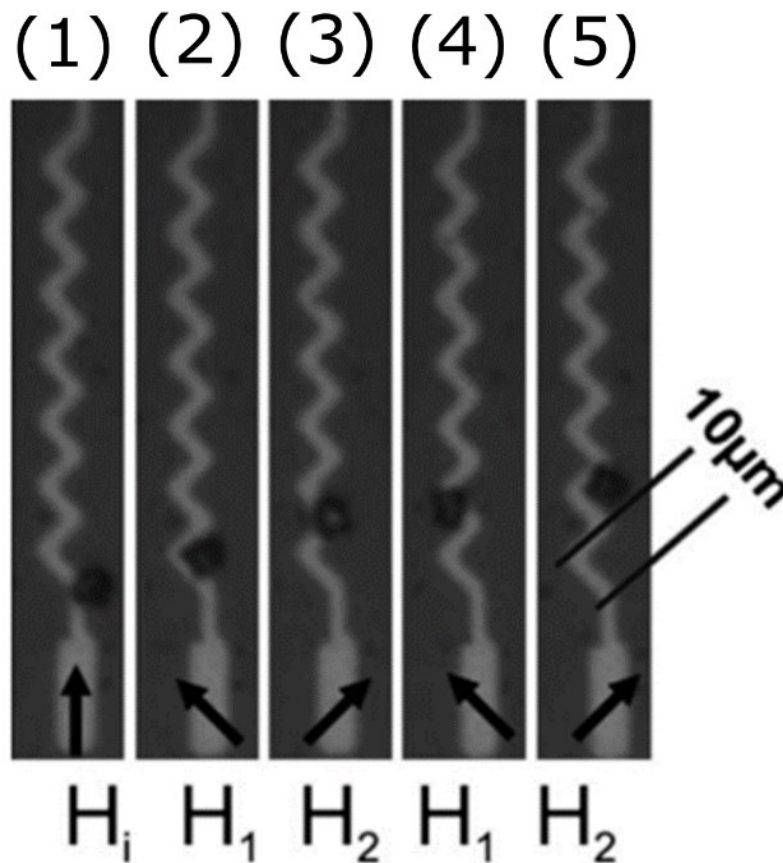
Figure 11. Zig-zag magnetic nanowire for transport of MBs. Numbers 1-5 represent different frames of a movie. Adapted from Ref.[109], with permission from the Royal Society of Chemistry.

However, despite the versatility of using DWs, moving each DW independently remains a difficult task, because when using an external field, it is very likely that the field affects all the nearby DWs at the same time. This is why, like in the memory applications mentioned before, recent studies have been centred towards manipulation of DWs using electrical

currents. Although, MB manipulation allows for other approaches, like building magnetic nanostructures on top of a piezoelectric substrate to manipulate locally the anisotropy of the nanostructure using a voltage across the piezoelectric. This has enabled for instance manipulation of DWs in ring nanostructures and movement of MBs without an external magnetic field[112].

3.4.2. MB detection

MB detection is also a fundamental part of Lab-On-a-Chip, either as stand-alone application or in combination with magnetophoresis. Because of that, there have been proposed many different solutions to achieve detection. Here we will discuss only the solutions proposed towards single MB detection, more suitable to be integrated with single MB DW-based magnetophoresis.

For instance, one successful approach to achieve single MB detection consists in tagging the MBs with agents that produce a strong optical contrast (e.g. fluorescence, by encapsulating quantum dots inside of the MBs)[113], and thus enabling optical detection with a microscope[114]. Figure 12(a) shows the schematics of such detection system, which consist in a microscope (1), an in-plane quadrupole electromagnet (2) and an out-of-plane electromagnet (3). This type of detection allows tracking MBs, when they are being manipulated in systems like the ones mentioned before, i.e. magnetophoresis based on magnetic nanostructures (Figure 12(b) and (c)); and MB movement based on DWs Figure 12(d) and (e).
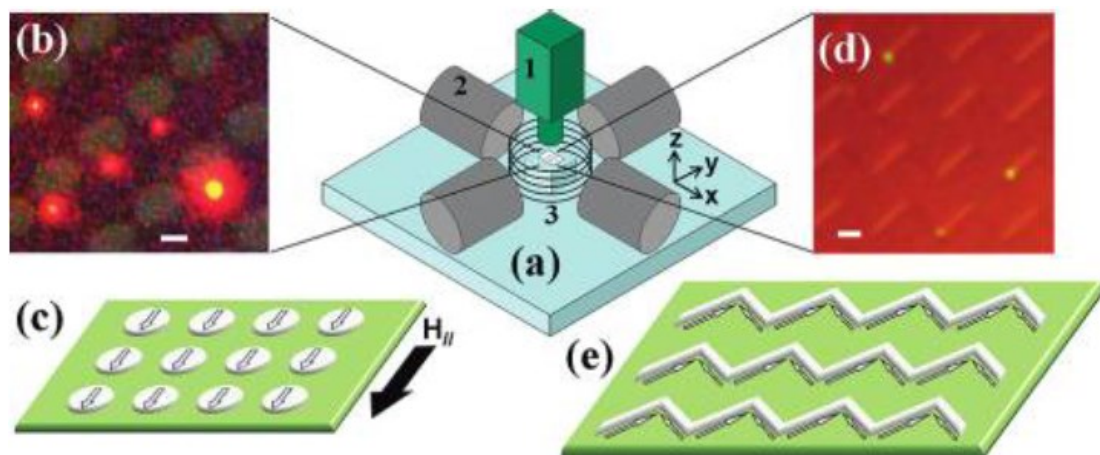
Figure 12. Optical detection of MBs using fluorescence. (a) Schematics of the system used: Microscope (1), in-plane quadrupole magnet (2), out-of-plane electromagnet (3). (b) and (d) optical images of MBs being manipulated over magnetic nanostructures: array of discs (c) and zigzag wires (e). Adapted from Ref[113]. Copyright (2010) by the American Physical Society.

The main limitations of this system reside in the necessity of an exciting light (e.g. ultraviolet light), which can damage the biological agents under study; the diffraction limit, which puts a restriction on the size of the details that can be observed; and the difficult to automatize the optical tracking system. However, as shown in Figure 12, optical detection can be integrated with DW-based magnetophoretic systems without special requirements.

In order to ease automatization by using electrical sensors, micro-Hall sensors have been studied as single MB sensors[115]–[119]. These non-magnetic sensors relay on the Hall effect to detect small magnetic moments near the sensing area. Detection takes place by biasing the Hall cross with a DC magnetic field and a DC current (Figure 13). The current is necessary for the sensor to operate, while the DC field can be adjusted depending on the type of MBs used. A second AC field superimposed with the DC field oscillates the magnetic moment of the MB resulting in a sinusoidal voltage in the Hall sensor which is detected by a lock-in operating at the same frequency as the AC field[117], [120]–[123]. This alternating field detection scheme allows isolating the system from external electrical noises and achieving high sensitivity.
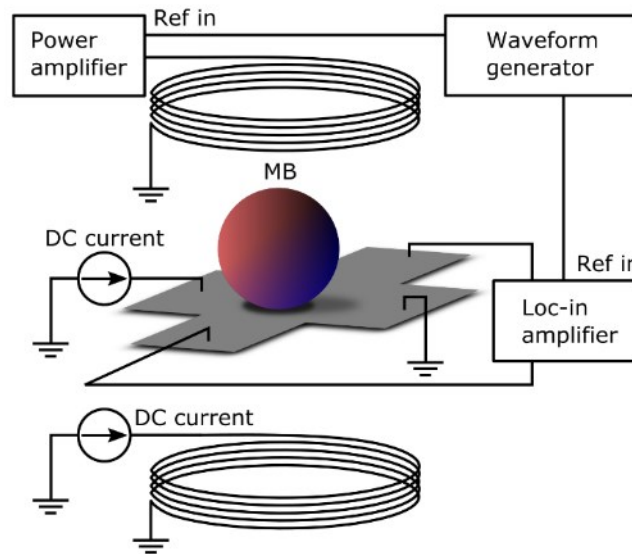
Figure 13. Single MB detection using a Hall sensor. Hall sensor is biased with a DC current, and both sensor and MB are biased with a DC magnetic field. An alternating magnetic field oscillates the MB's magnetic moment generating an AC voltage in the Hall sensor. A Lock-in amplifier is used to detect the AC voltage on the Hall sensor.

Although in the past semiconductor Hall sensors were used (Hall coefficients of ~1100 Ω/T) [115], [123], [124], recently it has been a shift towards graphene-based sensors (Hall coefficients of ~900 Ω/T)[119], since a single layer graphene cross can achieve sensitivities higher than many of the semiconductor-based Hall sensors, and requires a smaller number of

41

fabrication steps. The main disadvantage of semiconductor Hall sensors originates in the difficulty of integrating semiconductor fabrication, necessary for the Hall sensor, with magnetic materials deposition (necessary for magnetophoretic structures). With the development of graphene-based sensors this problem has been reduced greatly.

Spin valve (SV) sensors for instance, are a non-semiconductor alternative for electrical detection of MBs. SVs are multi-layered metallic nanostructures (i.e. non-pinned ferromagnetic layer/non-magnetic material layer/ pinned ferromagnetic layer/ pinning antiferromagnetic layer[118]) exhibiting large changes in resistance due to the giant magnetoresistance (GMR) effect. They have been used as MB detectors because of the large signal (~ 4% MR ratio[125]) and relatively ease of use[114], [116], [126]–[133]. For instance, Figure 14 shows the schematics of a SV-based MB sensor[125]. The SV sensor has been functionalized with biotin proteins, while the MBs have been functionalized with streptavidin proteins. Since the streptavidin-biotin conjugate is specific, only MBs with the streptavidin protein will be attached to the SV sensor. The magnetic field generated by the MBs affects the SV modifying its resistance and allowing detection.
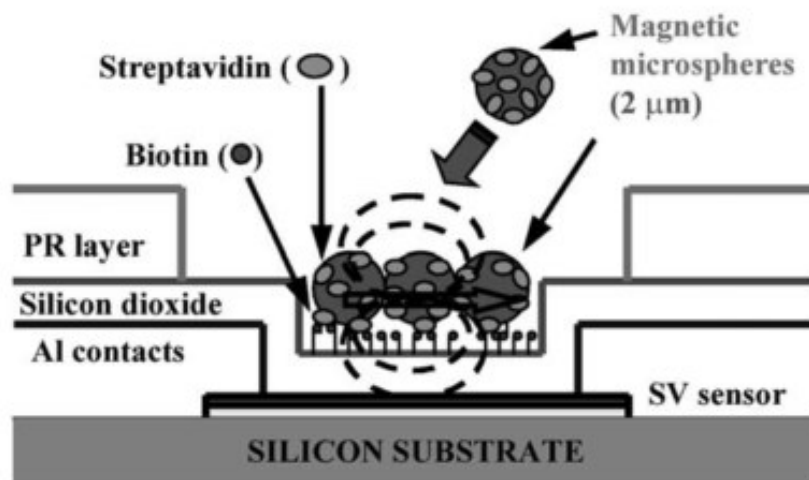
Figure 14. Schematics of a SV functionalized with Biotin antigen to trap Streptavidin coated MBs. Adapted from Ref.[125], with permission from Elsevier.

By adding different combinations of proteins, it is possible to create sensors where the MBs will only attach to the sensor if a third agent (e.g. antigen) is present[126]. This allows for a wide range of application, however this type of sensor has some challenges difficult to overcome. For instance, a magnetic field is required to operate the system. Either an external magnet or a current line have to be used to align the magnetic moments of the superparamagnetic MBs increasing the complexity of the sensor. Another challenge is

reduction of the number of MBs[134]. Since the detection is based on surface functionalization, the detection always involves more than one MBs.

An alternative to SV sensors are MTJ, which are based on the tunnel magnetoresistance (TMR) effect and allows achieving much higher MR ratio (~ 150% MR ratio)[135]–[138]. However, fabrication of MTMs (i.e. non-pinned ferromagnetic layer/tunnel barrier/ pinned ferromagnetic layer/ non-magnetic layer/ pining ferromagnetic layer/ pinning antiferromagnetic layer [118]) is more complex than in SV, whereas they have the same disadvantages.

Another MR-based solution to single MB detection is the usage of nanostructures. Magnetic nanostructures can be patterned into different shapes to exploit effects like the AMR (resistance change along the current direction) or the PHE (resistance change perpendicular to the current direction). One of the most used designs comprises a Hall cross where magnetization is constrained in one direction (e.g. by shape anisotropy or by interacting with a pinned layer) and the presence of nearby magnetic moments modifies the magnetization producing a transversal voltage[139]–[141]. It has been demonstrated that this approach can be used to detect single MBs[30], [142], [143], and the current trend of research is towards increasing the change in resistance produced by AMR and PHE, by using nanostructures with more complex patterns[93], [144]–[150] (e.g. Wheatstone bridges made of ferromagnetic nanowires as resistors[151]). A part from the simple fabrication process, using magnetic nanostructures enables for an easy integration with magnetophoretic devices, moreover, the magnetic nanostructures used on the sensors generate stray fields that trap MBs and hence contribute to the detection[152].

The last solution proposed for single MB detection it's based on DWs. The DW pinning potential inside of a nanostructure can be affected by material properties, temperature, geometrical features, and by local magnetic moments, e.g. the magnetic moment of a MB. Moreover, the DW presence modifies the electrical properties of the nanostructure (i.e. AMR effect), enabling electrical detection of DW pinning/depinning fields and hence detecting MBs through the change in those fields[9], [12], [15], [39], [153], [154].

The main advantage of using DWs for MB manipulation is that detection of MBs can be achieved without a need for extra magnetic nanostructures. For instance, Figure 15 shows optical images of a zigzag track for MB magnetophoresis using a DW[15], [153]. Numbers (i) to (iv) show different steps of the process of moving a DW with a MB attached (green circle).

The zigzag wire in Figure 15 is electrically connected through the yellow contacts which enable measurements of the resistance of the middle segment. This enables measurements of the DW pinning/depinning fields and detection of a MB attached to the DW. Thus this system allows for immediate integration with magnetophoretic circuits.
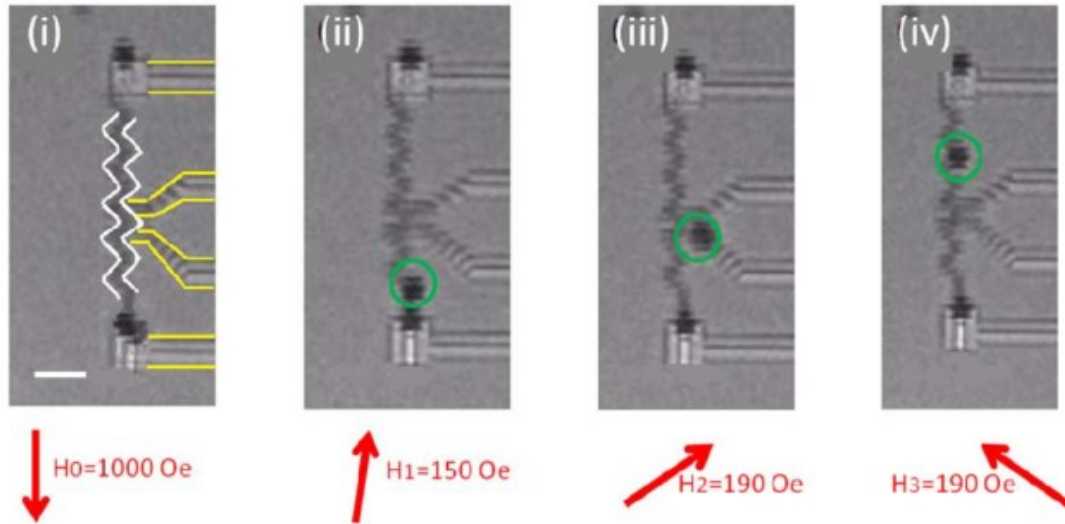
Figure 15. Manipulation of a MB (green circle) along a zigzag magnetic nanowire (white). (i – iv) Different steps in time with the field being applied in each step. Electrical connections (yellow) are used to track DW's by MR measurements. Adapted from Ref.[153], with permission from Cambridge University Press.

Other approaches either used different pinning sites and nanostructures[155]–[157] (e.g. square rings[154]) or implemented impedance measurements for DWs for manipulation and MB detection[4].

3.4. Summary

This literature review demonstrates that DW-based technology can be successfully used in many different applications, ranging from computer memory to Lab-On-a-Chip. However, there are still several challenges to overcome.

Both memory and logic circuits, based on DWs, can store information without a need for power supply, thus avoiding the heating problems associated with semiconductor-based devices. The two main challenges to solve in this area are stochastic DW pinning/depinning and the high current necessary to move DWs. Advances in spin current generation and manipulation hold the promise of solving the problem of DW dynamics.

In Lab-On-a-Chip applications, DW-based devices can be used to manipulate and detect MBs without a need to combine different operational blocks together (e.g. magnetic nanostructures or microfluidic channels for manipulations with semiconductor sensors). The

main advantage of DW-based systems resides in the ability to manipulate and detect single MBs efficiently, and thus allowing for a range of applications not available to other approaches. Although these applications will benefit from improvements in reducing DW pinning/depinning stochasticity, and manipulation with current, the main challenge consists in crossing the step between proof-of-concept and real life applications.

4 Methods

This chapter provides a brief introduction to the experimental methods used in this work. We first describe fabrication of Py and CoFeB nanodevices. The next section is dedicated to MFM. This is followed by a description of the fabrication of custom-made AFM probes as well as the system for MR measurements. We conclude this chapter by description of magneto-optical measurements.

4.1. Fabrication of nanostructures with in plane magnetization

Nanostructures with in-plane magnetization have been fabricated using a continuous polycrystalline Py film (25 nm) sputtered on top of a substrate made of 525 µm of p-Si + 50 nm of SiO$_x$. The Py layer was covered by a 2-nm Pt cap to prevent the oxidation. Fabrication starts by application of negative resist, AR N7520, span at 5000 rpm during 30 s and backed at 90 °C for 2 min (Figure 16.2). Then e-beam lithography (with a dose of 711 µC/cm^2) is used to irradiate the resist followed by the development (AR 300-47 during 5 min 30 s) which removes the excess of resist (Figure 16.4). In order to remove the undesired Py from the sample, Ar-ion etching is used.
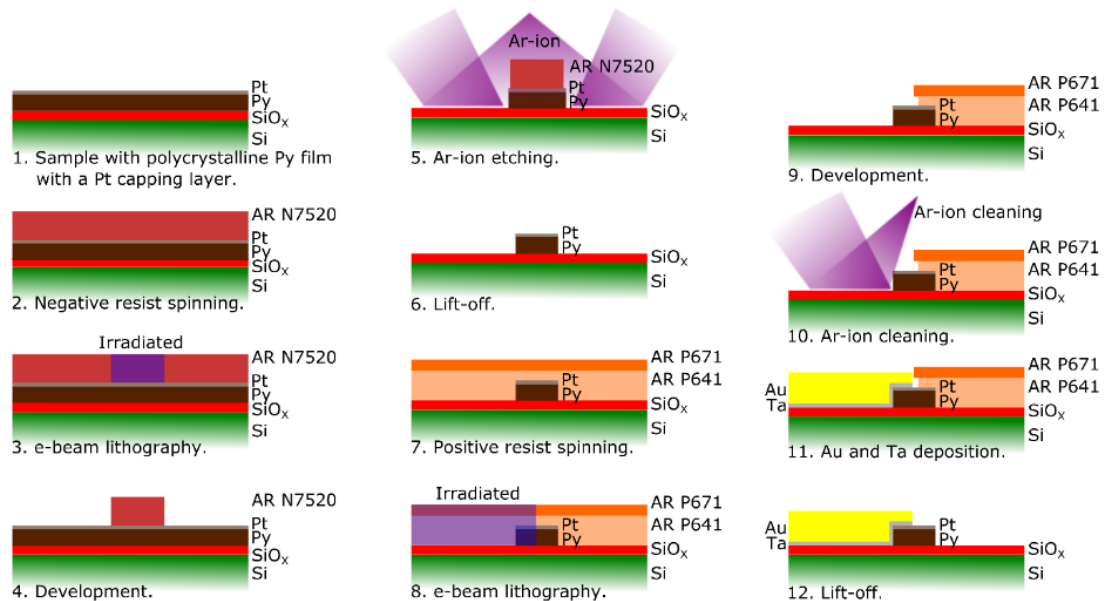
Figure 16. Fabrication steps for in-plane magnetization samples.

The remaining resist was lifted-off (sonicated for 90 s and left in acetone overnight), and the sample has been cleaned again with acetone and isopropanol. Then, we spin positive resist to pattern the electrical contacts. It is a two layer resist process using AR P641 (2000 rpm during 90 s and backed at 160 °C during 10 min) and AR P671 (2000 rpm during 90 s and backed at 160 °C during 10 min). The e-beam exposure with a dose of 692 µC/cm^2 was done

for the pattern of contacts (Figure 16.8). After development, the sample is cleaned in Ar plasma (Figure 16.10) and the contacts were deposited using thermal evaporation of Ta (~ 6 nm) and Au (~ 84 nm). Finally the resist was lift-off (sonicate 90 s and left in acetone overnight) and the sample has been cleaned.

4.2. Fabrication of nanostructures with out-of-plane magnetization

Nanostructures with out-of-plane magnetization were made out of a continuous polycrystalline multilayer film with stack composition Si/SiO(1000 nm)/Ta(4 nm)/Pt(3 nm)/$Co_{60}Fe_{20}B_{20}$(0.6 nm)/Pt(3 nm) deposited by successive sputtering in an unbroken vacuum at $0.5x10^{-7}$ mbar. The fabrication process is similar to the one of in-plane magnetization devices described in section 4.1. Fabrication starts by an application of the negative resist (Figure 17.1). The resist, AR N7520 was span at 5000 rpm for 30 s and backed at 90 °C for 2 min. Then e-beam lithography (with a dose of 711 $\mu C/cm^2$) is used to transfer the pattern to the resist. The developer, AR 300-47 during 5 min 30 s, removes the excess of resist (Figure 17.4). In order to remove the undesired material from the sample, Ar-ion etching is used.
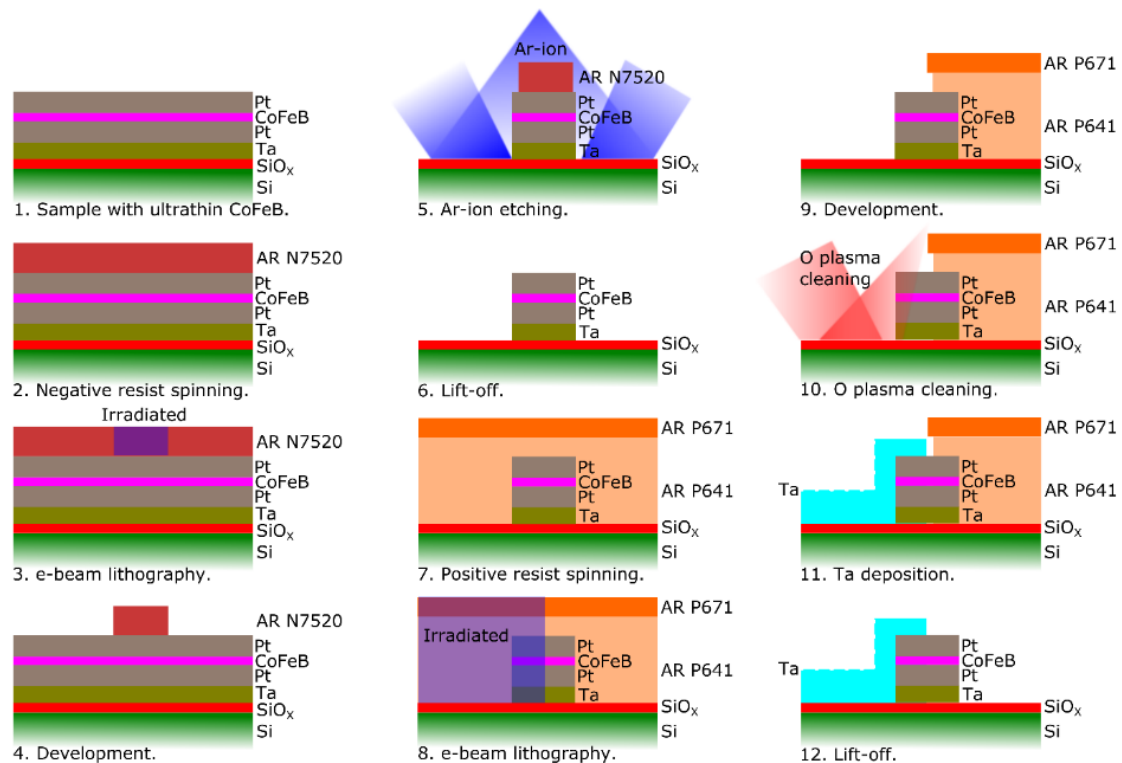
Figure 17. Fabrication steps for out-of-plane samples.

The remaining resist was lifted-off (sonicate 90 s and left in acetone overnight), and the sample was cleaned with acetone and isopropanol. For fabrication of the electrical contacts we use the e-beam lithography with positive resist. It is a two layer resist process using AR P641

(2000 rpm during 90 s and backed at 160 °C during 10 min) and AR P671 (2000 rpm during 90 s and backed at 160 °C during 10 min). The e-beam with a dose of 692 µC/cm^2 is used for the exposure (Figure 17.8). Resist is then developed in order to prepare the sample for depositing the contacts. The sample was cleaned using oxygen plasma (Figure 17.10) and without breaking the vacuum, Ta (~ 5 nm) was deposited. The oxygen is used instead of Ar, because Ar tends to modify the magnetic properties of the PMA thin film[158]. Finally the resist was lifted-off (sonicate 90 s and left in acetone overnight) and the sample was cleaned.

4.3. Scanning probe microscopy techniques

A number of scanning probe microscopy (SPM) techniques are based on AFM, which uses the Van der Waals forces between the sample and the scanning probe to obtain topographic information of the sample's surface[159].
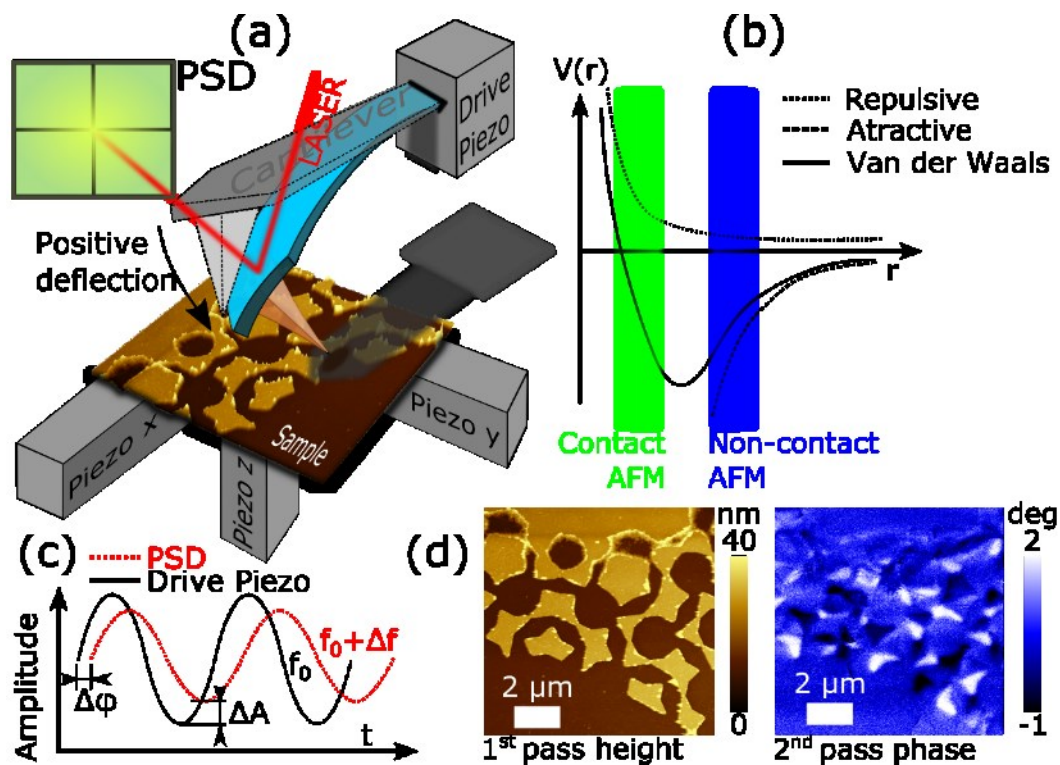
Figure 18. (a) AFM basic elements. (b) Van der Waals potential (c) Amplitude, phase, and frequency shift in AFM. (d) Example of height measured during the 1st pass scan and phase measured during the 2nd pass scan.

Typically the AFM probe is made with pyramidal or conic shape and it is attached to the end of a silicon or silicon nitride cantilever with mechanical resonance of f_0 ~ 50-350 kHz. The cantilever is placed in a holder containing a piezoelectric mechanical actuator whose sole purpose it to oscillate the cantilever at its resonant frequency. The holder (or the sample stage

as shown in Figure 18(a)) itself is attached to a piezoelectric platform that performs x, y and z movements dictated by the AFM feedback loop. The feedback loop has the task of maintain the cantilever's deflection set point, which is governed by the positive or negative force exerted between the sample and the probe. The cantilever's deflection is commonly measured using laser beam reflected from the top side of the cantilever onto a four-quadrant position sensitive detector (PSD) (Figure 18(a)).

One commonly used AFM mode is the tapping mode. In tapping mode the probe is oscillating close to its resonant frequency and maintained by the piezoelectric positioner in the attractive regime of the Van der Waals forces (i.e. positive deflection set point see Figure 18(b). The topographic information is extracted by comparing either the amplitude change or the phase change between the driving signal and the resulting cantilever's deflection (Figure 18(c)).

4.3.1. MFM imaging

MFM is an AFM technique were the magnetic interaction between probe and sample is imaged[160]. When performing an AFM scan, in tapping mode with a magnetic probe, the interaction between the sample and the probe is a convolution of magnetic and Van der Waals forces. However, typically Van der Waals forces are short-ranged, while the magnetic interaction is long ranged. For this reason, MFM is commonly a two-pass method. In the first pass, the probe-sample distance is small being the Van der Waals the dominant force. The second pass is taken at a higher distance where the Van der Waals force can be neglected but the magnetic interaction is still strong (approx. $30 - 100$ nm). During the second pass the feedback is turned off and the cantilever is made to trace the topography, which was recorded during the first pass.

When a ferromagnetic probe is exposed to a magnetic sample, the force due to the magnetic interaction can be expressed as[161]:

$$\boldsymbol{F} = \mu_0 \int \nabla \big(\boldsymbol{M}_{tip} \cdot \boldsymbol{H}_{sample}\big) dV_t \tag{23}$$

where μ_0 is the permeability of free space, M_{tip} is the probe magnetization and H_{sample} is the stray field emanating from the sample. The integral is over the volume of the probe.

If the MFM is recorded in tapping mode, close to the resonant frequency, then the change in phase, amplitude, and resonant frequency, are related with the force exerted over the tip by the relations[162], [163]:

$$\Delta\varphi \approx \frac{Q}{k}\frac{\partial F}{\partial z} \tag{24}$$

$$\Delta A \approx \left(\frac{2A_0 Q}{3\sqrt{3}k}\frac{\partial F}{\partial z}\right) \tag{25}$$

$$\Delta f_0 \approx \frac{f_0}{2k}\frac{\partial F}{\partial z} \tag{26}$$

where Q is the quality factor of the tip as a resonator and k is the spring constant.

Hence, by measuring one of the 3 quantities (phase, amplitude or resonant frequency) and using eq.(23), it is possible to have a qualitative image of the magnetic interaction between the probe and the sample.

4.3.2. Magnetic scanning gate microscopy

Magnetic scanning gate microscopy (mSGM) is a two-pass AFM technique where the magnetic field from the scanning probe affects the conductivity of the sample. During the first pass in tapping mode and at low height, the topography is recorded. During the second pass, at larger height, the feedback is turned off and the cantilever is made to trace the topography, which was recorded during the first pass. During the second pass the resistance of the sample is measured during the scanning, allowing to correlate the position of the tip with changes in the resistance. The oscillation of the cantilever is usually turned off, or it can be neglected if the resistance is measured with DC current or if the frequency of the electrical current is much lower than the frequency of oscillation of the tip.

4.3.3. Custom-made probes

Mainly two types of modified probes were custom-made using focused ion beam (FIB), probes with a MB attached, and probes whose tip has a nanostructure lithographed in one side of the tip's pyramid.

Probes with MB attached were fabricated by modifying non-magnetic silicon SPM probes (TESPA V1 or the new TESPA V2 by Bruker[164] with spring constant $k = 20$ - 80 N/m and a resonant frequency $f_0 = 230 - 410$ kHz). The process starts with MBs dispersed in a buffer solution. After cleaning the buffer solution, by diluting in distilled water, the MBs are drop-cast on a Si/SiO$_2$ substrate. Once the water has evaporated, both commercial probe and substrate with particles are placed inside the vacuum chamber of the FIB system. The FIB

system is equipped with micromanipulators with a single carbon fibre strand attached to them. After sharpening the carbon fibre with Ga-ions, a single MB is located (Figure 19(a)), and attached to the carbon fibre using a small burst of methylcyclopentadienyl-platinum (standard e-beam Pt deposition). The carbon fibre with the MB attached is then moved close to the probe (Figure 19(b)). Using Ga-ions the apex of the SPM probe is flattened (Figure 19(c)), and the MB is glued to the probe with Pt deposition. The final step is mechanically breaking the link between the carbon fibre and the MB (Figure 19(d)).

When compared with other techniques used to attach MBs[165], the advantage of this method is that it allows to manipulate a wide range of particles and probes, without relying in particular properties of the MB or the probe used.
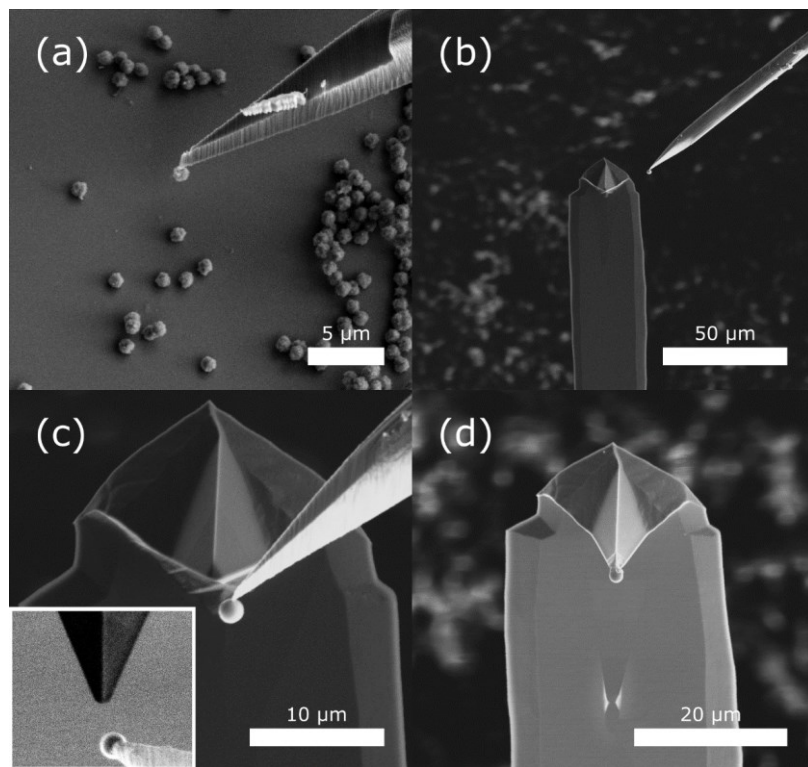
Figure 19. SEM images of the FIB fabrication process. (a) Selection of an isolated MB. (b) MB glued to the carbon fibre moves MB close to the AFM probe. (c) MB is placed at the apex. Inset: Top view of the process. (d) Once glued using Pt-based compound, the carbon fibre is taken away.

Modified probes with a lithographed structure were custom-made using magnetically coated commercial probes from NANOSENSORS™ PPP-MFMR AFM and a FIB system to etch away part of the magnetic coating. As it can be seen in Figure 20(a) to (c), the tip of these probes has 4 triangular sides which are uniformly coated with a CoCr alloy[3] (thickness $t \sim 30$

---

[3] Exact composition known only by the manufacturer.

nm). Typical dimensions of one of the tip's sides are ~ 8 µm in height by ~ 5 µm length of the base (Figure 20(c)). Using Ga-ions, FIB lithography is used to etch away the magnetic material, leaving only a V-shaped magnetic nanostructure (Figure 20(d)). The V-shaped nanostructure's arms are 4.48 µm in length by 200 nm in width, and they meet at 32.3º. The estimated thickness of the nanostructure is about 30 nm. Both arms of the V-shaped nanostructure end in a circular disc of 1 µm in diameter. It has been proved that for magnetic nanostructures with in-plane magnetization the presence of discs at the end of flat nanowires reduces the stray field produced[31].
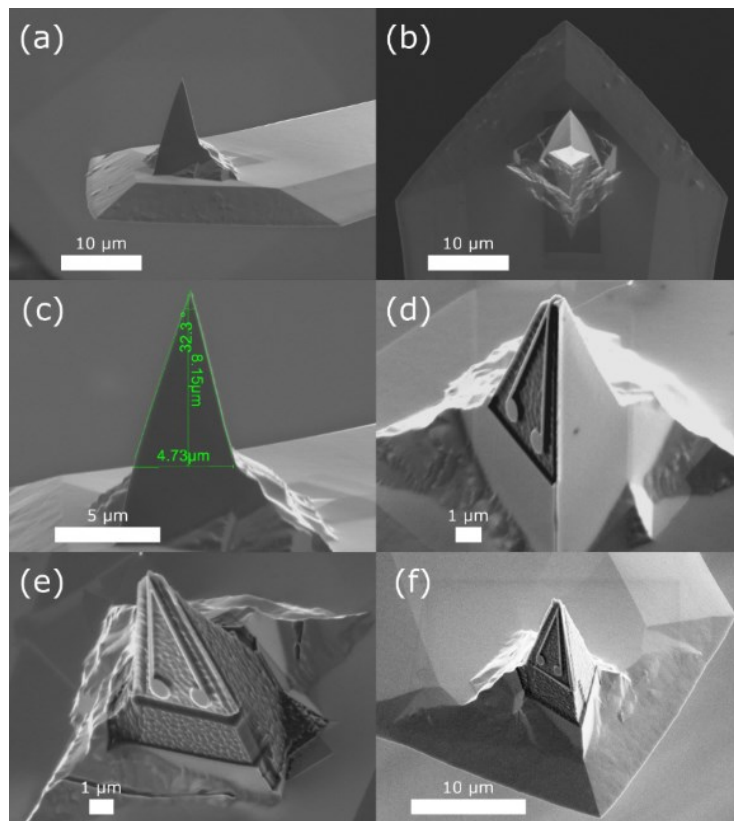
Figure 20. SEM images of the FIB fabrication process. (a) and (b) NANOSENSORS™ PPP-MFMR AFM probe before ion etching. (c) Dimensions of one of the sides. (d) Lithography of the nanostructure on one side of the probe apex. (e) and (f) Images of two different probes after etching away the magnetic coating of the probe.

Although the exact composition of the magnetic coating of the commercial probes is unknown, it is expected that it possesses in-plane magnetization, and hence the V-shaped should behave similarly to ferromagnetic structures of similar dimensions with in-plane magnetization (e.g. 25 nm thick Py L-shaped nanostructures[32]). The shape anisotropy of the L-shaped devices described in Ref[32] generates 4 stable magnetic states at remanence, 2 states with a DW) at the corner (i.e. head-to-head and tail-to-tail DW), and 2 states without a DW at

the corner (i.e. head-to-tail or tail-to-head). It is expected that the V-shaped nanostructures used here behave in similar way and hence have 2 states with a DW pinned at the corner of the V-shape and 2 states with no DW.

4.4. MR measurements

Devices fabricated using the methods described in sections 4.1. and 4.2. were designed in large batches, diced into chips with ~ 20 chips per batch, and ~ 8 devices per chip (see Figure 21(a)). The chips were typically 4 by 4 mm to be mounted on top of non-magnetic ceramic TO-headers (Figure 21(b)). Electrical contacts with the sample were done using gold wire bonding (Figure 21(c)).

Once the sample was mounted on the TO-header sample holder, it was placed inside a plastic insulating box connected by a plastic shaft to a step motor, which is 25 cm away from the sample and can rotate between fixed angles with a step of 0.9º (Figure 21(d)). The TO-header can be mounted horizontal for in-plane field or at 90º for out-of-plane experiments. The box with the sample fits in between the poles of a GMW Dipole Electromagnet (Figure 21(e)), fixing the pole separation to 5 cm. The electrical current on the electromagnet has been calibrated against a Hall linear sensor (Honeywell SS466A Hall Effect Sensor), which parameters where measured using one of the standard magnetic coils at NPL's metrological laboratory. For the conducted experiments the maximum value of the applied field was 180 mT and the applied magnetic field changed in steps of 0.6 mT. The reference for the rotation of the sample-holder was set by measuring MR hysteresis loops at different angles, and defining $\theta =$ 0º (90º) when the loop type changes abruptly, or when the measured switching field of sample's magnetization is maximum or minimum[32] (e.g. magnetic field parallel to a magnetic nanowire will switch magnetization of the nanowire at lower field than when the field is almost perpendicular).

Electrical connections to measurement system were done through a breakout box (Figure 21(f)) which allows connecting BNC cables to the sample (by using T-junctions on all the BNC cables, all connections are put to ground while changing leads' position). The whole setup guarantees that the sample and signals are always enclosed inside a Faraday cage, screening electrical noise or high frequency magnetic fields.

Using the setup described above, MR measurements were performed at room temperature. Both AC and DC measurements were typically done using voltage bias and a large resistor in series with the sample which fixes the current through the system (the circuit involving the sample plus the electrical connections has a resistance < 1 kΩ and the limiting resistance is ~

50 kΩ, for a desired current of 100 μA and a voltage bias of ~ 5 V). The voltage bias was generated with a lock-in amplifier SR830 (front output with maximum 5 V r.m.s. for the AC signal, auxiliary DC output with maximum voltage ±10 V for the DC signal, both with 50 Ω impedance and 10 mA as maximum current[166]). The current passing through the device was drained to ground through a 50 Ω resistor in series (this resistor prevented noise in the ground signal to damage the samples).
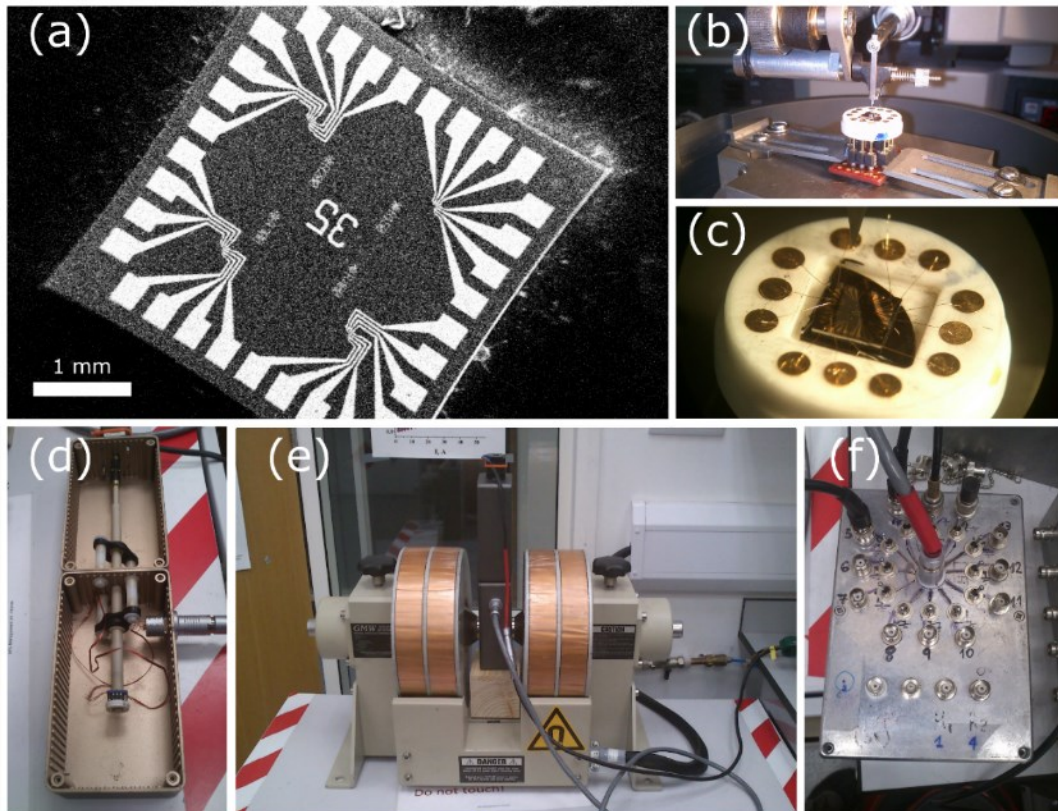
Figure 21. (a) SEM image of a typical chip with nanostructures. (b) Chip mounted on a TO-header inside of a wire bonding machine. (c) TO-header sample-holder with sample mounted and wires connecting sample to measurement system. (d) Sample-holder mounted inside conductive box and plastic shaft allowing sample to rotate. (e) Sample mounted inside electromagnetic coil. (f) Breakout box for connecting the sample-holder to measurement instruments.

In AC configuration, voltage signals from the sample are measured directly using the inputs of the lock-in amplifier (with a 10 MΩ impedance). Depending on the amplitude of the signal and the background offset, which vary due to differences in fabrication and/or quality of electrical connections, sometimes it was required to cancel the background. This was done internally by the lock-in or externally through an amplifier (SR560 voltage amplifier). If the lock-in performs digitalization of the signal directly on its inputs, then external offset

cancellation is needed. If the digitalization occurs after the lock-in measurement, then offset cancellation can be done by the lock-in. This requirement is due to the number of bits used by the lock-in to digitalize the signal, which remains constant for all the input ranges, and thus for a lock-in that digitalizes at its input, resolution decreases if the input range increases. Typically AC frequencies used were in range 72 Hz – 3 kHz, with a time constant in range 10 -300 ms.

In DC configuration, voltage signals are measured using a nanovoltmeter (Keysight 32220A Micro-Ohm meter with input resistance > 10 GΩ up to 10 V range[167]). Typically it was used between 1 and 10 PLC as an integration time (e.g. each PLC is 20 ms long and the total integration time when using 10 PLC is 200 ms per measurement).

4.5. MOKE measurements

MR measurements, in combination with micromagnetic simulations and MFM imaging, can be used to infer the magnetization spatial distribution and detect the presence of a DW. However, MFM imaging has a slow acquisition rate compared with MR, and hence, when studying dynamical effects (e.g. DW movement), it is not possible to use MFM to link MR measurements with numerical simulations. Another approach to extract information is through MOKE microscopy.

In MOKE microscopy, a beam of linearly polarized laser light (*s*-polarized if it is perpendicular to the incidence plane and *p*-polarized if it is parallel), interacts with the surface of a magnetic sample, and as a result, the reflected beam polarization is rotated. The interaction is due to the Kerr effect, and the rotation of the polarization is known as the Kerr angle. The possible scenarios for linearly polarized light are summarized in Figure 22. Those are longitudinal, transversal, or polar Kerr effects[168], [169].

The MOKE system used in some experiments is a custom-made system, and it was used to study magnetization dynamics in straight nanowires. The system works according to the scenario shown in Figure 22(a). A laser beam (λ ~ 650 nm) was focused on the surface of the samples using optical lenses, which produce a spot with diameter of~ 4 μm. Due to the Kerr effect, the polarization changes depending on the magnetization direction, then it is collected by a second polarizer and detected using a photodiode. The second polarizer is used to measure the rotation in the polarization of the laser light beam. By performing hysteresis loops and studying different parts of the nanostructures, it is possible to understand the dynamics of the magnetization reversal.
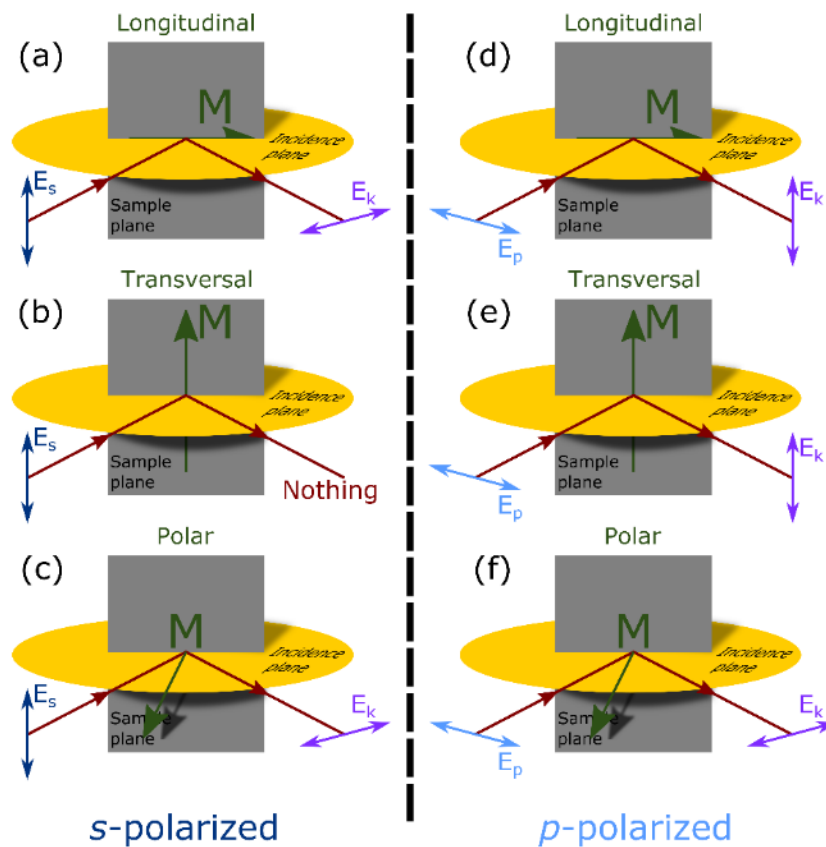
Figure 22. Different scenarios when light is being reflected at the surface of a magnetic sample.

It is important to notice that in our case the size of the spot limits the size of the features that can be analysed. In addition, the tails of the laser spot produce reflections from nearby objects (e.g. Au electrical contacts) reducing the amplitude of the change due to magnetization evolution. To overcome these problems two solutions were implemented. The first one was fabricating samples with longer distances between geometrical features and with electrical contacts far apart. The second solution was measuring several hysteresis loops and averaging the results. Typically the hysteresis loops were taken at 1 Hz (i.e. full cycle from positive saturation to negative to positive again). This frequency for the hysteresis loops was chosen in order to enable simultaneous MR measurements (i.e. much slower due to the small signal-to-noise ratio).

4.6. Summary

This chapter describes the experimental techniques used during the elaboration of this thesis.

It starts with the description of the fabrication techniques and the parameters used. These descriptions enable reproducing the type of devices studied here. Then we discuss AFM

imaging, focusing the attention in MFM and mSGM, which are used later on to characterize magnetic nanostructures.

The experimental set-up used to perform MR measurements was explained in detail, describing the different steps taken towards minimizing the electrical noise and the magnetic interaction with the samples.

The last part of this chapter is dedicated to MOKE measurements. This technique is used in the next chapters to characterize magnetic nanostructures and compare their performance.

5 DWs in L-shaped Py nanostructures

This chapter focuses on the study of MB detection by measuring the effect the MB produces on a DW pinned inside of a Py nanostructure. It is motivated by the works of M. Donolato, P. Vavassori, R. Bertacco et al.[12], [14], [39], [154], who initially proposed using DWs for MB detection. They studied an L-shaped Py nanostructure with two circular disks at the end of the arms. Because of the small dimensions (arms 2 μm long by 500 nm wide; disks of 1 μm in diameter), the shape anisotropy dominates, constraining the magnetization along the arms and creating a bi-stable state at the corner with/without DW. Due to the AMR effect, the presence/absence of the DW changes the electrical resistance across the corner by ~ 0.05%, and thus enable measuring the DW pinning/depinning fields and the effect of external magnetic fields on the DW dynamics. Using these devices, the authors deposit several nanoparticles near the corner of the nanostructures to demonstrate down to single magnetic nanoparticle detection. They used synthetic antiferromagnetic nanoparticles (pillars composed of several layers of FeCo separated by Ru), and MICCROMOD Nanomag®-D magnetic nanoparticles. The reported changes were ~ 2 mT for the synthetic nanoparticles, and ~ 1.5 - 2 mT for the superparamagnetic beads. The authors also observed that MB detection was possible using up to 50 nm of SiO_2 as a capping layer. It is noteworthy that these experiments were performed by ramping the external magnetic field along one of the arms, without experimenting at different angles. Further studies by the same group[104], [105], [108], [109] were focused on the use of the stray field generated by DWs for moving MBs.

In this chapter we perform experiments with Py nanostructures, which design is similar to the one proposed by Donolato et al.[12]. First, we characterize the behaviour of the nanostructures using MFM imaging and MR measurements. This allows creating a state-space map that correlates changes in resistance with changes in magnetization. Next, we study the effect of variations in the geometry on the pinning/depinning fields, concluding that L-shaped nanostructures with square corner and disks at the end of the arms are the best suited for the detection of MBs. We further perform single MB detection experiments (using Dynabeads® MyOne™ streptavidin T1 MBs) with a static MBs placed on top of the corner, and with MBs attached to AFM probes that can be moved around the DW position both in vertical and lateral dimensions. The experiments with a static MB demonstrate successful detection and up to ~ 18 mT change in the DW depinning field due to the effect of the MB on the DW. In the next experiment by using a MB attached to the AFM probe, we estimated the sensing volume and

quantified the maximum distance between the corner of the Py nanostructures and the MB (~ 1.2 μm).

5.1. AMR state space map of Py L-shaped DW pinning geometry

Using the fabrication process described in chapter 4, L-shaped Py nanostructures, were fabricated (Figure 23), using 25 nm thick Py, covered with 2 nm Pt cap to prevent oxidation.
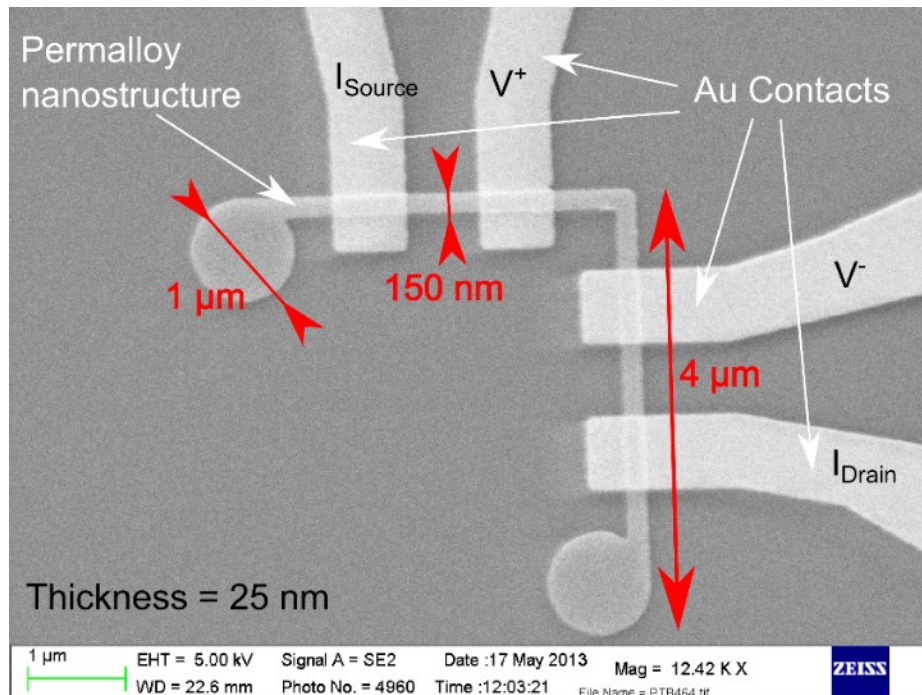
Figure 23. SEM image of the 150-nm wide L-shaped Py nanostructure with Au electrodes. Adapted from Ref[32], with permission from Nature.

The design includes 4 Au electrical contacts, Au 69 nm/ Ti 10 nm, to perform 4-point resistance measurements across the corner. Through this chapter, variations of this basic design were used. The variations include: different widths of the arms ($w = 50 - 400$ nm), short and long arms (4 μm or 10 μm), square or round corners, and nanostructures with/without disks at the end of the arms.

5.1.1. Remnant magnetic states

The first step towards characterizing the L-shaped nanostructures is the identification of the stable magnetic states at zero field. To do so, a $w = 150$ nm wide nanostructure (Figure 23) was imaged using MFM. This allowed to identify 4 stable states: two with a DW at the corner, and two without (Figure 24). These states were created by applying a magnetic field of 17 mT along the direction indicated by the white arrows.

In Figure 24(a) a DW is pinned at the corner of the L-shape with the magnetization of the

arms in a head-to-head configuration. This configuration is ascribed as state [-1,-1] referring to the magnetization orientation in the two arms, which is pointing towards the corner in respect to the (*x, y*) axes (Figure 24(c), inset). Figure 24(b) displays a state with no DW in a head-to-tail configuration of the arms. In this case, some inhomogeneity at the corner can be observed, which reflects a gradual spatial change of the magnetization from one arm to another. This state is named [1,-1].
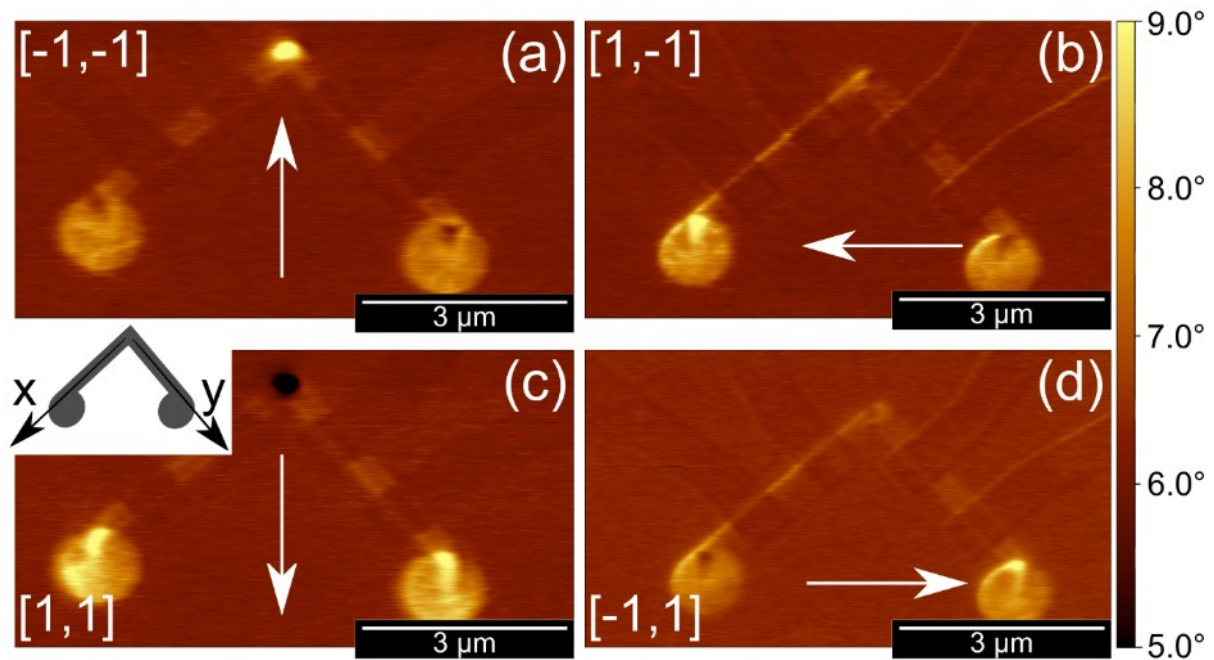
Figure 24. MFM images of the 4 stable magnetic states after applying a magnetic field along the white arrows. Assuming a constant magnetization along the nanowires and using the (x, y) coordinates, these states can be named as: (a) [-1,-1] with a DW at the corner, (b) [1,-1] with no DW, (c) [1,1] with a DW at the corner, (d) [-1,1] with no DW. Inset in (c) shows the Cartesian axes (x, y). Adapted from Ref[32], with permission from Nature.

Figure 24(c) shows a DW in a tail-to-tail configuration of the arms, or state [1,1]. Finally, Figure 24(d) depicts a state [-1,1] with no DW at the corner. The magnetization of the MFM tip does not change through the experiment, allowing proper comparison of all four possible stable states. This result is in agreement with the results obtained on similar devices using MOKE microscopy[170], [171]

5.1.2. MR measurements

With the 4 stable magnetic states identified, the next step is to link the changes in magnetization and resistance across the corner. To do so, we used the electrical connections shown in Figure 23 with the MR setup described in chapter 4 (I_{AC} = 10 μA, f = 72 Hz) and

performed two types of MR experiments accompanied by micromagnetic and MR modelling[4]. In the first type of the experiment (an angular mapping of MR curves), typical MR hysteresis loops across the corner[31], [171] were measured for different angular orientations β of the applied field, i.e. $0° < \beta < 90°$ and $90° < \beta < 180°$ where β is the angle between the applied field and the *x*-arm (Figure 25 insets). The objective of this experiment is to identify conditions for generating the stable states and provide data to fit the simulations. In the second type of the experiment (state space map), one of the 4 main domain configurations shown in Figure 24 was pre-set initially. Then the corner resistance was measured, while the magnetic field was ramped up at a certain angular orientation. The aim of this experiment is to test all combinations of initial magnetization states and orientations of the applied field in order to build a complete state-space map of the L-shaped nanostructure, where both the magnitude and orientation of the field change in small steps. Such state-space maps can be used to predict the evolution of the magnetization in a varying magnetic field without the need for additional transport measurements.

5.1.3. Angular mapping of MR curves

MR measurements were performed at different angles β (Figure 25 insets), and two types of reversal mechanisms were observed in the MR hysteresis loop as a function of the field orientation[31], [171]. It is noteworthy that the geometry of the nanostructure implies two-fold symmetry of the experimental results making the field orientations separated by 180° to be identical.

5.1.3.1. Angles $0° < \beta < 90°$

MR measurements were performed for $0° < \beta < 90°$ in 0.9° steps with the magnetic field changing from -120 to 120 mT in 0.6 mT steps. Figure 25 shows the experimental and modelling results for a $w = 150$ nm wide nanostructure at 4 representative angles. The micromagnetic modelling was performed using typical magnetic parameters for Py, 860 kA/m for the magnetization saturation and 13 pJ/m for the exchange constant, excluding magnetocrystalline anisotropy term, and ramping the magnetic field in 1.6 mT steps. In agreement with the thickness dependence of Py electrical properties[172], the MR simulations have been performed by fixing σ_0 (the electrical conductivity when the material is saturated due to an external field orthogonal to the current flow) to 4 MS/m (i.e. the resistivity to 25 $\mu\Omega$ cm). The modelled MR curves have been obtained by setting the AMR ratio at 1% in order to achieve the best agreement with the experimental results. This value belongs to the parameter

---

[4] Micromagnetic and MR modelling done at INRIM (Italy), by Alessandra Manzin and Vahid Nabaei.

range typical for Py, which varies from 1 to 5%, depending on the amount of Ni in the alloy[173]. For these experimental and modelling parameters, a very good agreement is reached for both the shape of the MR curves and the electrical resistance values. This confirms that for these Py nanostructures the MR is dominated by the AMR effect.
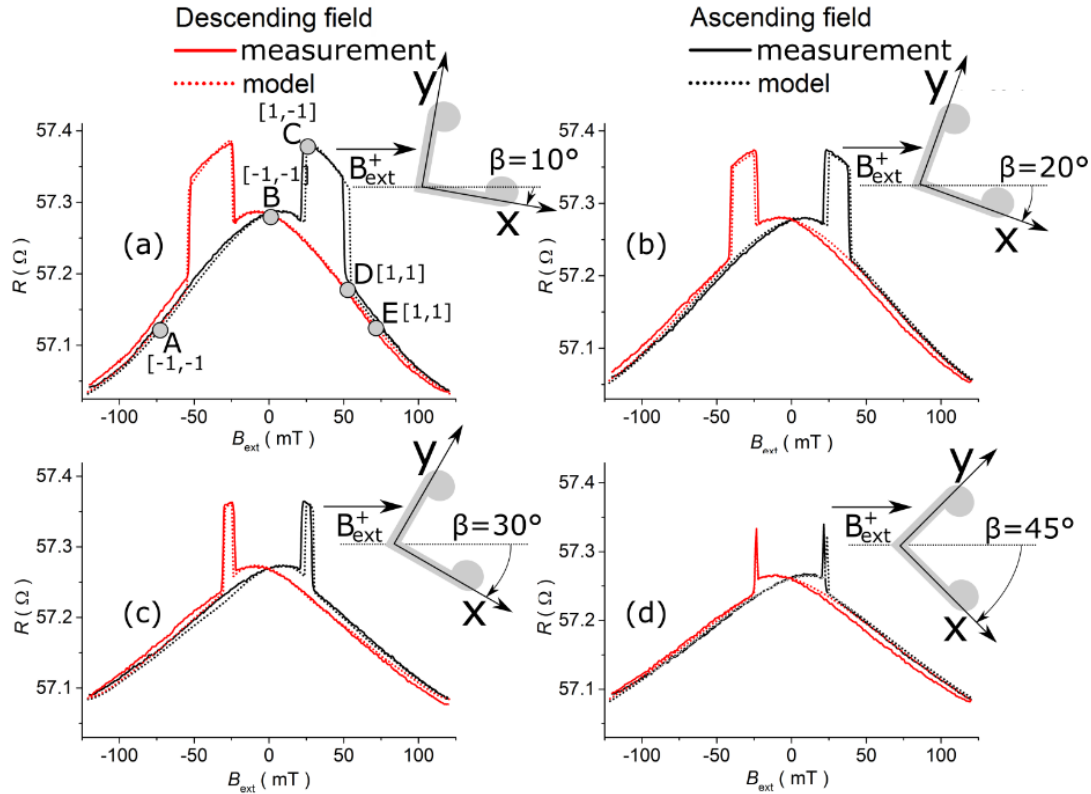
Figure 25. Measured and simulated AMR curves for β = 10° (a), β = 20° (b), β = 30° (c) and β = 45° (d). The black line represents the sweeping of the magnetic field from negative to positive values, while the red line shows the descending field branch. Insets show schematic orientation with respect to the magnetic field. Adapted from Ref[32], with permission from Nature.

Using the magnetic domain configuration obtained by micromagnetic modelling, it is possible to interpret AMR curves in terms of DW pinning/depinning processes. In the AMR curves presented in Figure 25(a), a number of equilibrium points have been labelled together with the corresponding magnetization states. The detailed magnetic configuration of the device at these points is shown in Figure 26.

Following the black line in Figure 25(a), starting from a high negative field value at point **A** (i.e. the maximum applied field is -120 mT, while point **A** is ~ -75 mT), the horizontal arm is uniformly magnetized along the *x*-negative axis, while the magnetization in another arm is aligned at a certain angle with respect to the field direction. This state corresponds to a low resistance value. When moving towards remanence (point **B** at 0 mT), the magnetization of the

vertical arm becomes parallel to the *y*-axis, hence increasing the resistance[174]. The state [-1, -1] corresponds to a DW pinned at the corner, where magnetizations of both arms are aligned along *x* and *y* axes. Point **C** (in the range 17.0-22.5 mT (±1 mT) depending on the exact angle) indicates depinning of the DW from the corner and the transition to state [1,-1]. Switching of the horizontal arm is favoured at small angles $\beta < 45°$, since in this case the component of the magnetic field along the *x*-axis is higher. When the magnetic field increases further, in point **D** (in the range 52-55 mT (±1 mT)) the vertical component of the magnetic field is high enough to allow the second switching event and the consequent pinning of another DW. This corresponds to a state [1,1]. Between equilibrium points **C** and **D** the resistance reaches the highest value because of the AMR effect (magnetization and current density vectors are nearly parallel). After point **D**, the resistance gradually decreases with the field, due to the rotation of the magnetization towards the external field direction. As the field increases, the magnetization tends to deviate from the easy direction, starting from the arm aligned along the y-axis, since it experiences the highest transversal magnetic field (point **E**). A symmetrical behaviour is observed when the external field is swept from high positive to high negative fields (red curve, in Figure 25(a)) for both simulated and experimental data.
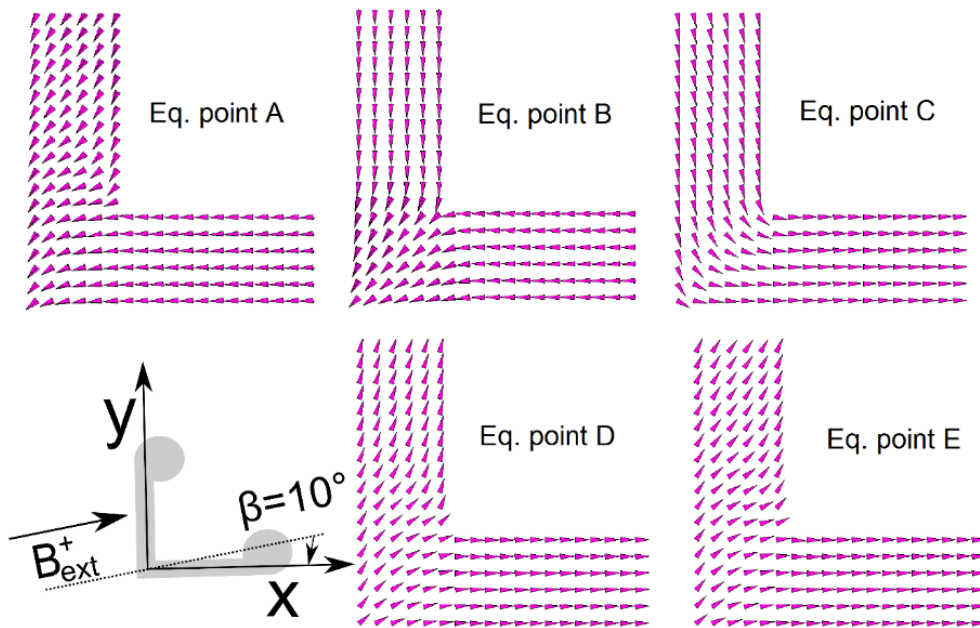
Figure 26. Computed magnetization spatial configurations near the corner for the equilibrium points indicated in Figure 25(a) at β = 10°. Adapted from Ref[32], with permission from Nature.

For the other angles in Figure 25, the behaviour is qualitatively the same as presented in Figure 25(a). However, when the angle β increases from 0° to 45°, the range of fields between equilibrium points **C** and **D** (i.e. the high resistance range characterized by the absence of the

DW) gets progressively narrower. For example, for $\beta = 0°$ the difference between points **C** and **D** is maximal, ~ 108 mT (i.e. point **C** is at ~ 21 mT and **D** is at ~ 129 mT), while at $\beta = 45°$ this difference is nearly zero, i.e. both **C** and **D** transitions occur at the same field of ~ 21 mT.

5.1.3.2. Angles 90° < β < 180°

The same type of measurements on the $w = 150$ nm wide nanostructure were repeated for $90° < \beta < 180°$, where a change in the switching pattern was observed. An example of the AMR curves modelled and measured at $\beta = 95°$, and relevant computed magnetic domain configurations are shown in Figure 27. For angles $90° < \beta < 180°$ (and $270° < \beta < 360°$), a higher magnetic field (120 mT) leads to a magnetization state without a DW at the corner. As the magnetic field decreases, first pinning of a DW indicated by a decrease in the resistance is observed at point **B** (in the range of 21-33 mT (± 1 mT)), which is followed by a depinning event at point **C** seen as the associated resistance increment (in the range of 35-141 mT (± 1 mT)), see Figure 27.
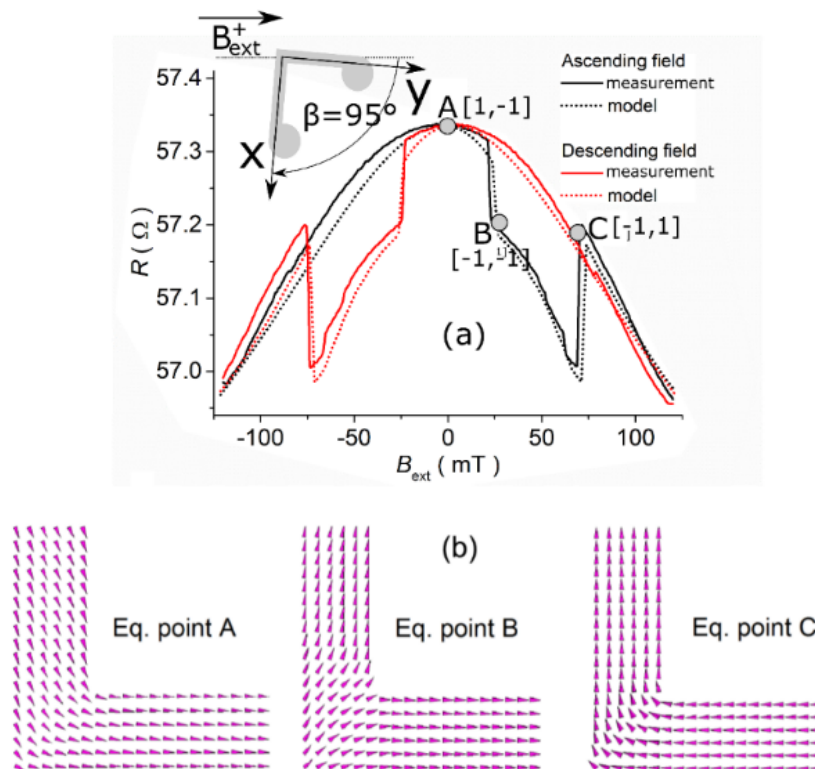
Figure 27. (a) Measured and simulated AMR curves at β = 95°. The black line represents the sweeping of the magnetic field from negative to positive values, while the red line is associated with the descending field branch. (b) Computed magnetization spatial configurations at the device corner for the equilibrium points indicated in (a). Adapted from Ref[32], with permission from Nature.

5.1.3.3. Complete angular mapping

In order to complete the characterization, 10 complete MR loops of the $w = 150$ nm wide nanostructure were measured and averaged for each orientation at $0° < \beta < 180°$ (with a step of 1.8°). The results from these measurements are shown in Figure 28, where the colour scale represents the resistance across the corner. The sweeping of the magnetic field from negative to positive values is plotted in the right-side panel, while the sweeping from positive to negative is reported in the left-side one. The DW pinning and depinning processes are observed as sharp borders between the areas of different shading. In the same figure, the different magnetization states as well as the pinning/depinning fields extracted from simulations are marked.
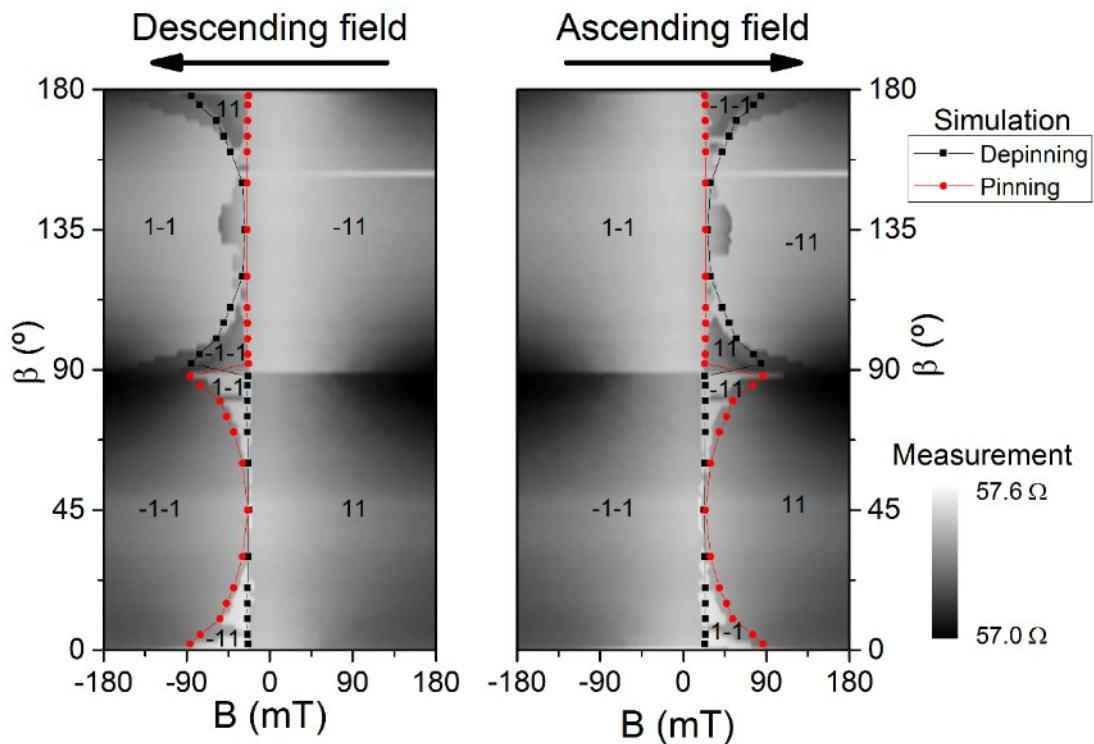
Figure 28. Averaged 2D maps of the AMR dependence on angular orientation β. The field sweeps from a high positive to a high negative value (left) and vice versa (right). Magnetization states are identified in respect to x-y axis, see Figure 25(a). The calculated DW pinning/depinning fields are identified by square and dot symbols, as specified in the legend. Adapted from Ref[32], with permission from Nature.

The maps in Figure 28 demonstrate an angular dependence of the reversal mechanism in the L-shaped Py nanostructure, and agree with reported results for non-interacting Py nanowires of similar width and thickness[175]–[177]. For $0° < \beta < 90°$ (Figure 28, lower part of the maps), the first resistance jump (DW depinning) occurs at 17-21 mT (±1 mT) and is nearly independent of β (i.e. variation is below 5 mT). On the contrary, the DW pinning field associated with the second resistance jump is strongly influenced by β and varies smoothly in

the range 23-130 mT (±1 mT). This angular dependence of the DW pinning/depinning fields can be explained as the result of projecting the applied field along the direction of each arm (i.e. $\cos(\beta)$ term for one arm and $\cos(\pi/2-\beta)$ term for the other). These dependencies are swapped at 45° and 135°. This consideration explains why the first resistance jump is only weakly influenced by the angular orientation. However, a larger influence is expected when the nanowire width is reduced, due to the increase in the arm coercivity and, consequently, in the field leading to magnetization reversal. The lowest field values are reached at $\beta \approx 45º$. In this case, the two critical fields are of approximately the same value, ~ 21±1 mT. This is due to the fact that the magnetization reversal takes place nearly simultaneously in both arms due to the L-shape symmetry, as also demonstrated in Figure 25(d). A similar situation is observed for $90º < \beta < 180º$ where, however, the characteristic behaviour of pinning/depinning fields is swapped (Figure 28 upper part of the maps). In this case, the DW pinning field has a small angular dependence, changing in the range 21-33 mT (±1 mT), while the DW depinning field is characterized by a strong angular dependence, changing in the range 35-141 mT (±1 mT).

The averaging procedure used here reduces the fine effects related to the internal structure of the DW. These effects appear stochastically during measurements and are experimentally observed as pinning/depinning events taking place at different fields[43], [178]–[181]. It also minimizes the effects of fabrication and film growth defects, however some fine features seen in Figure 28 still can be attributed to such device/material defects and inhomogeneities.

The angular dependence of DW pinning/depinning fields has also been studied using MR simulations, which show a good agreement with experimental data for both angular ranges (see dots in Figure 28). While the modelling results describe the main experimental tendency very well, there are still some additional experimental features not reflected in the modelling (see e.g. in Figure 28 transitions at ~ 10º, 80º, and 135°, where pinning events occur at a different value than the one simulated). Since the measurements have been averaged, these differences can be attributed to defects in the structure (i.e. edge roughness or internal defects). In some cases, these features could be attributed to development of a quasi-single domain state in low fields. An evidence for this can be seen as an additional domain sub-structure occupying a small part of the device corner in the remnant state after application of the field at $\beta = 135°$ (see, e.g. Figure 24 (b) and (d)). As the field evolves, these substructures propagate through the device causing the additional steps of the MR.

To separate the influence of defects from stochastic behavior, Figure 29(a) shows individual, not averaged, angular maps for two L-shapes of the same width $w = 150$ nm. This

figure demonstrates that in the case of stochastic pinning/depinning (as opposite as in Figure 28 at β = 135°) the switching field changes abruptly several times between consecutive measurements taken varying the angular orientation by only 0.9º (e.g. Figure 29(a) right map at $\beta \sim 12°$). However, overall 'shape' of the space-state and reliable working points remain the same for both devices (e.g. in all cases $\beta \sim 45º$ and $B \sim 60$ mT corresponds to a state [1,1]). To compare the effect of width variation, Figure 29(b) shows angular maps of two different devices with w = 100 nm (right) and 200 nm (left). From analysis of Figure 29, we conclude that the qualitative behaviour remains the same in the studied width range. Additionally, we observe reduction in the absolute values of pinning/depinning fields as well as the difference between them as the device width increases. Thus, for the presented width range, the stochastic behaviour is not significantly affected by variations in the DW structure.
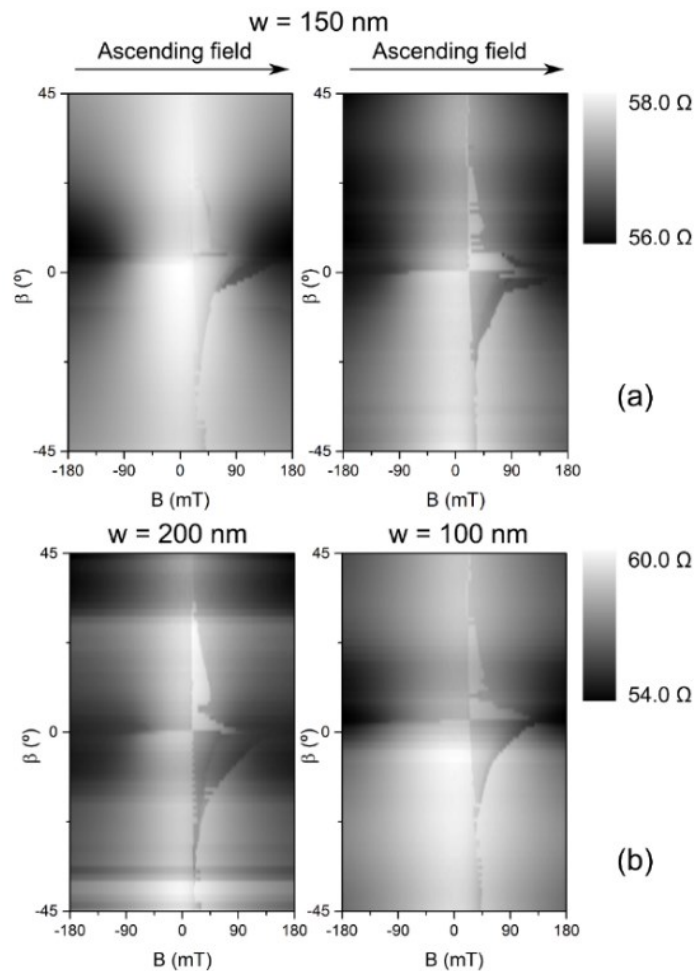
Figure 29. Not averaged angular maps demonstrate the effect of the stochastic behaviour between individual measurements and the width dependence of the pinning/depinning fields: (a) two different nanostructures of w = 150 nm; (b) w = 200 nm (left) and w = 100 nm (right). Adapted from Ref[32], with permission from Nature.

5.1.4. State-space map

The results shown in Figure 28 and Figure 29 allow to predict the behaviour of the L-shaped nanostructure upon exposure to either large or small external magnetic fields, as reported in [12], [39], however, not when both the magnitude and orientation of the magnetic field change at the same time. Thus, the second type of experiment is performed to create a state-space map linking the changes in resistance of the device with its magnetization. This experiment allows to predict the DW evolution under a time-dependent magnetic field that changes both magnitude and orientation (assuming a quasi-static magnetic field evolution).

A complete state-space map is shown in Figure 30(a) for a $w = 150$ nm wide nanostructure. The main difference with the previous results (Figure 28) is that the L-shape was initially set into one of the 4 stable and well-defined states, by applying a large external magnetic field (120 mT) at either 45º or 135º (as previously confirmed by MFM in Figure 24 and AMR in Figure 28). The state is then changed by applying another field at a fixed angle $0º < \beta < 180º$, while recording the resistance. This procedure is repeated for all 4 identified stable states as initial configurations and for all orientations of the second field. Data from Figure 28 is used to identify the exact conditions (i.e. magnitude and orientation of the external field) needed for generating each of the stable states. For example, to create a tail-to-tail state at zero field (state [1,1]), the device should be placed at an angle $40º < \beta < 50º$ and magnetic field $B \geq 60$ mT. Under these conditions state [1,1] is always observed experimentally, see Figure 28. Alternatively, to create a head-to-head configuration (state [-1,-1]), the device should be put at an angle $40º < \beta < 50º$ and magnetic field $B \leq -60$ mT. To create head-to-tail and tail-to-head configurations (i.e. [-1,1] and [1,-1], respectively) the same procedure can be used, using $140º < \beta < 150º$ and $B \geq 60$ mT or $B \leq 60$ mT, respectively.

Figure 30(a) also demonstrates how different initial states may evolve into other states (angular reference and state configurations in Figure 30(b)). As before, two magnetization configurations are considered identical if the transition between them occurs without a sharp change in the resistance (i.e. no pinning/depinning of DW is involved in the process) and without saturating the magnetization by the external magnetic field. Since no new stable states were observed, the state-space map can be considered complete, in the sense that the magnetization always evolves only into one of the already known states.
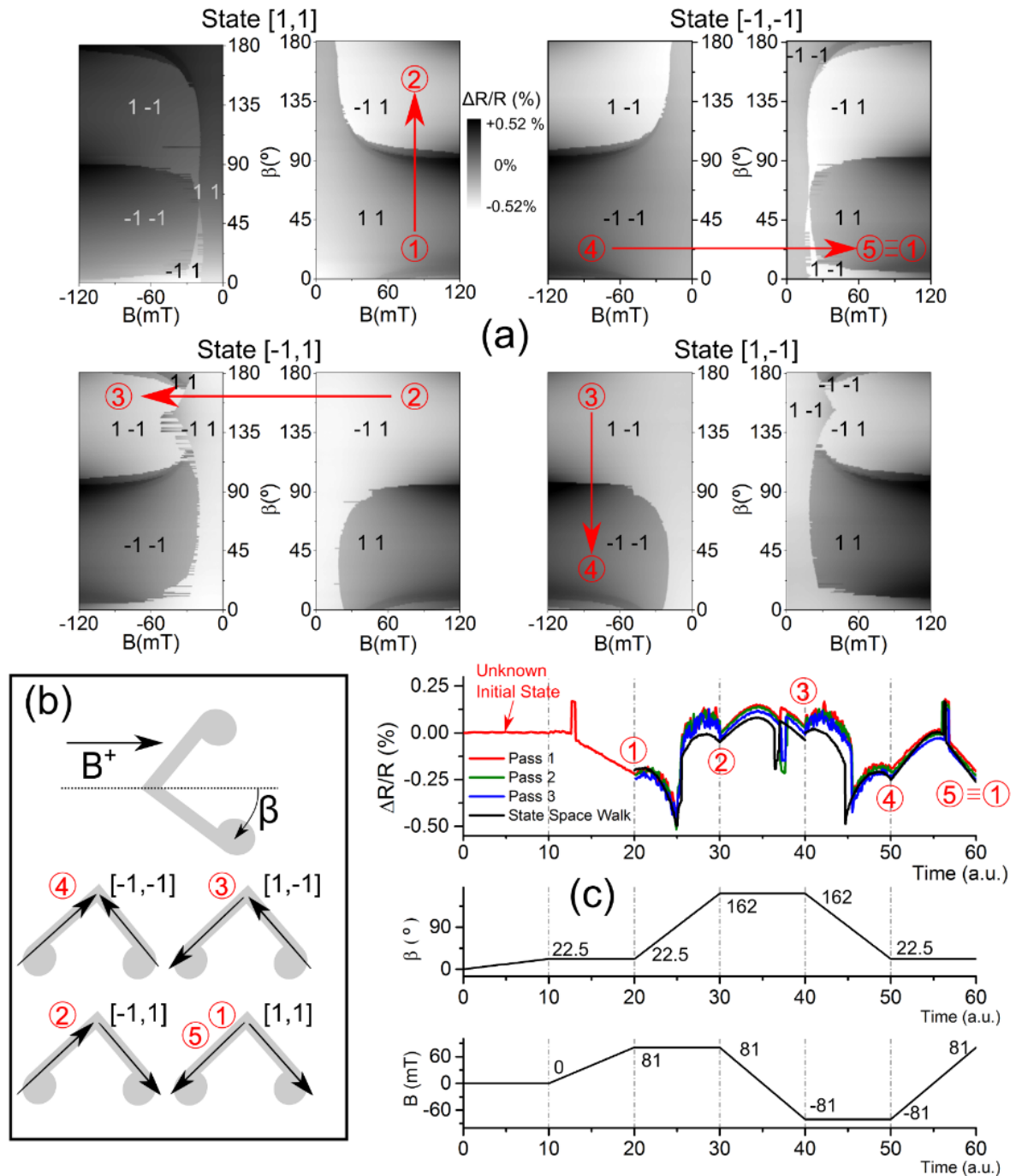
Figure 30. (a) Complete state space for an L-shaped Py nanostructure, w = 150 nm. The initial state at zero magnetic field is shown on top of each panel. The red numbers and arrows indicate the path followed by an individual AMR measurement to test the validity of the state-space. The greyscale represents the change of the AMR signal. (b) Schematic of the nanostructure orientation and state configuration with respect to x-y axis. (c) Top: (black) data extracted from (a) represents the evolution of the resistance, when the field follows the path 1-5. (Other colours) experimentally measured data when the field follows the path 1-5. Colours represent different experimental runs. Middle and bottom: Schematic change of the field orientation and magnitude, respectively. Adapted from Ref[32], with permission from Nature.

Whereas the majority of boundaries in Figure 30(a) are sharp, some exhibit significantly stochastic behaviour (e.g. bottom left panel in Figure 30(a)), indicating that either the transition is unstable, i.e. might occur at two different fields, or there are stochastic pinning/depinning events taking place[43] [178], [179]. An example of such behaviour is shown for the [-1,1] to [1,-1] transition at $\beta = 135°$ and $B < 0$, where for some of the runs switching occurs at different fields (Figure 30(a), bottom left).

The state-space map shown in Figure 30(a) allows to reliably predict the L-shaped magnetization evolution under a changing external magnetic field and define a procedure for the initialization of future DW-based sensors, i.e. putting them into a well-defined magnetization configuration. This last parameter is extremely important, since for sensing applications, the proximity of a small magnetic object (e.g. a MB) will result in a shift of the DW pinning/depinning fields[12] and some transitions might be more favourable than others. The state space map allows to select the optimal transition parameters to measure this effect.

In order to illustrate how to initialize the magnetization into a particular state and use the map to track this state, an arbitrary path (i.e. evolution of an applied magnetic field) has been selected to test the predicted transitions between different states. Red numbers in Figure 30(a) and data in Table 1 indicate the chosen path in the state space. The resistance changes of the nanostructure's corner along this path have been extracted from the existing map (i.e. without adding more measurements) and presented in Figure 30(c) as a black line which connects points 1 to 5, corresponding to evolution of the magnitude and orientation of the magnetic field as depicted in Figure 30(c) (middle and bottom) and Table 1.

Table 1 The orientation and magnitude of the applied field for the arbitrary path selected in Figure 30(a) and extracted in Figure 30(c) (black line). Adapted from Ref[32], with permission from Nature.

Path	Initial β (degrees) (± 0.9°)	Final β (degrees) (± 0.9°)	Initial Field (mT) (± 0.6mT)	Final Field (mT) (± 0.6mT)	State transition
1 – 2	22.5	162.0	81	81	[1,1] → [-1,1]
2 – 3	162.0	162.0	81	-81	[-1,1] → [1,1] → [1,-1]
3 – 4	162.0	22.5	-81	-81	[1,-1] → [-1,-1]
4 – 5	22.5	22.5	-81	81	[-1,-1] → [1,-1] → [1,1]

The red line in Figure 30(c) (top) represents experimental MR measurements for the same combination of the fields. Despite the unknown initial state, as soon as the external conditions,

i.e. magnetic field amplitude and orientation, approach the ones corresponding to point 1 (Figure 30(c), middle and bottom), the magnetization evolves into a [1,1] state. A small difference in the resistance between extracted data and measurements is likely to be caused by thermal effects. From point 1 to point 2, the magnetic field remains constant, while the angle increases from 22.5º to 162º. When the orientation is close to 90º, there is a change in the state from [1,1] to [-1,1], as predicted by the map (Figure 30(a)). From point 2 to point 3, the orientation remains constant and the field changes from +81 mT to -81 mT, corresponding to the change of states from [-1,1] to [1,-1]. Here, the measured profile agrees with the extracted one, but the transition occurs at a slightly different field. On the state space map, the transition 2 − 3 corresponds to the crossing of the border with significantly high density of stochastic switching and a strong angular dependence. At the transition 3 − 4, the nanostructure is rotated again and the state changes from [1,-1] to [-1,-1]. Finally, the transition 4 − 5 corresponds to sweeping of the magnetic field from -81 mT to +81 mT without a change of the field orientation and results in the change from [-1,-1] to [1,1]. The second sweep of the magnetic field occurs in an area with a low probability of stochastic transitions and small angular dependence. This results in a better agreement between experimental and extracted paths for the profile 4 − 5 in comparison to the profile 2 − 3 and indicates that such transition is potentially better suitable for detection of small shifts due to external magnetic fields (i.e. due to presence of a nanoparticle). Point 5 is identical to point 1, both in terms of the external conditions and the internal state ([1,1]). Thus, the cycle is completed. To test reproducibility of the states, a number of consecutive runs have been performed immediately afterwards (Figure 30(c), blue and green curves). All the curves demonstrate a very good match between individual runs and agreement with the predicted jumps in the resistance due to DW propagation. It is noteworthy that in all the runs the resistance measurements are less stable when the magnetic field changes its orientation rather than value. The effect is due to the physical rotation of the sample stage and the associated mechanical vibrations.

5.2. Tailoring of DW devices for sensing applications

In this section we define the optimal geometry and experimental conditions in order to improve the sensitivity of the Py L-shaped nanostructures. For that purpose MR measurements were performed to experimentally monitor the DW pinning/depinning processes in different nanostructures with variable width of the arms, $w = 50 - 400$. The fields, at which these events occur, have been measured and estimated by means of a micromagnetic numerical model for different orientations of the device with respect to the external magnetic field. In order to test the reproducibility of DW dynamics, all measurements have been repeated several times and averaged to find the conditions leading to the highest probability of stochastic DW pinning/depinning processes [182].
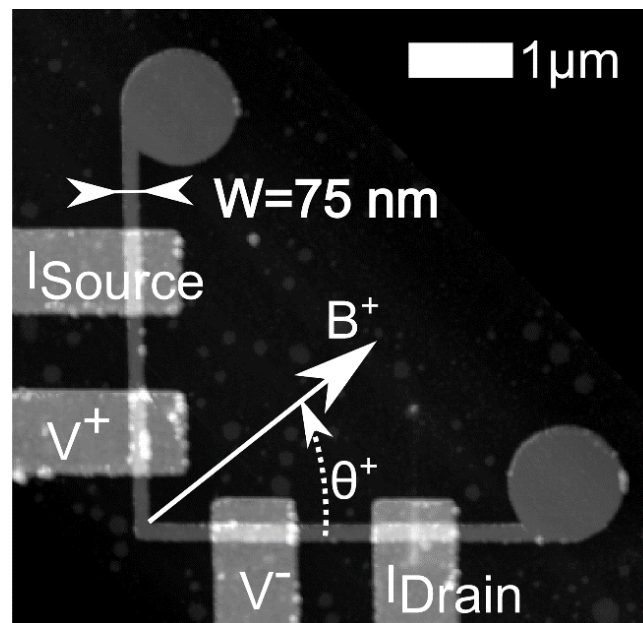
Figure 31. SPM image of the L-shaped nanostructure with width w = 75 nm. Adapted from Ref[183], with permission from IEEE.

The 4-point MR measurements were performed at room temperature using the electrical connections shown in Figure 31, with I_{AC} = 10 µA and f = 172 Hz. The in-plane external magnetic field was swept between -135 mT and +135 mT and back again (at a rate of ~ 4.5 mT/s). Figure 31 shows the angular orientation θ of the applied magnetic field with respect to the horizontal arm. The results from MR measurements were interpreted by means of micromagnetic simulations[5]. The modelling was performed using a micromagnetic solver[25]. The code adopts a norm-conserving scheme based on the Cayley transform [27] for the time

---

[5] Micromagnetic and MR modelling was done by Alessandra Manzin and Vahid Nabaei at INRIM (Italy).

integration of the Landau-Lifshitz-Gilbert equation and the efficient computation of magnetization at equilibrium.

Both experimental and modelling approaches were used to characterize the L-shaped nanostructures behaviour. First, MR measurements were performed to investigate the DW pinning/depinning mechanisms as a function of the nanostructure orientation with respect to the applied field. Second, the influence of the nanowire width on the magnitude of DW pinning/depinning fields was extracted from MR measurements and micromagnetic simulations.

5.2.1. DW pinning/depinning mechanism

Figure 32(a) shows a typical experimental MR curve for a 200 nm wide device-shaped nanostructure obtained by sweeping the magnetic field between -135 mT and +135 mT, at an angular orientation $\theta = 9°$. For this orientation, the magnetization pattern at negative saturation field corresponds to a state with a DW pinned at the corner (see Ref [171] and also the results from previous section for a nanostructure with w = 150 nm in Figure 25). As field increases towards positive values, the device passes the remanent state, while the DW is still trapped at the corner [31]. When the system reaches the point where the external field overcomes the depinning value, B_{depin}=16.2 mT for this orientation, the DW is annihilated and the magnetization in the horizontal arm (the one better aligned with the magnetic field, being θ <45°) switches. Due to the AMR effect, this first switching event corresponds to an increase in the MR value across the corner [12], [31], [171]. The further increase in the external field leads to a second switching event at B_{pin} = 40.5 mT, where a new DW is pinned at the corner, corresponding to the switching of the magnetization in the other (vertical) arm and the consecutive reduction of the resistance due to the AMR effect.

The reversal mechanism can be further clarified through micromagnetic simulations, analysing the magnetization domain pattern at different equilibrium points (see Figure 33 for a nanostructure with w = 150 nm at θ = 10°). Specifically, the simulations were performed by neglecting thermal effects and considering magnetic parameters typical for Py, i.e. a magnetization saturation of 860 kA/m, an exchange constant of 13 pJ/m and a negligible anisotropy constant. The calculated MR curve reported in the inset was obtained via the modelling approach described in [31] and used in the previous section, assuming in this case an AMR ratio equal to 1.5% for Py. At remanence (equilibrium point A), the simulations demonstrate the presence of vortex cores in the circular pads and of a transverse DW at the device corner. Before the depinning event, DWs nucleate in correspondence of the wire-pad

junctions (point B). Then, the DW at the pad connected to the horizontal arm propagates with an irreversible process towards the corner, leading to the annihilation of the pre-existing DW (point C) and to an increasing AMR effect. Also the switching in the vertical arm is influenced by the formation of a DW (e.g. vortex-like) at the joint region, propagating with a reversible process up to DW pinning at the corner (point D) and consequent decreasing AMR effect.

The L-shape symmetry implies that the same MR behaviour is found for 0º < θ < 90º and for 180º < θ < 270º, taking into account that for θ = 45º and 225º the two switching events occur nearly simultaneously. At 90º < θ < 180º and 270º < θ < 360º, the starting/finishing points of measurements (i.e. negative/positive high fields) correspond to magnetic states without a DW at the corner. For these orientations, the sweeping of the magnetic fields leads first to DW pinning followed by DW depinning at higher fields [31]. Thus, we have to emphasize that the order of the switching event depends on the original state of the device, i.e. initial presence/absence of a DW in the corner.
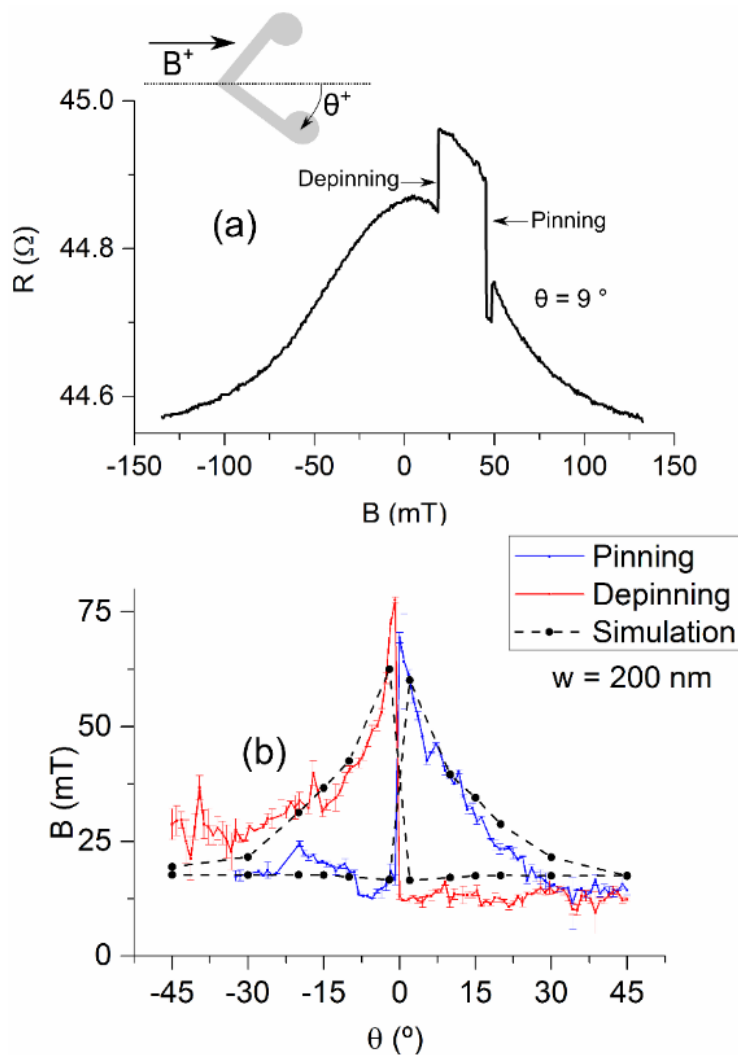
Figure 32. (a) Typical MR curve for a 200 nm wide nanostructure at θ = 9°. Field is ramped from a high negative to a high positive value. (b) Extracted pinning/depinning fields for the same device at different angular orientations. Error bars show standard deviation. Black points correspond to the simulated results. Adapted from Ref[183], with permission from IEEE.

Figure 32(b) shows the angular orientation of pinning/depinning fields extracted from MR measurements of the 200-nm wide nanostructure ($-45° < \theta < +45°$ in steps of 0.9°). At each angle, the field is swept 20 times, between -135 mT and +135 mT, to account for possible stochastic processes. Pinning and depinning fields were extracted from each experimental MR curve and averaged. Note, that for some angular values (i.e. $-45° < \theta < -30°$) only single transition is indicated, which is happening when the two switching events occur nearly simultaneously and it was not possible to distinguish the two fields on the MR curves. Figure 32(b) demonstrates how pinning and depinning fields depend on the angular orientation of the nanostructure (the same dependence was demonstrated in Figure 28 where pinning/depinning fields in red/black respectively extracted from simulations and along the x-axis, were superimposed over MR curves): the corresponding B_{pin}/B_{depin} values diverge for small angles, $\theta \sim 0°$, and converge to the same value at $\theta \sim \pm45°$. For example, for small positive angles B_{pin} = 77 mT and B_{depin} = 12 mT, whereas at $\theta = \pm45°$ $B_{pin} = B_{depin}$ = 14 mT. Figure 32(b) also shows how pinning and depinning events invert the order in which they occur when sample orientation is crossing zero field. It should be noted that the field corresponding to the first switching event has almost no angular dependence (i.e. field variation between 9 and 17 mT), while the second event is strongly angular dependent (i.e. field variation between 14 and 77 mT).
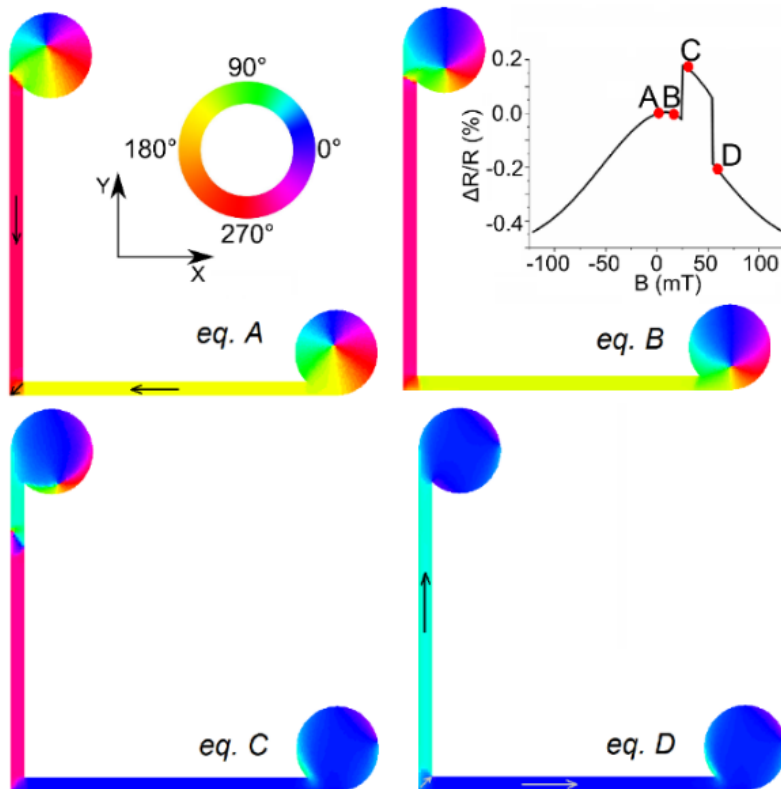
Figure 33. Simulated spatial distributions of the magnetization at specific equilibrium points shown in the calculated MR curve (inset) for a 150 nm wide device at θ = 10°. The colour scale identifies the magnetization angle (in degrees) with respect to x-axis. Adapted from Ref[183], with permission from IEEE.

The error bars[6] shown in Figure 32(b) provide the intervals of switching field variations, giving extra information about the reproducibility and control of the device behaviour [179], [180], [182], [184]. Differences in the size of the error bars can be attributed to the probability of the stochastic switching. This can be seen also in the angular behaviour of the random oscillations in field values on Figure 32(b). When orientation is in vicinity of $\theta \sim 0°$, there are random oscillations of ~ 0.4 mT in the switching fields from one angle to another, while the error bars have values ~ 0.2 mT. Close to $\pm 45°$, the oscillations in switching fields between different steps are ~ 1.2 mT, whereas the error bars size is ~ 1.1 mT. It is clear from these results that the stochastic contribution is the highest for angular orientations close to $\pm 45°$, because the pinning/depinning field values change significantly on small angle variations and the error bars are getting larger.

For comparison, the results from micromagnetic modelling are also shown in Figure 32(b). A very good correlation of experimental and modelling results is demonstrated for the considered range of angle variation, see also Ref. [31]. The simulations also prove that the second switching event, either DW pinning or depinning depending on the initial magnetic state of the device, is always strongly influenced by the angular orientation with higher pinning/depinning fields when $\theta \sim 0°$ (field oriented along one of the arms). This is a consequence of the increased difference between the field component along the arm in which the second switching takes place and its coercive field.

5.2.2. Width dependence

The same procedure was repeated for nanostructures with different widths in the range from 50 to 400 nm. Figure 34(a) shows the results obtained from MR measurements for a few selected widths, i.e. $w = 75, 200$ and 400 nm. The behaviour of these nanostructures is similar to that shown in Figure 32(b).

Figure 33(a) demonstrates that essentially the same symmetry with respect to $0°$ is observed for all widths, i.e. similar to the 200-nm wide nanostructure shown in Figure 32(b). Close to $0°$ the pinning and depinning fields have two significantly different values, while $B_{pin} = B_{depin}$ at $\theta = \pm 45°$. For the devices with $w = 400$ nm at $\theta = \pm 45°$, the pinning/depinning values are identical, i.e. $B_{pin} = B_{depin} = 5.9$ mT. However, for narrower widths ($w = 75$ and 200 nm) pinning and depinning values do not coincided at $\theta = \pm 45°$, for example being 41 and 21 mT for $\theta = +45°$ and $-45°$, respectively for the 75-nm wide device. Such asymmetry between switching field values at $+45°$ and $-45°$, as observed for narrower devices, can be attributed to

---

[6] Standard deviation.

a stronger effect of the disk-arm junction on the magnetization reversal of along the arms (i.e. the chirality of the disks has a stronger effect on the reversal of the arms).
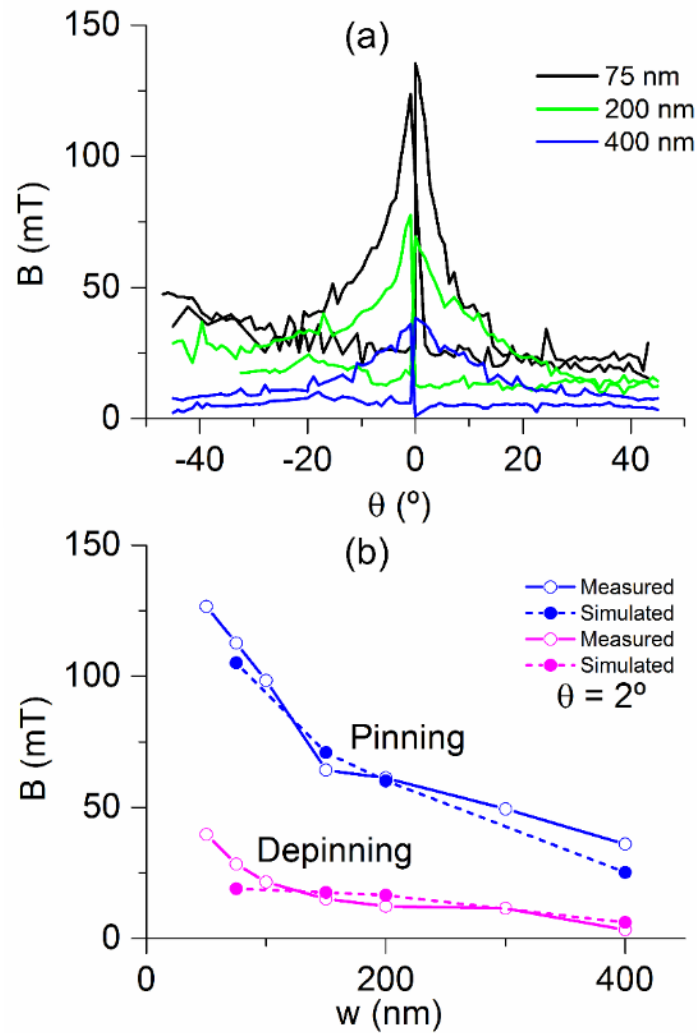
Figure 34. (a) Angular dependence of the DW pinning/depinning fields for L-shaped nanostructures with w = 50-400 nm. (b) Width dependence of pinning/depinning fields at θ = 2°. Adapted from Ref[183]*, with permission from IEEE.*

We further consider stochastic behaviour of DW pinning/depinning events. The largest width ($w = 400$ nm) shows the smoothest behaviour (Figure 34(a)), with all the error bars being below 2 mT. For this width the maximum difference between pinning and depinning fields is relatively small ($\Delta B = 32$ mT at zero angle with 22% relative error for the first switching event and 4% for the second), and pinning/depinning events do not overlap only at small angles, (i.e. $\theta < \pm 20°$). For the narrower width ($w = 75$ nm), the angular dependence is much more pronounced, nevertheless the error bars are always below ~ 1 mT ($\Delta B = 131$ mT at zero angle with 4% relative error for the first switching event and 0.6% for the second). Figure 34(a) demonstrates an inverse dependence between the magnitude of the pinning/depinning fields

and the width of the nanostructure, which is further analysed in Figure 34(b) where the variation of the DW pinning/depinning fields is reported as a function of device width. This behaviour is a consequence of the effect of nanowire width on the arm shape anisotropy, i.e. for narrower arms a strong geometric anisotropy is found leading to a higher coercivity and thus to higher switching fields. Other effects can also be seen in Figure 34(a), for example an asymmetric behaviour for 75-nm wide devices in positive and negative range of angles. This effect is likely to originate in the presence of disk-nanowire junction, i.e. while at +45° both junctions are oriented symmetrically in respect to the field, at -45° it is no longer the case, which is reflected in the corresponding increase of the MR.

The graph in Figure 34(b) compares experimental and simulated values for an angular orientation $\theta = 2°$. As the width decreases, both pinning and depinnig field increases. For this orientation, the DW depinning is the first switching event and B_{depin} value increases between 3.3 to 39.7 mT as the width changes from 400 nm to 50 nm. At the same time, the DW pinning (i.e. second switching event in this orientation) change is much more notably, i.e. from 36.0 to 126.6 mT as the width decreases from 400 to 50 nm. The graph demonstrates a good correlation between experimental and simulation results and is also in agreement with previous results on straight Py nanowires of similar width [185].

These results demonstrate that narrow devices are the best candidates for detection, since the difference between pinning/depinning fields is larger than in wider devices, and the uncertainty in the switching field is smaller. Thus variations on the switching fields are easier to detect in narrow devices than in wider ones.

5.3. Influence of geometry on DW dynamics in Py nanodevices

Here we compare different geometries of the L-shaped nanostructure in order to reduce stochasticity and increase differentiation of DW pinning/depinning. To do so L-shaped nanostructures with widths w ranging from 75 to 400 nm were fabricated as described in chapter 4, from a continuous polycrystalline Py/Pt film (25/2 nm) with Ta/Au (~ 6/84 nm) electric contacts. The basic design (studied in the previous sections) includes two arms of 20-μm in length with disks of 1 μm in diameter at each end (Figure 35(a)). In Figure 35(b) the square corner was substituted by a round one where the outer radius was always fixed to 0.5 μm and the inner radius changes to match the arms width. The square and rounded devices without disks are shown in Figs. 1c and 1d, respectively. Some devices had 8 contacts (Figure 35(b), (c) and (d)) but only the 4 closer to the corner were used.
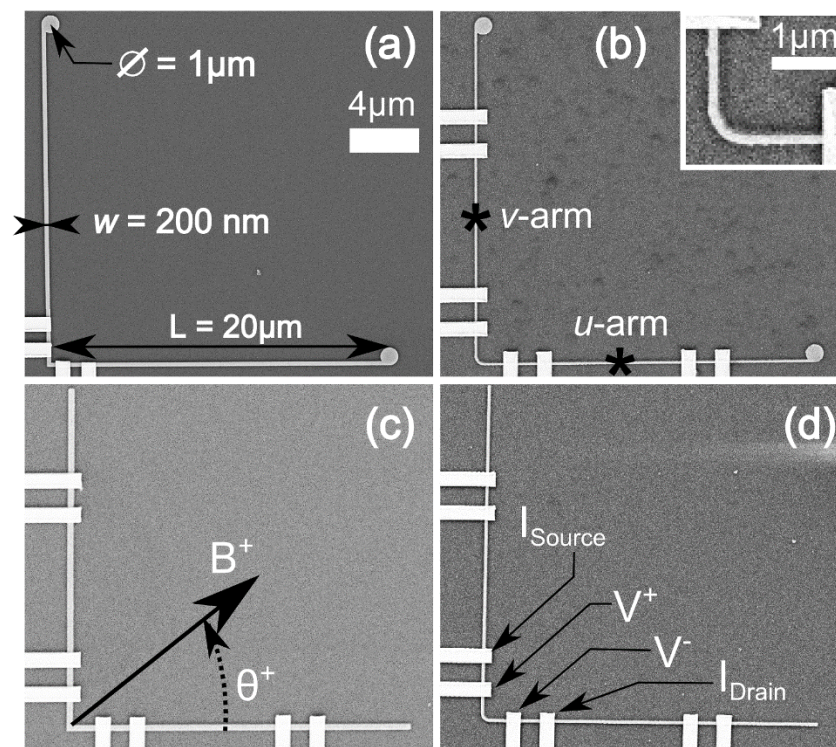
Figure 35. SEM images of the studied L-shaped geometries. (a) Square corner with disks; length and dimensions. (b) Round corner with disks; '' marks the MOKE laser spot. (c) Square corner without disks; angular reference for applied magnetic field. (d) Round corner without disks; electrical contacts. Adapted from Ref[186], with permission from IEEE.*

To characterize the DW behaviour, MR/MOKE measurements were performed at room temperature. An AC current with an amplitude of 10 μA and frequency of 5 kHz was injected through the device as the in-plane external magnetic field was applied. Figure 35(c) shows the angular orientation θ of the applied magnetic field, defined with respect to the u-arm. Figure

35(d) denotes the electrical contacts used to measure the resistance at the corner. MOKE measurements were performed simultaneously with MR at the points indicated with asterisks in Figure 35(b). In this experiment, MOKE measurements complement MR when the pinning/depinning process overlaps and is not possible to clearly distinguish transitions in the MR curves.

5.3.1. DW pinning/depinning mechanism

As it was discussed in section 5.1., four different remanent magnetization states can exist in L-shaped nanostructures depending on field orientation. These states are tail-to-tail DW, head-to-head DW, and states with no DW where the magnetization follows the nanowire curvature along the two possible directions [12], [31], [32], [39], [171]. The initial magnetization state strongly influences the field-induced MR response.
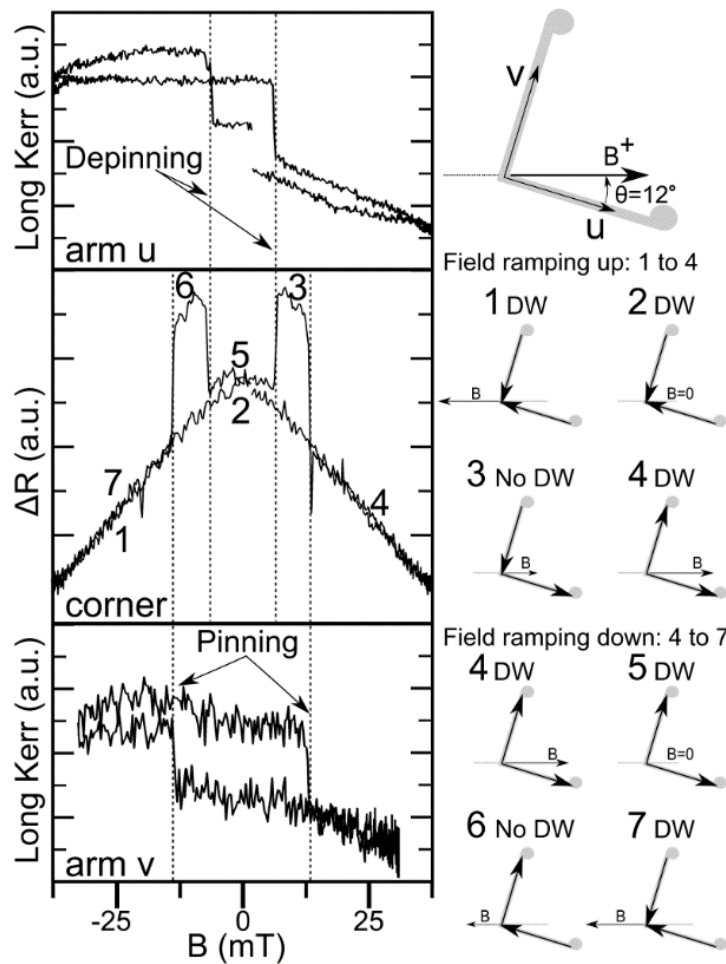
Figure 36. Pinning/depinning effects as measured by MOKE (top and bottom) and MR (middle). Measurements performed for a square device with no disks, w = 400 nm at θ = 12°. Numbers indicate schematic evolution of magnetization along the arms and presence/absence of DW. Adapted from Ref[186], with permission from IEEE.

81

Figure 36 shows the experimental results for a 400-nm wide nanostructure with square corner and without disks, obtained by sweeping the magnetic field between -40 mT and +40 mT, at $\theta = 12°$. Each graph is the result of the average of 20 curves, reducing the random deviation due to stochastic pinning/depinning ($\sim 0.2 - 1.1$ mT for square devices with disks as discussed in section 5.2.). The top/bottom graphs correspond to the MOKE measurements along the u-/v-arm, while the middle graph corresponds to the MR measurements across the corner. For this orientation, the magnetization pattern at negative fields (points 1 and 7 in Figure 36) and remanence (point 2 in same figure) corresponds to a state with a DW. When the external field overcomes the DW depinning value, $B_{depin} \sim 9$ mT for this orientation, the DW is pushed out from the corner and the magnetization in the u-arm switches (Figure 36 point 3, also seen as a jump in the MOKE signal). Due to the AMR effect, the removal of the DW corresponds to an increase in the resistance across the corner [12], [31], [32], [39], [171]. Further increase in the external field leads to a second switching event at $B_{pin} \sim 17$ mT, where a new DW is pinned, corresponding to the switching of the magnetization in the v-arm and the consecutive reduction of the resistance (Figure 36 point 4).
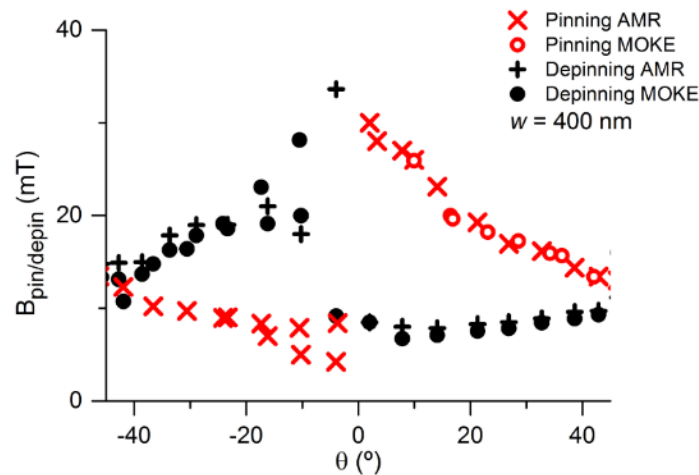
Figure 37. Angular dependence of pinning/depinning fields extracted from MR/MOKE measurements on a square corner nanostructure without disks and w = 400 nm. Adapted from Ref[186], with permission from IEEE.

The pinning/depinning fields for a $w = 400$ nm square nanostructure without disks are shown in Figure 37 for different field orientations. As discussed in previous sections, pinning/depinning fields swap when the angular orientation changes from positive to negative. This is due to the fact that for $-90° < \theta < 0$ the state at high fields has no DW, while for $0 < \theta < 90°$ it is associated with a DW trapped at the corner. The good agreement between MR and

MOKE measurements shown in Figure 37 demonstrates that the pinning/depinning of the DW from the corner corresponds to the magnetization reversal along the two arms.

5.3.2. Effect of geometry

The same experimental procedure, combining MR and MOKE, was repeated for the other geometries and widths (Figure 38). For square nanostructures with disks (Figure 38(a)), the results confirm the behaviour previously observed in section 5.2. For shorter nanostructures [32], [183], the results demonstrate an inverse dependence between the width and the fields required for DW pinning/depinning. When $w = 400$ nm (75 nm), the minimum switching field is ~ 5 mT (~ 17 mT) and the maximum one is ~ 38 mT (~ 136 mT). Moreover, the width reduction has proved to increase the difference between pinning/depinning events, due to the higher contribution of shape anisotropy effects, and thus this geometry has the most well-defined shape for all the device widths.
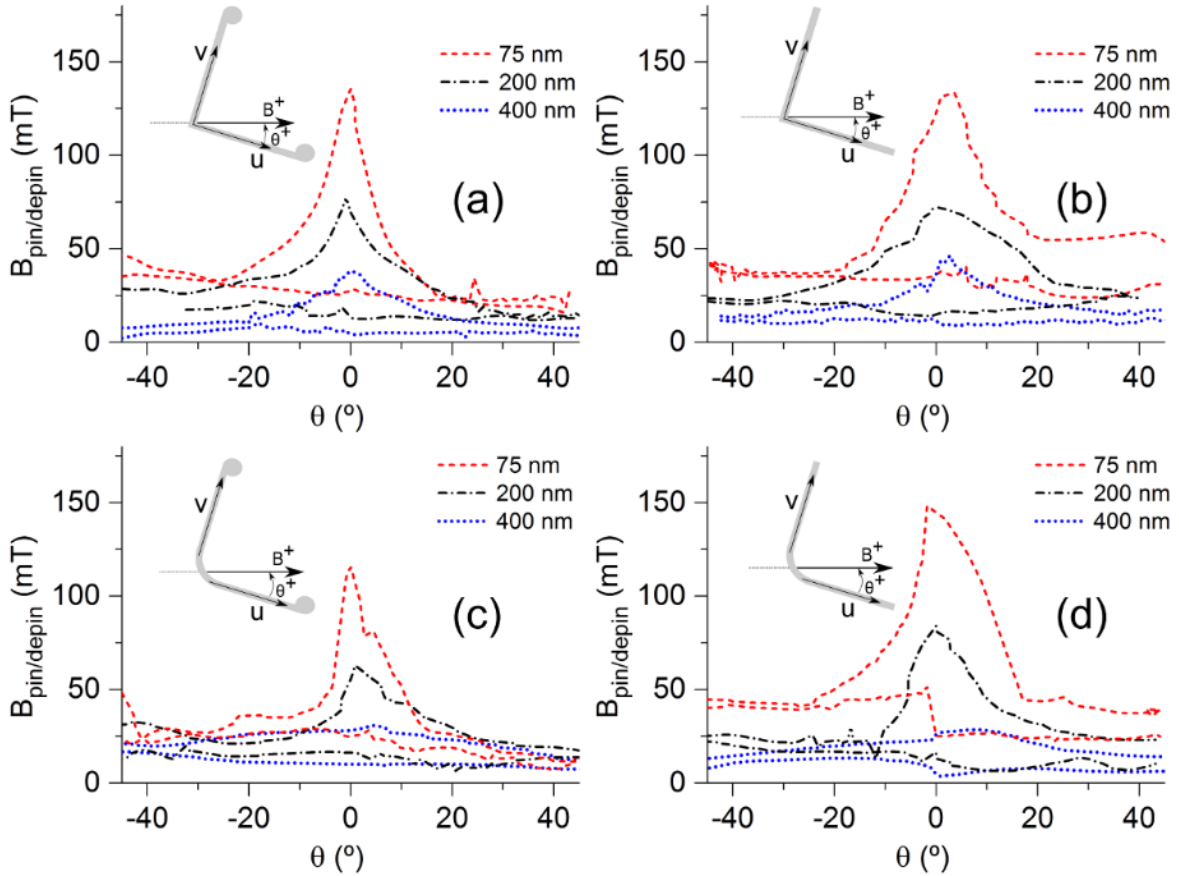
Figure 38. Angular and width dependencies of the switching fields for different L-shaped geometries: (a) square with disks; (b) square without disks; (c) round with disks; (d) round without disks. Adapted from Ref[186], with permission from IEEE.

Similar tendencies but with higher values of pinning/depinning fields are observed for

square nanostructures without disks (Figure 38(b)). However the peak indicating $\theta = 0°$ is not well defined and, thus, it is harder to align these nanostructures with the measurement setup. On the contrary, round nanostructures (Figure 38(c) and (d)) do not exhibit a well-pronounced curve shape as it has been seen for square geometries, which becomes particularly random for the round nanostructures without disks (Figure 38(d)). In addition, the width dependence is also significantly less prominent than in their square counterparts

Finally, it is also noticeable from the comparison of all the graphs in Figure 38 that the round corner introduces an asymmetry between negative and positive field angular orientations, which is associated with different energy landscapes and equilibrium states at remanence. This has been demonstrated by micromagnetic modelling for $w = 200$ nm, calculating the sum of magnetostatic and exchange energy densities versus applied field (ramped from negative to positive values) at $\theta = \pm 5°$. The small value of the angular orientations was chosen in order to have pinning/depinning fields separated in order to distinguish differences in behaviour. While the simulations have been performed on the entire nanostructures, the energy terms have been extracted from the corner region only, to eliminate shape energy contributions due to the arm ends.

Figure 39(a) compares the energy patterns obtained for a round-corner nanostructure without disks at $\theta = \pm 5°$, and shows magnetization spatial distributions in the equilibrium points at remanence and after irreversible jumps. For the negative field angular orientation, the remanent state (absence of a DW, state I in Figure 39(a)) is characterized by the lowest energy content, while the following state (with a DW near the corner, state II in Figure 39(a)) requires to overcome an energy barrier. An energy decrease occurs in correspondence of the second jump, leading to a lower energy state (no DW, state III in Figure 39(a)). For the positive field angular orientation, the remanent state is associated with a vortex close to the corner (state 1 in Figure 39(a)). This configuration is followed first by a lower energy state (no DW, state 2 in Figure 39(a)) and then by an energy increase (DW pinning, state 3 in Figure 39(a)). The first switching event is anticipated at $\theta = 5°$, being energetically favoured, while at $\theta = -5°$ it is the second one which is strongly anticipated, leading to the observed angular asymmetry effect. This effect is reduced when including circular pads. Because, with disks, the arm switching events are driven by the synchronous magnetization reversal in the two disks and DW pinning at the nanowire-disk junctions. Which is less affected by changing the angular orientation of the applied magnetic field [21].
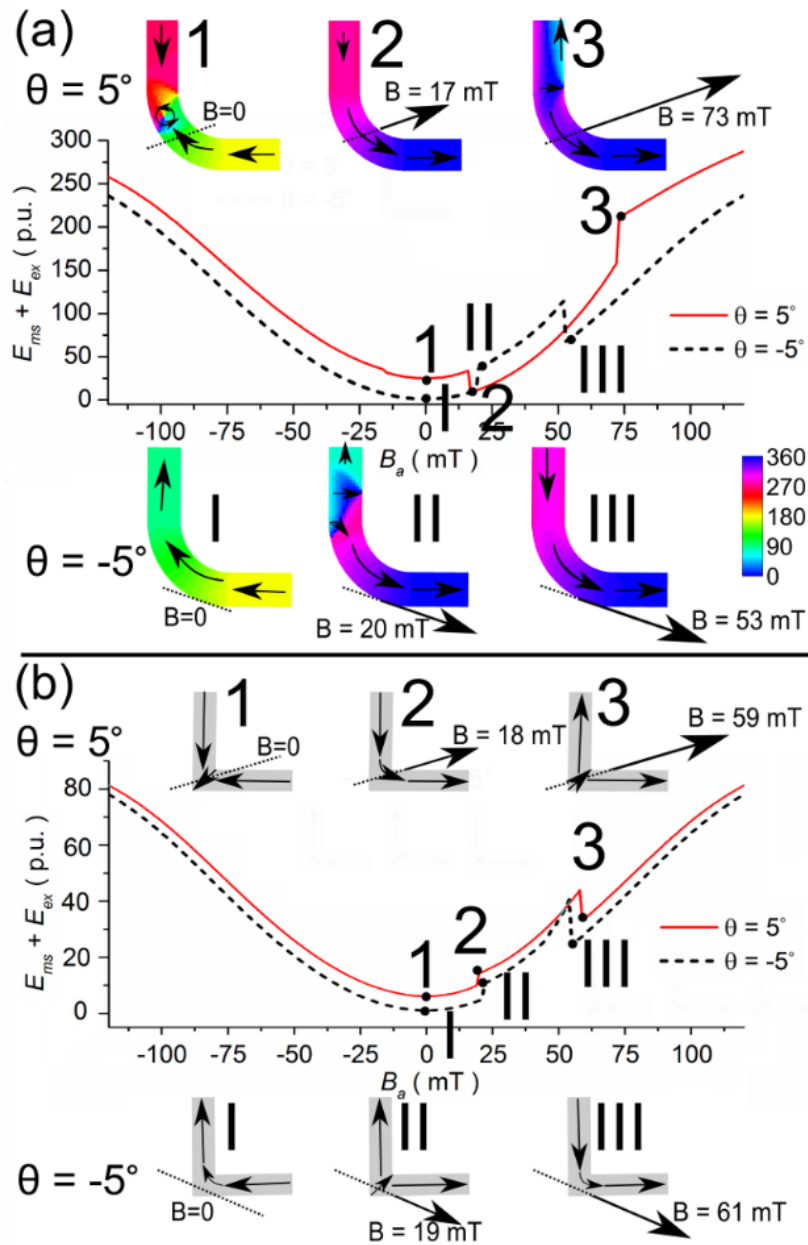
Figure 39. Sum of magnetostatic and exchange energy densities versus applied field for (a) round and (b) square 200 nm width devices without disks, normalized to remanence value for a negative angle. Top panel in (a): equilibrium magnetization spatial distributions at remanence and after irreversible jumps for θ = 5° (top) and θ = -5° (bottom). The colour scale refers to the magnetization angle (in degrees) with respect to u-axis. In (b): schematic equilibrium magnetic configurations. Adapted from Ref[186], with permission from IEEE.

A different behaviour is found for square-corner nanostructures, Figure 39(b), for which the DW pinning/depinning events occur at about the same applied fields for both positive and negative field angular orientations. Even if the remanent states are different (DW for $0 < \theta < 90°$, state 1 in Figure 39(b), and no DW for $-90° < \theta < 0$, state I in Figure 39(b)), they are always

followed by a first less favourable energy state (energy increase, states 2 and II in Figure 39(b)) and by a second more favourable one (energy decrease, state 3 and III in Figure 39(b)), as shown in Figure 39(b) for a 200-nm width nanostructure without disks at $\theta = \pm 5°$. The energy increment between the two switching events is mainly due to an exchange (magnetostatic) energy increase when $\theta = 5°$ ($\theta = -5°$), while for round-corner nanostructures the dominant contributions come from magnetostatic field.

From these results we conclude that square devices with disks are the best candidates for MB detection experiments:

1. The presence of disks generates a sharp peak on the angular dependence of the $B_{pin/depin}$ fields at $\theta = 0°$, thus enabling alignment of the device with the external magnetic field using MR measurements.

2. Disks also contribute to larger differences between B_{pin} and B_{depin} fields for all angular orientations, and thus $B_{pin/depin}$ fields are less likely to overlap in the case of shifts due to MBs.

3. Square corners also increase differences between B_{pin} and B_{depin} fields, in particular at negative angles.

5.4. MB detection using DW-based nanosensor

In the previous two sections it was shown that the most suitable geometry for MB detection is the square L-shaped nanostructure with disks at the end of the arms. The main reason is that this geometry presents the biggest difference between pinning/depinning fields, and thus it is easier to detect a shift in any of those fields. Moreover it has a clear maximum of the pinning/depinning fields at $\theta = 0°$ simplifying the alignment with an external magnetic field. For these reasons, in this section, square L-shaped nanostructures are chosen to perform MB detection experiments.

The aim of this section is to study the effect of a single superparamagnetic MB on the DW pinning/depinning fields. Py nanostructures of width $w = 50 - 400$ nm were fabricated as in previous sections (Figure 40(a)), with stack composition of Py/Pt (25/2 nm) for the magnetic nanostructures, and Ta/Au (6/84 nm) for the electrical contacts.
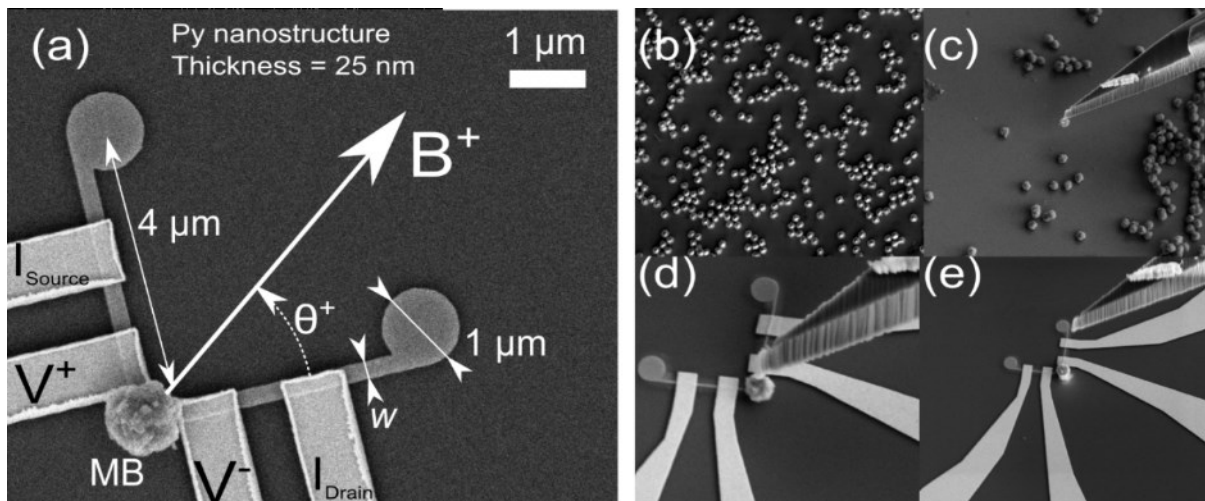
Figure 40. (a) SEM image of an L-shaped nanostructure with a MB attached at the corner. Labels show orientation of the magnetic field and position of voltage and current leads. (b)-(d) Individual steps of FIB-based nanomanipulation. (b) 1-µm MBs drop casted on top of a Si/SiO2 substrate. (c) Carbon fibre tip with an attached MB. (d) MB placed on top of the L-shaped nanostructure and glued with organic Pt-based compound. (e) Final position of the MB over the corner, when the tip is withdrawn. Adapted from Ref[156], with permission from AIP Publishing LLC.

The MBs used are Dynabeads® MyOne™ streptavidin T1, which have an average diameter of 1.05 µm with a size distribution coefficient of variation < 3%. Each bead contains nanometre sized ferrite particles embedded in a polymer matrix[124], [187]. The whole MB is covered by a monolayer streptavidin T1, which provides a strong attachment to biotin labelled biomolecules. Before manipulation, the storage buffer is cleaned from the MBs using deionized

water. After that, a droplet with MBs is placed on top of a Si substrate. Once the water evaporates, the MBs tend to be randomly distributed over the substrate. Less dense areas, containing single MBs, are used for MB manipulation (Figure 40(b)).

MB manipulation was done using a commercial FIB with a carbon fibre tip attached to micromanipulators. The tip is used to pick a MB by touching it and 'gluing' the MB with a deposition of organometallic Pt-based compound (Figure 40(c)). The tip is then moved to the chip with the L-shaped nanostructure and the MB is carefully placed on top of the corner (Figure 40(d) and (e)). A second Pt-based deposition between the MB and the substrate is used to fix the MB to its position at the corner. The used Pt-based compound and the MB manipulation does not deteriorate the nanostructure, since the MR curves are very sensitive to DW pinning sites and no new pinning sites are found after placing the MB.

To characterize the DW dynamics, MR measurements were performed applying an in-plane external magnetic field and using an AC current with an amplitude of 10 μA and frequency of 1.75 kHz (as discussed in chapter 4 and in the Refs:[31], [32], [171], [183], [186]). Figure 40(a) shows the angular orientation θ of the applied magnetic field with respect to the device and the electrical contacts used to measure the resistance at the corner.

5.4.1. Effect of MB on DW dynamics

A set of devices with widths w = 50-400 nm were characterized before MB placement. The angular switching dependence was measured in the same manner as shown in previous sections by extracting the pinning/depinning fields from MR measurements at different angles. The same measurements were repeated after the MB placement. Results for different device widths are shown in Figure 41. The blue lines are the switching fields for the as-prepared devices (no MB), and the red lines are the switching fields for devices decorated with a MB. To ensure that the difference between measurements is indeed due to the MB's stray field, rather than environmental and ageing changes or FIB-induced effects, control nanostructures were fabricated in each chip to be maintained without MB for comparative measurements. Figure 41(a) shows the pinning/depinning fields for one of the control devices before and after placement of MB on the other devices. In the case of the control device, no change of the switching field was detected.

Results in Figure 41(b) show the effect of the MB on the pinning/depinning field of a 50-nm wide device. The presence of the MB affects the depinning field for negative angles in the range -45º < θ < 0 with no effect on the other switching fields. The same effect is shown for 75-nm and 100-nm wide devices in Figure 41(c) and d, respectively. No notable effect of the

MB presence was detected in the 200, 300 or 400 nm devices (Figure 41(e), (f) and (g)). It can be explained by a more complex DW structure in wider devices accompanied by a decrease of the DW stray field and thus a decrease in the interaction between the MB and the DW.
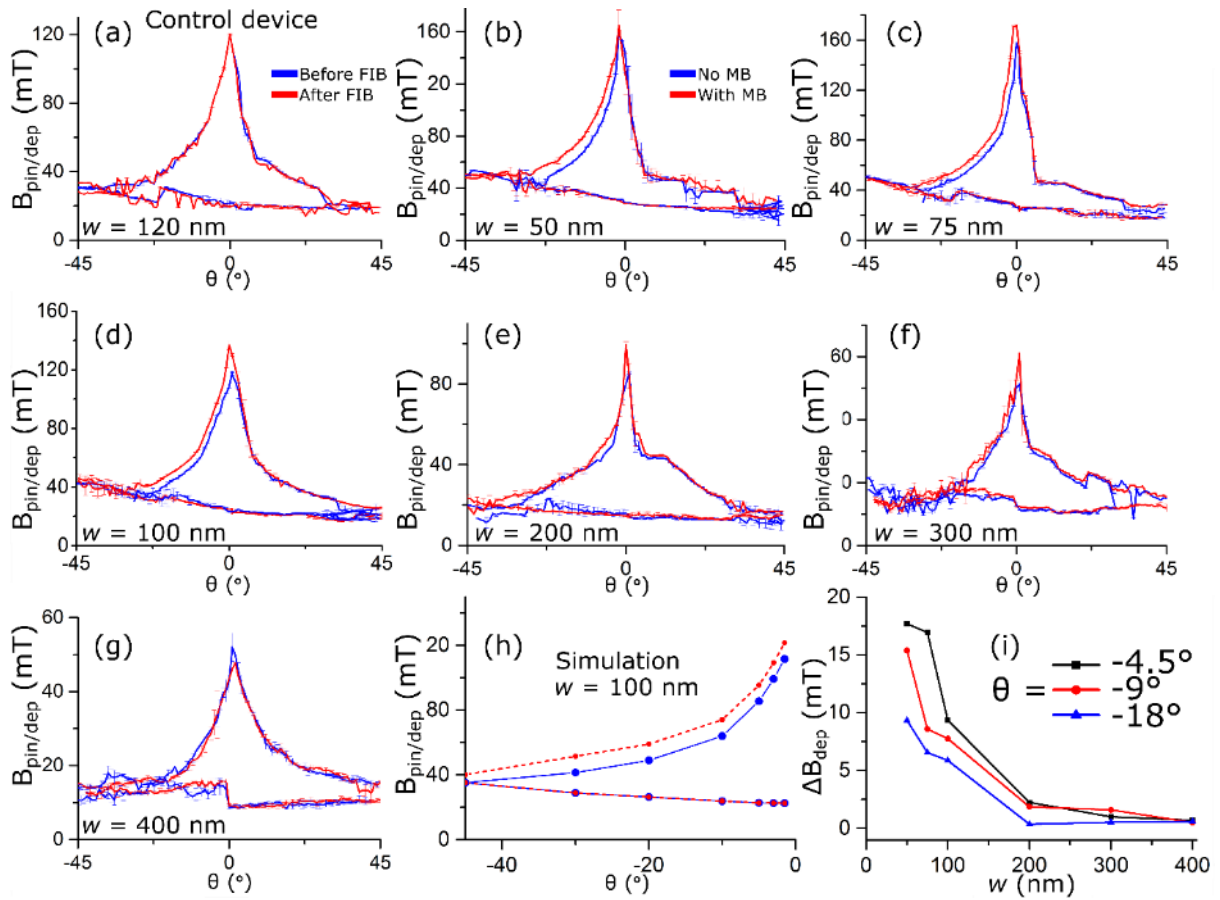
Figure 41. Angular dependence of the switching field for as-prepared and MB-decorated devices of different widths. (a) Control device with no MB; (b-g) devices of different widths (w=50-400 nm) decorated by MBs. The width is shown in each figure panel. In blue: pinning/depinning fields for the as-prepared devices (no MB). In red: pinning/depinning fields for the same device with before the MB placement. (h) DW pinning/depinning fields simulated for a 100-nm wide device with/without MB at the corner, -45° ≤ θ ≤ 1.5°. (i) Shift in the depinning field as a function of the device's width for three different orientations. Adapted from Ref[156], with permission from AIP Publishing LLC.

The measured shift of the depinning field due to the presence of a MB in the narrow devices is in the range of 9.5 - 18.0 mT, 4.5 - 27 mT and 5.5 - 17 mT for the 50, 75 and 100-nm wide devices, respectively, see Figure 41(b)-(d). Figure 41(i) shows the shift in the depinning field as a function of the device's width for three different angles. It demonstrates an inverse relation between the shift and the width of the device. The graph also demonstrates that the strongest effect is observed for small angles of the external field.

5.4.2. Micromagnetic simulations

The asymmetric behaviour in the dependence of DW pinning/depinning fields, found after MB placement, has been explained by micromagnetic modelling, focusing on the 100-nm wide nanostructure. In the simulations, the MB is represented as a magnetic dipole, the localized stray field of which is added to the device's effective field during the integration of the Landau-Lifshitz-Gilbert equation. The MB is assumed to be in the superparamagnetic state and its magnetic moment **m** is approximated by means of the Langevin function, where the magnetic field includes the contribution from both the applied external field $\boldsymbol{H_a}$ and the stray field produced by the nanostructure $\boldsymbol{H_{device}}$.

$$\boldsymbol{m} = N\mu_{particle}L\left[\frac{\mu_{particle}\mu_0(\boldsymbol{H_a} + \boldsymbol{H_{device}})}{k_B T}\right] \tag{27}$$

In Eq. (27), the MB is described as an aggregate of N nanoparticles, each with magnetic moment $\mu_{particle}$; k_B is the Boltzmann constant and T is the absolute temperature. Here, the MB parameters are derived by roughly fitting the magnetization curve reported in [187], [188]. Figure 41(h) shows the calculated values of the DW pinning/depinning fields for negative angles of the applied field orientation, comparing the cases with and without MB for $w = 100$ nm. The MB barycentre is located at a vertical distance of 505 nm from the device surface and its projection coincides with the centre of the device corner. The simulation results confirm the experimental behaviour, showing a zero variation of the pinning field and an increase in the depinning field when the MB contribution is included, with a maximum change of ~ 10 mT (17 mT experimentally). The negligible effect of the MB on the pinning field can be explained by analysing the magnetization reversal mechanism (see Figure 42(a) for $\theta = -10°$). For **negative** angles in the range $-90° < \theta < 0$, when varying the applied field from negative to positive values, the process starts with no DW at the corner. At remanence (Figure 42(a) I), the magnetization state is characterized by a vortex configuration in both disks and by the nucleation of a DW at the junction between the arm more closely aligned with the field and its attached disk. By increasing the field, the DW depins from the junction and moves towards the corner, where it remains anchored until the depinning field is reached (Figure 42(a) II-IV). The second switching event is strongly influenced by the MB presence, because it does not originate at the arm-disk junction, far from the MB position, but starts at the corner. It consists in a progressive deformation of the DW, which proceeds along the arm less aligned with the field, towards the attached disk (Figure 42(a) V-VII).
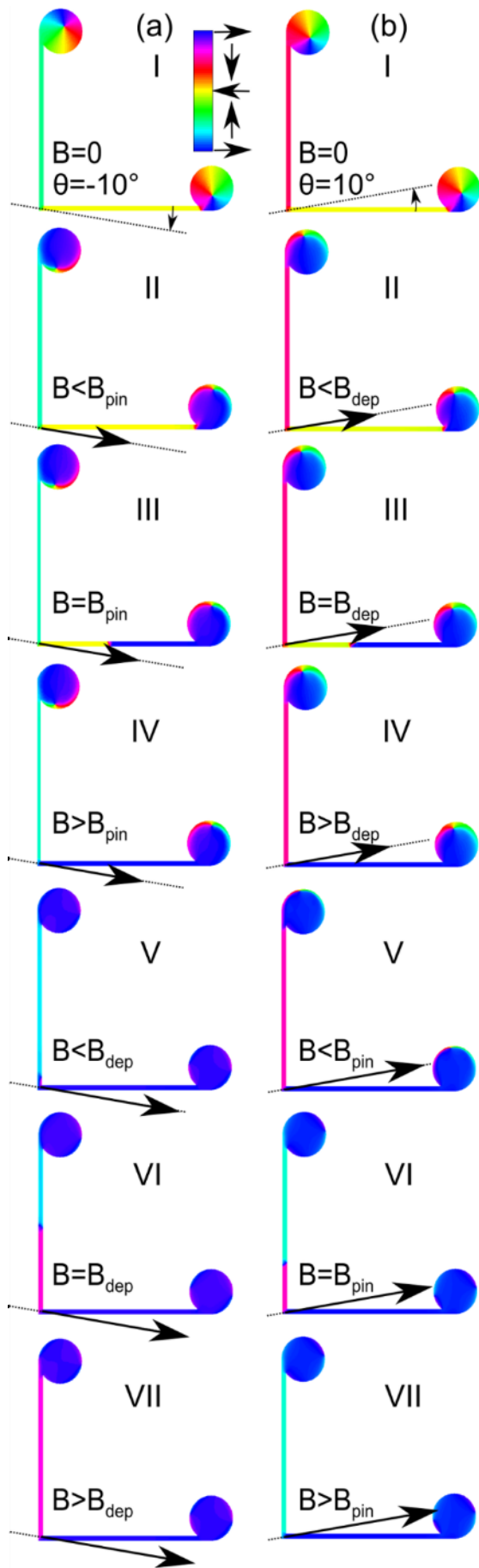
Figure 42. Simulated magnetization configurations through a DW pinning/depinning process for a 100-nm wide device with a MB at the corner, considering (a) θ = -10° and (b) θ = 10°. State I: remanence; II-IV first switching event, V-VII: second switching event (III and VI correspond to instantaneous configurations during irreversible switching processes). The colour scale identifies the magnetization vector angle with respect to the x-axis. Adapted from Ref[156], with permission from AIP Publishing LLC.

91

The micromagnetic simulations also confirm that the MB has a negligible influence on both the switching events for **positive** angles of the applied field orientation, as can be explained by the frames of magnetization spatial distribution during reversal (see Figure 42(b) for $\theta = 10°$). When varying the applied field from negative to positive values, the process starts with a DW at the corner. At remanence (Figure 42(b) I), there is again a vortex configuration in the two disks, with the formation of a well-defined DW at the junction between the arm better aligned with the field and the corresponding disk. This time the chirality of both disks is the same, and the applied field increase leads to the depinning of the DW at the disk-arm junction (rather than at the corner) and its irreversible motion towards the device corner, ending with the annihilation of the pre-existing DW, the depinning of which is driven by reversal processes starting in the disk and, thus not influenced by the MB presence (Figure 42(b) II-IV). The successive DW pinning at the corner is again a consequence of switching mechanisms originating at the arm ends, i.e. the DW at the junction between the arm less aligned with the field and the attached disk moves towards the corner, where it remains trapped (Figure 42(b) V-VII).

5.5. mSGM of DW-based nanosensor using modified probe

In the previous section it was demonstrated that L-shaped nanostructures with widths of w = 50, 75 and 100 nm were able to detect single superparamagnetic beads placed on top of the corner. However, a fixed MB doesn't provide information about the sensing volume (i.e. the volume were the MB can interact with the DW in the L-shaped nanostructures). Thus important information is missing towards the possible application of the L-shaped nanostructures as MB sensors.

Here we use a SPM system, and a probe modified with a MB, to study the sensing volume of the L-shaped nanostructures (Py/Pt (25/2 nm) with electrical contacts made of Ta (~ 6 nm) and Au (~ 150 nm) Figure 43(a)). The SPM system (Aura, NT-MDT with home-built transport measurement stage) allows the application of an in-plane magnetic field during scanning (field along x-axis in the range ±80 mT), as well as electrical connections to the sample using an external lock-in amplifier for resistance measurements with AC bias current. Figure 43 shows the schematics of the electrical circuit used in the experiments. In Figure 43(a), V_{AC} is the applied voltage, turned into current bias mode by the resistor R, which is set to a value much larger than the resistance of the nanostructure (i.e. 36 kΩ at the resistor, compared to typically 100 Ω at the nanostructure with ± 1% of maximum variation between saturation and remanence). The voltage, $V,$ in Figure 43(a) is measured by the lock-in and converted into resistance for the final mSGM image. The frequency of the AC current is 21 kHz and its amplitude 100 μA. The data acquisition time per point was chosen to be 3 times larger than the time constant of the lock-in.

The scanning probes for mSGM (Figure 43(b) and (c)) were custom-made by removing the apex of a commercial silicon AFM tip and placing a MB on the flattened tip using a FIB machine equipped with micromanipulators. The fixing method was similar to the one developed to attach small magnets on MEMS[189]. The tip's spring constant (56.29 N/m) and its resonant frequency (351.5 kHz) were measured using the standard thermal tune calibration technique. The large spring constant is used to reduce the deflection of the tip due to the extra mass and magnetic moment added. The MBs used in this work are commercial hard magnetic NdFeB microspheres with diameter of ~ 1.6 μm and moment, m ~ 2 – 10 x10^{-10} emu[190]. Prior to the experiment, the microspheres were magnetized by applying a magnetic field of ~ 2 T perpendicular to the cantilever. The coercivity of the NdFeB microspheres[190] is about 500 mT, which is more than ten times the magnetic field value applied during mSGM measurements. A commercial magnetic probe was selected to take the MFM images (MESP

by Bruker, with resonant frequency of about 75 kHz, spring constant of ~ 2 - 5 N/m, coated with CoCr magnetized along the vertical direction).

Both MFM and mSGM experiments were done first by imaging the complete topography of the sample in tapping mode, and then performing a sequence of MFM and mSGM scans at specified tip-sample distances, using the recorded topography as a reference. This scanning mode was used in order to reduce the tip-sample interaction during the topography scan. To study the different types of MB-DW interactions (i.e. tail-to-tail, head-to-head DW, or no DW), the magnetization state of the device was changed in between MFM or mSGM scans by ramping the magnetic field along the x-axis.
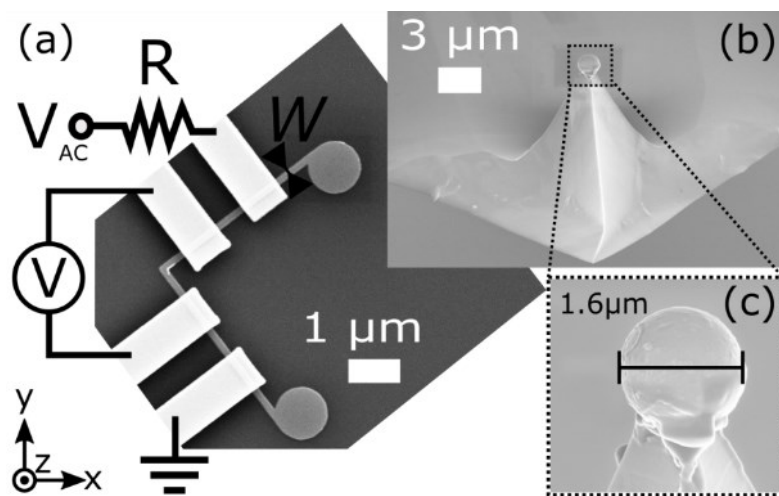
Figure 43. (a) SEM image of an L-shaped nanostructure with Au contacts and schematics of the electrical circuit. (b) and (c) SEM images of a modified tip with an NdFeB microsphere attached. Adapted from Ref[155], with permission from Elsevier.

5.5.1. Comparison between different magnetization states

Figure 44 shows MFM (left column, obtained with a commercial magnetic probe) and corresponding mSGM images (right column) of the corner of a nanostructure with $w = 75$ nm. mSGM images have been obtained using the customized tips with the attached MB. Both sets of images were taken as described above, by first imaging the topography of the whole area and saving it as a reference. The red lines indicate the edges of the Py nanostructure as obtained in the topography, prior to each MFM or mSGM measurement. In the case of the modified tip, convolution of the MB and the sample leads to an apparent broadening of the topography. The scanning height during MFM and mSGM is $h = 100$ nm. An in-plane magnetic field was applied along the x-axis, at 45° with respect to each arm, to place the device in the corresponding magnetic state. For the mSGM measurements, R_0 is the MR measured in

external field but when the MB is far away from the corner.

Figure 44(a) and (b) were taken with a head-to-head DW placed at the corner. A magnetic field of $B = -40$ mT was applied along the x-axis during the scan to prevent depinning the DW with the tip. The DW appears as a bright spot in the MFM image (Figure 44(a)) and as a bright/dark (i.e. increment/reduction of resistance) spot in the mSGM image (Figure 44(b)). Since the resistance across the corner is governed by the AMR effect (as shown in previous sections), the local modification of the resistance shown in Figure 44(b) can be attributed to changes of the spin distribution in the affected area due to the MB-DW interaction.
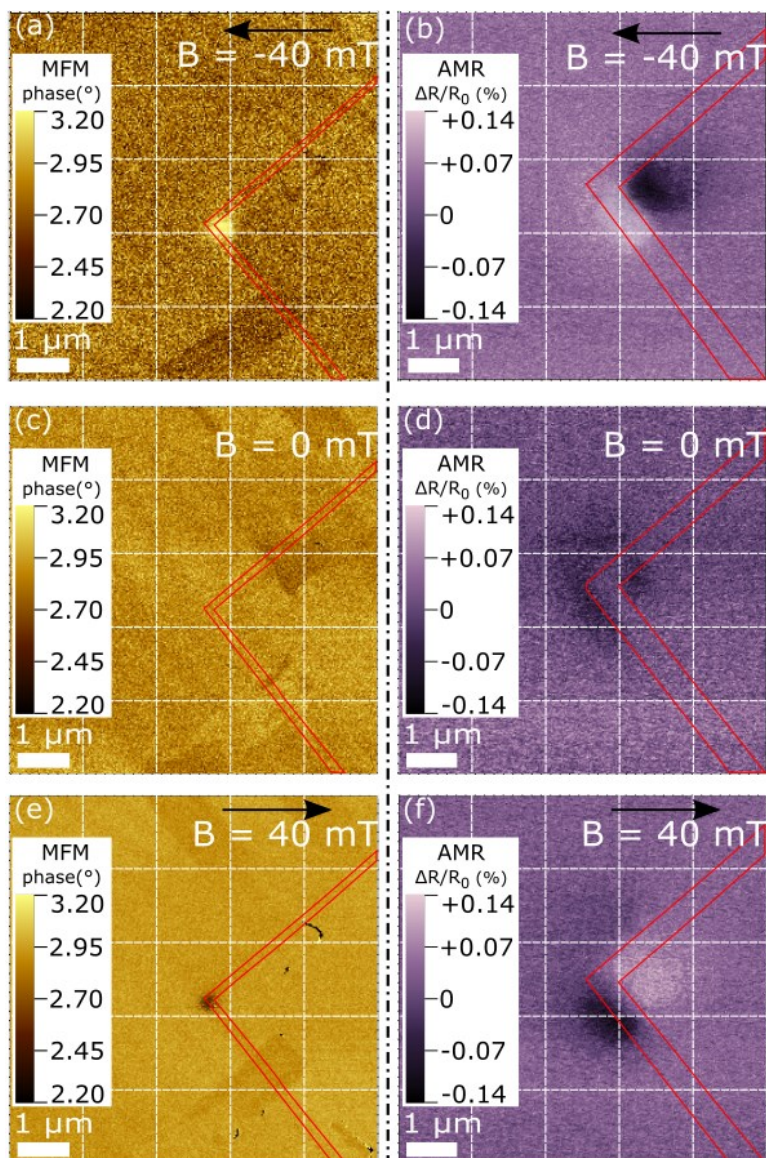
Figure 44. Corner of L-shaped nanostructure with w = 75 nm. Left: MFM images with a commercial MFM tip. Right: mSGM images with the modified MB tip. (a) in situ MFM and (b) mSGM images (i.e. mapping of the AMR signal) in the external field B=-40 mT. (c) MFM image (B=0) showing no DW trapped at the corner after ramping field; (d) mSGM measurement performed with no DW trapped at the corner; (e) in situ MFM and (f) mSGM images with a DW trapped at the corner obtained at B=+40 mT. All MFM and mSGM measurements were performed at h=100 nm. Red lines outline the geometrical contour of the nanostructure from the topography imaging. Adapted from Ref[155], with permission from Elsevier.

Figure 44(c) for MFM, and (d) for mSGM, depict measurements at $B = 0$, when the DW was removed from the corner by ramping the magnetic field. In this configuration, MFM confirms that there is no DW at the corner, however, mSGM shows some interaction around

the corner of the nanostructure (Figure 44(d)). This effect can be attributed to the interaction between the MB and local deviations of the magnetization from uniformity caused by the corner. In the latter case, the interaction is very weak in comparison with the MB-DW interaction (Figure 44(b)), as in absence of the DW, the stray field is significantly reduced.

Finally, Figure 44(e) for MFM, and (f) for mSGM, show results with a positive applied magnetic field ($B = 40$ mT) and a DW trapped at the corner. In this case, the DW is in a tail-to-tail configuration and appears as a dark spot in the MFM image as it has opposite polarity compared to the case described in Figure 44(a). The mSGM image (Figure 44(f)) also shows a bright/dark contrast as in Figure 44(b), but with different polarity and with an asymmetric orientation with respect to the arms. The asymmetry is much clearer in Figure 44(f) (although it is also present in Figure 44(b)) and could be attributed to the DW not being positioned exactly at the corner when measurements are performed in field. Our previous experimental and modelling results demonstrate that both the shape and the position of the DW depends on the orientation and magnitude of the applied field, hence a small angular misalignment of the MB magnetization direction or the applied field can lead to an asymmetrical distribution of the magnetization (e.g. in Ref[191] it is possible to see the effect of using different MFM probes on the DW shape and position).

5.5.2. 3D mSGM map

Figure 45 demonstrates the results of mSGM performed at different heights, i.e. $h = 50$ - 400 nm, on a nanostructure with $w = 75$ nm. The images in the left are taken for the case with a head-to-head DW, and the ones in the right for the case with a tail-to-tail DW. The mSGM images obtained at lower heights (i.e. $h = 50$ nm in Figure 45(a) and (b)) demonstrate the same type of asymmetry as discussed before (Figure 44(b) and (f)). However, increasing the scanning height to $h = 400$ nm (Figure 45(c) and (d)) leads to the appearance of a more symmetric distribution of the mSGM signal. It can be attributed to the fact that as the MB-DW interaction decreases with increasing separation, reducing both the amount of change in the magnetization distribution and the lateral mSGM resolution.

To compare MB-DW interaction strength, Figure 45(e) shows the peak-to-peak change in the resistance (i.e. difference between maximum and minimum for each image) as a function of the tip – sample distance. Figure 45(e) shows that these values decrease gradually (Figure 45(e)) and at $h = 400$ nm the peak-to-peak values are comparable with the noise in the resistance ($\sim 0.02\%$).
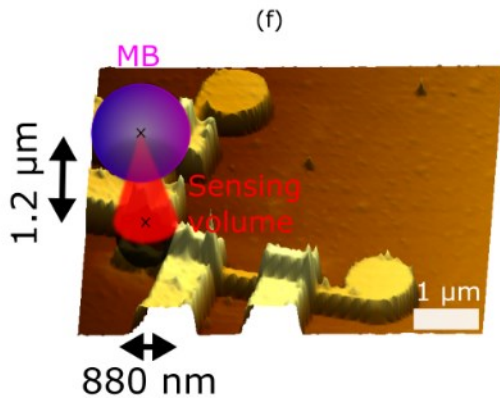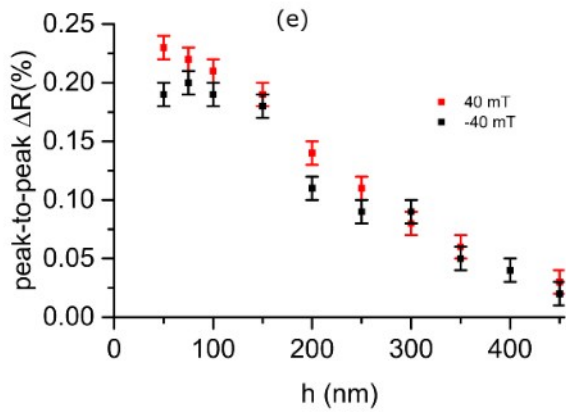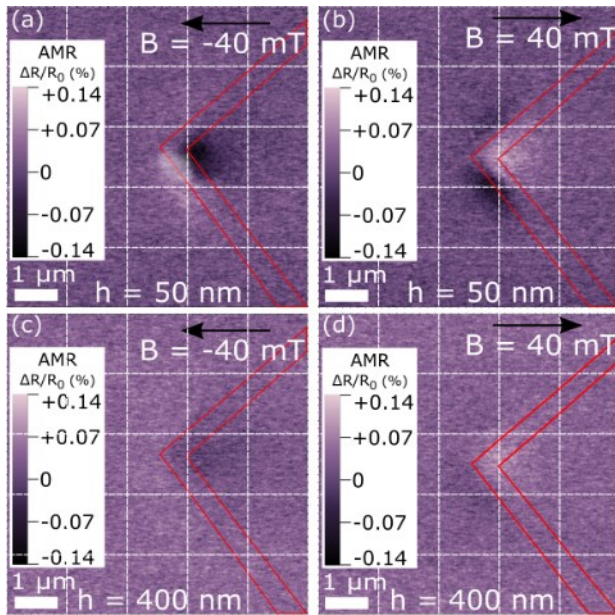
Figure 45. mSGM images of the nanostructure with w=75 nm, obtained at different scanning heights: (a) and (b) h=50 nm; (c) and (d) h=400 nm. (a) and (c) B=- 40 mT with a head-to-head DW. (b) and (d) B= 40 mT with a tail-to-tail DW. (e) Peak-to-peak change in the resistance for negative and positive fields in correspondence of the distance, h, between the tip and the sample. (f) Topography image with scaled representations of the estimated sensing volume (red) and the MB (purple). Adapted from Ref[155], with permission from Elsevier.

By using the values of the resistance change that are larger than ±0.02%, the measurable effect of the MB-DW interaction can be enclosed in a conical volume of about 880 nm in diameter by 1.2 µm in height (i.e. $h = 400$ nm plus the bead radius), where the centre of its base is located at about 400 nm from the inner edge of both arms. The concept of the sensing volume, a schematic of which is shown in Figure 45(f), signifies that if the centre of the MB is somewhere inside of the cone, then it is possible to detect its presence by measuring the resistance of the device. Naturally, MBs with higher/lower magnetic moment will result in

different sensing volumes. Whereas only a rough estimation of the sensing volume is given here, a detailed analyses of the MB-DW interaction, e.g. consideration of the monopole vs dipole magnetic field associated with the modified probe[192], will provide a more accurate value for the sensing volume.

It is important to note that the sensing volume may be larger when the DW depinning field (rather than change of the MR) is measured[12], [156], because the former parameter is more sensitive to variations of the external magnetic field.

5.5.3. Comparison between different widths

Figure 46 demonstrates a comparison between nanostructures with different widths, $w = 50$, 75 and 100 nm obtained at $h = 100$ nm for the positive applied field (negative field produces similar results). Figure 46 shows that narrower devices result in a stronger MB-DW interaction. Table 2 summarizes the values of the peak-to-peak resistance change (difference between maximum and minimum for each image) for each width due to the MB-DW interaction. It is noteworthy that the orientation of the bright-dark spots in Figure 46 becomes more symmetric in respect to the arms as the width decreases. This reduction in the asymmetry is expected, as narrower nanowires produce a deeper potential well and will force the DW to be positioned exactly at the corner, (i.e. in the state with lower energy).
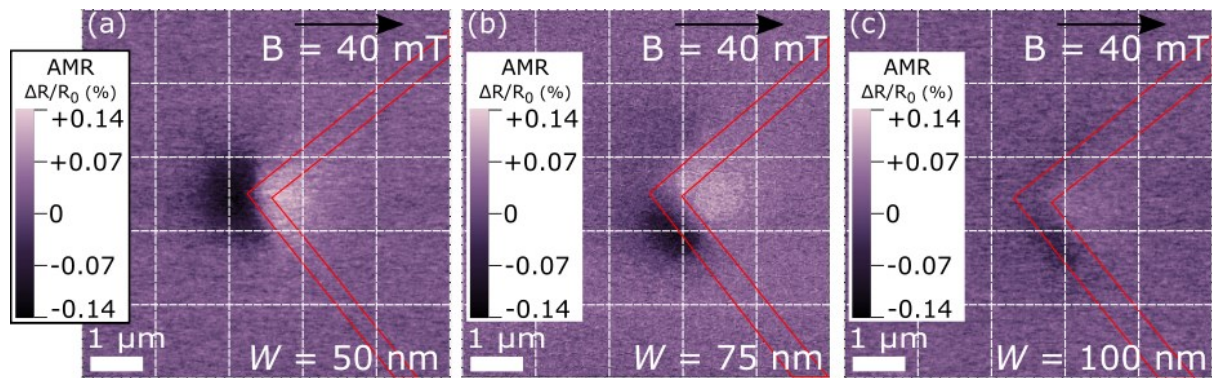
Figure 46. mSGM images of devices with different widths, w, for B =40 mT. (a)-(c) w = 50, 75, and 100 nm, respectively. All the scans were taken at h = 100 nm. Adapted from Ref[155], with permission from Elsevier.

3D mSGM maps reveal that the width does not significantly affect the shape or the diameter of the sensing volume, but modifies the height. For example, the sensing volume cone has a height of about 1.4 μm for $w = 50$ nm and decreases to 800 nm for $w = 100$ nm. These results agree with previous MB detection experiments[156], [186], and results shown in previous sections where the DW depinning field was used as the most sensitive parameter.

Table 2. Peak to peak change of the resistance, ΔR/R0, for different device widths as shown in Figure 46. Adapted from Ref[155], with permission from Elsevier.

W (nm)	50	75	100
ΔR/R0 (%)	0.27	0.21	0.18

5.6. Summary

In this chapter, Py L-shaped nanostructures were studied as potential DW-based sensors for single MB detection. The results shown here demonstrate the possibility of single MB detection and outline the geometrical constrains that enable sensing with a DW in the proposed L-shaped nanostructures.

The main discussed results include the identification of 4 stable magnetic states by means of MFM technique: head-to-head DW at the corner; tail-to-tail DW at the corner; and two states where the magnetization turns around the corner. These states are fully controllable by applying an external magnetic field.

Using MR measurements in combination with micromagnetic and transport modelling, the AMR effect was identified as the main source of resistance change when the magnetization was modified. Moreover, using a state-space map we tracked changes in magnetization by measuring the resistance across the corner of the L-shaped nanostructures.

Combining MR and MOKE measurements, we evaluated variations of the basic device geometry. The results, compared against micromagnetic modelling, demonstrate that L-shaped devices with a square corner and disks at the end of the arms provide the largest difference between DW pinning/depinning fields, and hence they are the best candidate for single MB detection. Moreover, the square geometry has a maximum/minimum of B_{pin}/B_{dep} at zero degrees that allows an easy alignment of the sample in the external field.

Single MB detection experiments were performed by placing a superparamagnetic MB on top of the corner of the L-shaped nanostructures. MB placement was done through micromanipulation inside of a FIB system. Using MR measurements, the DW pinning/depinning fields were measured before and after MB placement. The results demonstrated MB detection (for the type of MB used), but only with nanostructures whose width is below 200 nm, and only when the external magnetic field is ramped at negative angles. These results agree with previously published works, and expand the detection to a new type

of MBs. The angular dependence of the detection was elucidated by means of micromagnetic modelling, which demonstrated that for positive angles the DW does not move from the corner, i.e. it is annihilated by DWs originating from the disks. For this reason, at positive angles the L-shaped devices are not sensitive to the presence of a MB. On the contrary, for negative angles, the DW moves away from the corner when ramping the external magnetic field, thus allowing to detect interactions with nearby magnetic objects.

The last part of the chapter focuses on mSGM with a MB attached to the AFM probe. The mSGM measurements allow lateral and vertical displacement of the MB over the L-shaped nanostructure and measure the consequent effect on the resistance change. Using this method we estimated the sensing volume of the devices to detect MB detection, where larger volumes for narrower devices were verified.

Overall, this chapter demonstrates single MB detection and optimization of a DW-based nanosensor. Moreover, it outlines dynamics of DW propagation, revealing two distinct magnetization reversal mechanisms. The mSGM results presented here are particularly important, as they provide a quick way of characterizing and comparing magnetic nanosensors.

As discussed in chapter 3.4.1 about magnetophoresis, DW-based devices for MB detection and manipulation have the advantage of simple fabrication than other solutions with more sensitivity (e.g. SVs or MTJs). An additional advantage consists in the possibility to integrate several L-shaped devices as part of larger DW-based circuits for MB manipulation (e.g. as in Ref [153]). In particular, L-shaped devices can be used as a MB-trap[193] where the captured MBs are funnel to DW-based circuits to be used as manipulators in single cell tests[8].

6 PHE in Py-based hybrid junctions

In the previous chapter we studied a DW-based single MB detector made of a magnetic L-shaped nanostructure with electrical connections to measure MR. The presence/absence of a DW at the corner of the L-shaped nanostructure modifies the resistance across the corner, thus allowing measuring the DW pinning/depinning fields for different angular orientations of the applied field. The results show that the presence of a single MB over the corner can be detected as a shift in the pinning/depinning fields. Moreover, by using a MB attached to a SPM probe it was shown that the presence of a MB near the corner produces changes in the magnetization that can be detected through MR measurements.

These results contribute towards Lab-On-a-Chip applications using magnetic nanostructures. However, the measurements are based on the AMR effect, which creates two main problems to overcome. The first one is the small magnitude of the change in resistance due to AMR effect, which is typically only ~0.2% in Py nanodevices[12], [32]. The second problem is that due to the small MR, electrical contacts have to be placed close to each other as well as to the DW pinning site. This requirement imposes restrictions on the error of the alignment during the fabrication process.

In this chapter we study *transversal* MR in Py nanostructures as a possible alternative to *longitudinal* MR measurements. In these nanostructures, the longitudinal MR is dominated by the AMR effect (~0.2% change in resistance), while the transversal MR originates from the PHE, which produces a substantially larger change in resistance, *e.g.* the reversal of the magnetization in Py nanowire of similar dimensions produces a change in resistance of ~ 10 mΩ over a theoretical zero transversal resistance background[30].

In the past, ferromagnetic crosses were added to the device geometry in order to measure the PHE. However, this creates undesired pinning sites[194], causing an increase in the switching field of the overall nanostructure, and also making it more difficult to track magnetization. Since DW-based technology requires manipulation of a DW along a nanostructure, reduction of pinning sites is a major requirement. This explains why longitudinal AMR measurements were widely used to study magnetization in nanowires[12], [15], [32], [43], [155], [156], [177], [195]–[197], while there are fewer studies on the transversal PHE at the nanoscale[30], [194], [198]. To overcome the problem of adding extra pinning sites and with the aim of exploiting the large changes in resistance reported for PHE, we present an alternative

approach to PHE measurements, which consists in transversal resistance measurements using a hybrid normal metal (Au)/ferromagnetic (Py) nanojunction.

6.1. Comparison between transversal and longitudinal MR

Hybrid Py/Au L-shaped nanostructures (Figure 47) with a nominal width of a Py wire of 200 nm have been used to study longitudinal and transversal MR. AMR and PHE type of measurements have been performed both across the corner and along one of the straight segments in order to compare longitudinal and transversal MR as well as to investigate the effect of the DW presence.
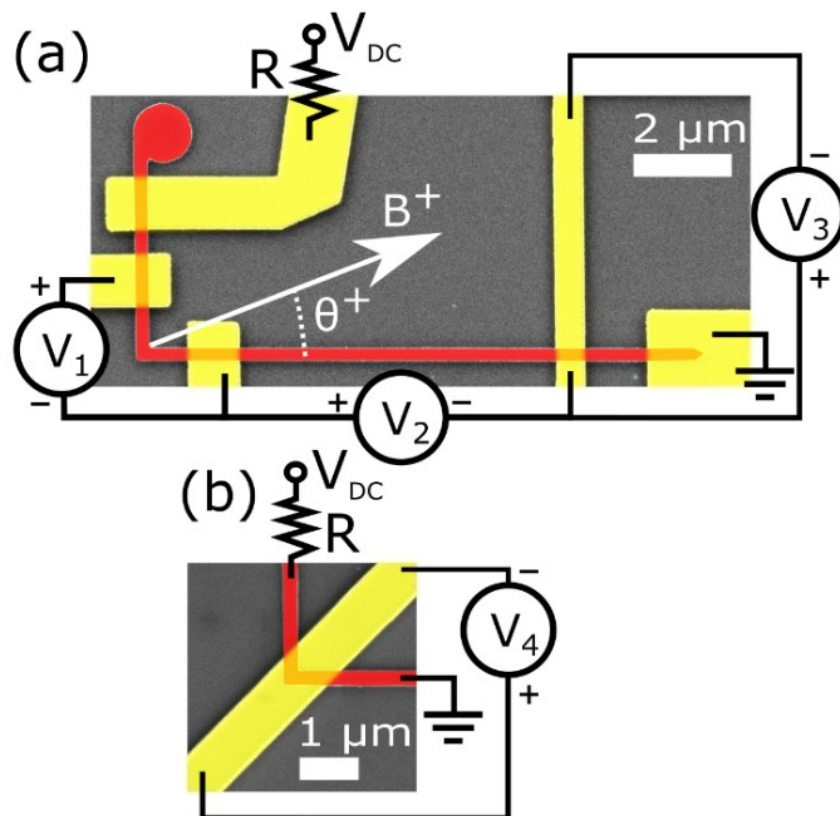
Figure 47. SEM images of Py/Au hybrid nanojunctions (red/yellow, respectively) using combined straight/corner (a) and corner only (b) geometries. Hybrid nanojunctions are formed of an L-shaped Py device and Au electrodes. References to the applied field and electrical circuit are shown.

6.1.1. Individual MR measurements

In order to analyse the different signals produced in transversal and longitudinal resistance measurements, the resistances for different types of configurations (both measured and simulated) are compared when the external magnetic field is ramped up from a negative saturating value at different angular orientations, $-90° < \theta < 90°$. Measurements and simulation

results shown in Figure 48 refer to the case of $\theta = 74°$, which corresponds to the formation of a longitudinal DW along the wire (to be discussed in detail later in the text). The experimental setup scheme of resistance measurements (R_1-R_4) corresponds to the positions of voltmeters (V_1-V_4) in Figure 47. In addition to the measured and simulated resistance curves (Figure 48), calculated magnetization maps and experimental *in situ* MFM images at $\theta = 74°$ are shown in Figure 49 at key values of the magnetic field.

As magnetic field ramps from negative to positive saturation values, four characteristic areas, labelled **1 – 4** (see grey circular markers on the top applied field-axis), can be distinguished in Figure 48.

Area 1 ($B < 11$ mT): first, saturating negative field is applied and then reduced to $B = 0$. The relevant modelled and experimentally measured (i.e. MFM) remanent magnetization states are shown in Figure 49 (state **1** and **I**, respectively). The state contains a DW trapped at the corner, with magnetization uniformly distributed along the arms and vortex configuration at the nucleation disk. At $B = 0$, a zero value for transversal resistances R_3 and R_4 is expected as also confirmed by micromagnetic simulations, which directly model the PHE in the ferromagnetic material. However, both experimentally obtained R_3 and R_4 have a small but finite value, associated with current circulating through the metal electrode. It is noteworthy that the transversal resistance R_3 (i.e. associated with the hybrid junction over the straight part of the nanostructure) has an approximately linear field dependence (~0.1 Ω/T) in the field range -30 mT < B < 30 mT (Figure 48). Although this sensitivity is quite small (a value of 144 Ω/T has been reported for other PHE sensors[152]), this result makes this type of junctions a good candidate for measurements of local magnetic fields, for example as the ones produced by magnetic nanoparticles[30], [143], [152], because of the wide range of operation, and the simple fabrication process (i.e. when compared to the fabrication steps required to produce a MTJ or a GMR based sensor composed of a multilayer stack). As an example, TMR sensors for MB detection has been demonstrated[135] with a sensitivity of 540 kΩ/T or up to 800 kΩ/T in the case of MTJ[199], but both with a linear range of only ~10 mT and in some cases with field bias of up to ~ 5mT.

Area 2 (11 mT < B < 45 mT): when the magnetic field is increased, the DW at the corner is annihilated and the magnetization in the vertical arm is reversed, as a consequence of the irreversible motion towards corner of the DW previously pinned at the disk-vertical arm junction occurring at 11 mT (transition **A** in Figure 48). Successively, magnetization spatial distribution in both arms gradually changes without re-formation of a DW at the corner, as

depicted by states **2** and **II** in Figure 49. At transition **A**, signals R_1 and R_4, which directly probe the corner state, show a step indicating a change in the resistance due to the annihilation of the DW pinned at the corner (Figure 48). On the contrary, as the DW disappears due to the reversal of the magnetization in the vertical arm, signals R_2 and R_3 do not show an abrupt change at **A**.

Area 3 (45 mT < *B* < 64 mT): by further increasing the magnetic field, at 45 mT the magnetization reaches a rather counterintuitive state with a longitudinal DW along the horizontal arm (Figure 49, states **3** and **III**). The associated change in the resistance (transition **B** at *B* = 45 mT) can be detected in all four resistance measurements, as changes in the magnetization distribution involve material beneath all the contacts. Also *in situ* MFM images (Figure 49 state **III**) demonstrate the existence of this state with a longitudinal DW along the horizontal arm[200], which for the L-shaped nanostructure used here is not stable and thus cannot be imaged at remanence. Although this state is metastable, it is highly reproducible and always appears in a well-defined space state, i.e. combination of the field magnitude and orientation (see grey and yellow areas in Figure 51), and can be possibly exploited in spin-wave propagation studies[201].
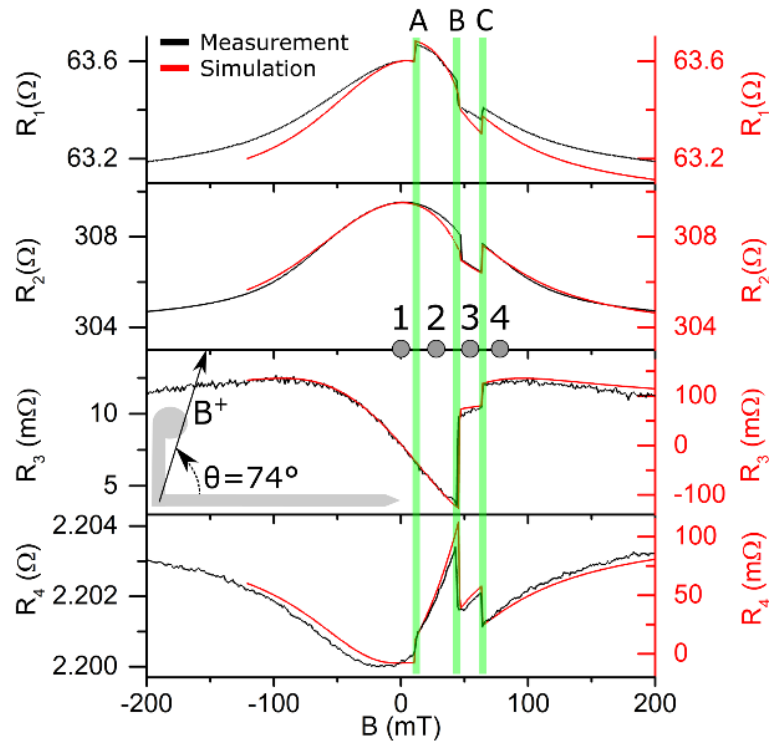
Figure 48. MR versus applied field in different measurement geometries: black - experimental and red – modelling results. Magnetic field is applied at θ = 74°, ramping from negative to positive saturation values. Longitudinal resistance along device corner (R1), straight wire (R2), hybrid junction resistance across a straight wire (R3), and hybrid junction resistance across device corner (R4) (see Figure 47 for electrical set-up).

Area 4 ($B > 64$ mT): when the magnetic field is increased even more, the longitudinal DW annihilates at 64 mT moving orthogonally to the nanowire axis (transition **C** in Figure 48), while a new DW is formed at the corner accompanied by uniform magnetization distribution along both arms (states **4** and **IV** in Figure 49). This transition is reflected by steps in the resistances as measured in all the configurations R_1-R_4.
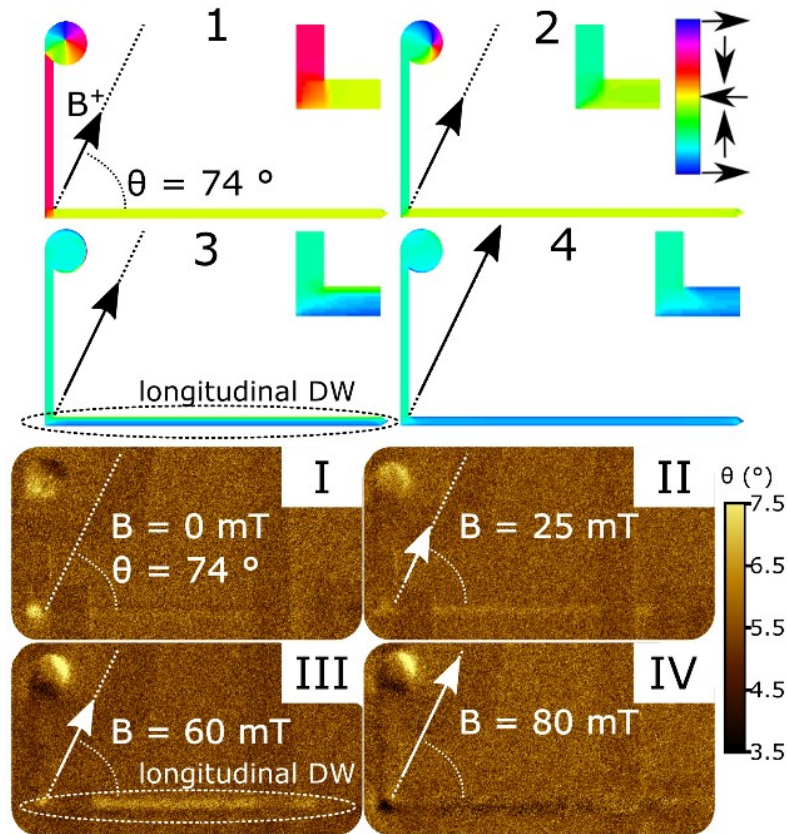
Figure 49. Top: Simulated magnetization spatial distribution in the L-shaped Py nanostructure at equilibrium, the magnetic field is applied at θ = 74°. Colour scale refers to the magnetization direction with respect to the x-axis. Numbers (1-4) correspond to the identically labelled areas in Figure 48. Insets show magnified images of the L-shape corner. Bottom: in situ MFM images (I–IV) obtained in the conditions identical to (1-4) simulations.

As follows from Figure 48, the absolute change in the transversal resistance in R_3 geometry is smaller than the analogous longitudinal measured ones (R_1 and R_2). However, when the change in the resistance is compared with the resistance before the transition[7], the relative change in R_3 is several orders of magnitude bigger than the changes in R_1 and R_2. On the other hand, for the resistance measured at the corner, the transversal component, i.e. R_4, is accompanied by even smaller values than analogous longitudinal resistance (R_1). Thus, while

---

[7] Note that usually it is the value at zero field which is used as a comparison. Here, since the resistance at zero field theoretically should take value zero, it is used the value immediately before the transition.

there is no significant difference in terms of DW tracking as measured at the corner (i.e. R_4 or R_1 for transversal and longitudinal measurements, respectively), there is a massive difference between longitudinal and transversal measurements in the straight configuration. It is noteworthy that, when compared to the simulated values reported in Figure 48, the transversal measurements show a finite background resistance in both R_3 and R_4 geometries, while the simulations predict nearly zero resistance at $B = 0$. The reason for this discrepancy is associated with a significant amount of current passing through the Au contact instead of the Py nanowire at the nanojunction[202]. This is not taken into account in the numerical model, which simulates only the PHE in the Py material. The resulting background resistance reduces the relative change for the experimental transversal measurements, thus it is expected that with a more resistive material, instead of Au, relative resistance changes in R_3, and in particular in R_4, could be significantly larger than the values reported in Figure 48.

6.1.2. Effect of the device widths

To complement the results relative to the junction on the straight Py wire (R_3), nanostructures with different widths of Py and Au were fabricated and tested. Figure 50(a) shows the change in resistance R_3 at transition **B** ($\theta = 74°$). Figure 50(b) shows the same transversal resistance at zero field for the same angle.
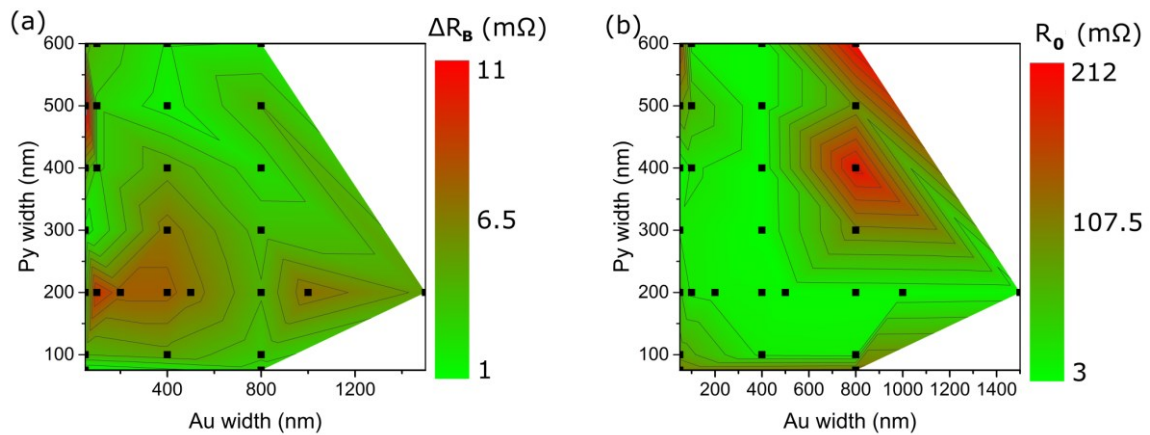
*Figure 50. (a) Colour map showing the average change in the resistance R_3 at transition **B** for $\theta = 74°$ considering different widths of Py and Au layers. (b) Colour map of the average resistance R_3 at $B = 0$ for the same widths as in (a). Dots indicate for which widths experimental values have been measured.*

The black dots in Figure 50 represent the measured values for tested widths (as averaged for 2 to 6 devices), the colour map is an interpolation of the measured values. Thus, the overall change in the resistance associated with transition **B** for all the widths tested is in the range 1-11 mΩ. For the device studied here (i.e. $w = 200/400$ nm for Py/Au respectively) the change in resistance is ~ 6 mΩ. Hence, the reported results shown in the previous section can be

considered as representative for this type of hybrid junctions. In terms of zero field resistance (Figure 50(b)) the device tested in the previous section (i.e. $w = 200/400$ nm for Py/Au respectively) has a resistance R_3 of ~ 5 mΩ. This is a low value when compared with the devices in Figure 50(b), but for devices of similar widths it is close to the average value.

6.1.3. Angular dependence

Coming back to the device under study (i.e. $w = 200/400$ nm for Py/Au respectively) (Figure 47), The combined results presented in Figure 48 and Figure 49 demonstrate that for $\theta = 74°$ all the irreversible transitions observed in the experimental curves in Figure 48 can be fully interpreted by changes in the spatial distribution of magnetization as predicted by the simulations (Figure 49), which signifies absence of any additional pinning sites due to the presence of the hybrid junction. However, in order to fully characterize the hybrid nanojunctions and corroborate the predictions made by micromagnetic simulations, the angular dependence of the DW pinning/depinning fields (i.e. transitions **A**, **B**, and **C** in resistances R_1 $– R_4$) was studied (results can be seen in Figure 51). In this case, the resistances for each angular orientation were measured twice and the average field of the transition is plotted (transitions are considered the same, if their field separation is less than 0.5 mT).

Figure 51 top panel demonstrates that measurements across the corner (R_1 and R_4) show similar angular transitions occurring at the same fields. Correspondently, measurements of the straight nanostructure (R_2 and R_3) also provide the same angular transitions (Figure 51 bottom panel), though different from the set of measurements at the corner. This demonstrates the absence of any additional DW pinning sites induced by the electrical contacts in the whole field angular range (e.g. a DW pinned at the hybrid junction position would appear as an extra transition in R_3 or R_2).

Figure 51 also shows the different magnetization states that appear in the nanostructure when the field is ramped at different angles (states are shown by different colours, i.e. pink, blue, grey and yellow), classified by analysing the sign of the resistance change in measurements R_1-R_4, MFM images at specific angles, and simulation results. Depending on the orientation of the applied field, either two or three transitions can be observed, as for example shown for $\theta = 20°$ and 74°, respectively. In particular, when $\theta = 20°$, the magnetization reversal first occurs in the vertical nanowire and followed by the horizontal one. However, in this case the switching mechanism in the horizontal nanowire is no more characterized by two steps, as when at $\theta = 74°$ occurs the formation of the longitudinal DW.
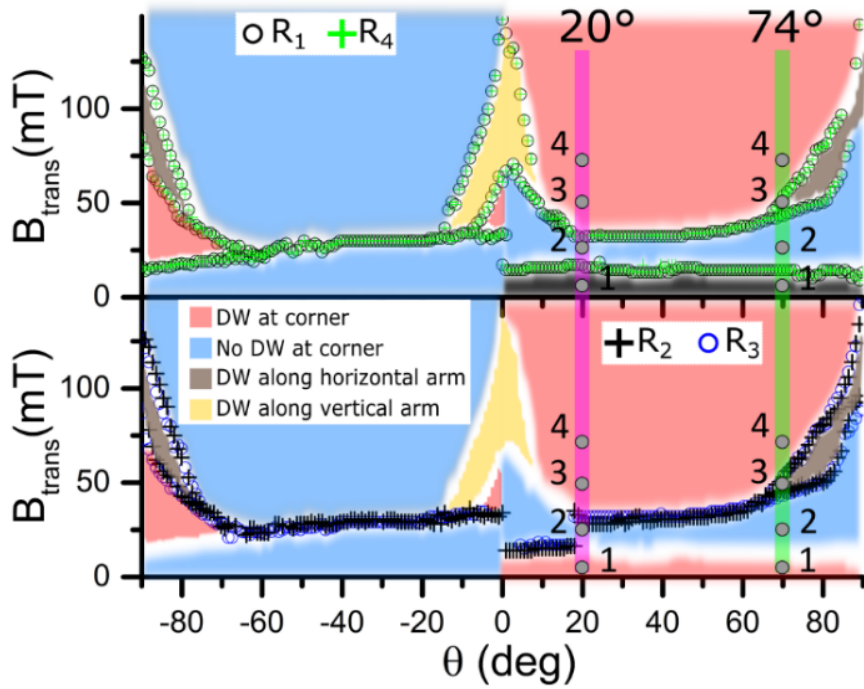
Figure 51. Angular dependence of irreversible transition fields and main magnetization states extracted from MR, MFM measurements, and simulations (used to infer the magnetization spatial distribution), for -90° < θ < 90°: top panel – resistances R1 and R4 measured at the corner; bottom panel – resistances R2 and R3 measured along the straight nanostructure. The colours correspond to the main magnetization states according to the legend. Note that the magnetization states are characteristic for the given magnetic nanostructure, whereas a specific resistance measurement serves as a probe for their determination. White bands correspond to transitions between states, which cannot be probed in specific resistance geometries (e.g. at θ = 10° the formation of a DW along the vertical arm can be seen as a step in R1 or R4, but it produces no change in R2 or R3). Numbers 1-4 (grey circles) on the green line at θ = 74 ° correspond to the areas described in Figure 48 and Figure 49, numbers 1-4 on the purple line at θ = 20° correspond to energy evolution described in Figure 52.

By analysing Figure 51, it is possible to define the state space conditions favourable for the generation of the metastable states with a longitudinal DW along the horizontal/vertical arm[203], as depicted by the grey/yellow colour in Figure 51 (i.e. as shown in Figure 49, state **III** for a horizontal DW). In particular, Figure 51 shows that metastable states with a longitudinal DW along one of the arms can only be observed when the magnetic field ramps, at a fixed angular orientation, from a negative saturation field to the field values highlighted in Figure 51 by grey and yellow, being -90° ≤ θ ≤ -80° or 70° ≤ θ ≤ 90° for DW along the horizontal arm (grey), and -15° ≤ θ ≤ 15° for DW along the vertical arm (yellow). For this reason, θ = 74° was chosen as a characteristic angle allowing the observation of unusual magnetic states both in resistance (Figure 48) and MFM measurements (Figure 49 bottom).
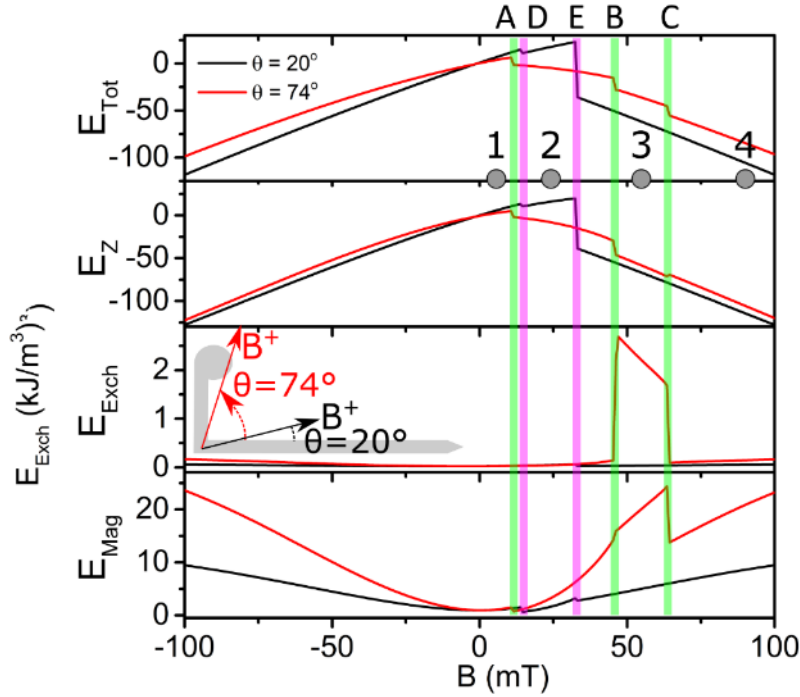
Figure 52. Calculated energy density contributions versus applied field for two angular orientations of the applied field, θ = 20° and 74°. Note different scales for individual energy components. Even although the entire nanostructure has been micromagnetically simulated, corresponding energy values have been estimated eliminating the shape energy contributions due to the arm ends.

We further analyse the transitions and states between them at angular orientation $\theta = 20°$. At this angle, no longitudinal DW formation is observed (i.e. contrary to $\theta = 74°$). The calculated energy density evolution versus the applied field is shown in Figure 52 for $\theta = 20°$ and 74° (black and red lines, respectively). Steep decrease in the total energy E_{tot} occurs when the system undergoes one of the transitions: **A**, **B**, or **C** for $\theta = 74°$ (green vertical line); **D** and **E** for $\theta = 20°$ (pink vertical line). The presence of the longitudinal DW at $\theta = 74°$, between transitions **B** and **C**, contributes to the overall reduction in the total energy. Considering the individual energy terms, presence of the longitudinal DW in this field range unavoidably results in an increase in the exchange, E_{Exch}, and magnetostatic, E_{Mag}, energies. However, it is overcompensated by the consequent reduction of the Zeeman energy, E_Z, note a significantly different scales for individual energy terms in Figure 52. Since the Zeeman energy depends on the external field, the longitudinal DW is stable only in field and does not exist at remanence. Moreover, this type of magnetization configuration appears only when the applied field has a predominant component along the direction orthogonal to the involved nanostructure arm. A stronger minimization of E_Z would require complete alignment of the magnetization with the applied field (i.e. perpendicular to the arm), but this would imply a great increase in the

magnetostatic energy, E_{Mag}. The formation of the longitudinal DW corresponds to minimization of the total energy E_{tot} and thus represents a good compromise between a moderate reduction in E_Z and a limited increment of E_{Mag} (whereas E_{Exch} provides a less important contribution).

For $\theta = 20°$, the evolution from **D** to **E** increases the total energy, with an increment of all the three terms. At transition **E**, the system evolves reducing the total energy with the generation of a DW at the corner. In this case, the formation of a longitudinal DW is not possible, since it would imply a strong increase in E_Z.

6.2. mSGM over a hybrid Py/Au junction

In the previous section it was shown that Py/Au junctions can be a good candidate for measuring localized small magnetic moments, like the ones produced by MBs. Here, we study nanoscale hybrid Py/Au junctions as a single MB detector.

In a typical MB detection experiment using DWs, a MB suspended in a fluid is attracted by the magnetic force due to the stray field gradient generated by a DW [104] pinned inside a nanowire. Detection of the MB can be made by tracking the DW pinning/depinning process performing a longitudinal MR measurement (AMR configuration) [156], as it has been shown in the previous chapter. However, the intrinsic changes in the resistance due to the presence/absence of the DW are relatively small, i.e. typically ~0.2% [32]. Moreover, longitudinal MR measurements are highly affected by the stochastic DW pinning/depinning process. In order to overcome these problems without modifying the basic elements, sensors based on ferromagnetic crosses (PHE configuration) have been proposed [117], [143], [148], [151], [152], [204]–[209]. However, such devices still have to deal with DW pinning at the cross corners [194], [209], [210]. An alternative solution exploited here, based on the results achieved in the previous chapter, is a sensor based on transversal MR measurements on a cross made of a magnetic nanowire and an overlaying metallic non-magnetic wire (i.e. a hybrid Py/Au nanojunction). In this geometry, a straight Py nanowire is a track for DW propagation and an active sensing element with no pinning sites, whereas the Au overlaying nanowire is used for the electrical signal detection. This approach has the advantage of being able to track the magnetization along the Py without modifying the DW propagation, and hence can be integrated into other DW-based devices.

In order to study these nanojunctions as single MB detectors, we perform a set of MR measurements, mSGM with a MB attached to the scanning probe[155], [211], and coupled micromagnetic-MR simulations.

6.2.1. Experimental setup and numerical model

Asymmetrical L-shaped magnetic nanostructures (see Figure 47) had been used in section 6.1 to study PHE. Here, in order to reduce the complexity of the magnetization, we have used a symmetrical L-shaped geometry, where each arm is of 20 μm long by 400 nm wide, and has disks of 1 μm in diameter at the end (Figure 53(a)). The hybrid cross-shaped junctions, included as part of the design (Figure 53(a) inset), are composed of a straight 400 nm wide Py wire with an overlaying 400 nm wide Au wire.
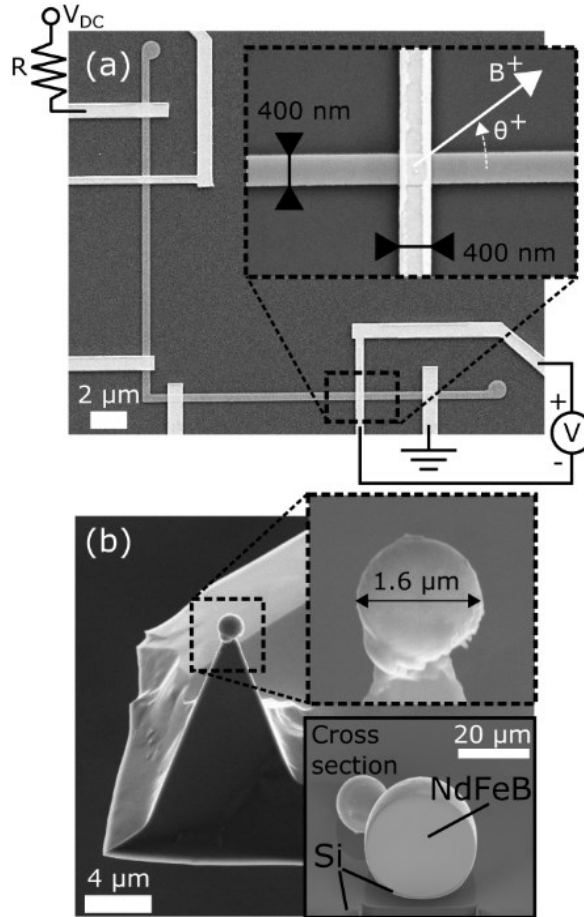
Figure 53. (a) SEM image of the whole L-shaped device with electrical connections. Inset: hybrid Py/Au junction studied in this work. (b) AFM probe with a NdFeB MB attached. Top inset: magnified image of the MB. Bottom inset: cross section of a large NdFeB MB milled down using FIB. Adapted from Ref[30], with permission from AIP publishing LLC.

As it has been shown in chapter 5, the L-shaped Py nanostructure possesses 4 well-defined remanent magnetization states, all of which are characterized by uniform magnetization distribution along the arms. Thus allowing the Py/Au hybrid junction to be treated as an individual device, where magnetization is uniformly distributed in the Py wire without taking into account the overall geometry.

To perform the single MB detection experiments, the SPM system (Aura, NT-MDT with home-built transport measurement stage) was used for mSGM studies in ambient conditions. This system allows application of an in-plane magnetic field during scanning, as well as electrical connections to the sample. In mSGM mode, the sample's topography is recorded in non-contact mode during the first scan. Then, during the second scan performed at an elevated height using the previously recorded topography to keep a constant height with the surface, the oscillation amplitude of the probe is set to zero and the transversal resistance at the junction is

112

measured in correspondence to the position of the scanning probe. To minimize the electrostatic interactions, the probe is grounded. The transversal resistance is measured using the same electrical circuit as for the MR measurements (i.e. as can be seen in Figure 53(a) and with I_{DC} = 103 µA), but employing an external lock-in amplifier with AC bias current of 100 µA at 44 kHz (as described in chapter 4 for AC MR measurements). This precaution is taken to reduce AC noise introduced by the AFM system, which is difficult to filter, once verified that the AC response of the junction at the selected frequency is similar to the DC response.

The modified probes used in mSGM (Figure 53(b)) have been custom-made by removing the apex of a commercial silicon AFM tip (TESPA, Bruker) and placing a MB on the flattened pyramid using a FIB system equipped with micromanipulators [156] (as described in chapters 4 and 5). The tip's spring constant (56.29 N/m) and its resonant frequency (351.5 kHz) were measured using the standard thermal tune calibration technique. A high spring constant value is chosen in order to minimize the static bending of the cantilever due to the MB-sample force; in this way, the MB-sample height remains constant all over the mSGM scan. The MBs used in this work are commercial magnetic NdFeB microspheres (MQP-S-11-9-20001-070 Isotropic Powder [190]) with diameter of ~1.6 µm (Figure 53(b) top inset). Considering a remanence magnetization for the powder with value M_r = 57.60 Am^2/kg, and a density of the powder in bulk, ρ = 3600 kg/m^3 [190], the estimated magnetic moment of the MB, assumed as a sphere with 1.6 µm diameter, is $m \sim 4.48 \times 10^{-13}$ Am^2 (measured with a SQUID magnetometer). The coercivity of the NdFeB microspheres is ~ 840 mT. Prior to the experiment, the microspheres were magnetized by applying a magnetic field of ~2 T perpendicular to the cantilever.

In order to check the homogeneity of the material distribution inside the NdFeB MBs, a MB of significantly larger diameter than used in this work has been selected and milled with FIB (Figure 53(b) bottom inset). Even the large MB appears to be uniform with no cavities, inclusions and visible defects, thus implying homogeneity of smaller MBs used in mSGM (Si on the bottom side of the MB was deposited from the substrate during the milling process).

The mSGM results are interpreted by means of a modelling approach that combines micromagnetic simulations with a MR model including both AMR and PHE effects. First, the magnetization configuration is calculated with a parallelized micromagnetic solver [23], [25], which time-integrates the Landau-Lifshitz-Gilbert (LLG) equation by means of a norm-conserving scheme based on Cayley transform [27]. Second, at each equilibrium point the spatial distribution of the electric field, expressed as the gradient of scalar potential ϕ, is obtained by numerically solving the following equation

$$\nabla \cdot [\overleftrightarrow{\sigma}(r)\nabla\phi(r)] = 0 \qquad (28)$$

For thin film-based nanostructures, the spatially dependent conductivity tensor $\overleftrightarrow{\sigma}(r)$ reduces to

$$\overleftrightarrow{\sigma}(r) = \frac{1}{\rho_\parallel \rho_\perp}\begin{bmatrix} \rho_\parallel - \Delta\rho \cos^2 \eta(r) & -\frac{1}{2}\Delta\rho \sin 2\eta(r) \\ -\frac{1}{2}\Delta\rho \sin 2\eta(r) & \rho_\parallel - \Delta\rho \sin^2 \eta(r) \end{bmatrix} \qquad (29)$$

where $\Delta\rho = \rho_\parallel - \rho_\perp$, with $\rho_\parallel$ and $\rho_\perp$ being the resistivities parallel and orthogonal to the magnetization direction, which forms an angle $\eta(r)$ with respect to x-axis [173], [207], [212].

The non-linear equation (28), coupled to ad hoc boundary conditions on current contacts (i.e. treated as not present in the circuit) and insulating boundaries, is iteratively solved until convergence of conductivity [31].

In the micromagnetic simulations, the saturation magnetization of Py is fixed to 860 kA/m, the exchange constant to 13 pJ/m and the magnetocrysalline anisotropy to zero. In the MR model, $\rho_\parallel = 0.34$ μΩm and $\rho_\perp = 0.333$ μΩm [172]. The interaction between the device and the NdFeB MB is taken into account by adding to the effective field in the LLG equation the magnetic stray field of the MB, which is approximated as a magnetic dipole located at a height corresponding to the distance between the device surface and the MB barycentre.

6.2.2. MR characterization

Experimental results are divided into three parts. First, we perform the electrical characterization of the junction by means of MR measurements using in-plane applied field. Second, mSGM mapping is done at a constant height (h in range $100 - 700$ nm), while the magnetization of the Py wire is aligned along two different directions.

MR measurements have been performed using the electrical circuit shown in Figure 53(a) in presence of an in-plane external magnetic field as indicated in Figure 53(a) inset. The resulting field dependence of the transversal resistance (i.e. transversal voltage divided by the bias current) is shown in Figure 54. The individual curves for the field ramped from negative to positive saturating values are shown for different angular orientations: $\theta = \pm 90°$, $\pm 45°$ and $0°$ in Figure 54(a), (b) and (c), respectively. Figure 54(d) shows the combined results for all angular orientations between -90° and +90° with a small angular step of 0.9°. As expected from Equation (29), there is almost no variation in the resistance when the field is applied along the

nanowire (Figure 54(c)), and the variation is maximum in the low field range when the field is perpendicular to the nanowire (Figure 54(a)). At $\theta = 90°$ a linear fitting in the range of -20 mT $< B < 20$ mT allows to estimate the maximum sensitivity of the junction, $S = 0.46$ Ω/T (Figure 54(a)).
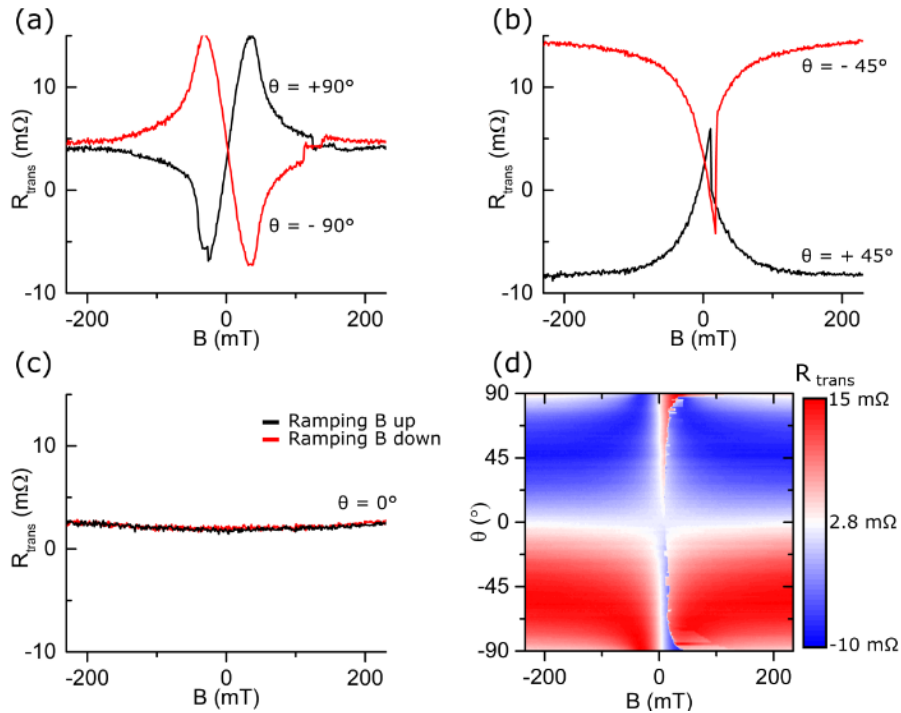
Figure 54. (a)-(c) Transversal resistance of the hybrid junction when the field is applied at (a) $\theta = \pm90°$; (b) $\theta = \pm45°$; (c) $\theta = 0°$. (d) Transversal resistance for different angles of the applied field, -90° < θ < +90°, $\Delta\theta = 0.9°$, when the field is ramped from negative to positive saturating values. Adapted from Ref[30], with permission from AIP publishing LLC.

Steps in the transversal resistance correspond to magnetization switching events along the Py wire and propagation of a DW (Figure 54(a) and (b)). A summary of angular measurements of the magnetization reversal is presented in Figure 54(d) where the steps occur at different fields depending on the angular orientation. In addition, Figure 54(d) demonstrates absence of the DW pinning at the junction, as a DW pinned at the junction would be associated with two steps in the resistance. As in the previous chapter, experimental curves show a constant background resistance of ~ 2.8 mΩ (Figure 54), associated with current through the Au at the junction.

6.2.3. Single MB detection

In mSGM, first the topography of the sample is recorded in a non-contact mode (Figure 55(a)), then the probe is retracted and magnetic field is applied to the device in a set direction.

Finally, the probe is brought into the device proximity again and resistance is measured, while the probe moves at a constant height over the surface using the previously recorded topography as a reference, and setting the oscillation amplitude to zero [155]. It is important to note that due to the MB-surface convolution, the topography recorded in Figure 55(a) shows a junction significantly wider than the one imaged using SEM (Figure 53(a)).
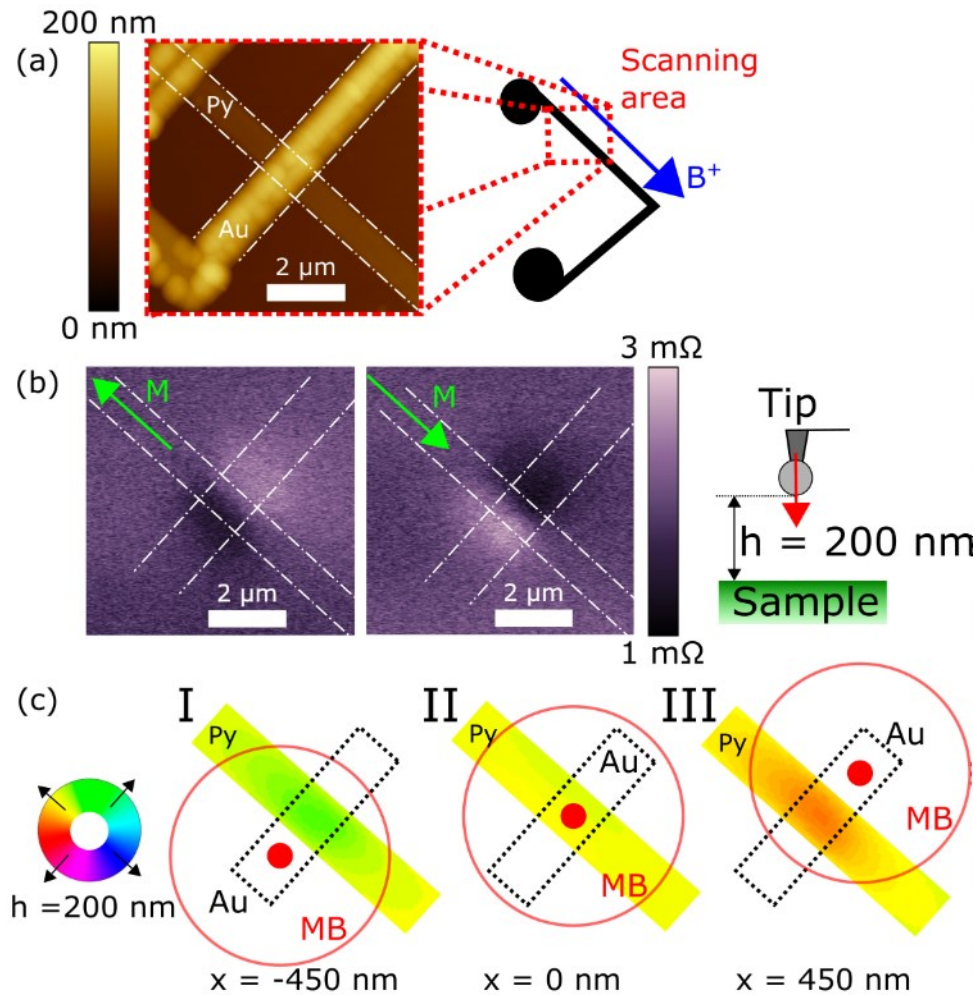
Figure 55. (a) Left: topography image of the hybrid junction taken with the MB-modified probe. Right: schematics of the scanned area in relation to the whole nanostructure. (b) Left: mSGM images of the transversal resistance over the junction at h = 200 nm. Green arrow indicates direction of the magnetization in the Py. Right: schematics of the mSGM experiment. (c) Simulated spatial distributions of magnetization for different positions of the MB along the Au contact at h = 100 nm with centre of the bead at: I) -450nm; II) 0 nm; III) +450 nm. Colour disk indicates the direction of the magnetization inside the Py. Adapted from Ref[30], with permission from AIP publishing LLC.

Results of the transversal resistance mapping when the probe is at 200 nm above the surface are shown in Figure 55(b). Left and right panels of Figure 55(b) report the cases of different magnetization orientation along the Py wire (indicated by the green arrow). A cross-

116

section of one of the images (shown in Figure 56(b) left) demonstrates variations of the MR behaviour along the Au wire in correspondence to the junction, as also confirmed by simulation results obtained for different distances h between the device surface and the MB bottom (Figure 56(b) right). Figure 55(b) demonstrates that the presence of the MB produces a detectable signal on the transversal resistance (Figure 55(b)), hence the junction can be used as a detector, and the direction of the magnetization along the Py nanowire determines the sign of the interaction as follows from Eq. (29). The background resistance Figure 55(b) also shows that, despite using AC bias signal for this experiment, the resistance is about 2 mΩ even at $B = 0$, i.e. similar to that obtained in the MR measurements using DC current. It should be also notice that although MB was magnetized perpendicular to the cantilever, the MB magnetization direction and the sample surface are not exactly perpendicular to each other. This is due to the angle introduced by the tip holder ~ 15º, the tilt angle of the sample, and the unknown angle introduced by the tip holder support (i.e. the scanning head of the Aura SPM system). However, since the mSGM images in Figure 55(b) show a symmetric influence when the MB is at one or another side of the Py wire, it can be concluded that the magnetization of the MB and the wire are nearly orthogonal.

The influence of the MB stray field on the magnetization configuration in the nanowire is depicted in Figure 55(c), which reports the magnetization spatial distribution for three different positions of the MB in respect to the Py wire, considering a height of 100 nm. When the MB is close to one side of the nanowire, e.g. $x = \pm 450$ nm, (where $x = 0$ corresponds to the centre of the wire, Figure 55(c) I, III), the MB's stray field produces a local deviation of the magnetization distribution leading to an angle η between magnetization and current density vectors different from zero. This results in an increase or decrease in the resistance depending on the sign of $sin(2\eta)$, which reaches the maximum amplitude when the MB stray field causes a rotation of the magnetization in the Py nanowire of 45˚, without effects of compensation between the stray field lines pointing in opposite directions. For the given bead/device geometry and vertical separation, this happens for $x \sim \pm 450$ nm. When the MB is exactly over the centre of the nanowire (Figure 55(c) II), its stray field is responsible for a symmetric distribution of the magnetization in the nanowire, i.e. areas of both positive and negative contributions to the resistance, resulting in a zero overall change in the resistance.

6.2.4. Sensing volume of a hybrid nanojunction

By scanning at different heights, it is possible to estimate how far the interaction between the MB and the hybrid junction extends, i.e. to define spatial and volume sensitivity of the

junction [155]. Figure 56(a) shows the transversal resistance taken at h = 200 nm. Applying Rose criterion for signal-to-noise detection [213], we assume MB detection when the signal (positive or negative change in respect to background resistance) to noise ratio is higher than 5 (red contour in Figure 56(a)). Following this criterion, the effect of the MB cannot be distinguished from the background signal higher than 400 nm from bottom of the MB to top of the junction (Figure 56(b) left).
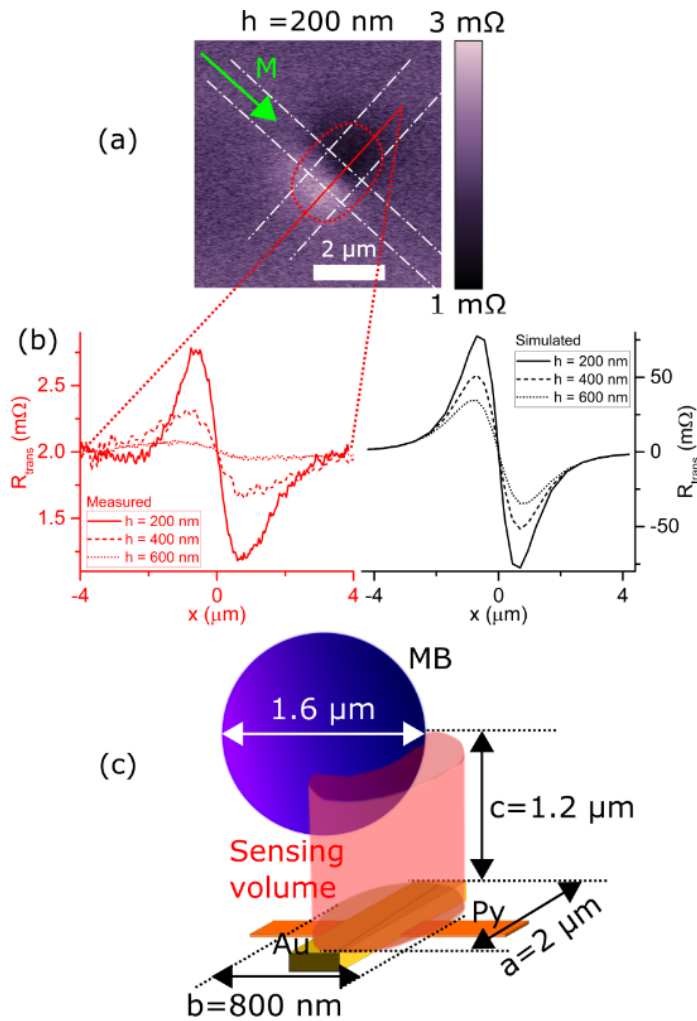
Figure 56. (a) mSGM map of transversal resistance at h = 200 nm. Green arrow: direction of the magnetization. Red area: boundary where the signal meets the Rose criterion. (b) Left: Cross section taken from (a) and measurements taken at different heights. Right: Cross sections extracted from simulations. (c) Schematics of the sensing volume (not to scale). Adapted from Ref[30], with permission from AIP publishing LLC.

By applying the same rule for the lateral distance, one can estimate the sensing volume (i.e. the volume where the centre of the MB has to be located to allow detection) as an elliptical cylinder of volume about 1.51 μm^3 with dimensions c = 1.2 μm (height), a = 2 μm (along the Au wire) and b = 800 nm (along the Py wire) (see Figure 56(c)). This result is similar to the sensing volume reported in chapter 5 for DW-based devices, where we reported a conical sensing volume of 0.24 μm^3 (i.e. 880 nm diameter of the base by 1.2 μm in height) for a 75 nm-wide Py L-shape device using the same type of MB.

When comparing the measured cross sections (Figure 56(b) left) with results from the

simulation (Figure 56(b) right), the modelled resistance results are about 100 times higher than the measured one, since they correspond to the transverse resistance in the Py nanowire due to the PHE effect, while the measured ones are extracted from the Au contact (the electrical resistivity of Au and Py differ by a factor of 10-15). Hence, it is expected that by increasing the resistivity of the overlying metal wire the value of the transversal resistance will increase, allowing much bigger sensing volume.

6.3. Summary

Is this chapter, hybrid ferromagnetic (Py)/metal (Au) junctions were studied by means of longitudinal, AMR, and transversal, PHE, MR measurements, *in situ* MFM and mSGM, as well as micromagnetic simulations.

Using an L-shaped magnetic nanostructure, longitudinal and transversal MR measurements have been compared for different types of junctions (i.e. over a straight wire and over a corner with a DW pinned). For both the corner and the straight segment, the comparison reveals a larger resistance change in the case of longitudinal measurements (for absolute change). However, based on micromagnetic simulations it is expected that the transversal resistance change could be significantly larger if a high resistive material is used for electrical connections. Thus, transversal resistance measurements hold the promise of much larger relative signals between different magnetization states, improving DW tracking and facilitating the sensing approach.

Moreover, we demonstrated that the same information about equilibrium magnetization states can be accessed either from longitudinal or transversal MR measurements. In particular, the results obtained from all the experimental measurements and micromagnetic simulations have proved that the hybrid junctions do not add new pinning sites for the DWs. In addition, the measurements identified a rare metastable state with a DW along the Py nanowires with a DW length of ~10 μm. The existence of such unusual metastable state was further proven by means of *in situ* MFM and energy considerations from micromagnetic simulations.

Due to the linearity of the PHE to small fields, and the good sensitivity measured for hybrid junctions (0.46 Ω/T for a 400 nm wide Py by 400 nm wide Au), we use mSGM, with a MB attached to the scanning probe, to demonstrate single MB detection using hybrid junctions. The mSGM studies demonstrate that the junction can be used to detect NdFeB MBs with size of ~1 μm and above, and that the measured signal depends on the direction of magnetization in the

Py. Micromagnetic and MR modelling accurately describes the experimental results based on the PHE in the Py wire.

Performing mSGM imaging at different heights, we estimated the sensing volume to be approximated by an elliptical cylinder of volume about 1.51 μm^3 with dimensions 1.2 µm in height, 2 µm along the Au wire and 800 nm along the Py wire. This allows designing microfluidic channels or magnetophoresis devices to guide MBs towards the sensing volume of the sensor. In particular, when the sensing volume determines the maximum thickness of capping layers that can be deposited on top of the sensor.

In conclusion, the proposed hybrid junctions can be used to measure small in-plane magnetic fields and, in particular, the fields created by single MBs, proving that hybrid junctions can be used as a single MB detector.

7 AHE and ANE in nanostructures with perpendicular magnetic anisotropy

In the previous chapters DW manipulation inside of magnetic nanostructures was achieved using an external magnetic field. However, in order to integrate multiple devices in a Lab-On-a-Chip, it is required to be able to operate individual devices. To do so, DW manipulation through spin transfer torque (STT) allows operating DW-based devices without using external magnetic fields. But when the STT originates from a charge current, it creates heat that damages the devices and increases the power demand. An interesting alternative is the use of spin currents, which can produce STT with much less associated heat production. For this reason LSVs, which can generate in-plane spin currents, play a central role in spintronics, and enable a new range of spintronic devices[214]. In particular, thermally-driven LSVs are of interest because they produce much more efficient[214]–[217] spin-injection per unit of current than charge current spin-injection[78]. However, when operated in the thermal mode, LSVs also exhibits other effects such as the ANE and the AHE that superimpose with the spin signal and require a characterization.

Here, we investigate a LSV comprised of two perpendicular magnetic anisotropy (PMA) elements, connected by a metal channel that inhibits spin diffusion. This device allows evaluating the contribution of both the AHE and the ANE to the overall signal produced by the LSV and, in particular, how the LSV is affected by a local magnetic field (i.e. the stray field produced by a MB), and how it can be integrated with DW-based devices for MB manipulation/detection.

In a LSV operated in the thermal mode (Figure 57(a)), a charge current, I, in the first ferromagnet (injector), creates a spin accumulation in the non-magnetic channel and generates Joule heating. The resulting heat gradient facilitates spin diffusion through the channel and generates a voltage between the channel and the second ferromagnet (detector), due to the imbalance between populations of electrons with spins up and down. PMA materials, such as Pt/CoFeB/Pt studied here, also exhibit AHE perpendicular to both the electrical current, I, and the magnetization, M. Hence the final voltage is a combination of spin signal (affected by both injector and detector), and the AHE (affected only by the injector), and thus it is difficult to differentiate the effect of a local field in the injector from the detector.

While in Figure 57(a) the ANE due to the heat gradient is insignificant, when the electrical current in the injector is high (Figure 57(b)), the final voltage on the LSV becomes affected

also by the ANE[218] in the detector, i.e. the current in the injector creates a temperature gradient perpendicular to the magnetization in the detector and thus an electrical field orthogonal to both appears (see Figure 57 (b)). In this case the final voltage is affected by the spin signal, the AHE, and the ANE (affected only by the detector), and is the most complex case, since there is mixed contributions from injector and detector.
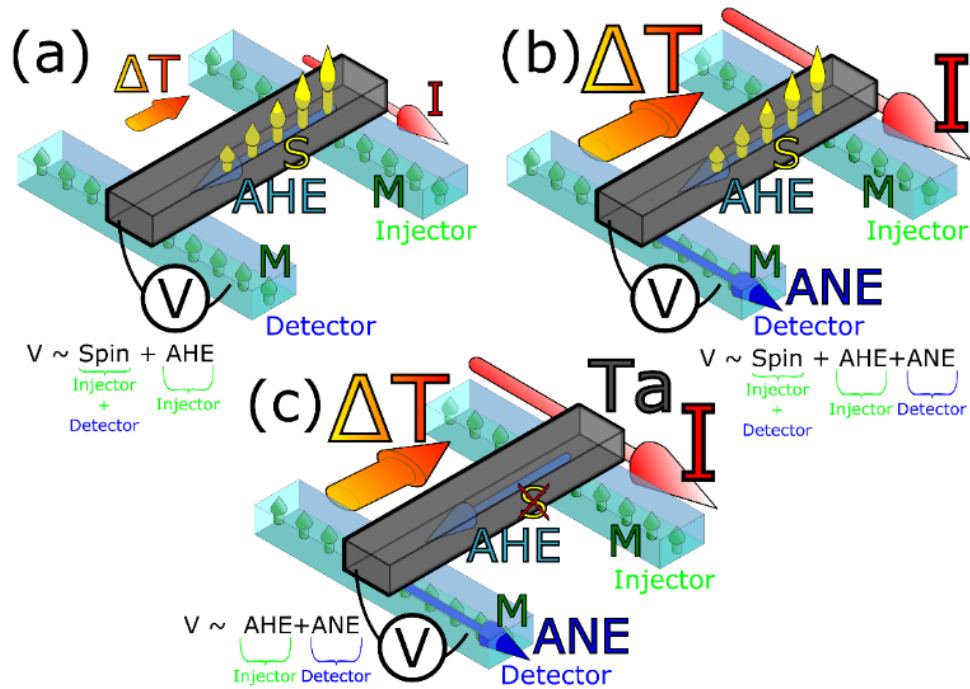
Figure 57. LSV diagram, in blue ferromagnetic elements, in grey the non-magnetic channel, green arrows indicate magnetization M. (a) LSV in thermal injection mode where an electrical current I (red arrow) across the injector creates spin diffusion S across the channel (yellow arrows) and produces a voltage in the detector. The final voltage includes AHE (blue arrow) created by the current I in the injector. (b) At high currents, the ANE (blue arrow), generated by the heat gradient (red and yellow arrow), becomes large enough to modify the final voltage. (c) By using Ta in the channel the spin signal is suppressed.

However, if the non-magnetic channel is made of Ta (Figure 57(c)), a material that supresses spin diffusion[219] due to a very short spin-diffusion length ~1 - 2 nm, then the final voltage depends only on the AHE and the ANE, and hence injector and detector are decoupled and it is easier to study the effect of a local magnetic moment in the injector or the detector (e.g. the effect of a MB).

7.1. AHE and ANE in a LSV

The LSV studied here was fabricated following the process described in chapter 4 from a continuous polycrystalline multilayer film with stack composition Ta(4 nm)/Pt(3

nm)/$Co_{60}Fe_{20}B_{20}$(0.6 nm)/Pt(3 nm) deposited by successive sputtering in an unbroken vacuum at 0.5×10^{-7} mbar on Si/SiO_2(1000 nm) substrate. Each LSV was comprised of two magnetic nanostructures, 6 μm in length by 200 nm in width, and a non-magnetic Ta channel (30 nm thick, 1 μm in length and 500 nm wide). In Figure 58(a), the top nanostructure is the injector and the bottom one is the detector. The magnetic nanostructures have a disk of 1 μm in diameter in one side and a tapered end at the other side (forming a 15° angle in the top nanostructure and a 60° angle in the bottom one, see pink structures in Figure 58(a)). In PMA nanostructures, the tapered end acts as a nucleation point for magnetization reversal, where sharper tapered ends enable lower coercive field[158], [220]. Different coercive fields for each device are important as they allow to investigate the device in parallel and antiparallel configurations.
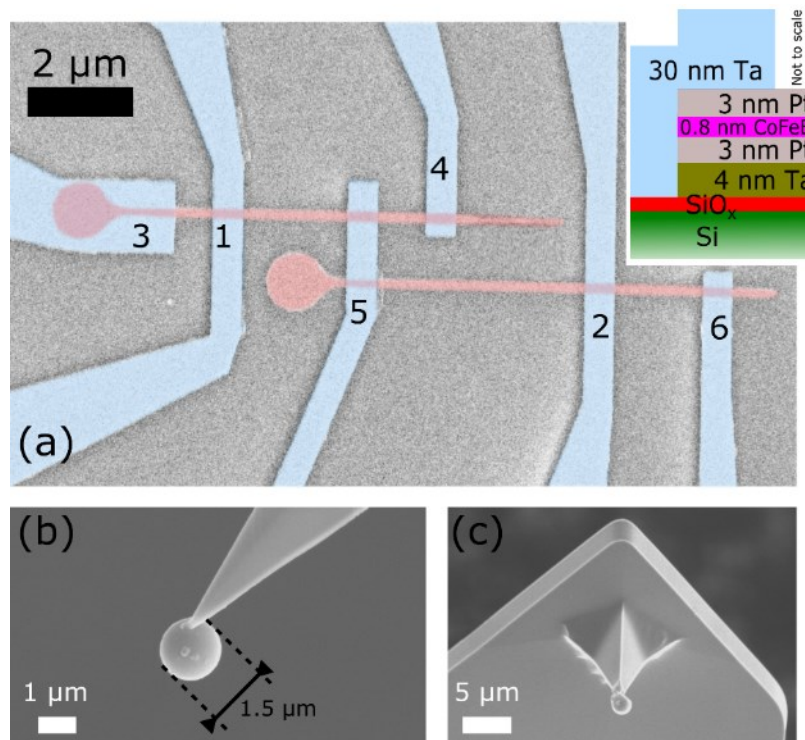
Figure 58. (a) False colour SEM image of the LSV with numbered electrical contacts. Inset: stack composition. (b)-(c) An AFM probe modified with a NdFeB MB attached at the apex. Adapted from Ref[221], with permission from AIP publishing LLC.

To characterize the LSV, MR measurements were performed in different electrical schemes (Figure 59) in an out-of-plane magnetic field using a DC current ($I = 502$ μA) at room temperature (as described in chapter 4). The output voltage was measured using a nanovoltmeter with 10 PLCs as an integration time.

The effect of local magnetic fields over the LSV was studied using mSGM with a modified probe in ambient conditions. The SPM system (Aura, NT-MDT with home-built transport

measurement stage) allows application of an out-of-plane magnetic field during scanning as well as electrical connections to the sample. The modified probes used in mSGM (Figure 58(c)) were custom-made by removing the apex of a commercial silicon AFM probe (TESPA V2, Bruker) and placing a MB on the flattened pyramid using a FIB system (Figure 58 (b-c), fabricated as described in chapter 4)[156]. The MBs used here are commercial NdFeB microspheres (MQP-S-11-9-20001-070 Isotropic Powder [190]) with diameter of ~1.5 μm (Figure 58(b)). Prior to the experiment, the modified probes were magnetized by applying ~2 T along the pyramid of the probe (i.e. stray field pointing towards +z direction in Figure 59(d) and Figure 60(a)).

In order to characterize the stray field generated by the modified probe, we used differential phase contrast (DPC), which is a scanning tunnelling electron microscopy (STEM) method where the electron beam is focused in the specimen plane and a quadrant detector is situated in the far field. The deflection, ζ, of the electron beam (of wavelength λ) is directly related to the magnetic induction component perpendicular to the beam integrated along the beam path[222]–[224]:

$$\zeta = \frac{e\lambda}{h} \int_{-\infty}^{\infty} B_\perp dl \tag{30}$$

By taking the difference between the signals from opposite segments of the detector, components of the integrated induction are determined. This technique was previously used to image the magnetic field around standard MFM probes[224] and is used here to image the magnetic field distribution around the MB (Figure 59(f)). The images were acquired on a JEOL ARM 200CF instrument equipped with a probe aberration corrector and a cold field emission gun. The imaging conditions used in this instance were with a condenser aperture of radius 10 microns which corresponds to an imaging resolution of 3 nm.

Experimental results are divided into three parts. First, we perform MR measurements using out-of-plane magnetic field. Second, DPC measurements of the modified probes have been performed and the magnetic field distribution and intensity around the MB have been estimated. Finally, by performing mSGM measurements with no applied field we show that the probe remagnetizes the CoFeB nanostructures, while by applying the external magnetic field, the probe's stray field is partially compensated allowing its effect on the magnetic nanostructures near the non-magnetic channel to be studied.

7.1.1. MR characterization

MR measurements have been performed in the presence of an out-of-plane external magnetic field (see Figure 59(a-b)). Figure 59(a) shows the AHE signals at crosses 1 and 2 (see Figure 58(a) for reference) as black and red lines, respectively, when a current passes from contact 3 to 4 (black) or from contact 5 to 6 (red). As expected, Figure 59(a) shows a hysteresis loop with two characteristic values of MR (i.e. corresponding to the magnetization up/down). The change in the resistance is ~ 0.15 Ω and the background resistance is ~ 0.100-0.125 Ω. The different tapered ends (i.e. 15º/60º angles) result in different coercive fields for the magnetic elements.
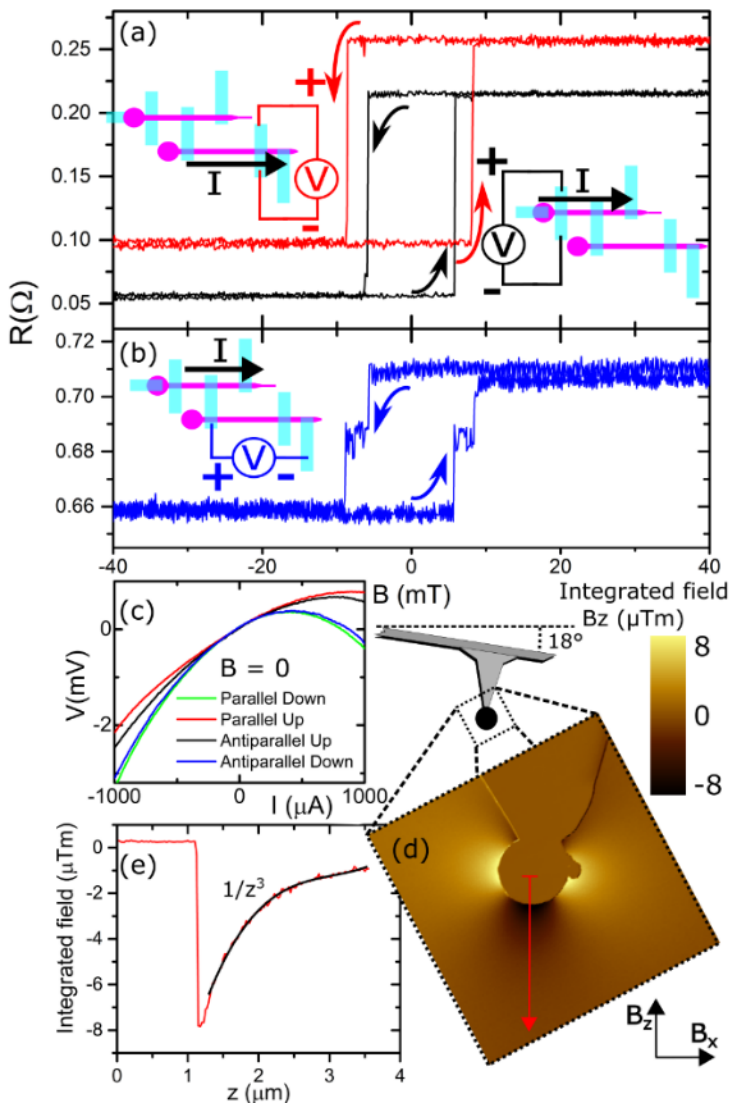
Figure 59. MR measurements of the LSV device: (a) the AHE measured at crosses 1 and 2; (b) the thermal LSV configuration (i.e. current between contacts 3 and 4, voltage measured between contacts 5 and 6, see Figure 58(a) for reference). (c) Voltage as a function of the applied current at zero field for four magnetization states, demonstrating combination of linear and quadratic components. (d) DPC image of the modified probe, the colour indicates the value of the integrated field along Bz direction. (e) Profile from the red line in (d) with 1/z3 fitting shown in black. Adapted from Ref[221], with permission from AIP publishing LLC.

Figure 59(b) shows the resistance in the thermal LSV configuration, where the current is passed between contacts 3 and 4 of the injector and the voltage is measured between contacts 5 and 6 of the detector. The steps on the blue curve (Figure 59(b)) match the magnetization reversal of each device (i.e. steps on the black and red curves in Figure 59(a)), with a total

change in resistance of $\sim 0.05\ \Omega$ and a background resistance of about $\sim 0.69\ \Omega$. The double-step switching originates in the combination of the ANE produced by the heat transmitted from the injector to the detector through the non-magnetic channel and the AHE from the injector. It is possible to identify and separate the two effects as the ANE is quadratic, while the AHE is linear with current. Figure 59(c) demonstrates that the total signal is a combination of quadratic and linear responses.

7.1.2. Probe stray field characterization

Figure 59(d) shows a DPC image of the modified probe. As DPC measures only the integrated field perpendicular to the detector (Eq. (30)), Figure 59(d) demonstrates the intensity of the integrated B_z component of the field, and Figure 59(e) shows the profile along the z-direction (i.e. perpendicular to the sample). The field distribution is very similar to the one produced by a uniformly magnetized sphere. Hence, outside the sphere with radius, R, it is the same field distribution as from a magnetic dipole with moment m at a position r, with $r > R$:

$$B = \frac{1}{4\pi}\left(\frac{3r(m \cdot r)}{r^5} - \frac{m}{r^3}\right) \tag{31}$$

The field of the magnetic dipole decays as $1/z^3$ along the dipole direction. As shown in Figure 59(e) black line, the integrated field of the probe has the same decay dependency, thus the field of the MB can be approximated by a dipole.

7.1.3. mSGM on a thermal LSV

Figure 60(a) shows an mSGM image taken with the modified probe in non-contact mode. The probe oscillates at a resonant frequency of 352 kHz with an oscillation amplitude of 400 nm peak-to-peak (i.e. the average distance between the device and bottom of the probe is 200 nm). Before scanning, the device is saturated with a field pointing in $-z$ direction (Figure 60(a)). During the scan, the external field is set to zero and the field from the MB is pointing in $+z$ direction. The probe scans from $+x$ to $-x$ (i.e. from right to left). As the probe scans over the device, it produces changes in the thermal LSV signal creating three regions of clearly distinguished resistance, marked I, II, and III in Figure 60(a). During the scanning, the probe remagnetizes consecutive parts of magnetic elements from $-z$ to $+z$ magnetization (i.e. from red to blue in Figure 60(a) right-hand side schematics). These changes in magnetization only appear in the thermal LSV signal when the MB reaches electrical contacts (i.e. first contact 2 and then contact 5). Initially in region I, the probe remagnetizes the tapered end of the bottom element, with no effect on the resistance $\sim 0.6\ \Omega$, as this part of the device does not contribute to the electrical signal. As the MB (and the induced change in magnetization) reaches contact

2, the resistance increases up to ~ 0.7 Ω (region II in Figure 60(a)). In region III, after the probe passes contact 5, the resistance increases up to ~ 0.8 Ω and does not change anymore, as the remaining parts of both magnetic structures are being magnetized in +z direction. By repeating the scan in both directions no further changes are observed, as the device is now fully magnetized in the direction of the MB's stray field.
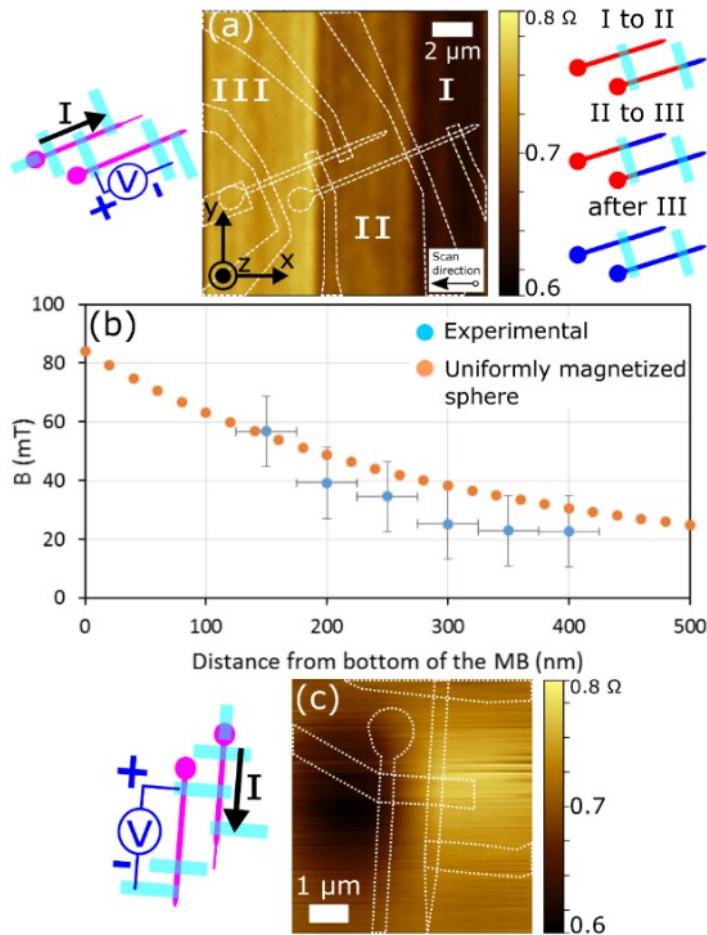
Figure 60. (a) mSGM image of the device in thermal LSV configuration, no external field applied. Numbers I to III indicate the regions where magnetization changes. Left inset: electrical circuit. Right inset: magnetization of the magnetic elements in -z/+z (red/blue) orientation when the probe reaches the boundary of each region. (b) Measured magnetic field from the MB, and calculated values for the field created by a sphere of the same radius. (c) mSGM image of the non-magnetic channel in thermal LSV configuration, when a magnetic field is applied to prevent remagnetization of magnetic elements. White dotted lines in (a) and (c) outline the device. Adapted from Ref[221], with permission from AIP publishing LLC.

Thus, in this experiment, the MB remagnetizes the device preventing observation of any possible local effects. Similar problem is faced when using a commercial MFM probe. One of the main advantages of using the modified probe is its spherical shape, which leads to a less complex and much more symmetrical field distribution than the one from a commercial MFM probe. Additionally, it allows to tailor the coercive field of the probe. For example, in the case presented here the coercive field of the modified probe is much higher (~840 mT)[30] than that of a commercial probe (~ 7.5 - 65 mT)[163].

In order to partly compensate for the magnetic field of the probe and be able to perform mSGM over the channel without remagnetizing the device, the magnetic field produced by the modified probe was estimated. First, the device was saturated in −z direction, then, without

removing the external field, it was scanned with the MB (saturated in +z direction). By reducing the external field step-by-step in each scan, it was possible to find the external field value where the device switches magnetization, which means that the field from the MB plus the external field (pointed in opposite directions) are equal to the coercive field of the device (10 mT for cross 2 as extracted from the switching field of the red curve in Figure 59(a)). Using this method and monitoring the AHE signal at cross 2, the stray field of the modified probe has been estimated for several distances between the top of the device and the bottom of the probe (Figure 60(b)). Because the coercive field of the device was measured in a uniform field, whereas the field from the probe is non-uniform and the probe is oscillating, some difference between the measured and real field could be expected. However, the larger size of the MB compared with size of the device allows the field to be considered as being uniform with a good degree of approximation. Variations of the field produced by the oscillation of the probe are addressed by the fact that the probe oscillation amplitude was about 15 nm peak-to-peak, while the closest average distance between the bottom of the MB and the top of the device was 100 nm. In order to further minimize possible variations, the measurements were performed several times and the error bars take into account the dispersion of the results. The values for a uniformly magnetized sphere with diameter 1.5 μm and moment ~3.66 × 10-13 Am^2 have also been plotted on the same graph. These results were calculated with (Eq. (31)) using remanent magnetization and density of NdFeB powder[190][30], i.e. M_r = 57.60 Am^2/kg and ρ = 3600 kg/m^3, respectively. The dipole approximation, the validity of which was confirmed by the DPC technique, and the measured field values agree very well, e.g. providing ~85 mT at the surface of the MB and ~40 mT at 200 nm away, allowing to properly compensate the field produced by the modified probe. It is noteworthy that the stray field from commercial probes ranges from ~ 32 to ~ 73 mT at 50 nm [163].

Figure 60(c) shows an mSGM image of the non-magnetic channel taken with the modified probe when recording the thermal LSV signal. Scanning direction is from –y to +y (i.e. from bottom to top). The average distance between the device and bottom of the probe is 200 nm. The external magnetic field of 35 mT is applied along the –z direction to prevent the device from remagnetization, since the probe's field is ~ 40 mT in the +z direction, the resulting field immediately below the MB is 5 mT. As the coercive field of the device (obtained from Figure 59(a)), is ~10 mT, i.e. larger than the accumulated external field, in this experiment the device has not been switched. Instead of different regions appearing as the probe scans over the surface (as in Figure 60(a)), Figure 60(c) shows two areas of locally/increase/decrease resistance

centred at the metallic channel, a bright spot (maximum of ~ +0.1 Ω) when probe is near the injector, and a dark spot (minimum of ~ -0.1 Ω) when the probe is near the detector. This confirms that the signal measured in the thermal LSV depends on both injector (i.e. AHE, bright spot) and detector (i.e. ANE effect, dark spot), and also that by partial compensation of the stray field of the probe it is possible to affect the device magnetization without reversing it.

7.2. Summary

LSV made of ultra-thin Pt/CoFeB/Pt and operated in thermal mode has been studied by means of MR measurements and mSGM imaging using a MB attached to the scanning probe. The transport measurements demonstrate the sequential switching of the two magnetic elements that form the LSV (at ~ 10 and ~ 7 mT), evidencing that the magnetization can be tracked either by AHE or by using the thermal LSV configuration. As a non-magnetic element (Ta) with a very short spin-diffusion length was used as the channel, the thermal LSV signal implies a combination of ANE and AHE.

The DPC imaging of the modified probe shows that the MB field can be described using a dipole approximation (i.e. decays with z^3 from the centre of the MB) with a field of about 85 mT on the surface of the probe and about 40 mT at a distance of 200 nm away from the MB.

By performing mSGM in zero external field, it was demonstrated that the field from the MB switches the magnetization of the CoFeB elements as it hovers over them. Alternatively, by applying an external compensating magnetic field, we estimate the MB stray field intensity and directly measure its decay. The measurements performed in this way agree with the DPC results and the analytical model of a uniform magnetized sphere. Moreover, we demonstrate that by partial compensation of the MB stray field with an external field, it is possible to locally study the various magnetic phenomena in ultrathin film nanostructures. In particular, in the studied geometry we have demonstrated that the output signal originates in a combination of ANE and AHE.

8 Imaging with DWs

MFM enables imaging magnetization distribution with nanoscale resolution[225], ~ 10 nm, which is a key requirement for studying novel magnetic nanostructures such as high density magnetic recording media[161], magnetoresistive random-access memory devices[226], or magnetic sensors used for Lab-On-a-Chip applications[53]. Through the previous chapters, MFM was used to identify different magnetization states and magnetization evolution. However, as it was demonstrated with the multiple mSGM experiments, smaller and more complex nanostructures require not only higher resolution MFM, but also an ability to extract detailed and accurate information about the magnetization of the sample without modifying the state either of the sample or the probe. Thus, the main challenges of the modern MFM technology are i) to increase the sensitivity (i.e. both magnetic sensitivity and spatial resolution)[227] and ii) to have a low moment probe with high coercivity, in order to minimize the interference with sample magnetization[155], [228]–[230] and, hence, being able to image, e.g. heterogeneous samples comprised of areas with high and low anisotropy and magnetization, or with high gradients, e.g. the stray field created by DWs[229].

Different solutions have been previously proposed to the above challenges. For instance, sharp probes with thin (or partial) magnetic coating provide better spatial resolution[230]–[235]. However, it is commonly achieved at the price of a reduced magnetic moment, a lowered magnetic sensitivity, or a decreased probe coercive field, all due to the smaller amount of magnetic material. Alternatively, thicker coatings, or hard magnetic materials, produce a larger magnetic moment[163], [189], [225], [235]–[237] that increases the magnetic sensitivity and the probe's coercive field, but at the cost of increasing interaction with the sample's magnetization and the physical radius of the probe's apex (i.e. reducing spatial resolution).

When using a uniform magnetic coating, its thickness is linked to the sharpness of the probe's apex, as well as the stray field and coercivity of the probe. This does not allow for much freedom in the variation/optimization of the probe's properties[237], apart from a most common scenario of matching sample – probe properties in each particular case. This becomes problematic when the sample under study is heterogeneous. In this case, the stray field generated by the probe may induce changes in the magnetization of low anisotropy regions[238], alternatively regions with high magnetization generate intense stray fields that may affect the magnetic moment of the probe if its anisotropy is not strong enough[239]. Both of these effects will severely reduce reliability of MFM measurements; hence it is desirable to

use a probe with a sufficiently large coercivity and a moment, which can be controllably switched between the high or low moment states.

In order to increase the resolution alongside imaging heterogeneous samples, probes modified with magnetic nanoparticles[234], [240] or nanowires[228], [241]–[246] were used previously. By using magnetic nanoparticles it is possible to increase lateral resolution, but usually it was achieved at the cost of a reduced magnetic signal, accompanied by a low probe anisotropy. Thus, imaging areas with high stray fields still remains inaccessible.

Also with the aim of having a very small and localized magnetic moment, a different approach utilizes multilayer magnetic probes, where an un-compensated magnetic moment at the probe's apex results in the simultaneous increase of the magnetic resolution and probe's magnetic anisotropy[247], [248]. However, it unavoidably results in a much larger probe radius, hence leading to lower spatial resolution and distortion of the topographical image. Other approaches involved modification of the MFM technique, e.g. imaging the same sample twice but with the probe magnetized in opposite directions[249], [250]; driving the probe at different frequencies during topography and lift scans[251], [252], or use of dual probes, where one of the probes records the topography signal, while the second one (at higher distance from the surface), records the magnetic signal[253]. However, none of the solutions mentioned above fully addresses all the aforementioned challenges.

In this chapter a custom-made DW-probe is used to perform MFM and overcome the problems stated above. In particular, to reduce sample-probe interaction when imaging DWs and thus ease the study of DW-based devices. This is achieved using a patterned magnetic nanostructure on one side of the probe's pyramid (see Figure 61), instead of a uniform magnetic coating. The probe has several characteristics that make it suitable for studying heterogeneous samples with low and high magnetic anisotropy and/or magnetization. Using an external magnetic field, the patterned nanostructure on the probe can be set into four different stable magnetization states [see Figure 61(d) inset], namely two states with a head-to-head or tail-to-tail (HH or TT, respectively) DW, and two states without a DW described as "curl" states (i.e. head-to-tail or tail-to-head). The ability to switch the DW-probe's magnetic state during the MFM scan using an external magnetic field allows for studies of heterogeneous samples where probes with both high and low magnetic moments are required. Moreover, such probe enables the efficient utilization of the shape anisotropy of the nanostructure to increase the coercive field of the probe, which is otherwise dominated by the bulk material anisotropy.

The study presented here uses *in situ* MFM to demonstrate controllable switching of magnetization of the DW-probe, and to compare the performance of the DW-probe with standard and low moment commercial probes. Electron holography (EH) studies[254] and numerical simulations of the DW-probe in different states, are used to identify four possible magnetic states (i.e. two states with a DW and two curl states).

8.1. DW-probe

The modified probes were custom-made out of magnetically coated commercial probes from NANOSENSORS™ PPP-MFMR AFM[255] using FIB to etch away the excess of magnetic coating. Figure 61(a) to (c) show stages of the FIB milling process with Ga-ions, used to etch away the magnetic material from the tip's sides, i.e. completely from three sides while leaving only a V-shaped magnetic nanostructure on one of them (Figure 61(d)). The V-shaped nanostructure's arms are 4.48 µm in length by 200 nm in width, meeting at 32.3°. The estimated thickness[163] of the nanostructure is about 30 nm. Both arms of the V-shaped nanostructure end in a circular disc of 1µm in diameter to reduce the stray field produced by the arms' end, also allowing to increase/decrease the coercive field [12], [31].
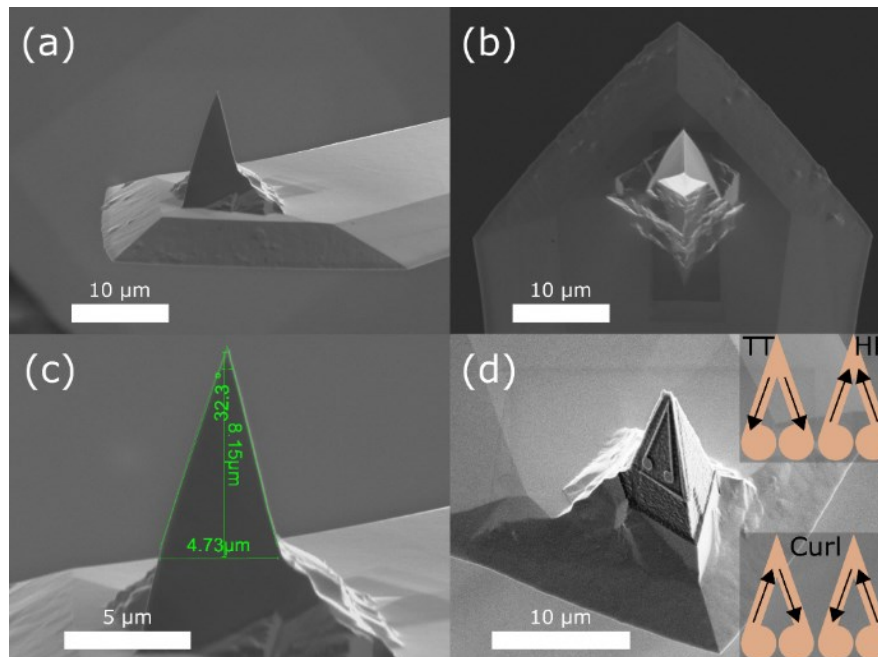
Figure 61. SEM images of commercial and custom-made DW-probes. (a) - (c) Commercial NANOSENSORS™ PPP-MFMR AFM probe before ion etching, where (c) shows dimensions of the probe pyramid. (d) V-shape nanostructure obtained by FIB ion etching on one side of the probe apex. Inset: schematics of 4 possible magnetization states.

Although the exact composition of the magnetic coating of the commercial probes from NANOSENSORS™ PPP-MFMR AFM is unknown, it is expected to be a soft magnetic material with in-plane magnetization, and hence the V-shaped structure will behave similarly to ferromagnetic structures of similar dimensions with in-plane magnetization and made of soft magnetic material (e.g. 25 nm thick Py L-shaped nanostructures studied in previous chapters)[12], [32] which show four stable magnetic states depending on the magnetization along the arms.

8.2. Stray field of the probe

EH imaging[256] of the stray magnetic field produced by the modified probes was carried out in a Hitachi HF3300 (I2TEM-Toulouse) microscope, a transmission electron microscope (TEM) specially designed to perform *in situ* EH experiments with a high resolution and phase shift sensitivity. Equipped with a cold field emission gun and a spherical aberration corrector (aplanator B-COR from CEOS) applied to both TEM and Lorentz modes[256]. For this study, EH experiments were performed in a corrected Lorentz mode for the normal stage of the microscope. In this stage the sample is placed within the pole pieces of the objective lens which is switched off to favour a free-field condition. However, a controlled magnetic field can be applied by exciting the objective lens which act parallel to the electron trajectory. The *in situ* magnetic field capability of the microscope was used to change the magnetic states of the MFM probes. EH holograms were recorded operating the microscope at 300 kV, and using a double bi-prism setup to avoid the formation of Fresnel fringes in the lateral edges of the hologram. The reconstruction of the stray field around the probe was carried out by retrieving, from the holograms, the magnetic component of the phase shift of the object electron wave, $\varphi_{MAG}(z, y)$, which is directly proportional to the magnetic flux[256], $\Phi(z, y)$, [$\varphi_{MAG}(z, y) = (e/\hbar)\,\Phi(z, y)$, where e and $\hbar$ are the electron charge and the reduced Planck constant, respectively] so images of the phase shift will directly provide maps of the magnetic flux. In addition, $\varphi_{MAG}(z, y)$ and the projected magnetic induction, $B_{proj}(z, y)$ are related as $\nabla\varphi_{MAG}(z,y)\,B_{proj}(z,y) = 0$, meaning that the variation of the magnetic phase shift is perpendicular to the direction of the projected magnetic induction, following the right-hand rule between $\nabla\varphi_{MAG}(z, y)$, $B_{proj}(z, y)$ and the electron trajectory. This relationship allow us determining the direction of the magnetic flux[257].

Figure 62 displays the results of EH experiments taken with pyramid along $+ z$-axis as shown in Figure 62(g). Images in Figure 62(a-c) show the electron beam phase shift (in radians)

due to the stray field emanating from the DW-probe at remanence after applying a pulse of external magnetic field in order to change the magnetization state of the probe. Images in Figure 62(d-e) show the magnetic flux line representations of the corresponding phase shift images in Figure 62(a-c). To facilitate the interpretation of the stray field configuration, magnetic flux line representation [Figure 62(d-e)] was produced by applying a sinusoidal function to the amplified magnetic phase shift images, i.e. $\Phi(z, y) \sim cos(n\varphi_{MAG}(z, y))$, where Φ is the magnetic flux representation, n is an enhancement factor, and φ_{MAG} is the electron beam phase shift.
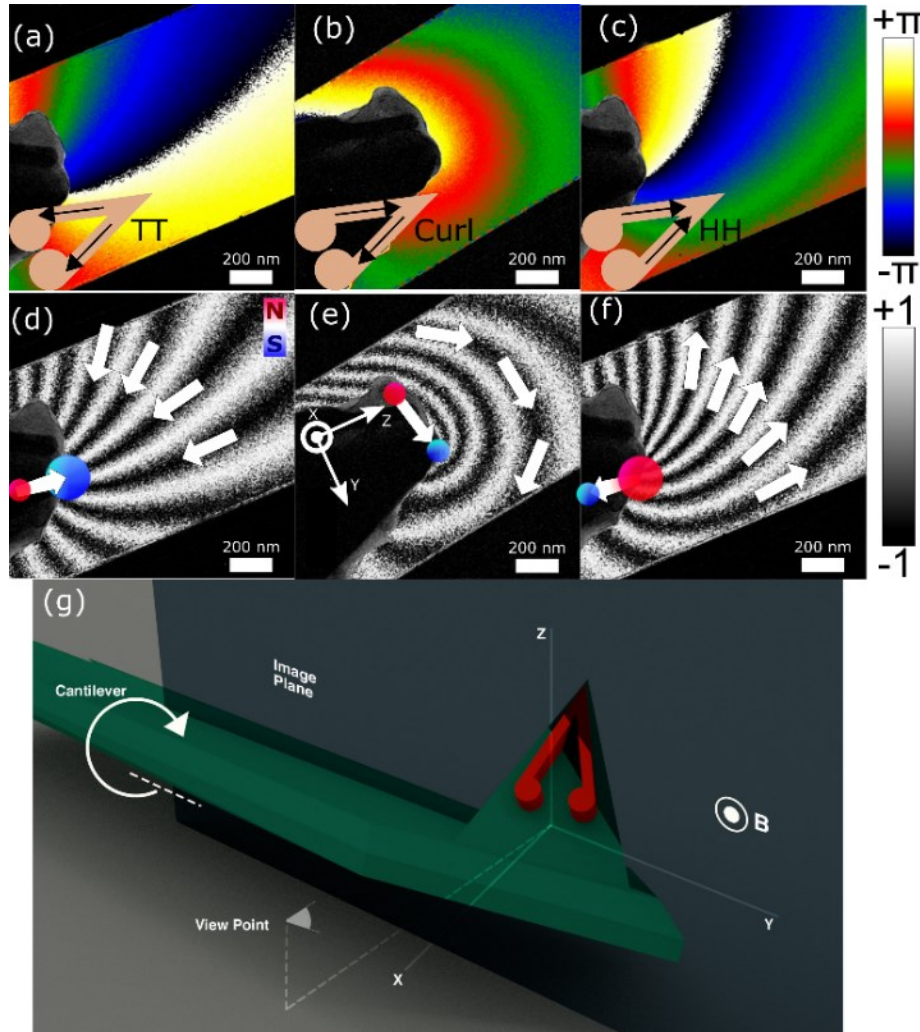
Figure 62. EH results for the DW-probe: (a-c) phase and (d-f) magnetic flux images. (a) and (d) TT configuration, (b) and (e) curl state. (c) and (f) HH state configuration (i.e. a DW trapped at the corner). Schematics in (d-f) represent dipole approximation of the stray field, with arrows indicating field direction and size of the circles the relative strength of the magnetic poles. (g) Schematics of the relative orientation of the probe and the image plane: the probe's pyramid is oriented along + z-axis while during the imaging (i.e. images (a-f)); cantilever is rotated as shown by the white arrow to be oriented along the - x-axis when the magnetic field is swept to change the magnetization state of the probe. The axis shown in (e) are the same as in (g).

To identify all the stable magnetization states, the DW-probe is placed inside of the TEM with the pyramid along the $+z$-axis to perform EH (schematically shown in Figure 62(g)). Then it is rotated to align the pyramid along the $+x$-axis, while a saturation field is applied towards $-x$-axis [Figure 62(g)]. According to the probe position inside the TEM, such condition should induce a TT DW. At $B = 0$ condition, the DW-probe is tilted back with the pyramid pointing at 45º in respect to both x and z-axes, as depicted in Figure 62(g). In such configuration, the applied magnetic field was progressively increased until each representative magnetic state was obtained. However, whenever a change in the magnetization was detected, the magnetic field was reduced to zero and the probe was tilted with the apex pointing towards $+z$-axis in order to image the state at remanence.

The different magnetization states identified are shown in Figure 62 and correspond to the TT [Figure 62(a) and Figure 62(d)] and HH [Figure 62(b) and Figure 62(e)] configurations, as well as the curl states [Figure 62(c) and Figure 62(f)] (only one curl state is shown). The two states referred to as TT and HH generate a strong stray field emanating from the apex, which corresponds to a monopole-like magnetic charge localized at the corner of the V-shaped nanostructure (i.e. equivalent charge distributions schematically shown as 'north pole' in red for HH and 'south pole' in blue for TT configurations, with size of the circles indicating which pole dominates, and arrows pointing along the field direction). The curl state [Figure 62(c) and Figure 62(f)] produces field lines that close around the apex of the probe, which corresponds to a small magnetic dipole aligned perpendicular to the V-structure bisector. The stray field images shown in Figure 62 agree with the interpretation of the V-shaped nanostructure acting as a four-state device where two states have a DW pinned at the apex of the probe with strong stray field, and two states without DW and much weaker stray field.

8.3. Numerical simulations

The stray field distribution, and the presence of a DW, was further corroborated by micromagnetic simulations of the V-shape (shown in Figure 63) using of OOMMF[258]. The parameters used were the standard for Py, i.e. cell size of $5 \times 5 \times 5$ nm³, $Ms = 800 \times 10^3$ A/m, $A = 13 \times 10^{-12}$ J/m, $k = 0$.

The results obtained at remanence after applying a saturating magnetic field either parallel or perpendicular to the V-shape bisector are shown in Figure 63. The state in Figure 63(a) and Figure 63 (c) corresponds to HH state, with a DW pinned at the corner of the nanostructure and a strong stray field emanating from the corner, where the spatial distribution is similar to the field shown in Figure 62(f). The state shown in Figure 63(b) and Figure 63(e) corresponds to

the curl state, where the field lines close across the corner similarly to Figure 62(e).

Thus, the OOMMF simulations displayed in Figure 63 are in good agreement with the EH results (Figure 62). Both results confirm the presence of a DW at the corner of the V-shaped nanostructure for two of the stable states, producing a high, monopole-like, stray magnetic field (i.e. TT and HH states). Consequently, both experimental and modelling methods are also in agreement regarding the two curl states, which do not incorporate a DW and have a dipolar-like stray field, representing a close flux around the probe with a significant fraction of in-plane magnetization component.
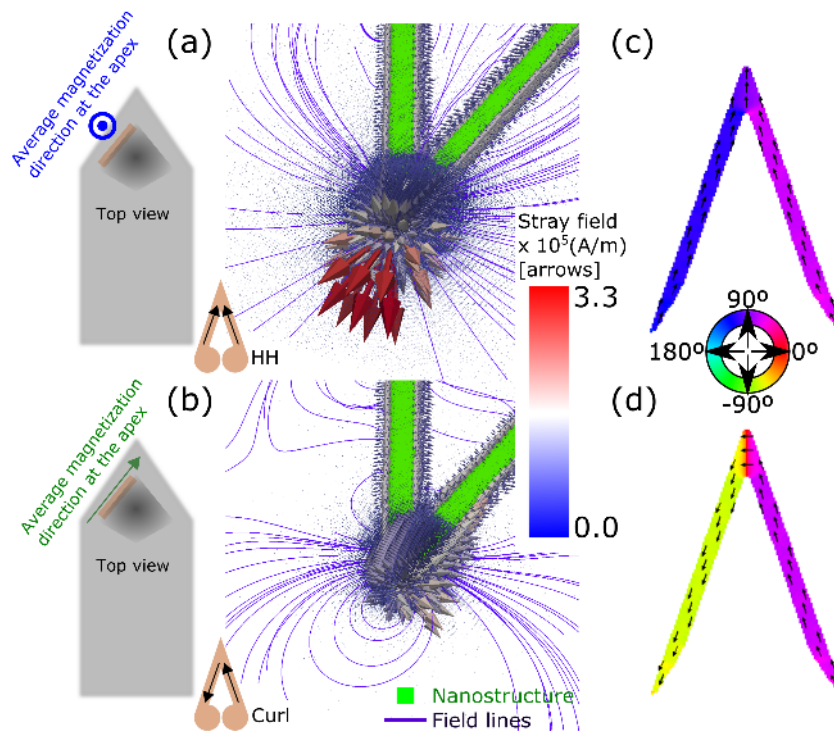
Figure 63. Numerical simulations of the stray field created by the V-shaped magnetic nanostructure when magnetization is in HH (a) or curl state (b). Left schematics show direction of the stray field when performing MFM imaging with the probe. (c) and (d) show the magnetization inside of the V-shape nanostructure in HH (c) or curl state (d). The arrows indicate the direction of the magnetization and the colours - the angular orientation.

8.4. DW-probe switching magnetization while scanning

To compare the DW-probe with two commercial probes with similar mechanical properties (Table 3), a non-modified NANOSENSORS™ PPP-MFMR AFM probe[255], and a low moment NT-MDT MFM_LM probe[259] are used along the DW-probe to scan the same area of a floppy disk.

A standard two-pass MFM mode with a lift height of 40 nm is used, where the oscillation

amplitudes of all the three probes were adjusted to be the same (14 nm). All the probes were exposed to the north pole of a permanent magnet prior to the scan. The non-modified NANOSENSOR™ PPP-MFMR AFM probe shows the greatest phase contrast (~ 7.3º), whilst the low moment NT-MDT MFM_LM probe has the smallest contrast difference (~ 1.3 º), see Figure 64(a). The DW-probe in the TT state has an intermediate contrast (~ 2.13 º). This demonstrates that despite having much less magnetic material than the non-modified probe, the localization of the magnetic moment at the probe apex enabled by the localization of a DW at the corner of the V-shaped nanostructure results in a sizeable interaction between probe and sample magnetization (via its stray field), larger than the one occurring with a low moment probe.

Table 3. Mechanical properties of the MFM probes compared.

PROBE	RESONANT FREQUENCY, f_0 (KHZ)	Q-FACTOR	SPRING CONSTANT k (N/M)
DW-PROBE	72.245	205	3.63
NANOSENSORS™ PPP-MFMR AFM	67.346	201	4.00
NT-MDT MFM_LM	65.033	195	2.46

To demonstrate different states of the probe, Figure 64(b) shows MFM phase images from a floppy disk scanned with the DW-probe, while an out-of-plane magnetic field of varying intensity is being applied:

0 μm < y < 15 μm. A magnetic field of B = 70 mT is applied at y = 0 μm (i.e. a TT state is induced in the V-shaped nanostructure). Then the field is reduced step-wise to 0 mT. No change on the state of the DW-probe or in the floppy disk bits can be seen through this process in Figure 64(b), nor in the profiles shown in Figure 64(c).

15 μm < y < 20 μm. The applied field, B = -40 mT, nucleates the curl state, reducing and inverting the signal amplitude (i.e. -0.5 times the signal at y = 0 μm). This can be seen by following the red and blue dotted lines in Figure 64(b) and the corresponding profiles in Figure 64(c).

20 μm < y < 35 μm. At y = 20 μm a magnetic field of B = -70 mT nucleates a HH state, opposite to the initial state at y = 0 μm, this can be seen in Figure 64(c) as the red and blue lines have inverted their values in respect to the initial values. Then the field is reduced step-wise to 0 mT.

35 μm < y < 40 μm. An applied magnetic field of B = 40 mT nucleates again switched a curl state, yielding to a MFM signal of much smaller amplitude (again, -0.5 times the amplitude seen in the previous state).

40 μm < y < 60 μm. A saturating field of B = 70 mT, nucleates a TT state, leaving the probe in the same state as at y = 0 μm.
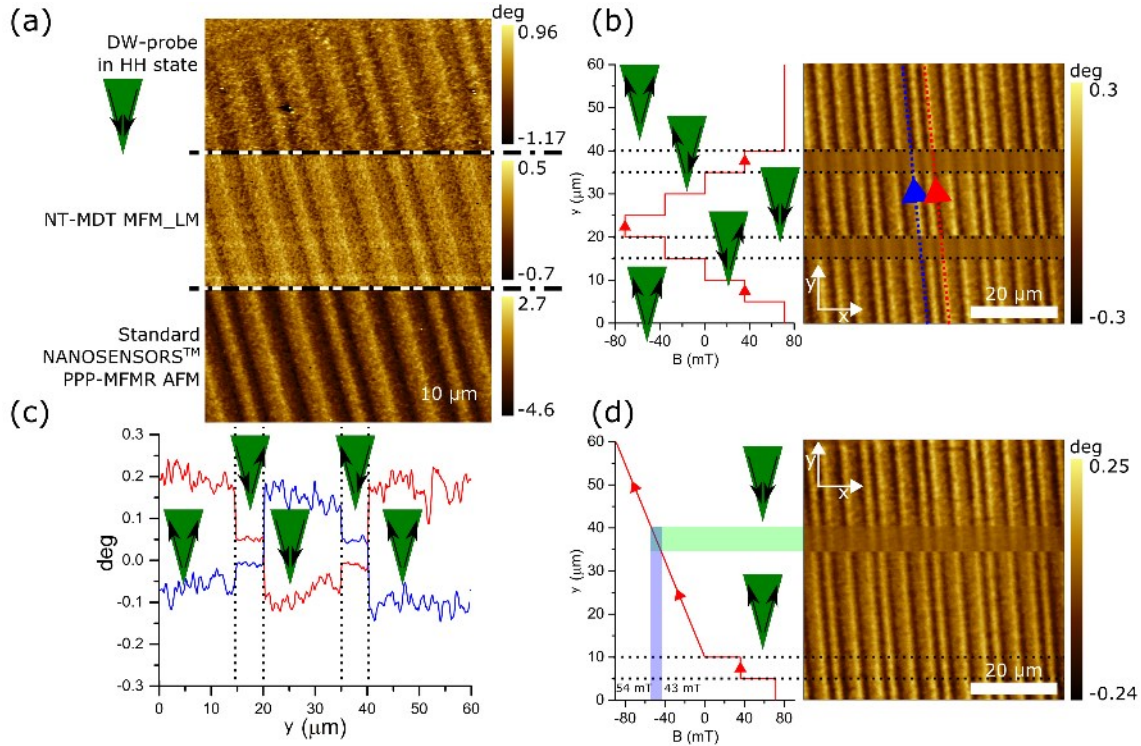
Figure 64. (a) Comparison of 3 MFM probes, during MFM imaging on the same area of a floppy disk with the same lift height (40 nm) and oscillation amplitude (14 nm): top - DW-probe, middle - NT-MDT MFM_LM probe and bottom - NANOSENSORS™ PPP-MFMR AFM probe. (b) and (d) in situ MFM images taken with DW-probe for different applied fields. Scan direction is from bottom to top. The field changes (b) in the step-wise manner to demonstrate different states of the probe and (d) gradually during the scan to extract the probe switching fields. Schematics of the probe states and field evolution is shown on the left hand side in (b) and (d). (c) Profiles along the corresponding red/blue lines in (b).

In order to measure the DW-probe switching fields, an *in situ* MFM image has been obtained, while the magnetic field was continuously swept. First, the probe is saturated at 70 mT at the beginning of the scan, then the field is reduced to 40 and 0 mT in a step-wise manner, Figure 64(d). When the probe is at 10 < y < 60 μm, the field is ramped down gradually. The probe transforms into the curl state at -43 mT and then completely switches into HH state at -54 mT, Figure 64(d). By repeating the cycle several times, we can estimate the field required to change the TT or HH state into a curl state being in the order of 40 mT and that for changing

a curl state to a TT or HH - in the order of 50 mT. This is a relatively large field, which is determined by the shape anisotropy of the V-shaped nanostructure. This filed is also much larger than the stray field generated by the sample (at the probe-sample distance used in the experiment), which is estimated to be smaller than 1 mT[250], [260], [261]. This demonstrates that our DW-probe possesses a large coercivity, which implies a strong stability against external perturbations including the stray field generated by the sample. Therefore, our DW-probe embodies the two desirable characteristics for improving reliability and resolution of MFM measurements, namely: a relatively small, highly localized magnetic moment and a high anisotropy. Moreover, by exploiting stable low and high moment states, it is possible to use these probes in specialized MFM modes such as differential phase imaging, or controlled magnetization MFM[250].

8.5. DW-based MFM

To further compare different types of probes, MFM imaging of a patterned magnetic nanostructure made of Py (25 nm thick) was performed (Figure 65). The chosen nanostructure is part of a Penrose pattern used for e-beam alignment in nanofabrication[262], [263]. This pattern forms a complex domain structure localized in a small area, enabling to compare different probes relatively easy. An approach to compare probes through the real-space probe transfer function and quantitative MFM was recently presented for similar a concept of DW-probes[191].

Topography and MFM images (as taken with the low moment NT-MDT MFM_LM probe) of the Penrose pattern are shown in Figure 65(a) and Figure 65(b), respectively. Then the probe was replaced with the DW-probe and the next set of images was obtained (the probe being in TT and curl states, see Figure 65(c) and Figure 65(d), respectively). After imaging the sample with the DW probe, the commercial NANOSENSORS™ PPP-MFMR probe with the standard magnetic coating was used (Figure 65(e)). It is noteworthy that for both commercial probes, and TT state of the DW-probe, boundaries between the different domains appear as a change in contrast, hence the probes detect orientation of magnetic domains. On the other hand, for the DW-probe in the curl state it is possible to identify DWs, which can be seen as double contrast in Figure 65(d) and (f). Moreover, by further analysing Figure 65(f), two types of DWs are identified: one that has half-sine shape (i.e. one peak); and another one that has the shape of a full-sine (i.e. two peaks, one positive and the other one negative). When this classification is compared with the orientation of the DW-probe during imaging (Figure 65(f)) we identify that the full-sine DWs with two peaks (white doted lines) are perpendicular to the field created by

the DW-probe in the curl state, while the DWs that are parallel to the probe's stray field are seen as a half-sine with only one peak (blue doted lines). This can be interpreted as a dipolar interaction using a simplified magnetic dipolar model.
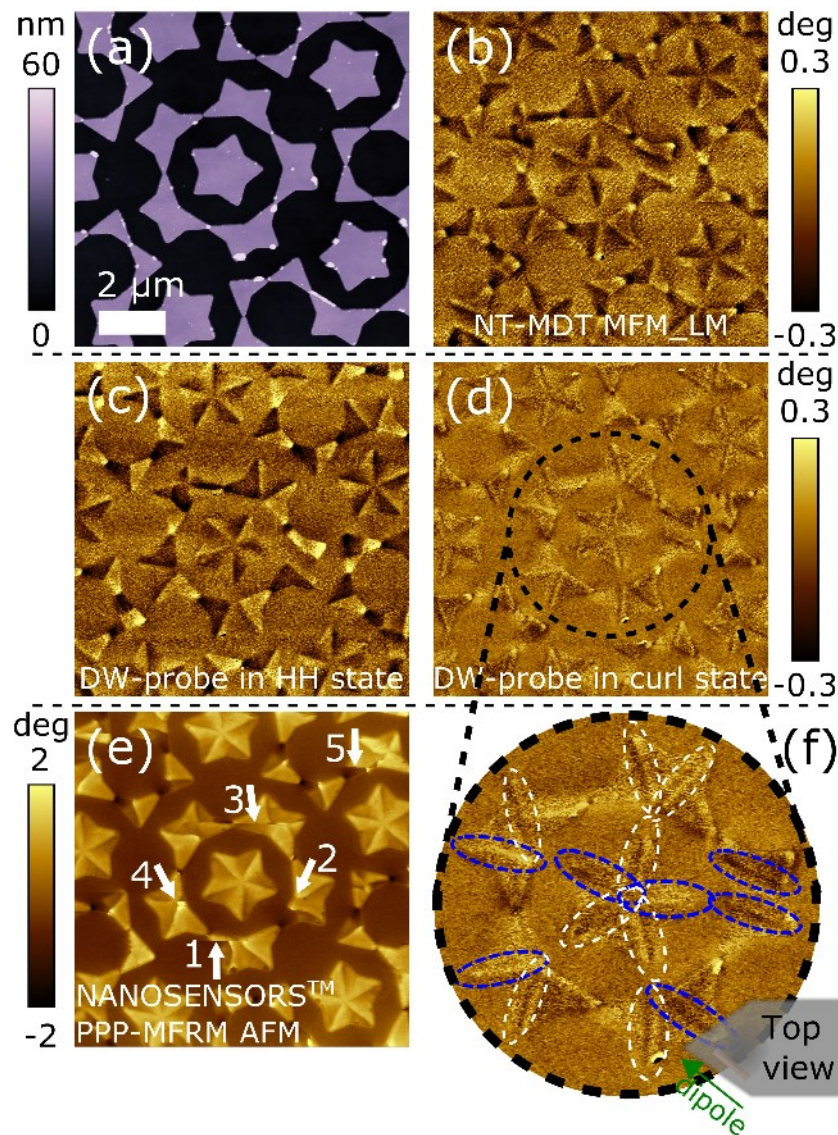
Figure 65. (a) Topography of a small area of a Penrose pattern. MFM image obtained using (b) the low moment NT-MDT MFM_LM probe; (c) - (d) the DW-probe [where (c) TT and (d) curl states] and (e) NANOSENSORS™ PPP-MFMR probe. Numbers in (e) indicate the cases where the probe changes the sample magnetization. (f) Enlarged area of the MFM image obtained with the DW-probe in the curl state: the blue/white contours highlight the single/double (i.e. bright – dark) contrast, respectively. Inset: Orientation of the probe during scanning.

Simulations of dipolar interaction between the DW-probe in the curl state (approximated as a point dipole) and the DWs in the Penrose pattern (approximated as a line of point dipoles) were carried out using a simplified magnetic dipolar model. The curl state was approximated

by two magnetic charges $q_1^{probe} = +1$ and $q_2^{probe} = -1$ separated by 1 arbitrary units (a.u.), and aligned either along x or y-axis (as shown in Figure 66 (d) and (e), respectively). A small tilt of 14º was introduced to take into account the tilting created by the probe holder. The DWs in the Penrose pattern were approximated by 200 +1 and -1 surface charges along the y-axis as illustrated in Figure 66 (d) and (e). Each pair of charges is separated by 0.00125 a.u. and the 200 pairs spanning 10 a.u. along the y-axis. The vertical distance between the dipole representing the probe and the line of dipoles representing the DW is 1.125 a.u. The magnetic force used in the model was:

$$\vec{F} = \sum_{i=1}^{2} \sum_{j=1}^{200} \frac{q_i^{probe} q_j^{sample}}{r_{ij}^2} \hat{r_{ij}} \qquad (32)$$

Figure 66 shows the interaction between an ideal probe represented by an in-plane dipole and the charge accumulation created by the DWs in the Penrose pattern represented by a chain of dipoles. Figure 66(d) and Figure 66(e) show the cases of probe's dipole aligned parallel/perpendicular to surface dipoles respectively. Maps in Figure 66(f) and Figure 66(g) show the force gradient along the z-axis. In the case of the parallel alignment of probe's and surface dipoles, the resulting gradient in the Penrose pattern is characterized mainly by a half-sine curve, whilst in the case of perpendicular alignment, the force gradient demonstrates a full-sine shape. Thereby, our measurements demonstrate that the DW-probe in the curl state has a dipole-like interaction with DWs, and hence is better suited for visualization and studies of DWs in planar structures. Moreover, by combining imaging with HH/TT states with images taken with the curl state, it is possible to extract 3D information about the sample's magnetization, and hence the DW-probe allows for detailed studies of 3D distribution of magnetization on nanoscale.

By further analysing Figure 65(e), the image taken with the commercial NANOSENSORS™ PPP-MFMR probe. It is possible to note that in this case, the change in the amplitude is significantly (i.e. almost an order of magnitude) larger than for both previous probes, due to a stronger interaction between the probe and the sample. This can be seen by comparing the all MFM images in Figure 65. When comparing the MFM images taken with the different probes, we can identify the areas (numbered 1 to 5) in Figure 65(e) where the NANOSENSORS™ PPP-MFMR probe interfered with the domain structure of the sample and altered it. For instance, in the position marked by 1, the boundary between different magnetic domains was an inverted V-shape (Figure 65(b)-(d)), while in Figure 65(e) has a different shape. Thus, we conclude that in addition to being able to image DWs, the DW-probe interferes

less with the sample magnetization than the standard NANOSENSORS™ PPP-MFMR probe.
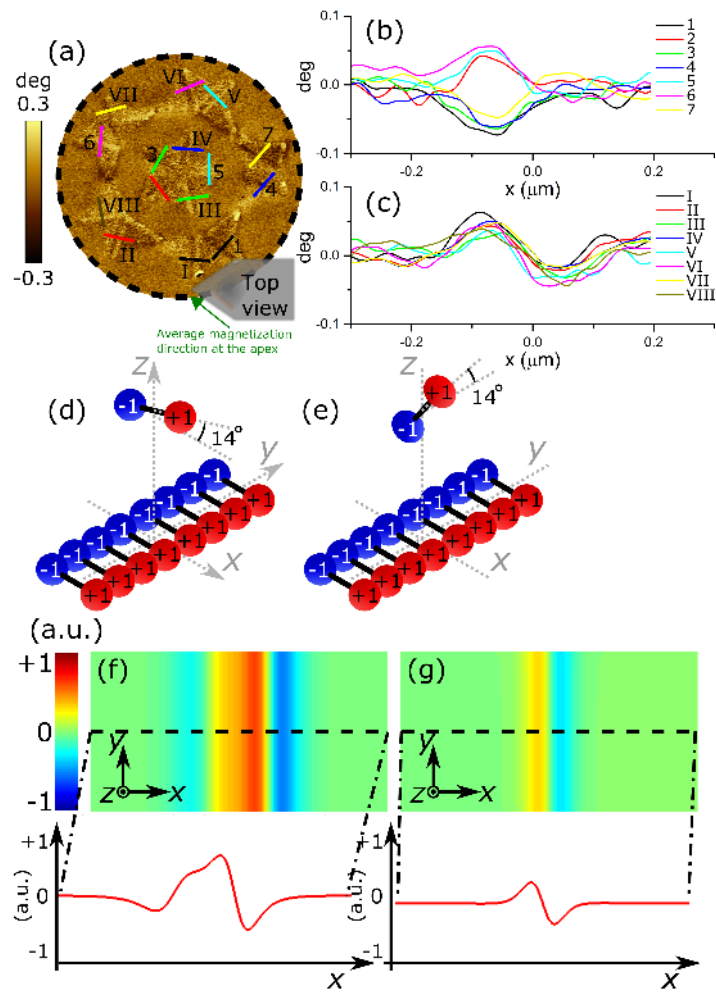
Figure 66 (a) MFM image of a small area of a Penrose pattern taken using the DW-probe in the curl state. Coloured lines indicate profiles shown in (b) and (c). (d) and (e) schematic representation of the probe and surfaces dipole when they are parallel (d) and perpendicular (e) to each other. (f) and (g) simulated maps of the z-component of the force derivative obtained for orientation (d) and € respectively. Red curves in (f) and (g) represent cross-sections of the maps.

8.6. Summary

A commercial MFM probe (NANOSENSOR™ PPP-MFMR AFM) was modified by removing the magnetic coating from the probe and leaving only a V-shaped nanostructure on one of the sides. This magnetic nanostructure possesses four stable magnetic states: two with a DW at the corner of the V-shape, and two states without a DW. EH results and numerical simulations demonstrate that the two DW states generate a strong stray field in the direction of the probe axis (monopole-like), while the 2 states without DW produce much weaker stray field perpendicular to the previous one (dipole-like).

143

In situ MFM imaging demonstrates that the phase contrast achieved with the DW-probe is smaller than the one from a commercial probe with a standard magnetic moment, but higher than the one from a commercial low moment probe. We have also demonstrated that by applying an external magnetic field it is possible to controllably switch magnetization of the DW probe during scanning. The DW probe also has a large coercive field making it stable to image samples with a strong stray field. In addition, while the state with a DW produces a stray field comparable to the one from a non-modified probe, it was shown that the state without DW (curl configuration) produces a much weaker signal. Thus, this probe is controllably bi-stable with high/low stray field, enabling to scan heterogeneous samples with variable coercive field. Using a Penrose pattern as a test magnetic nanostructure, it was shown that the DW probe is able to achieve comparable resolution to the two commercial probes used here, without modifying the magnetization of the sample.

Hence, the DW-probe meets the requirements to overcome the two main limitations of MFM, i.e. demonstrates increase sensitivity and reduce probe's stray field, as the DW-probe has large coercivity induced by the shape anisotropy, a low magnetic moment, and resolution comparable to the non-modified precursor probe. Additionally, the curl state provides information about the 3D structure of DWs inside of the magnetic nanostructure, which is difficult to assess by other conventional techniques.

9 Summary, conclusions, and future outlook

The aim of this work was to investigate effect of local magnetic moments on DWs. This has been achieved by combining MR measurements to track DWs inside of magnetic nanostructures, *in situ* MFM experiments to study magnetization evolution, and by placing MBs near to the DWs to simulate the effect of local magnetic moments.

L-shaped Py nanostructures with different geometries (varying widths from 50 to 400 nm, with/without disks and round/square corner) were tested in order to identify the most reliable conditions for DW pinning/depinning. By combining electrical measurements with micromagnetic simulations, MFM imaging, and an electrical transport model, four stable magnetic states at zero field were identified, and it was demonstrated that they can be tracked by MR measurements and a state-space map. Through comparison of different geometries for the L-shaped nanostructure it was found that square corner devices with disks and narrow arms (i.e. below 200 nm) have the most reliable pinning/depinning mechanism.

Single MB detection was demonstrated by the shift of the DW depinning field produced by immobilised MBs (superparamagnetic beads MyOne^{TM}) placed on top of the L-shaped devices corner. It was found that only devices with $w < 200$ nm were able to detect the presence of the MB. The average shift in the depinning field observed was ~ 5 mT. In addition, it was found that DW depinning occurs through two different mechanisms in the L-shaped devices. For positive angles (i.e. if one arm of the L-shape device is placed at zero degrees and the other at 90º then positive angles are 0-90 and 180-270) the DW at the corner does not move away from the corner and thus the presence of the MB does not affect the depinning field. For negative angles, the DW at the corner does move during the depinning and it can sense the presence of the MB.

mSGM with modified probes allowed to estimate the sensing volume of the DW-based L-shaped nanosensors. The probes were modified by attaching an NdFeB MB of 1.6 μm in diameter, and used to estimate the volume above the nanostructures where the DW shape is affected by the MB. This sensing volume was estimated as a cone of about 1.2 μm in height by 800 nm diameter of the base for L-shaped devices with $w = 75$ nm. With this technique we outlined a way of comparing different sensors using the same MB, or different MBs against the same sensor. Moreover, the ability to repeatable place a MB on the same position in respect to a sensor, allows improving the design of microfluidic channels or magnetophoretic devices that will guide MBs towards the sensor.

Transversal MR measurements on hybrid junctions (Py/Au) demonstrated that changes in resistance due to the PHE can be used to track magnetization in simple magnetic nanostructures. Moreover, it was observed that when compared to AMR, PHE provides larger changes in resistance. Thus, PHE represents an alternative to AMR when tracking DWs in magnetic nanostructures. In addition, since hybrid junctions show sensitivity to external magnetic fields, $\sim 0.1\ \Omega/T$, they were tested as single MB detectors. The test was carried out with mSGM using modified probes. The results demonstrated detection and a sensing volume similar to that produced by DW's in L-shaped nanostructures of similar width.

The effect of local magnetic fields on LSVs was tested using a CoFeB LSV and mSGM with modified probes. Since the spin diffusion on the CoFeB was suppressed by the Ta channel, it was possible to evaluate the effect of the local fields in both injector and detector through AHE and ANE respectively. Moreover, during this study we established a procedure to measure the stray field produced by the modified probe by monitoring the effect of the probe on the injector. Comparison between the measured stray field and that calculated using the approximation of a uniformly magnetized sphere agrees on the magnetic field magnitude and its decay.

DW-probes designed as an MFM probe for hybrid samples with low/high magnetization were studied and compared against standard probes. The results demonstrate that the DW-probes interact with the sample as a low moment probe but with high coercivity, and thus providing additional stability when scanning over samples with high stray field. Moreover, it was shown that the probes possess a state with no DW at the apex, and in that configuration it is possible to extract information about the in-plane component of the stray field created by the sample.

Overall, the results presented here demonstrate the potential of DW-based sensors for single MB detection. In particular, we outlined the steps necessary to characterize such devices and evaluate their performance. The mSGM experiments performed with modified probes are of particular importance, since they allow direct comparison of different nanosensors or different types of MBs. Through the process, we also found a way of measuring the stray field from MFM probes, demonstrating the importance of MFM as a qualitative tool.

Future outlook | Silicon-based electronics is reaching the theoretical limit in terms of miniaturization and speed. That's why the current research trends are now looking towards many potential solutions, including 3D structures, organic devices, graphene,

superconductivity… and also magnetic devices. Although silicon-based devices got much smaller than the magnetic counterpart, magnetism has a real advantage when it comes to 3D structures, because possibility of aligning the magnetization towards specific directions, combined with the low power consumption, makes them ideal to take advantage of 3D fabrication.

The results presented in this thesis serve as a tool box for DW-based devices, and they can be used in both biomedical and logical/memory devices. However, it is important to expand this work to search different magnetic materials, particularly interesting are the PMM, which present very small DWs and can be read out by either AHE or ANE.

The work on biomedicine points towards functionalization of the surface of ferromagnetic nanostructures, so the presence of certain biological agents will allow MB to get attached to the surface affecting the pinning/depinning of DWs. In particular, manipulation and detection of MBs is of great interest. Such devices will combine most of the ideas studied here and tools developed by other groups, e.g. tracks for moving DWs, electrical contacts for MR measurements, and microfluidic channels.

These are only a few examples of possible lines of work. The work presented here can be used with many more applications, including live cell manipulation, environmental sensors, radiofrequency generators, spintronic devices, and many more…

Bibliography

[1]   M. Hejazian, W. Li, and N.-T. Nguyen, "Lab on a chip for continuous-flow magnetic cell separation," *Lab Chip*, vol. 15, no. 4, pp. 959–970, 2015.

[2]   J. Struckmeier, R. Wahl, M. Leuschner, J. Nunes, H. Janovjak, U. Geisler, G. Hofmann, T. Jähnke, and D. J. Müller, "Fully automated single-molecule force spectroscopy for screening applications.," *Nanotechnology*, vol. 19, no. 38, p. 384020, 2008.

[3]   A. Chen, T. Byvank, W.-J. Chang, A. Bharde, G. Vieira, B. L. Miller, J. J. Chalmers, R. Bashir, and R. Sooryakumar, "On-chip magnetic separation and encapsulation of cells in droplets," *Lab Chip*, vol. 13, no. 6, pp. 1172–1181, 2013.

[4]   M. Carminati, G. Ferrari, S. U. Kwon, M. Sampietro, M. Monticelli, A. Torti, D. Petti, E. Albisetti, M. Cantoni, and R. Bertacco, "Towards the impedimetric tracking of single magnetically trailed microparticles," in *2014 IEEE 11th International Multi-Conference on Systems, Signals & Devices (SSD14)*, 2014, pp. 1–5.

[5]   H. C. Tekin and M. a M. Gijs, "Ultrasensitive protein detection: a case for microfluidic magnetic bead-based assays.," *Lab Chip*, vol. 13, no. 24, pp. 4711–39, 2013.

[6]   Y. Pan, X. Du, F. Zhao, and B. Xu, "Magnetic nanoparticles for the manipulation of proteins and cells.," *Chem. Soc. Rev.*, vol. 41, no. 7, pp. 2912–42, Apr. 2012.

[7]   Q. A. Pankhurst, N. T. K. Thanh, S. K. Jones, and J. Dobson, "Progress in applications of magnetic nanoparticles in biomedicine," *J. Phys. D. Appl. Phys.*, vol. 42, no. 22, p. 224001, Nov. 2009.

[8]   M. Monticelli, D. V. Conca, E. Albisetti, A. Torti, P. P. Sharma, G. Kidiyoor, S. Barozzi, D. Parazzoli, P. Ciarletta, M. Lupi, D. Petti, and R. Bertacco, "Magnetic domain wall tweezers: a new tool for mechanobiology studies on individual target cells," *Lab Chip*, vol. 16, no. 15, pp. 2882–2890, 2016.

[9]   B. Lim, P. Vavassori, R. Sooryakumar, and C. Kim, "Nano/micro-scale magnetophoretic devices for biomedical applications," *J. Phys. D. Appl. Phys.*, vol. 50, no. 3, p. 33002, 2017.

[10]   A. Barbot, D. Decanini, and G. Hwang, "On-chip Microfluidic Multimodal Swimmer toward 3D Navigation.," *Sci. Rep.*, vol. 6, no. January, p. 19041, Jan. 2016.

[11] M. Medina-Sánchez, L. Schwarz, A. K. Meyer, F. Hebenstreit, and O. G. Schmidt, "Cellular Cargo Delivery: Toward Assisted Fertilization by Sperm-Carrying Micromotors," *Nano Lett.*, vol. 16, no. 1, pp. 555–561, Jan. 2016.

[12] M. Donolato, M. Gobbi, P. Vavassori, M. Leone, M. Cantoni, V. Metlushko, B. Ilic, M. Zhang, S. X. Wang, and R. Bertacco, "Nanosized corners for trapping and detecting magnetic nanoparticles," *Nanotechnology*, vol. 20, no. 38, p. 385501, Sep. 2009.

[13] G. Vieira, A. Chen, T. Henighan, J. Lucy, F. Y. Yang, and R. Sooryakumar, "Transport of magnetic microparticles via tunable stationary magnetic traps in patterned wires," *Phys. Rev. B*, vol. 85, no. 17, p. 174440, May 2012.

[14] R. Bertacco, M. Donolato, M. Gobbi, M. Cantoni, D. Petti, S. Brivio, V. Metlushko, B. Ilic, and P. Vavassori, "On-chip manipulation of single magnetic nano- particles via domain walls conduits," vol. 8, pp. 485–486, 2009.

[15] M. Monticelli, A. Torti, M. Cantoni, D. Petti, E. Albisetti, A. Manzin, E. Guerriero, R. Sordan, G. Gervasoni, M. Carminati, G. Ferrari, M. Sampietro, and R. Bertacco, "On-Chip Magnetic Platform for Single-Particle Manipulation with Integrated Electrical Feedback," *Small*, vol. 12, no. 7, pp. 921–929, Feb. 2016.

[16] N. Locatelli, V. Cros, and J. Grollier, "Spin-torque building blocks," *Nat. Mater.*, vol. 13, no. 1, pp. 11–20, 2013.

[17] S. Blundell, *Magnetism in Condensed Matter*. Oxford University Press, 2007.

[18] S. Szczeniowski and L. Wojtczak, "Band Model of Ferromagnetic Thin Films," *J. Appl. Phys.*, vol. 39, no. 2, pp. 1377–1378, Feb. 1968.

[19] A. Hubert and R. Schafer, *Magnetic Domains - The Analysis of Magnetic Microstructures*, 3rd ed. Springer, 2009.

[20] A. Morrish, *The physical principles of magnetism. Wiley series on the science and technology of materials*. Wiley, 1965.

[21] W. F. Brown, *Micromagnetics*. Interscience, 1962.

[22] O. Bottauscio, M. Chiampi, and A. Manzin, "A Finite Element Procedure for Dynamic Micromagnetic Computations," *IEEE Trans. Magn.*, vol. 44, no. 11, pp. 3149–3152,

Nov. 2008.

[23]   A. Manzin and O. Bottauscio, "A Micromagnetic Solver for Large-Scale Patterned Media Based on Non-Structured Meshing," *IEEE Trans. Magn.*, vol. 48, no. 11, pp. 2789–2792, Nov. 2012.

[24]   A. Manzin and O. Bottauscio, "A Coupled Multipole Expansion — Finite Element Approach for Dynamic," *IEEE Trans. Magn.*, vol. 45, no. 11, pp. 5208–5211, 2009.

[25]   O. Bottauscio and A. Manzin, "Parallelized micromagnetic solver for the efficient simulation of large patterned magnetic nanostructures," *J. Appl. Phys.*, vol. 115, no. 17, p. 17D122, May 2014.

[26]   O. Bottauscio and A. Manzin, "Critical Aspects in Micromagnetic Computation of Hysteresis Loops of Nanometer Particles," *IEEE Trans. Magn.*, vol. 45, no. 11, pp. 5204–5207, Nov. 2009.

[27]   A. Manzin and O. Bottauscio, "Connections between numerical behavior and physical parameters in the micromagnetic computation of static hysteresis loops," *J. Appl. Phys.*, vol. 108, no. 9, p. 93917, 2010.

[28]   O. Bottauscio, M. Chiampi, and A. Manzin, "Multiscale Finite Element Solution of the Exchange Term in Micromagnetic Analysis of Large Bodies," *IEEE Trans. Magn.*, vol. 45, no. 11, pp. 5200–5203, Nov. 2009.

[29]   O. Bottauscio and A. Manzin, "Spatial Reconstruction of Exchange Field Interactions With a Finite Difference Scheme Based on Unstructured Meshes," *IEEE Trans. Magn.*, vol. 48, no. 11, pp. 3250–3253, 2012.

[30]   H. Corte-León, P. Krzysteczko, F. Marchi, J.-F. Motte, A. Manzin, H. W. Schumacher, V. Antonov, and O. Kazakova, "Detection of a magnetic bead by hybrid nanodevices using scanning gate microscopy," *AIP Adv.*, vol. 6, no. 5, p. 56502, May 2016.

[31]   A. Manzin, V. Nabaei, H. Corte-León, O. Kazakova, P. Krzysteczko, H. W. Schumacher, H. Corte-Leon, O. Kazakova, P. Krzysteczko, and H. W. Schumacher, "Modeling of anisotropic magnetoresistance properties of permalloy nanostructures," *IEEE Trans. Magn.*, vol. 50, no. 4, pp. 1–4, Apr. 2014.

[32]   H. Corte-León, V. Nabaei, A. Manzin, J. Fletcher, P. Krzysteczko, H. W. Schumacher, and O. Kazakova, "Anisotropic Magnetoresistance State Space of Permalloy

Nanowires with Domain Wall Pinning Geometry," *Sci. Rep.*, vol. 4, p. 6045, Aug. 2014.

[33]   A. P. Malozemoff and J. Watson, "Anisotropic magnetoresistance," vol. 34, no. 3, 1986.

[34]   A. Fert and I. A. Campbell, "Two-Current Conduction in Nickel," *Phys. Rev. Lett.*, vol. 21, no. 16, pp. 1190–1192, Oct. 1968.

[35]   P. M. Levy and S. Zhang, "Resistivity due to Domain Wall Scattering," *Phys. Rev. Lett.*, vol. 79, no. 25, pp. 5110–5113, Dec. 1997.

[36]   L. Thomas, B. Hughes, C. Rettner, and S. S. P. Parkin, "Racetrack Memory: A high-performance, low-cost, non-volatile memory based on magnetic domain walls," in *2011 International Electron Devices Meeting*, 2011, p. 24.2.1-24.2.4.

[37]   D. A. Allwood, G. Xiong, C. C. Faulkner, D. Atkinson, D. Petit, and R. P. Cowburn, "Magnetic domain-wall logic.," *Science*, vol. 309, no. 5741, pp. 1688–92, Sep. 2005.

[38]   A. Torti, V. Mondiali, A. Cattoni, M. Donolato, E. Albisetti, A. M. Haghiri-Gosnet, P. Vavassori, and R. Bertacco, "Single particle demultiplexer based on domain wall conduits," *Appl. Phys. Lett.*, vol. 101, no. 14, p. 142405, 2012.

[39]   M. Donolato, M. Gobbi, P. Vavassori, M. Cantoni, V. Metlushko, B. Ilic, M. Zhang, S. X. Wang, M. F. Hansen, and R. Bertacco, "Detection of a single synthetic antiferromagnetic nanoparticle with an AMR nanostructure: Comparison between simulations and experiments," *J. Phys. Conf. Ser.*, vol. 200, no. 12, Jan. 2010.

[40]   S. S. P. Parkin, M. Hayashi, and L. Thomas, "Magnetic domain-wall racetrack memory.," *Science*, vol. 320, no. 5873, pp. 190–4, Apr. 2008.

[41]   S. Parkin and S.-H. Yang, "Memory on the racetrack," *Nat. Nanotechnol.*, vol. 10, no. 3, pp. 195–198, Mar. 2015.

[42]   X. Jiang, L. Thomas, R. Moriya, M. Hayashi, B. Bergman, C. Rettner, and S. S. P. Parkin, "Enhanced stochasticity of domain wall motion in magnetic racetracks due to dynamic pinning.," *Nat. Commun.*, vol. 1, no. 3, p. 25, Jan. 2010.

[43]   M. Muñoz and J. L. Prieto, "Suppression of the intrinsic stochastic pinning of domain walls in magnetic nanostripes.," *Nat. Commun.*, vol. 2, no. May, p. 562, Jan. 2011.

[44] M. Hayashi, L. Thomas, R. Moriya, C. Rettner, and S. S. P. Parkin, "Current-controlled magnetic domain-wall nanowire shift register.," *Science*, vol. 320, no. 5873, pp. 209–11, Apr. 2008.

[45] X. Jiang, L. Thomas, R. Moriya, and S. S. P. Parkin, "Discrete domain wall positioning due to pinning in current driven motion along nanowires.," *Nano Lett.*, vol. 11, no. 1, pp. 96–100, Jan. 2011.

[46] Y. Jang, M. D. Mascaro, G. S. D. Beach, and C. a. Ross, "Current-driven domain wall motion in heterostructured ferromagnetic nanowires," *Appl. Phys. Lett.*, vol. 100, no. 11, p. 112401, 2012.

[47] J. Curiale, A. Lemaître, T. Niazi, G. Faini, and V. Jeudy, "Joule heating and current-induced domain wall motion," *J. Appl. Phys.*, vol. 112, no. 10, p. 103922, Nov. 2012.

[48] T. Koyama, K. Ueda, K.-J. Kim, Y. Yoshimura, D. Chiba, K. Yamada, J.-P. Jamet, a Mougin, a Thiaville, S. Mizukami, S. Fukami, N. Ishiwata, Y. Nakatani, H. Kohno, K. Kobayashi, and T. Ono, "Current-induced magnetic domain wall motion below intrinsic threshold triggered by Walker breakdown.," *Nat. Nanotechnol.*, vol. 7, no. 10, pp. 635–9, Oct. 2012.

[49] P. J. Metaxas, J. Sampaio, A. Chanthbouala, R. Matsumoto, A. Anane, A. Fert, K. a Zvezdin, K. Yakushiji, H. Kubota, A. Fukushima, S. Yuasa, K. Nishimura, Y. Nagamine, H. Maehara, K. Tsunekawa, V. Cros, and J. Grollier, "High domain wall velocities via spin transfer torque using vertical current injection.," *Sci. Rep.*, vol. 3, p. 1829, Jan. 2013.

[50] Y. P. Ivanov, A. Chuvilin, L. G. Vivas, J. Kosel, O. Chubykalo-Fesenko, and M. Vázquez, "Single crystalline cylindrical nanowires – toward dense 3D arrays of magnetic vortices," *Sci. Rep.*, vol. 6, no. March, p. 23844, Mar. 2016.

[51] E. Berganza, C. Bran, M. Jaafar, M. Vázquez, and A. Asenjo, "Domain wall pinning in FeCoCu bamboo-like nanowires," *Sci. Rep.*, vol. 6, no. 1, p. 29702, Sep. 2016.

[52] Y. P. Ivanov, A. Chuvilin, S. Lopatin, and J. Kosel, "Modulated Magnetic Nanowires for Controlling Domain Wall Motion: Toward 3D Magnetic Memories," *ACS Nano*, vol. 10, no. 5, pp. 5326–5332, May 2016.

[53] Y. P. Ivanov, A. Alfadhel, M. Alnassar, J. E. Perez, M. Vazquez, A. Chuvilin, and J.

Kosel, "Tunable magnetic nanowires for biomedical and harsh environment applications," *Sci. Rep.*, vol. 6, no. April, p. 24189, Apr. 2016.

[54] L. A. Rodríguez, C. Bran, D. Reyes, E. Berganza, M. Vázquez, C. Gatel, E. Snoeck, and A. Asenjo, "Quantitative Nanoscale Magnetic Study of Isolated Diameter-Modulated FeCoCu Nanowires," *ACS Nano*, vol. 10, no. 10, pp. 9669–9678, Oct. 2016.

[55] E. M. Palmero, C. Bran, R. P. del Real, and M. Vázquez, "Vortex domain wall propagation in periodically modulated diameter FeCoCu nanowire as determined by the magneto-optical Kerr effect," *Nanotechnology*, vol. 26, no. 46, p. 461001, 2015.

[56] R. Hertel, "Ultrafast domain wall dynamics in magnetic nanotubes and nanowires," *J. Phys. Condens. Matter*, vol. 28, no. 48, p. 483002, 2016.

[57] M. Yan, C. Andreas, A. Kákay, F. García-Sánchez, and R. Hertel, "Fast domain wall dynamics in magnetic nanotubes: Suppression of Walker breakdown and Cherenkov-like spin wave emission," *Appl. Phys. Lett.*, vol. 99, no. 12, pp. 1–4, 2011.

[58] A. Singh and A. Ghosh, "Domain-wall creep driven by spin torque in nanoscale ferromagnetic cylinders," *Phys. Rev. B - Condens. Matter Mater. Phys.*, vol. 84, no. 6, pp. 10–13, 2011.

[59] H. Mohammed, E. V. Vidal, Y. P. Ivanov, and J. Kosel, "Magnetotransport Measurements of Domain Wall Propagation in Individual Multisegmented Cylindrical Nanowires," *IEEE Trans. Magn.*, vol. 52, no. 7, 2016.

[60] Ó. Iglesias-Freire, C. Bran, E. Berganza, I. Mínguez-Bacho, C. Magén, M. Vázquez, and A. Asenjo, "Spin configuration in isolated FeCoCu nanowires modulated in diameter," *Nanotechnology*, vol. 26, no. 39, p. 395702, Oct. 2015.

[61] X. Zhu, D. a. Allwood, G. Xiong, R. P. Cowburn, and P. Grütter, "Spatially resolved observation of domain-wall propagation in a submicron ferromagnetic NOT-gate," *Appl. Phys. Lett.*, vol. 87, p. 62503, 2005.

[62] D. A. Allwood, G. Xiong, M. D. Cooke, C. C. Faulkner, D. Atkinson, N. Vernier, and R. P. Cowburn, "Submicrometer ferromagnetic NOT gate and shift register.," *Science*, vol. 296, no. 5575, pp. 2003–6, Jun. 2002.

[63] H. T. Zeng, D. Read, L. O'Brien, J. Sampaio, E. R. Lewis, D. Petit, and R. P.

Cowburn, "Asymmetric magnetic NOT gate and shift registers for high density data storage," *Appl. Phys. Lett.*, vol. 96, no. 26, p. 262510, 2010.

[64]   D. A. Allwood, G. Xiong, and R. P. Cowburn, "Magnetic domain wall serial-in parallel-out shift register," *Appl. Phys. Lett.*, vol. 89, no. 102504, pp. 8–11, 2006.

[65]   L. O'Brien, D. E. Read, H. T. Zeng, E. R. Lewis, D. Petit, and R. P. Cowburn, "Bidirectional magnetic nanowire shift register," *Appl. Phys. Lett.*, vol. 95, no. 23, 2009.

[66]   D. Ilgaz, J. Nievendick, L. Heyne, D. Backes, J. Rhensius, T. a. Moore, M. Á. Niño, A. Locatelli, T. O. Menteş, A. v. Schmidsfeld, A. v. Bieren, S. Krzyk, L. J. Heyderman, and M. Kläui, "Domain-Wall Depinning Assisted by Pure Spin Currents," *Phys. Rev. Lett.*, vol. 105, no. 7, p. 76601, Aug. 2010.

[67]   Y. Wang, H. Yu, L. Ni, G.-B. Huang, M. Yan, C. Weng, W. Yang, and J. Zhao, "An Energy-efficient Nonvolatile In-memory Computing Architecture for Extreme Learning Machine by Domain-wall Nanowire Devices," *IEEE Trans. Nanotechnol.*, no. c, pp. 1–1, 2015.

[68]   A. Vahid, G. Mappouras, D. J. Sorin, and R. Calderbank, "Correcting Two Deletions and Insertions in Racetrack Memory," pp. 1–8, Jan. 2017.

[69]   C. H. Marrows, "Spin-polarised currents and magnetic domain walls," *Adv. Phys.*, vol. 54, no. 8, pp. 585–713, Dec. 2005.

[70]   M. Johnson, "Spin injection in metals and semiconductors," *Semicond. Sci. Technol.*, vol. 17, no. 4, pp. 298–309, Apr. 2002.

[71]   P. Sethi, C. Murapaka, G. J. Lim, and W. S. Lew, "In-plane current induced domain wall nucleation and its stochasticity in perpendicular magnetic anisotropy Hall cross structures," *Appl. Phys. Lett.*, vol. 107, no. 19, p. 192401, Nov. 2015.

[72]   B. N. Filippov, M. N. Dubovik, and L. G. Korzunin, "Spin polarized current controlled dynamics of domain walls in magnetic films with in-plane anisotropy," *Tech. Phys.*, vol. 61, no. 6, pp. 904–912, Jun. 2016.

[73]   A. Yamaguchi, S. Nasu, H. Tanigawa, T. Ono, K. Miyake, K. Mibu, and T. Shinjo, "Effect of Joule heating in current-driven domain wall motion," *Appl. Phys. Lett.*, vol. 86, no. 1, p. 12511, Jan. 2005.

[74]   S. Lepadatu, a. Vanhaverbeke, D. Atkinson, R. Allenspach, and C. Marrows, "Dependence of Domain-Wall Depinning Threshold Current on Pinning Profile," *Phys. Rev. Lett.*, vol. 102, no. 12, p. 127203, Mar. 2009.

[75]   C. Kurniawan and D. Djuhana, "Current driven domain wall depinning in notched Permalloy nanowires," 2016, p. 20001.

[76]   A. Pfeiffer, R. M. Reeve, M. Voto, W. Savero-Torres, N. Richter, L. Vila, J.-P. Attane, L. Lopez-Diaz, and M. Kläui, "Geometrical control of pure spin current induced domain wall depinning," *J. Phys. Condens. Matter*, vol. 29, no. 8, p. 85802, 2017.

[77]   W. Savero Torres, V. T. Pham, G. Zahnd, P. Laczkowski, V. D. Nguyen, C. Beigné, L. Notin, M. Jamet, A. Marty, L. Vila, and J. P. Attané, "Using domain walls to perform non-local measurements with high spin signal amplitudes," *Appl. Phys. Lett.*, vol. 109, no. 4, 2016.

[78]   P. Laczkowski, L. Vila, V. D. Nguyen, A. Marty, J. P. Attané, H. Jaffrès, J. M. George, and A. Fert, "Enhancement of the spin signal in permalloy/gold multiterminal nanodevices by lateral confinement," *Phys. Rev. B - Condens. Matter Mater. Phys.*, vol. 85, pp. 2–5, 2012.

[79]   T. Yang, T. Kimura, and Y. Otani, "Giant spin-accumulation signal and pure spin-current-induced reversible magnetization switching," *Nat. Phys.*, vol. 4, no. 11, pp. 851–854, Nov. 2008.

[80]   Y. P. Liu, H. Idzuchi, Y. Fukuma, O. Rousseau, Y. Otani, and W. S. Lew, "Spin injection properties in trilayer graphene lateral spin valves," *Appl. Phys. Lett.*, vol. 102, no. 3, 2013.

[81]   W. Han, R. K. Kawakami, M. Gmitra, and J. Fabian, "Graphene spintronics," *Nat Nano*, vol. 9, no. 10, pp. 794–807, 2014.

[82]   Q. A. Pankhurst, J. Connolly, S. K. Jones, and J. Dobson, "Applications of magnetic nanoparticles in biomedicine," *Journal of Physics D: Applied Physics*, vol. 36. pp. R167–R181, 2003.

[83]   E. P. Furlani, "Magnetic Biotransport: Analysis and Applications," *Materials (Basel).*, vol. 3, no. 4, pp. 2412–2446, Mar. 2010.

[84]   B. D. Plouffe, S. K. Murthy, and L. H. Lewis, "Fundamentals and application of

magnetic particles in cell isolation and enrichment: a review.," *Rep. Prog. Phys.*, vol. 78, no. 1, p. 16601, 2014.

[85]   J. H. Kang, M. Super, C. W. Yung, R. M. Cooper, K. Domansky, A. R. Graveline, T. Mammoto, J. B. Berthet, H. Tobin, M. J. Cartwright, A. L. Watters, M. Rottman, A. Waterhouse, A. Mammoto, N. Gamini, M. J. Rodas, A. Kole, A. Jiang, T. M. Valentin, A. Diaz, K. Takahashi, and D. E. Ingber, "An extracorporeal blood-cleansing device for sepsis therapy," *Nat. Med.*, vol. 20, no. 10, pp. 1211–1216, Sep. 2014.

[86]   L. Johansson, K. Gunnarsson, S. Bijelovic, K. Eriksson, A. Surpi, E. Göthelid, P. Svedlindh, and S. Oscarsson, "A magnetic microchip for controlled transport of attomole levels of proteins.," *Lab Chip*, vol. 10, no. 5, pp. 654–661, 2010.

[87]   T. P. Forbes and S. P. Forry, "Microfluidic magnetophoretic separations of immunomagnetically labeled rare mammalian cells.," *Lab Chip*, vol. 12, no. 8, pp. 1471–9, 2012.

[88]   R. S. Bejhed, B. Tian, K. Eriksson, R. Brucas, S. Oscarsson, M. Strömberg, P. Svedlindh, and K. Gunnarsson, "Magnetophoretic Transport Line System for Rapid On-Chip Attomole Protein Detection," *Langmuir*, vol. 31, no. 37, pp. 10296–10302, 2015.

[89]   A. D. Henriksen, M. F. Hansen, and N. Rozlosnik, "Magnetic manipulation and sensing of beads for bioapplications.," Technical University of Denmark, 2015.

[90]   H. Lee, a. M. Purdon, and R. M. Westervelt, "Manipulation of biological cells using a microelectromagnet matrix," *Appl. Phys. Lett.*, vol. 85, no. 6, p. 1063, 2004.

[91]   M. Prikockis, A. Chen, T. Byvank, G. B. Vieira, B. Peters, F. Yang, and R. Sooryakumar, "Programmable self-assembly, disassembly, transport, and reconstruction of ordered planar magnetic micro-constructs," *IEEE Trans. Magn.*, vol. 50, no. 5, 2014.

[92]   B. Lim, S. R. Torati, K. W. Kim, X. Hu, V. Reddy, and C. Kim, "Concentric manipulation and monitoring of protein-loaded superparamagnetic cargo using magnetophoretic spider web," *NPG Asia Mater.*, vol. 9, no. 3, p. e369, Mar. 2017.

[93]   G. Rizzi, F. W. Østerberg, A. D. Henriksen, M. Dufva, and M. F. Hansen, "On-chip magnetic bead-based DNA melting curve analysis using a magnetoresistive sensor," *J.*

Magn. Magn. Mater., vol. 380, pp. 215–220, Apr. 2015.

[94]   A. Chen, T. Byvank, G. B. Vieira, and R. Sooryakumar, "Magnetic Microstructures for Control of Brownian Motion and Microparticle Transport," *IEEE Trans. Magn.*, vol. 49, no. 1, 2013.

[95]   S. Rampini, D. Kilinc, P. Li, C. Monteil, D. Gandhi, and G. U. Lee, "Micromagnet arrays for on-chip focusing, switching, and separation of superparamagnetic beads and single cells," *Lab Chip*, vol. 15, no. 16, pp. 3370–3379, 2015.

[96]   A. Jarosz, D. Holzinger, M. Urbaniak, A. Ehresmann, and F. Stobiecki, "Manipulation of superparamagnetic beads on patterned Au/Co/Au multilayers with perpendicular magnetic anisotropy," *J. Appl. Phys.*, vol. 120, no. 8, p. 84506, Aug. 2016.

[97]   D. Holzinger, I. Koch, S. Burgard, and A. Ehresmann, "Directed Magnetic Particle Transport above Artificial Magnetic Domains Due to Dynamic Magnetic Potential Energy Landscape Transformation," *ACS Nano*, vol. 9, no. 7, pp. 7323–7331, Jul. 2015.

[98]   M. Donolato, B. T. Dalslet, and M. F. Hansen, "Microstripes for transport and separation of magnetic particles.," *Biomicrofluidics*, vol. 6, no. 2, pp. 24110–241106, Jun. 2012.

[99]   F. Dumas-Bouchiat, L. F. Zanini, M. Kustov, N. M. Dempsey, R. Grechishkin, K. Hasselbach, J. C. Orlianges, C. Champeaux, A. Catherinot, and D. Givord, "Thermomagnetically patterned micromagnets," *Appl. Phys. Lett.*, vol. 96, no. 10, p. 102511, Mar. 2010.

[100]   S. Rampini, P. Li, and G. U. Lee, "Micromagnet arrays enable precise manipulation of individual biological analyte–superparamagnetic bead complexes for separation and sensing," *Lab Chip*, vol. 327, pp. 1072–1074, 2016.

[101]   R. S. Conroy, G. Zabow, J. Moreland, and A. P. Koretsky, "Controlled transport of magnetic particles using soft magnetic patterns," *Appl. Phys. Lett.*, vol. 93, no. 20, p. 203901, Nov. 2008.

[102]   M. T. Bryan, K. H. Smith, M. E. Real, M. A. Bashir, P. W. Fry, P. Fischer, Mi-Young Im, T. Schrefl, D. A. Allwood, and J. W. Haycock, "Switchable Cell Trapping Using Superparamagnetic Beads," *IEEE Magn. Lett.*, vol. 1, pp. 1500104–1500104, 2010.

[103] E. Rapoport and G. S. D. Beach, "Transport dynamics of superparamagnetic microbeads trapped by mobile magnetic domain walls," *Phys. Rev. B*, vol. 87, no. 17, May 2013.

[104] M. Donolato, P. Vavassori, M. Gobbi, M. Deryabina, M. F. Hansen, V. Metlushko, B. Ilic, M. Cantoni, D. Petti, S. Brivio, and R. Bertacco, "On-Chip Manipulation of Protein-Coated Magnetic Beads via Domain-Wall Conduits," *Adv. Mater.*, vol. 22, no. 24, pp. 2706–2710, Jun. 2010.

[105] A. Sarella, A. Torti, M. Donolato, M. Pancaldi, and P. Vavassori, "Two-Dimensional Programmable Manipulation of Magnetic Nanoparticles on-Chip," *Adv. Mater.*, vol. 26, no. 15, pp. 2384–2390, Apr. 2014.

[106] P. Vavassori, M. Gobbi, M. Donolato, M. Cantoni, R. Bertacco, V. Metlushko, and B. Ilic, "Magnetic nanostructures for the manipulation of individual nanoscale particles in liquid environments (invited)," *J. Appl. Phys.*, vol. 107, no. 9, p. 09B301, 2010.

[107] E. Rapoport and G. S. D. Beach, "Dynamics of superparamagnetic microbead transport along magnetic nanotracks by magnetic domain walls," *Appl. Phys. Lett.*, vol. 100, no. 8, 2012.

[108] M. Donolato, F. Lofink, S. Hankemeier, J. M. Porro, H. P. Oepen, and P. Vavassori, "Characterization of domain wall–based traps for magnetic beads separation," *J. Appl. Phys.*, vol. 111, no. 7, 2012.

[109] M. Donolato, A. Torti, N. Kostesha, M. Deryabina, E. Sogne, P. Vavassori, M. F. Hansen, and R. Bertacco, "Magnetic domain wall conduits for single cell applications.," *Lab Chip*, vol. 11, no. 17, Sep. 2011.

[110] M. L. Howdyshell, M. Prikockis, S. Lauback, G. B. Vieira, K. Mahajan, J. Winter, and R. Sooryakumar, "Deterministic and Stochastic Trajectories of Magnetic Particles: Mapping Energy Landscapes for Technology And Biology," *IEEE Trans. Magn.*, vol. 50, no. 11, pp. 1–7, 2014.

[111] M. Monticelli, E. Albisetti, D. Petti, D. V Conca, M. Falcone, P. P. Sharma, and R. Bertacco, "Towards an on-chip platform for the controlled application of forces via magnetic particles: A novel device for mechanobiology," *J. Appl. Phys.*, vol. 117, p. 17B317, 2015.

[112] H. Sohn, M. E. Nowakowski, C. Liang, J. L. Hockel, K. Wetzlar, S. Keller, B. M. McLellan, M. A. Marcus, A. Doran, A. Young, M. Kläui, G. P. Carman, J. Bokor, and R. N. Candler, "Electrically Driven Magnetic Domain Wall Rotation in Multiferroic Heterostructures to Manipulate Suspended On-Chip Magnetic Particles," *ACS Nano*, vol. 9, no. 5, pp. 4814–4826, May 2015.

[113] G. Ruan, G. Vieira, T. Henighan, A. Chen, D. Thakur, R. Sooryakumar, and J. O. Winter, "Simultaneous Magnetic Manipulation and Fluorescent Tracking of Multiple Individual Hybrid Nanostructures," *Nano Lett.*, vol. 10, no. 6, pp. 2220–2224, Jun. 2010.

[114] T. A. P. Rocha-Santos, "Sensors and biosensors based on magnetic nanoparticles," *TrAC Trends Anal. Chem.*, vol. 62, pp. 28–36, Nov. 2014.

[115] A. Sandhu, Y. Kumagai, A. Lapicki, S. Sakamoto, M. Abe, and H. Handa, "High efficiency Hall effect micro-biosensor platform for detection of magnetically labeled biomolecules," *Biosens. Bioelectron.*, vol. 22, no. 9–10, pp. 2115–2120, 2007.

[116] D. L. Graham, H. A. Ferreira, and P. P. Freitas, "Magnetoresistive-based biosensors and biochips," *Trends Biotechnol.*, vol. 22, no. 9, pp. 455–462, Sep. 2004.

[117] M. S. Gabureac, L. Bernau, G. Boero, and I. Utke, "Single Superparamagnetic Bead Detection and Direct Tracing of Bead Position Using Novel Nanocomposite Nano-Hall Sensors," *IEEE Trans. Nanotechnol.*, vol. 12, no. 5, pp. 668–673, 2013.

[118] C. R. Tamanaha, S. P. Mulvaney, J. C. Rife, and L. J. Whitman, "Magnetic labeling, detection, and system integration," *Biosens. Bioelectron.*, vol. 24, no. 1, pp. 1–13, 2008.

[119] V. Panchal, D. Cox, R. Yakimova, and O. Kazakova, "Epitaxial Graphene Sensors for Detection of Small Magnetic Moments," *IEEE Trans. Magn.*, vol. 49, no. 1, pp. 97–100, 2013.

[120] P. a. Besse, G. Boero, M. Demierre, V. Pott, and R. Popovic, "Detection of a single magnetic microbead using a miniaturized silicon Hall sensor," *Appl. Phys. Lett.*, vol. 80, no. 2002, pp. 4199–4201, 2002.

[121] O. Kazakova, J. C. Gallop, P. See, D. Cox, G. K. Perkins, J. D. Moore, and L. F. Cohen, "Detection of a micron-sized magnetic particle using insb hall sensor," *IEEE*

Trans. Magn., vol. 45, no. 10, pp. 4499–4502, 2009.

[122] O. Kazakova, V. Panchal, J. Gallop, P. See, D. C. Cox, M. Spasova, and L. F. Cohen, "Ultrasmall particle detection using a submicron Hall sensor," *J. Appl. Phys.*, vol. 107, no. 9, pp. 2010–2013, 2010.

[123] L. Di Michele, C. Shelly, J. Gallop, and O. Kazakova, "Single particle detection: Phase control in submicron Hall sensors," *J. Appl. Phys.*, vol. 108, no. 10, pp. 1–6, 2010.

[124] L. Di Michele, C. Shelly, P. de Marco, P. See, D. Cox, and O. Kazakova, "Detection and susceptibility measurements of a single Dynal bead," *J. Appl. Phys.*, vol. 110, no. 6, p. 63916, 2011.

[125] D. L. Graham, H. A. Ferreira, P. P. Freitas, and J. M. S. Cabral, "High sensitivity detection of molecular recognition using magnetically labelled biomolecules and magnetoresistive sensors," *Biosens. Bioelectron.*, vol. 18, no. 4, pp. 483–488, Apr. 2003.

[126] M. Volmer and M. Avram, "Detection of magnetic-based bio-molecules using MR sensors," *AIP Conf. Proc.*, vol. 1025, pp. 125–130, 2008.

[127] M. Megens and M. Prins, "Magnetic biochips: a new option for sensitive diagnostics," *J. Magn. Magn. Mater.*, vol. 293, no. 1, pp. 702–708, May 2005.

[128] D. R. Baselt, G. U. Lee, M. Natesan, S. W. Metzger, P. E. Sheehan, and R. J. Colton, "A biosensor based on magnetoresistance technology," *Biosens. Bioelectron.*, vol. 13, no. 7–8, pp. 731–739, 1998.

[129] S. X. Wang and Guanxiong Li, "Advances in Giant Magnetoresistance Biosensors With Magnetic Nanoparticle Tags: Review and Outlook," *IEEE Trans. Magn.*, vol. 44, no. 7, pp. 1687–1702, Jul. 2008.

[130] M. M. Miller, P. E. Sheehan, R. L. Edelstein, C. R. Tamanaha, L. Zhong, S. Bounnak, L. J. Whitman, and R. J. Colton, "A DNA array sensor utilizing magnetic microbeads and magnetoelectronic detection," *J. Magn. Magn. Mater.*, vol. 225, no. 1–2, pp. 138–144, Jan. 2001.

[131] G. Li, V. Joshi, R. L. White, S. X. Wang, J. T. Kemp, C. Webb, R. W. Davis, and S. Sun, "Detection of single micron-sized magnetic bead and magnetic nanoparticles using spin valve sensors for biological applications," *J. Appl. Phys.*, vol. 93, no. 2003,

p. 7557, 2003.

[132] X. J. A. Janssen, L. J. van IJzendoorn, and M. W. J. Prins, "On-chip manipulation and detection of magnetic particles for functional biosensors," *Biosens. Bioelectron.*, vol. 23, no. 6, pp. 833–838, Jan. 2008.

[133] J. C. Rife, M. M. Miller, P. E. Sheehan, C. R. Tamanaha, M. Tondra, and L. J. Whitman, "Design and performance of GMR sensors for the detection of magnetic microbeads in biosensors," *Sensors Actuators A Phys.*, vol. 107, no. 3, pp. 209–218, Nov. 2003.

[134] J. Schotter, P. . Kamp, A. Becker, A. Pühler, G. Reiss, and H. Brückl, "Comparison of a prototype magnetoresistive biosensor to standard fluorescent DNA detection," *Biosens. Bioelectron.*, vol. 19, no. 10, pp. 1149–1156, May 2004.

[135] F. Li, R. Kodzius, C. P. Gooneratne, I. G. Foulds, and J. Kosel, "Magneto-mechanical trapping systems for biological target detection," *Microchim. Acta*, vol. 181, no. 13–14, pp. 1743–1748, Oct. 2014.

[136] C. Gooneratne, R. Kodzius, F. Li, I. Foulds, and J. Kosel, "On-Chip Magnetic Bead Manipulation and Detection Using a Magnetoresistive Sensor-Based Micro-Chip: Design Considerations and Experimental Characterization," *Sensors*, vol. 16, no. 9, p. 1369, Aug. 2016.

[137] C. Albon, A. Weddemann, A. Auge, K. Rott, and A. Hütten, "Tunneling magnetoresistance sensors for high resolutive particle detection," *Appl. Phys. Lett.*, vol. 95, no. 2, pp. 95–98, 2009.

[138] E. Albisetti, D. Petti, M. Cantoni, F. Damin, A. Torti, M. Chiari, and R. Bertacco, "Conditions for efficient on-chip magnetic bead detection via magnetoresistive sensors," *Biosens. Bioelectron.*, vol. 47, no. March, pp. 213–217, Sep. 2013.

[139] F. W. Østerberg, B. T. Dalslet, D. Snakenborg, C. Johansson, M. F. Hansen, U. Häfeli, W. Schütt, and M. Zborowski, "Chip-Based Measurements of Brownian Relaxation of Magnetic Beads Using a Planar Hall Effect Magnetic Field Sensor," 2010, no. January 2016, pp. 176–183.

[140] G. Rizzi, F. Westergaard Østerberg, M. Dufva, and M. Fougt Hansen, "Magnetoresistive sensor for real-time single nucleotide polymorphism genotyping,"

Biosens. Bioelectron., vol. 52, pp. 445–451, Feb. 2014.

[141] B. T. Dalslet, C. D. Damsgaard, M. Donolato, M. Strømme, M. Strömberg, P. Svedlindh, and M. F. Hansen, "Bead magnetorelaxometry with an on-chip magnetoresistive sensor," *Lab Chip*, vol. 11, no. 2, pp. 296–302, Jan. 2011.

[142] T. Q. Hung, S. Oh, J. R. Jeong, and C. Kim, "Spin-valve planar Hall sensor for single bead detection," *Sensors Actuators, A Phys.*, vol. 157, pp. 42–46, 2010.

[143] H. Kim, V. Reddy, K. W. Kim, I. Jeong, X. H. Hu, and C. Kim, "Single Magnetic Bead Detection in a Microfluidic Chip Using Planar Hall Effect Sensor," *J. Magn.*, vol. 19, no. 1, pp. 10–14, Mar. 2014.

[144] M. Volmer and M. Avram, "Signal dependence on magnetic nanoparticles position over a planar Hall effect biosensor," *Microelectron. Eng.*, vol. 108, pp. 116–120, Aug. 2013.

[145] T. Q. Hung, F. Terki, S. Kamara, K. Kim, S. Charar, and C. Kim, "Planar Hall ring sensor for ultra-low magnetic moment sensing," *J. Appl. Phys.*, vol. 117, no. August, p. 154505, 2015.

[146] F. W. Østerberg, G. Rizzi, M. Donolato, R. S. Bejhed, A. Mezger, M. Strömberg, M. Nilsson, M. Strømme, P. Svedlindh, and M. F. Hansen, "On-Chip Detection of Rolling Circle Amplified DNA Molecules from Bacillus Globigii Spores and Vibrio Cholerae," *Small*, vol. 10, no. 14, pp. 2877–2882, Jul. 2014.

[147] L. K. Quynh, B. D. Tu, D. X. Dang, D. Q. Viet, L. T. Hien, D. T. Huong Giang, and N. H. Duc, "Detection of magnetic nanoparticles using simple AMR sensors in Wheatstone bridge," *J. Sci. Adv. Mater. Devices*, vol. 1, no. 1, pp. 98–102, Mar. 2016.

[148] L. Ejsing, M. F. Hansen, A. K. Menon, H. A. Ferreira, D. L. Graham, and P. P. Freitas, "Magnetic microbead detection using the planar Hall effect," in *Journal of Magnetism and Magnetic Materials*, 2005, vol. 293, no. 1, p. 677.

[149] A. D. Henriksen, G. Rizzi, F. W. Østerberg, and M. F. Hansen, "Optimization of magnetoresistive sensor current for on-chip magnetic bead detection using the sensor self-field," *J. Magn. Magn. Mater.*, vol. 380, pp. 209–214, Apr. 2015.

[150] L. T. Hien, L. K. Quynh, V. T. Huyen, B. D. Tu, N. T. Hien, D. M. Phuong, P. H. Nhung, D. T. H. Giang, and N. H. Duc, "DNA-magnetic bead detection using

disposable cards and the anisotropic magnetoresistive sensor," *Adv. Nat. Sci. Nanosci. Nanotechnol.*, vol. 7, no. 4, p. 45006, Oct. 2016.

[151] F. W. Østerberg, G. Rizzi, A. D. Henriksen, and M. F. Hansen, "Planar Hall effect bridge geometries optimized for magnetic bead detection," *J. Appl. Phys.*, vol. 115, no. 18, p. 184505, May 2014.

[152] M. Volmer and M. Avram, "Using permalloy based planar hall effect sensors to capture and detect superparamagnetic beads for lab on a chip applications," *J. Magn. Magn. Mater.*, vol. 381, pp. 481–487, May 2015.

[153] M. Monticelli, D. Petti, E. Albisetti, M. Cantoni, E. Guerriero, R. Sordan, M.Carminati, G. Ferrari, M. Sampietro, and R. Bertacco, "Closed loop microfluidic platform based on domain wall magnetic conduits: a novel tool for biology and medicine," *MRS Proc.*, vol. 1686, p. mrss14-1686-v02-06, Nov. 2014.

[154] P. Vavassori, V. Metlushko, B. Ilic, M. Gobbi, M. Donolato, M. Cantoni, and R. Bertacco, "Domain wall displacement in Py square ring for single nanometric magnetic bead detection," *Appl. Phys. Lett.*, vol. 93, no. 20, p. 203502, 2008.

[155] H. Corte-León, B. Gribkov, P. Krzysteczko, F. Marchi, J.-F. Motte, H. W. Schumacher, V. Antonov, and O. Kazakova, "Magnetic scanning gate microscopy of a domain wall nanosensor using microparticle probe," *J. Magn. Magn. Mater.*, vol. 400, pp. 225–229, Feb. 2016.

[156] H. Corte-León, P. Krzysteczko, H. W. Schumacher, A. Manzin, D. Cox, V. Antonov, and O. Kazakova, "Magnetic bead detection using domain wall-based nanosensor," *J. Appl. Phys.*, vol. 117, no. 17, p. 17E313, May 2015.

[157] J. Wells, P. Krzysteczko, A. Caprile, B. Gribkov, H. W. Schumacher, J. H. Lee, R. Cowburn, and O. Kazakova, "Magnetic Particle Nanosensing by Nucleation of Domain Walls in Ultra-Thin CoFeB/Pt Devices," *IEEE Trans. Magn.*, vol. 52, no. 7, pp. 1–5, Jul. 2016.

[158] J. Wells, J. H. Lee, R. Mansell, R. P. Cowburn, and O. Kazakova, "Controlled manipulation of domain walls in ultra-thin CoFeB nanodevices," *J. Magn. Magn. Mater.*, vol. 400, pp. 219–224, 2016.

[159] F. J. Giessibl, "Advances in atomic force microscopy," *Rev. Mod. Phys.*, vol. 75, no. 3,

pp. 949–983, Jul. 2003.

[160] Y. Martin and H. K. Wickramasinghe, "Magnetic imaging by '"force microscopy"' with 1000 Å resolution," *Appl. Phys. Lett.*, vol. 50, no. 20, p. 1455, May 1987.

[161] S. Porthun, L. Abelmann, and C. Lodder, "Magnetic force microscopy of thin film media for high density magnetic recording," *J. Magn. Magn. Mater.*, vol. 182, no. 1–2, pp. 238–273, Feb. 1998.

[162] D. Rugar, H. J. Mamin, P. Guethner, S. E. Lambert, J. E. Stern, I. McFadyen, and T. Yogi, "Magnetic force microscopy: General principles and application to longitudinal recording media," *J. Appl. Phys.*, vol. 68, no. 3, pp. 1169–1183, 1990.

[163] M. Jaafar, A. Asenjo, and M. Vázquez, "Calibration of coercive and stray fields of commercial magnetic force microscope probes," *IEEE Trans. Nanotechnol.*, vol. 7, no. 3, pp. 245–250, 2008.

[164] Bruker, *New TESP / TESPA Silicon AFM Probes http://www.brukerafmprobes.com/images/product/specPDF/3844.pdf*. 2015.

[165] Y. Gan, "Invited Review Article: A review of techniques for attaching micro- and nanoparticles to a probe's tip for surface force and near-field optical measurements," *Rev. Sci. Instrum.*, vol. 78, no. 2007, 2007.

[166] S. R. Systems, *Stanford Research SR830 Lock-in Amplifier Manual http://www.thinksrs.com/downloads/PDFs/Manuals/SR830m.pdf*, vol. 5, no. 408. 2011.

[167] K. Technologies, *Keysight 34420A Nano Volt / Micro Ohm Meter User's Guide http://literature.cdn.keysight.com/litweb/pdf/34420-90001.pdf?id=1000003601:epsg:dow*. 2014.

[168] E. Hetch, *Optics*, 4th ed. Addison Wesley, 2002.

[169] M. Ali, "Growth and study of magnetostrictive FeSiBC thin films for device applications," University of Sheffield, 1999.

[170] D. A. Allwood, N. Vernier, G. Xiong, M. D. Cooke, D. Atkinson, C. C. Faulkner, and R. P. Cowburn, "Shifted hysteresis loops from magnetic nanowires," *Appl. Phys. Lett.*, vol. 81, no. 21, p. 4005, 2002.

[171] A. Beguivin, H. Corte-León, A. Manzin, V. Nabaei, P. Krzysteczko, H. W. Schumacher, D. Petit, R. P. Cowburn, and O. Kazakova, "Simultaneous magnetoresistance and magneto-optical measurements of domain wall properties in nanodevices," *J. Appl. Phys.*, vol. 115, no. 17, p. 17C718, May 2014.

[172] L. K. Bogart and D. Atkinson, "Domain wall anisotropic magnetoresistance in planar nanowires," *Appl. Phys. Lett.*, vol. 94, no. 4, p. 42511, 2009.

[173] T. R. McGuire and R. I. Potter, "Anisotropic Magnetoresistance in Ferromagnetic 3d Alloys," *IEEE Trans. Magn.*, vol. MAG-11, no. 4, pp. 1018–1038, 1975.

[174] T. Manago, K. Kanazawa, and T. Kera, "Magneto-resistance of NiFe nanowire with zigzag shape," *J. Magn. Magn. Mater.*, vol. 321, no. 15, pp. 2327–2330, Aug. 2009.

[175] A. Oliveira, S. Rezende, and A. Azevedo, "Magnetization reversal in permalloy ferromagnetic nanowires investigated with magnetoresistance measurements," *Phys. Rev. B*, vol. 78, no. 2, p. 24423, Jul. 2008.

[176] K. Moon, J. Lee, M. Jung, K. Shin, and S. Choe, "Incoherent Domain Configuration Along Wire Width in Permalloy Nanowires," *IEEE Trans. Magn.*, vol. 45, no. 6, pp. 2485–2487, Jun. 2009.

[177] J.-E. Wegrowe, D. Kelly, A. Franck, S. Gilbert, and J.-P. Ansermet, "Magnetoresistance of Ferromagnetic Nanowires," *Phys. Rev. Lett.*, vol. 82, no. 18, pp. 3681–3684, May 1999.

[178] M. Hayashi, L. Thomas, C. Rettner, R. Moriya, X. Jiang, and S. Parkin, "Dependence of Current and Field Driven Depinning of Domain Walls on Their Structure and Chirality in Permalloy Nanowires," *Phys. Rev. Lett.*, vol. 97, no. 20, p. 207205, Nov. 2006.

[179] J. Akerman, M. Muñoz, M. Maicas, and J. L. Prieto, "Stochastic nature of the domain wall depinning in permalloy magnetic nanowires," *Phys. Rev. B*, vol. 82, no. 6, p. 64426, Aug. 2010.

[180] M. Hayashi, L. Thomas, C. Rettner, R. Moriya, and S. S. P. Parkin, "Direct observation of the coherent precession of magnetic domain walls propagating along permalloy nanowires," *Nat. Phys.*, vol. 3, no. 1, pp. 21–25, Dec. 2007.

[181] S. N. Holmes, J. H. Lee, B. Hong, M. D. Mascaro, D. Anderson, G. a. C. Jones, C. a.

Ross, and C. H. W. Barnes, "Magnetic vortex stability in Ni80Fe20 split rings," *J. Appl. Phys.*, vol. 113, no. 4, p. 44508, 2013.

[182] J. Briones, F. Montaigne, M. Hehn, D. Lacour, J. R. Childress, and M. J. Carey, "Stochastic and complex depinning dynamics of magnetic domain walls," *Phys. Rev. B*, vol. 83, no. 6, p. 60401, Feb. 2011.

[183] H. Corte-León, P. Krzysteczko, H. W. Schumacher, A. Manzin, V. Antonov, and O. Kazakova, "Tailoring of domain wall devices for sensing applications," *IEEE Trans. Magn.*, no. 11, pp. 2–5, Nov. 2014.

[184] C. Wuth, P. Lendecke, and G. Meier, "Temperature-dependent dynamics of stochastic domain-wall depinning in nanowires.," *J. Phys. Condens. Matter*, vol. 24, no. 2, p. 24207, Jan. 2012.

[185] T. Y. Chung and S. Y. Hsu, "Magnetization reversal in single domain Permalloy wires probed by magnetotransport," *J. Appl. Phys.*, vol. 103, no. 7, p. 07C506, 2008.

[186] H. Corte-Leon, A. Beguivin, P. Krzysteczko, H. W. Schumacher, A. Manzin, R. P. Cowburn, V. Antonov, and O. Kazakova, "Influence of Geometry on Domain Wall Dynamics in Permalloy Nanodevices," *IEEE Trans. Magn.*, vol. 51, no. 1, pp. 1–4, Jan. 2015.

[187] J. Andreassen, "One micron magnetic beads optimised for automated immunoassays," *CLI*, no. April, 2005.

[188] G. Fonnum, C. Johansson, A. Molteberg, S. Mørup, and E. Aksnes, "Characterisation of Dynabeads® by magnetization measurements and Mössbauer spectroscopy," *J. Magn. Magn. Mater.*, vol. 293, no. 1, pp. 41–47, 2005.

[189] H. Campanella, R. P. Del Real, M. Díaz-Michelena, M. Duch, H. Guerrero, J. Esteve, and J. a. Plaza, "Focused-ion-beam-assisted magnet fabrication and manipulation for magnetic field detection applications," *ACS Appl. Mater. Interfaces*, vol. 1, no. 3, pp. 527–531, 2009.

[190] Magnequench, "January 8, 2009," 2009.

[191] R. Puttock, H. Corte-Leon, V. Neu, D. Cox, A. Manzin, V. Antonov, P. Vavassori, and O. Kazakova, "V-Shaped Domain Wall Probes for Calibrated Magnetic Force Microscopy," *IEEE Trans. Magn.*, vol. 53, no. 11, pp. 1–5, Nov. 2017.

[192] J. Lohau, S. Kirsch, A. Carl, G. Dumpich, and E. F. Wassermann, "Quantitative determination of effective dipole and monopole moments of magnetic force microscopy tips," *J. Appl. Phys.*, vol. 86, no. May 2014, p. 3410, Sep. 1999.

[193] C. Vautrin, M. Vyazmensky, S. Engel, S. M. Murtry, M. Hehn, F. Montaigne, D. Lacour, and R. S. Marks, "Biochip based on arrays of switchable magnetic nano-traps," *Sensors Actuators B Chem.*, vol. 251, no. May, pp. 699–705, Nov. 2017.

[194] M. Donolato, B. T. Dalslet, C. D. Damsgaard, K. Gunnarsson, C. S. Jacobsen, P. Svedlindh, and M. F. Hansen, "Size-dependent effects in exchange-biased planar Hall effect sensor crosses," *J. Appl. Phys.*, vol. 109, no. 6, p. 64511, 2011.

[195] L. Thomas, M. Hayashi, R. Moriya, C. Rettner, and S. Parkin, "Topological repulsion between domain walls in magnetic nanowires leading to the formation of bound states.," *Nat. Commun.*, vol. 3, no. may, p. 810, Jan. 2012.

[196] L. Thomas, R. Moriya, C. Rettner, and S. S. P. Parkin, "Dynamics of magnetic domain walls under their own inertia.," *Science*, vol. 330, no. 6012, pp. 1810–3, Dec. 2010.

[197] M. Hayashi, L. Thomas, Y. Bazaliy, C. Rettner, R. Moriya, X. Jiang, and S. Parkin, "Influence of Current on Field-Driven Domain Wall Motion in Permalloy Nanowires from Time Resolved Measurements of Anisotropic Magnetoresistance," *Phys. Rev. Lett.*, vol. 96, no. 19, p. 197207, May 2006.

[198] L. Ejsing, M. F. Hansen, a. K. Menon, H. a. Ferreira, D. L. Graham, and P. P. Freitas, "Planar Hall effect sensor for magnetic micro- and nanobead detection," *Appl. Phys. Lett.*, vol. 84, no. 23, p. 4729, 2004.

[199] P. P. Sharma, E. Albisetti, M. Massetti, M. Scolari, C. La Torre, M. Monticelli, M. Leone, F. Damin, G. Gervasoni, G. Ferrari, F. Salice, E. Cerquaglia, G. Falduti, M. Cretich, E. Marchisio, M. Chiari, M. Sampietro, D. Petti, and R. Bertacco, "Integrated platform for detecting pathogenic DNA via magnetic tunneling junction-based biosensors," *Sensors Actuators B Chem.*, vol. 242, no. December, pp. 280–287, Apr. 2017.

[200] X. Liu, J. N. Chapman, S. McVitie, and C. D. W. Wilkinson, "Introduction and control of metastable states in elliptical and rectangular magnetic nanoelements," *Appl. Phys. Lett.*, vol. 84, no. 22, p. 4406, 2004.

[201] K. Wagner, A. Kákay, K. Schultheiss, A. Henschke, T. Sebastian, and H. Schultheiss, "Magnetic domain walls as reconfigurable spin-wave nanochannels," *Nat. Nanotechnol.*, vol. 11, no. 5, pp. 432–436, Feb. 2016.

[202] F. Montaigne, A. Schuhl, F. N. Van Dau, and A. Encinas, "Development of magnetoresistive sensors based on planar Hall effect for applications to microcompass," *Sensors Actuators A Phys.*, vol. 81, no. 1–3, pp. 324–327, Apr. 2000.

[203] X. Liu, J. N. Chapman, S. McVitie, and C. D. W. Wilkinson, "Reversal mechanisms and metastable states in magnetic nanoelements," *J. Appl. Phys.*, vol. 96, no. 9, p. 5173, 2004.

[204] K. Kim, S. R. Torati, V. Reddy, and S. Yoon, "Planar Hall Resistance Sensor for Monitoring Current," *J. Magn.*, vol. 19, no. 2, pp. 151–154, Jun. 2014.

[205] B. D. Tu, L. V. Cuong, D. T. H. Giang, T. M. Danh, and N. H. Duc, "Optimization of planar Hall effect sensor for magnetic bead detection using spin-valve NiFe/Cu/NiFe/IrMn structures," *J. Phys. Conf. Ser.*, vol. 187, p. 12056, Sep. 2009.

[206] A. Schuhl, F. N. Van Dau, and J. R. Childress, "Low-field magnetic sensors based on the planar Hall effect," *Appl. Phys. Lett.*, vol. 66, no. 20, p. 2751, 1995.

[207] A. D. Henriksen, B. T. Dalslet, D. H. Skieller, K. H. Lee, F. Okkels, and M. F. Hansen, "Planar Hall effect bridge magnetic field sensors," *Appl. Phys. Lett.*, vol. 97, no. 1, p. 13507, 2010.

[208] C. D. Damsgaard, S. C. Freitas, P. P. Freitas, and M. F. Hansen, "Exchange-biased planar Hall effect sensor optimized for biosensor applications," *J. Appl. Phys.*, vol. 103, no. 2008, pp. 5–8, 2008.

[209] Y. C. Chang, C.-R. C. Chang, I. Chang, J. C. Wu, Z.-H. Wei, and M.-F. Lai, "Investigation of Permalloy cross structure using magnetic force microscope and magnetoresistance measurement," *J. Appl. Phys.*, vol. 99, p. 08B710, 2006.

[210] B. T. Dalslet, M. Donolato, and M. F. Hansen, "Planar Hall effect sensor with magnetostatic compensation layer," *Sensors Actuators A Phys.*, vol. 174, pp. 1–8, Feb. 2012.

[211] M. Megens, F. de Theije, B. de Boer, and F. van Gaal, "Scanning probe measurements on a magnetic bead biosensor," *J. Appl. Phys.*, vol. 102, no. 2007, p. 14507, 2007.

[212] K. J. M. Eijkel and J. H. J. Fluitman, "Optimization of the response of magnetoresistive elements," *IEEE Trans. Magn.*, vol. 26, no. 1, pp. 311–321, 1990.

[213] A. Rose, *Vision: Human and electronic*. New York: Plenum Press, 1973.

[214] S. Hu and T. Kimura, "Significant modulation of electrical spin accumulation by efficient thermal spin injection," *Phys. Rev. B - Condens. Matter Mater. Phys.*, vol. 90, no. 13, pp. 3–6, 2014.

[215] A. Hojem, D. Wesenberg, and B. L. Zink, "Thermal spin injection and interface insensitivity in permalloy/aluminum metallic nonlocal spin valves," *Phys. Rev. B*, vol. 94, no. 2, p. 24426, Jul. 2016.

[216] S. Hu, H. Itoh, and T. Kimura, "Efficient thermal spin injection using CoFeAl nanowire," *NPG Asia Mater.*, vol. 6, no. 9, p. e127, Sep. 2014.

[217] A. Slachter, F. L. Bakker, J.-P. Adam, and B. J. van Wees, "Thermally driven spin injection from a ferromagnet into a non-magnetic metal," *Nat. Phys.*, vol. 6, no. 11, pp. 879–882, 2010.

[218] A. Slachter, F. L. Bakker, and B. J. van Wees, "Anomalous Nernst and anisotropic magnetoresistive heating in a lateral spin valve," *Phys. Rev. B*, vol. 84, no. 2, p. 20412, Jul. 2011.

[219] E. Montoya, P. Omelchenko, C. Coutts, N. R. Lee-Hone, R. Hübner, D. Broun, B. Heinrich, and E. Girt, "Spin transport in tantalum studied using magnetic single and double layers," *Phys. Rev. B*, vol. 94, no. 5, p. 54416, Aug. 2016.

[220] R. Mansell, A. Beguivin, D. C. M. C. Petit, A. Fernández-Pacheco, J. H. Lee, and R. P. Cowburn, "Controlling nucleation in perpendicularly magnetized nanowires through in-plane shape," *Appl. Phys. Lett.*, vol. 107, no. 9, pp. 4–8, 2015.

[221] H. Corte-León, A. F. Scarioni, R. Mansell, P. Krzysteczko, D. Cox, D. McGrouther, S. McVitie, R. Cowburn, H. W. Schumacher, V. Antonov, and O. Kazakova, "Magnetic scanning gate microscopy of CoFeB lateral spin valve," *AIP Adv.*, vol. 7, no. 5, p. 56808, May 2017.

[222] S. McVitie and G. S. White, "Imaging Amperian currents by Lorentz microscopy," *J. Phys. D. Appl. Phys.*, vol. 37, no. 2, pp. 280–288, 2004.

[223] S. McVitie, R. P. Ferrier, J. Scott, G. S. White, and A. Gallagher, "Quantitative field measurements from magnetic force microscope tips and comparison with point and extended charge models," *J. Appl. Phys.*, vol. 89, no. 2001, p. 3656, 2001.

[224] R. P. Ferner, S. McVitie, A. Gallagher, and W. A. P. Nicholson, "Characterisation of MFM tip fields by electron tomography," *IEEE Trans. Magn.*, vol. 33, no. 5 PART 2, pp. 4062–4064, 1997.

[225] R. Nagatsu, M. Ohtake, M. Futamoto, F. Kirino, and N. Inaba, "Spatial resolution and switching field of magnetic force microscope tips prepared by coating Fe/Co-Pt layers," *AIP Adv.*, vol. 6, no. 5, p. 56503, 2016.

[226] Jinhee Heo, Kyohyeok Kim, Taewan Kim, and Ilsub Chung, "Characterization of domain switching behavior of MTJ cells using magnetic force microscopy(MFM) and H-R loop analysis," in *2006 IEEE Nanotechnology Materials and Devices Conference*, 2006, vol. 2667, no. 1999, pp. 618–619.

[227] S. N. Piramanayagam, M. Ranjbar, R. Sbiaa, A. Tavakkoli K. G., and T. C. Chong, "Characterization of high-density bit-patterned media using ultra-high resolution magnetic force microscopy," *Phys. status solidi - Rapid Res. Lett.*, vol. 6, no. 3, pp. 141–143, 2012.

[228] J. M. García-Martín, A. Thiaville, J. Miltat, T. Okuno, L. Vila, and L. Piraux, "Imaging magnetic vortices by magnetic force microscopy: experiments and modelling," *J. Phys. D. Appl. Phys.*, vol. 37, no. 7, pp. 965–972, Apr. 2004.

[229] O. Iglesias-Freire, J. R. Bates, Y. Miyahara, A. Asenjo, and P. H. Grütter, "Tip-induced artifacts in magnetic force microscopy images," *Appl. Phys. Lett.*, vol. 102, no. 2, p. 22417, 2013.

[230] M. R. Koblischka, U. Hartmann, and T. Sulzbach, "Improvements of the lateral resolution of the MFM technique," in *Thin Solid Films*, 2003, vol. 428, pp. 93–97.

[231] N. Amos, A. Lavrenov, R. Fernandez, R. Ikkawi, D. Litvinov, and S. Khizroev, "High-resolution and high-coercivity FePtL1[sub 0] magnetic force microscopy nanoprobes to study next-generation magnetic recording media," *J. Appl. Phys.*, vol. 105, no. 7, p. 07D526, 2009.

[232] I. Utke, P. Hoffmann, R. Berger, and L. Scandella, "High-resolution magnetic Co

supertips grown by a focused electron beam," *Appl. Phys. Lett.*, vol. 80, no. 25, p. 4792, 2002.

[233] D. Litvinov and S. Khizroev, "Orientation-sensitive magnetic force microscopy for future probe storage applications," *Appl. Phys. Lett.*, vol. 81, no. 10, p. 1878, 2002.

[234] H. Campanella, M. Jaafar, J. Llobet, J. Esteve, M. Vázquez, A. Asenjo, R. P. del Real, and J. a Plaza, "Nanomagnets with high shape anisotropy and strong crystalline anisotropy: perspectives on magnetic force microscopy.," *Nanotechnology*, vol. 22, no. 50, p. 505301, Dec. 2011.

[235] Y. Lisunova, J. Heidler, I. Levkivskyi, I. Gaponenko, A. Weber, C. Caillier, L. J. Heyderman, M. Kläui, and P. Paruch, "Optimal ferromagnetically-coated carbon nanotube tips for ultra-high resolution magnetic force microscopy.," *Nanotechnology*, vol. 24, no. 10, p. 105705, Mar. 2013.

[236] A. Thiaville, L. Belliard, D. Majer, E. Zeldov, and J. Miltat, "Measurement of the stray field emanating from magnetic force microscope tips by Hall effect microsensors," *J. Appl. Phys.*, vol. 82, no. 7, p. 3182, 1997.

[237] Ó. Iglesias-Freire, M. Jaafar, E. Berganza, and A. Asenjo, "Customized MFM probes with high lateral resolution," *Beilstein J. Nanotechnol.*, vol. 7, no. 1, pp. 1068–1074, Jul. 2016.

[238] J. . García, a Thiaville, and J. Miltat, "MFM imaging of nanowires and elongated patterned elements," *J. Magn. Magn. Mater.*, vol. 249, no. 1–2, pp. 163–169, Aug. 2002.

[239] A. Alekseev, A. Popkov, A. Shubin, F. Pudonin, and N. Djuzhev, "Effect of horizontal magnetization reversal of the tips on magnetic force microscopy images," *Ultramicroscopy*, vol. 136, pp. 91–95, Jan. 2014.

[240] T. Uhlig, U. Wiedwald, A. Seidenstücker, P. Ziemann, and L. M. Eng, "Single core–shell nanoparticle probes for non-invasive magnetic force microscopy," *Nanotechnology*, vol. 25, no. 25, p. 255501, Jun. 2014.

[241] F. Wolny, Y. Obukhov, T. Mühl, U. Weissker, S. Philippi, A. Leonhardt, P. Banerjee, A. Reed, G. Xiang, R. Adur, I. Lee, a J. Hauser, F. Y. Yang, D. V Pelekhov, B. Büchner, and P. C. Hammel, "Quantitative magnetic force microscopy on permalloy

dots using an iron filled carbon nanotube probe.," *Ultramicroscopy*, vol. 111, no. 8, pp. 1360–5, Jul. 2011.

[242] S. Vock, F. Wolny, T. Mühl, R. Kaltofen, L. Schultz, B. Büchner, C. Hassel, J. Lindner, and V. Neu, "Monopolelike probes for quantitative magnetic force microscopy: Calibration and application," *Appl. Phys. Lett.*, vol. 97, no. 25, p. 252505, Dec. 2010.

[243] F. Wolny, T. Mühl, U. Weissker, K. Lipert, J. Schumann, A. Leonhardt, and B. Büchner, "Iron filled carbon nanotubes as novel monopole-like sensors for quantitative magnetic force microscopy.," *Nanotechnology*, vol. 21, no. 43, p. 435501, Oct. 2010.

[244] N. Yoshida, M. Yasutake, T. Arie, S. Akita, and Y. Nakayama, "Quantitative Analysis of the Magnetic Properties of Metal-Capped Carbon Nanotube Probe," *Japanese Journal of Applied Physics*, vol. 41, no. Part 1, No. 7B. pp. 5013–5016, 30-Jul-2002.

[245] F. Wolny, T. Mühl, U. Weissker, A. Leonhardt, U. Wolff, D. Givord, and B. Büchner, "Magnetic force microscopy measurements in external magnetic fields—comparison between coated probes and an iron filled carbon nanotube probe," *J. Appl. Phys.*, vol. 108, no. 1, p. 13908, Jul. 2010.

[246] T. Arie, N. Yoshida, S. Akita, and Y. Nakayama, "Quantitative analysis of the magnetic properties of a carbon nanotube probe in magnetic force microscopy," *Journal of Physics D: Applied Physics*, vol. 34. pp. L43–L45, 2001.

[247] N. Amos, R. Ikkawi, R. Haddon, D. Litvinov, and S. Khizroev, "Controlling multidomain states to enable sub-10-nm magnetic force microscopy," *Appl. Phys. Lett.*, vol. 93, no. 20, p. 203116, 2008.

[248] Y. Shen and Y. Wu, "Response Function Study of a New Kind of Multilayer-Coated Tip for Magnetic Force Microscopy," *IEEE Trans. Magn.*, vol. 40, no. 1, pp. 97–100, Jan. 2004.

[249] V. Cambel, D. Gregušová, P. Eliáš, J. Fedor, I. Kostič, J. Maňka, and P. Ballo, "Switching magnetization magnetic force microscopy - An alternative to conventional lift-mode MFM," *J. Electr. Eng.*, vol. 62, no. 1, pp. 37–43, 2011.

[250] L. Angeloni, D. Passeri, M. Reggente, D. Mantovani, and M. Rossi, "Removal of electrostatic artifacts in magnetic force microscopy by controlled magnetization of the

tip: application to superparamagnetic nanoparticles," *Sci. Rep.*, vol. 6, no. September 2015, p. 26293, May 2016.

[251] J. Schwenk, M. Marioni, S. Romer, N. R. Joshi, and H. J. Hug, "Non-contact bimodal magnetic force microscopy," *Appl. Phys. Lett.*, vol. 104, no. 11, p. 112412, Mar. 2014.

[252] B. I. Kim, "Effects of long-range tip-sample interaction on magnetic force imaging: A comparative study between bimorph driven system and electrostatic force modulation," *J. Appl. Phys.*, vol. 111, no. 10, p. 104313, May 2012.

[253] M. Precner, J. Fedor, J. Šoltýs, and V. Cambel, "Dual-tip magnetic force microscopy with suppressed influence on magnetically soft samples," *Nanotechnology*, vol. 26, no. 5, p. 55304, Feb. 2015.

[254] S. Signoretti, C. Beeli, and S.-H. Liou, "Electron holography quantitative measurements on magnetic force microscopy probes," *J. Magn. Magn. Mater.*, vol. 272–276, pp. 2167–2168, 2004.

[255] "NANOSENSORSTM Magnetic Force Microscopy Silicon-MFM-Probes http://www.nanosensors.com/downloads," 2016.

[256] D. Shindo and Y. Murakami, "Electron holography of magnetic materials," *J. Phys. D. Appl. Phys.*, vol. 41, no. 18, p. 183002, 2008.

[257] H. Lichte and M. Lehmann, "Electron holography—basics and applications," *Reports Prog. Phys.*, vol. 71, no. 1, p. 16102, Jan. 2008.

[258] M. J. Donahue and Porter D.G., "OOMMF User's Guide, Version 1.0. Interagency Report NISTIR 6373," Gaithersburg, 1999.

[259] "MFM_LM http://ntmdt-tips.com/products/view/mfm-lm," 2017.

[260] D. Passeri, C. Dong, L. Angeloni, F. Pantanella, T. Natalizi, F. Berlutti, C. Marianecci, F. Ciccarello, and M. Rossi, "Thickness measurement of soft thin films on periodically patterned magnetic substrates by phase difference magnetic force microscopy," *Ultramicroscopy*, vol. 136, pp. 96–106, Jan. 2014.

[261] I. G. Hughes, P. A. Barton, T. M. Roach, and E. A. Hinds, "Atom optics with magnetic surfaces: II. Microscopic analysis of the `floppy disk' mirror," *J. Phys. B At. Mol. Opt. Phys.*, vol. 30, no. 9, pp. 2119–2132, May 1997.

[262] K. E. Docherty, K. A. Lister, J. Romijn, and J. M. R. Weaver, "High robustness of correlation-based alignment with Penrose patterns to marker damage in electron beam lithography," *Microelectron. Eng.*, vol. 86, no. 4–6, pp. 532–534, 2009.

[263] K. E. Docherty, S. Thoms, P. Dobson, and J. M. R. Weaver, "Improvements to the alignment process in a commercial vector scan electron beam lithography tool," *Microelectron. Eng.*, vol. 85, no. 5–6, pp. 761–763, 2008.